DEVELOPMENT OF A NONDESTRUCTIVE TESTING TECHNIQUE TO DETERMINE FLAW CRITICALITY

C. E. HARTBOWER, C. F. MORAIS, W. G. REUTER, ET AL

AEROJET SOLID PROPULSION COMPANY

FOREWORD

This report was prepared by personnel of the Materials Technology Department, Aerojet Solid Propulsion Company, a Division of Aerojet-General Corporation, Sacramento, California. The research was supported by the Advanced Project Agency of the Department of Defense and was monitored by the Air Force Materials Laboratory, MAMN, under Contract F33615-68-C-1705.

This report covers the period of 1 March 1969 through 30 June 1971.

Effective Date of Contract: 1 July 1968

Expiration Date of Contract: 30 June 1971

Principal Investigator: C. E. Hartbower

Telephone: (916) 355-5048

Acknowledgement is given to P. P. Crimmins, the fourth author of this report and to Allen Green who served as Project Engineer in the initial phases of this investigation.

The authors are indebted to the following for their support and many helpful suggestions: Mr. Richard R. Rowand, Technical Manager for Nondestructive Testing and Lt. James W. Bohlen (USAF), both of the Processing and Nondestructive Testing Branch, Metals and Ceramics Division; and Dr. O. C. Trulson, Deputy Director for Material Sciences, Advanced Research Projects Agency.

This technical report has been reviewed and is approved.

Thomas D. Cooper
Chief, Processing and
Non Destructive Testing Branch
Metals and Ceramics Division

ABSTRACT

This report presents the findings of a study to develop a nondestructive testing technique to determine flaw criticality based upon stress-wave emission. The research included an evaluation of various sensors and instrumentation systems, and several materials and material conditions tested to failure in rising load and low-cycle, high-stress-intensity fatigue. The fracture testing utilized a linear-elastic fracture-mechanics approach. Acoustic emission was the basis of the nondestructive inspection technique.

The stress-wave-analysis technique (SWAT) was shown to be a highly sensitive nondestructive inspection method, capable of detecting growing defects at least an order of magnitude smaller than any other known NDI method and, with a computerized system, capable of locating one or more defects in real time. Thus, the stress-wave-analysis technique (SWAT) can be used for in-service, continuous, NDI. When defects emit stress-waves and yet are too small to be confirmed by conventional nondestructive inspection, the suspect area is placed under surveillance using an array of transducers. When the defect approaches critical crack size, the acoustic-emission count rate increases markedly, providing a precursor of crack instability and failure.

TABLE OF CONTENTS

TABLE LIST

FIGURE LIST

FIGURE LIST (contd)

FIGURE LIST (contd)

FIGURE LIST (contd)

FIGURE LIST (contd)

FIGURE LIST (contd)

FIGURE LIST (contd)

SECTION I

INTRODUCTION

A. HISTORICAL BACKGROUND

1. Two Decades of R&D

The use of acoustic emission as a nondestructive inspection technique has been under development for approximately two decades. The technique is based upon the elastic energy which is spontaneously released when a material undergoes plastic deformation and/or cracking. Thus, acoustic emission constitutes a unique nondestructive inspection method in that a material defect when propagating transmits a signal, with the sensor acting as the receiver. In other words, a material undergoing crack growth both generates and transmits the signal (acoustic emission) which then can be detected by suitable instrumentation and the source located using seismic techniques. In Germany, Kaiser[1]* reported what was apparently the first comprehensive investigation of acoustic emission in 1950. In the U.S.A. the researches of Schofield, et al[2-4] and studies at Aerojet-General Corporation[5-28] were largely responsible for triggering the current high activity in this new field of nondestructive inspection. Dunegan[29-32] at the University of California Lawrence Radiation Laboratory also did pioneering work in this area, but most of his early research was for the U.S. Atomic Energy Commission and, therefore, was not publicized. Graduate students at Michigan State University started working in this field around 1960 and continue to work with the stress-wave-emission phenomenon[33-36]. Likewise, other colleges and universities have been working with acoustic emission in the last five years[37-45].

Extensive research has been performed at Aerojet[13,14,18,23] which employed acoustic-emission to obtain a better understanding of crack-growth mechanisms. The most noteworthy observations from these researches are that acoustic emission (1) provides a sensitivity to crack growth that is unequaled by any other known method, and (2) provides a recognizable, reproducible characteristic that can be used to predict the onset of crack instability. A variety of materials have been tested including 7075, 2014 and 2219 aluminum alloys, HY-80, HY-100 and HY-150 steels, 6Al-4V titanium and D6aC steel. In each of the materials with useful toughness, stress-wave amplitude and rate of emission were found to provide a precursor to crack instability. Thus, in proof testing a pressure vessel or in monitoring a structure in service, one can not only detect and locate flaw growth but also make judgments as to the severity of a flaw.

---

* References appear at the end of the text, page 82.

2. Subcritical Crack Growth

In practice, conventional nondestructive inspection is not as reliable as one might expect. Quality Control is a vital consideration in man-rated vessels used in space exploration (including the deep-ocean environment). Practical experience has shown that occasionally a dangerous flaw will escape detection and cause premature failure in service. Some of these flaws are detected in proof testing tankage; i.e., if the proof test is successful, the tankage is destroyed in proof test before it gets into service. However, not all structures are suitable for proof testing, (a bridge, for example). Furthermore, proof testing sometimes causes subcritical crack growth, and sometimes subcritical crack growth occurs in service after proof test. Obviously, however thorough and effective the conventional nondestructive inspection (NDI) method, subcritical crack growth is a serious complication to quality control. The investigation reported here shows that the stress-wave analysis technique (SWAT) offers a new dimension in NDI sensitivity and a new capability for continuous inspection of critical structures.

3. Subcritical Crack Growth in Proof Testing

The basic philosophy of the proof test is that once a pressure vessel has withstood the proof pressure, subsequent loading to a lesser pressure will not produce failure. Obviously, this assumes that there will be no fatigue cracking in service and no slow crack growth of existing subcritical defects due to time-dependent mechanisms such as hydrogen, stress corrosion and/or strain aging. Without SWAT, experience shows that failure can occur in proof testing as a result of undetected subcritical crack growth. Moreover, when a material is susceptible to slow crack growth, the concept of the proof test is invalid; i.e., after proof testing, tankage can fail at a lesser load if stress-corrosion, strain aging, hydrogen or cyclic loading are involved in service. There are numerous examples to illustrate the fact of subcritical crack growth in proof testing as well as in service.

Consider the second-stage Minuteman[46], a 42-in.-dia rocket motor case which was proof tested with three cycles of ninety seconds each to 1.1 of the mean expected operating pressure (MEOP) with inhibited water. One chamber failed "prematurely" during the fourth cycle (a test-rig malfunction on the first cycle necessitated the 4th cycle to proof pressure). The failure occurred after 40 sec at pressure during the last cycle of proof testing. Thus, the chamber withstood a total of 220 sec at maximum pressure. The fabricator's failure analysis reported that failure initiated in the ID surface, in the fusion and heat-affected zone of the center girth weld. No cracks

were found by nondestructive inspection prior to proof testing. The only logical explanation for such a failure is subcritical crack growth during proof testing.

Consider also a first-stage Polaris rocket motor case which was proof tested with inhibited water at 1150 psig and held at pressure for 180 sec, with two or more pressure cycles. In the early development of the Polaris, there were numerous failures in proof test, and some had all the characteristics of subcritical crack growth. One chamber, for example, failed after 120 sec at proof pressure on the second test cycle. The chamber had been inspected by magnetic-particle, dye-penetrant, radiographic and visual procedures; all failed to reveal cracking. Another Polaris chamber failed after the second proof cycle during the first few seconds of depressurization, after withstanding a total of 360 sec at proof pressure.

The above examples show that incipient flaws in a pressure vessel can increase in size as a result of proof testing. The concern here is not only with those pressure vessels that fail during proof test (an economic loss) but also with those that suffer subcritical crack growth without failure in the proof test. The latter then enter service with enlarged cracks which may be subject to additional slow crack growth at service loads. However, if the proof test does not fail the pressure vessel and if a system is employed to detect and locate flaw(s) undergoing subcritical crack growth, the information gained from the proof test outweighs the damage done by slow crack growth. Furthermore, with the safeguard of SWAT, proof testing significantly above the pressure anticipated in service can be advantageous. For example, if a vessel survives the first cycle to 1.5 MEOP, then the largest flaw that can be present in the successfully proof-tested vessel is smaller than that at 1.1 MEOP[47]. Thus, a vessel which survives the first cycle at a proof pressure of 1.5 MEOP is less likely to fail in service because of the significantly smaller defects demonstrated to be present by the proof test. However, if SWAT is not used to detect flaw growth and permit unloading before a crack reaches critical size, the higher proof pressure (1.5 MEOP) will increase the probability of failure in the proof test itself.

The examples of subcritical crack growth cited in the earlier paragraphs involved high-strength materials. Some who are primarily concerned with lower-strength materials will take comfort in this. However, one other example should be considered. During the routine air-leak test of a large steel pressure vessel, a catastrophic brittle failure occurred at a pressure

of about 3,200 psig, even though the vessel previously had passed two hydrostatic tests at 7,500 psig. The pressure vessel was in the form of a sausage-shaped flask, about 15-ft long with a 19-1/2-in. ID and a 1-1/4-in. minimum wall thickness; it was manufactured in accordance with ASTM Spec. A372 Class 4, modified to a minimum yield strength requirement of 80,000 psi. Investigation of the failure[48] reveal that, following the hydrostatic test prior to leak test, the pressure vessel had been galvanized twice, including a five to eight hour warm-acid-stripping operation prior to the second galvanize. Hydrogen embrittlement arising from the acid stripping was suspected to be a factor contributing to the brittle failure. Standard Charpy V-notch impact tests revealed the 15-ft-lb transition to be 100°F and the FATT to be 125°F; the drop-weight NDT was approximately 80°F. Thus, the brittle condition of the steel was confirmed by the high transition temperatures of the pressure-vessel material (although the material met all requirements of the applicable ASTM specification). Nevertheless, the failure was considered to be unusual inasmuch as the pressure vessel had successfully passed two cycles of proof test to 7,500 psig and then failed at 3,200 psig in a routine air-leak test.

Positive assurance of the structural integrity of pressure vessels depends upon determination of (1) the initial flaw size, (2) the rate at which pre-existing flaws grow under operating conditions, and (3) the maximum flaw size the material can tolerate under operating conditions. Before proof testing (or leak testing, as in the preceding example), the only basis for estimating the initial flaw size is a knowledge of the quality-control procedures employed during fabrication. For example, if X-ray is the nondestructive inspection method used, then the largest crack in the pressure vessel at the time of proof testing might be estimated as being 2 percent of the thickness. If the critical crack size at the proof pressure is less than 2 percent of the wall thickness, then the pressure vessel may fail during proof test. (With acoustic emission as a nondestructive inspection method employed during proof test, one should be able to detect the growth of such a defect at loads well below the proof pressure, and discontinue the test before failure occurs.) If there are no cracks in the pressure vessel of critical size at proof pressure, then one can estimate the largest flaw at the start of service to be no larger than the critical crack size at the proof pressure. This then is the estimated <u>initial</u> flaw size.

One of the prime objectives of the ARPA research at Aerojet was to obtain quantitative relationships between crack size and acoustic emission cumulative count. Studies at Lawrence Radiation Laboratory[31] and

at Aerojet[23] have repeatedly shown a relationship to exist between stress-intensity factor and acoustic emission count. The importance of the relationship between stress intensity factor and acoustic emission lies in the possibility of estimating flaw size and failure load based on in-service, real-time nondestructive inspection of a flawed structure utilizing SWAT. Thus, in addition to providing a means to monitor subcritical crack growth, acoustic emission promises to provide a measure of a crack size at any particular time in service.

B. OBJECTIVE AND SCOPE OF THE CONTRACT

The overall objective of this study was to develop a nondestructive inspection system capable of detecting and locating flaws in structures and assessing their criticality. In the initial phase of the work, acoustic-emission instrumentation was evaluated including sensors, filters, and amplifiers, for their applicability to the detection, monitoring and analysis of stress wave emissions associated with material failure processes. In the final phase, quantitative relationships between emission data and flaw size were sought. Unflawed specimens were tested as well as specimens containing varying degrees of crack growth. Materials representing widely varying modulus, strength and fracture toughness were employed in these evaluations. Concurrent with the search for quantitative, reproducible relationships between fracture-mechanics parameters and crack growth, the following related factors were investigated: flaw-source-location techniques, high-noise-background discrimination, stress-wave characterization, wave form and attenuation, and the use of acoustic emission in detection of low-cycle, high-stress-intensity fatigue.

C. MATERIALS AND PROPERTIES

The materials used in this investigation are shown in Table I.

The D6aC steel was obtained in the mill-annealed condition as 0.1 in. and 0.3 in. thick surface-ground sheet and plate. The chemical composition (weight percent) and heat numbers of each are shown below. Both mill-certified analyses (supplied by Republic Steel) and check analyses performed at Aerojet are shown and indicate the composition of the materials are within the ranges specified for D6aC steel.

Thickness	Heat	C	Mn	Si	P	S	Ni	Cr	Mo	V
0.1-in.	3910262[a]	0.45	0.75	0.21	0.004	0.005	0.55	1.08	0.99	0.09
	Check[b]	0.47	0.70	0.23	-	-	0.54	1.08	0.94	0.12
0.3-in.	3952092[a]	0.48	0.74	0.23	0.005	0.006	0.56	1.07	1.00	0.09
	Check[b]	0.49	0.78	0.23	-	-	0.51	1.01	0.97	0.09

(a) Supplier Analysis
(b) AGC Check Analysis

Table 1. Materials and Properties

Material	Modulus psi x 10^6	Yield Strength (ksi)	Toughness K_{Ic} (a)	Toughness K_c (b)
D6aC	30			
600 temper		230	58	100
1100 temper		200	108	285
6Al-4V	16.4			
1000 aged		155	70	90
Annealed		130	56	174
7076-T6	10.4	80	31	52

(a) Plane-strain toughness based on COD pop-in
(b) Apparent fracture toughness at failure load for 0.1-in. thick material

The heat-treat procedure employed for processing the D6aC tensile, single-edge-notch and part-through-crack, tensile specimens is shown below. The indicated tempering cycles were employed to produce widely varying strength levels and fracture toughness. In order to prevent carburization, decarburization or other surface attack, austenitization was performed using a neutral salt bath followed by quenching directly to room temperature in agitated oil. Tempering was performed in an air atmosphere at the indicated temperature and time.

Austenitize - 1700°F - 30 minutes at temperature

Quench - Agitated oil at room temperature

Temper - High Strength/Low Toughness: 600°F - 2 hours
Low Strength/High Toughness: 1100°F - 2 hours

The 6Al-4V Titanium was procured as mill-annealed 0.1-in. and 0.25-in.-thick sheet and plate. The chemical composition (weight percent) of these materials supplied by the material producer (Reactive Metals, Inc.) is shown below.

Thickness	Type	Heat	C	N	Fe	Al	V	O	H(ppm)
0.1-in.	ELI	302443	0.03	0.009	0.08	6.3	4.2	0.110	48
	Standard	292796	0.02	0.007	0.09	6.1	4.2	0.126	33
0.25-in.	ELI	303109	0.02	0.011	0.16	6.1	4.4	0.120	103
	Standard	393412	0.02	0.014	0.08	6.4	4.2	0.125	129

The ELI grade was tested in the as-received annealed condition, while the STA grade was solution treated and aged as described below. Through this approach both a relatively low-strength, high-toughness (ELI grade) and a higher-strength, lower-toughness condition were evaluated.

Solution Treat: 1750°F for 15 min at heat, argon atmosphere

Quench: Water at room temperature

Age: 1000°F for 8 hours

The 7075-T6 aluminum was obtained in the heat-treated condition as 0.1 in. and 0.25 in. thick sheet.

SECTION II

ACOUSTIC-EMISSION INSTRUMENTATION

A. SENSOR RESPONSE

Continuous-wave and pulse responses were evaluated for nine stress-wave emission sensors. A reciprocity technique, as used in underwater-sonar-transducer calibration, was utilized in the continuous wave response determination. The pulse responses were obtained from shock waves produced by explosive squibs. Table II lists the sensors evaluated.

Table II. Sensors Evaluated for Continuous-Wave and Pulse Response

Manufacturer	Model	Type	Resonant Frequency
Endevco	2217	Mass Loaded	27 KHz
Endevco	2213	Mass Loaded	32 KHz
Panametrics	PZT-5	Unhoused	100 KHz
Dunegan	MHS140X	Backed Magnetic Case	120 KHz
Dunegan	S140A	Backed	140 KHz
Dunegan	D140A	Backed Differential	140 KHz
Aerojet	Experimental	Backed	200 KHz
Branson	X271A	Backed	400 KHz
Branson	X271	Backed	4000 KHz

1. Continuous-Wave Technique

a. Procedure

Response curves of voltage amplitude versus frequency were developed for each sensor by the substitution method. With this technique, the sensor being evaluated for sensitivity was substituted for a transducer of known sensitivity in an acoustic field varied over the range of interest. Seven of the sensors listed in Table II were evaluated over the frequency range of 1 KHz to 1200 KHz. The remaining two sensors (Panametrics PZT-5 and Aerojet-Experimental) were evaluated over the range of 50 Hz to 500 KHz and 10 Hz to 500 KHz, respectively.

These calibrations were performed at the Aerojet-General Corporation's Oceanic Systems Department's Transducer Laboratory in Azusa, California using the test setup shown in Figure 1. The sensor and projector were submerged in a large tank of water. The acoustic field was generated by

applying a known ac voltage of the desired frequency across the terminals of the projector. The standard transducer was placed in the sound field and its output recorded. The standard transducer was then replaced by the sensor whose sensitivity was to be measured and a record made of its response. The responses of the two transducers were compared and the results plotted over the frequencies investigated.

The standard transducers used in calibrating seven of the sensors listed in Table II, were obtained on loan from the U.S. Navy's Underwater Sound Reference Division (USRD), Naval Research Laboratory, Orlando, Florida. An Atlantic-Research Type LC-32 hydrophone was used as the standard over the frequency range from 1 KHz to 100 KHz and a USRD Type E-8 hydrophone was used as a standard from 100 KHz to 1.2 MHz. An Atlantic Research Type LC-5 hydrophone was used as the standard for the remaining two sensors (Panametrics PZT-5 and Aerojet-Experimental) for the frequency region below 100 KHz. Direct comparison of responses between 90 KHz and 150 KHz was not made in some cases because the lack of sensitivity of hydrophones at low sonic pressure levels. In such cases, particularly for the Type-E8 hydrophone, the hydrophone was subjected to a sound field high enough to produce a clear signal and the data were corrected accordingly. Figure 2 presents the standard transducer calibration response curves for the USRD-E8, LC-32 and LC-5 hydrophone standards, respectively. The USRD-E8 hydrophone was returned to the Navy prior to the calibration of the Panametrics and Aerojet sensors; therefore, the LC-5 hydrophone was used in place of the USRD-E8.

A Scientific-Atlanta Sound-Measuring System was used to produce the signal supplied to the projector and to process and record the data. In addition to the Sound Measuring System, an Ithaca Type 1446 low-noise amplifier was used at the sensors. Two of these amplifiers were used for the calibration of the Dunegan Research Differential transducer, and in addition, a Tektronix Type 545B with a Type-D differential plug-in amplifier also was used.

b. Results

The continuous-wave (CW) response of each sensor is shown in Figures 3 through 11, whereas Figure 12 is a comparison of the response of each sensor type on common axes. Since each sensor was calibrated in identical setups, the only variable in these data is the sensor itself. The capacitance due to the length of cable between the sensor and the preamplifier will alter each sensor sensitivity; however, a relative comparison between their responses is considered valid. The overall response of the mass-loaded accelerometers is better than the other sensors to slightly over 100 KHz, at which point the mass-loaded sensors drop off in sensitivity. Above 100 KHz both Branson sensors show the highest sensitivities at approximately 200 to 300 KHz.

2. Pulse Responses

a. Technique

These tests were conducted at Aerojet-General's Oceanic Systems Department's Transducer Laboratory in Azusa, California. The response of each sensor was evaluated by subjecting them to a shock wave produced by Hercules Type-SR Vibrocaps. The sensors were submerged five feet in a tank of fresh water, 45 ft from the explosive caps. Two 4-ft copper leads were attached to the caps and these leads were used to apply 12 volt ac to activate the charge.

The sensor's output signal was provided to a Tektronix Type 545B oscilloscope using a Type CA plug-in amplifier. The Type-CA plug-in amplifier and oscilloscope provided a dc to 24 MHz frequency-response capability. The oscilloscope was operated in the external-single-sweep mode. The sweep was started by a voltage applied to the trigger input, which, for these tests, was produced by an Atlantic-Research Type LC-32 hydrophone that was positioned approximately 1.5 in. in front of the sensor under calibration. Figure 13 shows a block diagram of the test setup used for these sensor pulse-response determinations.

b. Results

The photographs reproduced as line drawings in Figure 14 shows the response of eight commercially available transducers to the shock wave produced by a cap detonated underwater. Note that the output of the Branson sensor was approximately 15 volts as compared to 0.15 volts for the PZT-5 sensor. Figure 15 shows the response of the USRD E-8 hydrophone and the Aerojet experimental transducer.

3. Discussion of Results from Continuous-Wave and Pulse Response Tests

A comparison of the responses of the various sensors to continuous-wave and pulse signals must be made under guidelines determined by (1) the phenomena to be measured and (2) the application to which the measurement will be made. If it is assumed that the phenomenon of interest (acoustic emission) is created by rapid, discrete movements within the material, any sensor will be useful in an acoustically noisy environment if its response over a broad frequency range will allow selective electronic filtering to improve the signal-to-noise ratio. In this event, band-pass or high-pass electronic filtering may significantly reduce the background noise levels so that pulse-shaped transients can be received.

The continuous-wave response of each sensor indicates the lack of high-frequency sensitivity for the mass-loaded (accelerometric) and

PZT-5 (unhoused) crystal. The accelerometric sensor shows substantially better response to the lower frequencies. The low sensitivity of the unhoused PZT-5 crystal is noteworthy since many of the workers in the acoustic-emission field are apparently using it in their programs. It is interesting to note that resonance in the range of 400 to 700 KHz in the Endevco 2213E accelerometer produced higher signal level (-110 db) than the Panametrics PZT-5 (-115 db) in the range of 300 to 500 KHz.

In general, all sensors appear to have sufficient sensitivity, when coupled with low-noise-amplification stages. This study was not extended beyond 1.2 MHz because of the lack of a suitable standard transducer and the additional complexities involved in the entire instrumentation system. As previously mentioned, sensor usage is generally accomplished with low-noise amplification and selective filtering to reduce background noise levels and enhance signal detection; through this approach, all sensors evaluated can be used satisfactorily in an emission system where detection, and not fidelity of signal wave form, is of prime importance.

The method used in conducting these response calibrations is such that a compressional wave is transmitted and thus the sensor response curves are for the compressional wave. The relative response on some of these same sensors was also obtained by a back-to-back mounting method, in air, over a frequency range of 0 to 200 KHz or 100 to 200 KHz by Lawrence Radiation Laboratory, Livermore, California. Difference in response sensitivity levels were shown between the back-to-back air-and-water immersion calibrations; however, the shape of the response curves were in good agreement. The primary reason presented for this difference in response sensitivity appears to be in the capacitance of the sensor's crystal and the variable loading effect which the same length of cable would have on each sensor. Adjustments to the sensor's crystal capacitance and/or variations in the length of cable used will affect sensitivity. Again, however, since only the sensor was varied in the tests conducted for this program, the comparative analysis of responses between the sensors is considered valid.

4. Pulser Simulation of Stress-Wave Emission

a. Instrumentation Systems Based on a Single-Type of Transducer

Aerojet research[5-28] has been directed primarily to mechanisms of slow crack growth and use of stress-wave emission as a precursor of failure. One of the basic instrumentation systems used in these laboratory studies is shown schematically in Figure 16. The sensor in the Aerojet studies generally has been a mass-loaded piezoelectric accelerometer (Endevco Model 2213) with a mounted resonant frequency of approximately 30 KHz. Figures 17, 18 and 19 are included here to illustrate the information that can be obtained

with such an instrumentation system. In obtaining the data for each of these figures, a fatigue precracked tension specimen was held under constant load in an environment producing stress-corrosion cracking. Other mechanisms producing subcritical crack growth also were investigated, including strain aging, hydrogen embrittlement and fatigue. Figures 18 and 19 illustrate the detailed data that can be obtained; each plotted point corresponds to an increase in stress-wave emission count. Note the periods of dormancy punctuated with bursts of stress-wave activity.

One of the most recent researches, again using an Endevco 2213 accelerometer as the sensor, was a study of delayed cracking in submarine steel. Figure 20 is a schematic of the system used. Note that the Dunegan totalizer is used instead of electronic counters. In this case, the weldments were under no external load, only the inherent residual stresses produced by welding. From Figure 21, it will be seen that the sensor detected tremendous activity during and immediately after welding; and from Figure 22, note that the bursts of stress-wave emission continued for many hours after the weldment had cooled to room temperature.

Many have questioned the use of an accelerometer which according to the manufacturer's data has a mounted resonant frequency of 30 KHz in a system involving 100 to 200 KHz high-pass filtering. Section II,A,1 of this report has shown why this can be done when there is adequate signal amplification. However, much needs to be learned about sensors and their response to stress-wave emission. To facilitate such study, a device was utilized to simulate the stress wave under controlled, reproducible conditions. The device is called a "pulser".

b. Pulser Determination of Wave Shape and Duration

In fracture testing, stress-wave emission is routinely observed on an oscilloscope; in such testing, one observation that repeatedly has been made is that the duration and ring down of the signals vary throughout a given test. Therefore, the pulser was used to determine the stress-wave shape and frequency as a function of load. The test piece was a single-edge-notched specimen without a fatigue precrack. The overall system including the pulser design is shown in Figures 23 and 24.

Two sensors were used, viz., an Endevco 2213 accelerometer and a Dunegan S-5-250 sensor, both mounted on the test specimen as shown in Figure 24. The electrical input to the pulser was in the form of a square wave 5μ-sec wide, 150 millivolts amplitude and 10 nano-sec rise and fall time. This input signal was held constant for these observations.

If the signals observed on the oscilloscope at zero load are compared with those at 10-kip increments (Figures 25 to 30), it will be

noted that the wave duration and amplitude fluctuated, decreasing in duration at first and then increasing as the load was increased. The frequency of the output signals, on the other hand, remained essentially constant, with a predominant frequency of approximately 225 KHz from the accelerometer and approximately 150 KHz from the S-5-250 sensor.

Further comparisons are unwarranted because the sensors were mounted in different ways (stud versus cement) and at different locations on the test specimen.

c. Use of Pulser to Determine Sensor Response

The pulser described in the previous paragraphs was used to simulate the signal emitted from an increment of flaw growth. With the pulser, it was possible to transmit a reproducible signal to the sensors under study and determine their response as a function of gain, filter mode (high-pass versus band-pass), filter frequency, pulse width and input voltage. Unless otherwise stated, all pulser data in this and the following sections were taken from an unloaded single-edge notch tension specimen.

(1) Sensor Response as a Function of Total System Gain and Model of Amplifier

(a) Total System Gain

The results of two tests are shown in Figure 31 using the input signal and instrumentation shown in the figure. The input signal and system used to collect the data will be shown on all figures and tables. The input signal had an amplitude of 2.0 volts, a pulse width of 5.0μ-sec and a rise time and fall time of 10 N-sec. The rise and fall time were held constant at 10 N-sec for all pulse data, whereas the amplitude and pulse width varied. Observe that the only difference between the two plots was that the amplifier Model 1027C was set at 20 db (X10) for the first test and 40 db (X100) for the second test. Figure 31 shows the output voltage and signal-to-noise ratio versus high-pass-filter frequency for three sensors, viz., Endevco accelerometer Model 2213, Endevco Compression Piezite-15 experimental sensor, and Dunegan Model S-140B. Observe that in all instances the output voltage and signal-to-noise ratio decreased with increasing high-pass filter setting. Note also that the Compression P-15 sensor has the highest output signal as well as the greatest signal-to-noise ratio, followed by that of the 2213 and finally the S-140B. From Figure 31, it is obvious that the Compression P-15 would give more information as it would yield a larger stress-wave-emission signal for the same increment of flaw growth, and since the signal-to-noise ratio is higher, it would be possible to observe smaller increments of flaw growth. A comparison of the 20-db gain and 40-db gain amplification in Figure 31 shows that the signal-to-noise ratio increased between 2-1/2 and 3 times, and the voltage output increased between 9 and 10 times when the

amplifier was increased from 20 to 40 db. As the output signal was amplified to a greater degree than the noise, increasing the gain can be a simple method to elevate the signal above the noise. However, this technique is limited by saturation of the amplifier; when an amplifier is saturated no additional output will be obtained regardless of how much the gain is increased (see Figure 32). Figure 32 illustrates another possible limiting factor, in that at some point the noise increases faster than the stress-wave signal.

(b) Amplifiers

As the above section illustrated the sensor response to a change in gain, it was questioned whether or not the signal-to-noise ratio could be altered simply by using a noisier or quieter (manufacturer supplied information) amplifier. A Model 102E amplifier (operated at 40 db) was substituted for the Model 1027C preamplifier used in obtaining the data of Figure 31. The manufacturer's specifications for the amplifiers are listed in Table III. Based on the manufacturer's specifications, the Model 1027C preamplifier has a lower noise level than Model 102E. Figure 33 is a plot of output voltage and signal-to-noise ratio versus high-pass-filter level for the three sensors using the Model 102E preamplifier. Observe by comparing Figures 31 and 33 that although the output voltage was approximately 10 percent greater for the 1027C amplifier than for the 102E amplifier, the signal-to-noise ratio was from 2 to 3 times greater for the 102E than for the 1027C, This observation would lead one to the conclusion that the 102E amplifier is a better choice for the detection of small stress-wave emissions, i.e., small increments of flaw growth. There is nothing in the manufacturer's specifications that would lead one to this conclusion, illustrating the need for testing. In Figure 33, the Compression P-15 sensor had the highest output voltage,and for high-pass filtering above 125 KHz it had the highest signal-to-noise ratio. When high-pass filtering below 125 KHz, the 2213 sensor exhibited the highest signal-to-noise ratio. The signal-to-noise ratio is a measure of a sensor's ability to detect a signal from the background noise.

(2) Sensor Response as a Function of Filter Mode

The above results were obtained with high-pass filtering; as much of the specimen testing is done with band-pass filtering, a series of tests were conducted with this filter mode. Figure 34 is a plot of filter frequency versus output voltage with the low side of the band variable and the upper side of the band constant at 2000 KHz. It is apparent that a higher output voltage was obtained for the band-pass filter mode. Apparently the filter dynamics are such that gain is obtained from the band-pass mode; this occurred for all three sensors.

The same observations concerning high pass and band pass was made for data shown in Table IV where results obtained by filtering

TABLE III

CHARACTERISTICS OF AMPLIFIERS AS SUPPLIED BY MANUFACTURER

	Model Number	
	102E	1027C
Voltage gain	40 db ± 10% @ 5 KHz	40 ± .5 (non inverting)
Gain Steps	-	10 db
Frequency Resonance	1 Hz to 5 MHz for 3 db band width	3 Hz to 400 KHz for 2 db band width
Noise	2-5 microvolts	over 150 db below 1 volt
Equivalent Input Noise	5 microvolts	-
Distortion	less than 1%	-
Input Resistance	150 K	over 1000 meg ohms
Input Capacitance	20 pf	less than 4 pf
Output Impedance	200 ohms	30 ohms
Maximum Output Current	1.3 ma (rms) for 100 ohm load	.7 ma
Maximum Output	4 volts (rms) at mid band	12 volts (pK-pK) to 100 KHz (increases proportionally with increase of supply voltage)
Power Supply	-	Internal

in a high-pass mode were compared to that of band pass. The results shown in Table IV were obtained from five sensors; note that the output voltages for all five sensors were larger for band pass than for the high-pass mode. The results in Table IV were not as clean as those in Figure 34 because of the desire to obtain cumulative stress-wave emission counts (TSWE) which required some changes in the set point. However, the variations in set point would cause a maximum change in the gain of 0.2 percent which does not explain the increased output voltage observed with band-pass filtering.

(3) Sensor Response as a Function of Input Voltage and Pulse Width

(a) Input Voltage

Plots of input voltage versus output for a constant pulse width are shown in Figure 35 for five sensors, including two not evaluated in the previous tests, viz., Endevco Shear P-15 and an Electra Scientific sensor. Note that each section of the figure is for a different band-pass with the upper side of the band constant at 2000 KHz. Essentially, there is a straight line relationship between input and output voltage for a constant band-pass region. As would be expected, the output voltage decreased with decreasing band-pass size. For 2000 mv input, the band-pass filter started at 200 KHz for some of the sensors, as the amplifiers were saturated when filtered at 100 KHz. Observe in Figure 35 that the Endevco Shear P-15 exhibited the maximum output voltage. In Figures 31 and 33, the Compression P-15 had the highest output, whereas Figure 35 shows that the 2213 now has a higher output, but only for the 100 to 2000 and 200 to 2000 KHz band-pass regions. Of interest is the observation that the output voltages were essentially the same in the 100 to 2000 KHz band for the 2213 and the Electra-Scientific sensors. None of the sensor characteristics supplied by the manufacturers explain why the output voltages are the same for the Endevco 2213 and the Electra-Scientific sensors.

(b) Pulse Width

Plots of pulse width versus voltage output are shown in Figure 36. The data for this figure were obtained using the same system as above, but each plot for a different band-pass filtering frequency. For band-pass filtering in the range of 100 to 2000 KHz, the 2213, the Electra-Scientific and the Shear P-15 gave a sawtooth pattern whereas the output for the Dunegan and Compression P-15 remained essentially constant, but at a lower value. As the band-pass filter range decreased from 100 to 2000 KHz to 500 to 2000 KHz it is apparent that the scatter in voltage output decreased appreciably until at 400 to 2000 KHz the data could be plotted as a narrow band. In the band-pass regions, 100 to 2000 KHz and 200 to 2000 KHz, it is apparent that the output voltage would vary with pulse width for the 2213, Electro-Scientific and Shear P-15 sensors which could explain some of the scatter observed in the

TABLE IV

OUTPUT VOLTAGE AND TSWE/PULSE FOR HIGH-PASS AND BAND-PASS FILTERING

Sensor	Set Point		Output Voltage		TSWE Counts	
	High Pass	Band Pass	High Pass	Band Pass	High Pass	Band Pass
Electra-Scientific						
ES-6017	2.48	2.66	14.0	17.0	543	537
Endevco						
Shear	2.20	2.08	14.0	16.0	532	641
Model 2213	2.55	2.78	10.0	14.0	428	620
Compression	2.76	2.15	8.0	14.0	456	597
Dunegan						
S-140B	2.65	2.70	-	3.5	-	408

(a) High-pass filtering 1000 KHz
(b) Band-pass filtering 1000 KHz to 2000 KHz

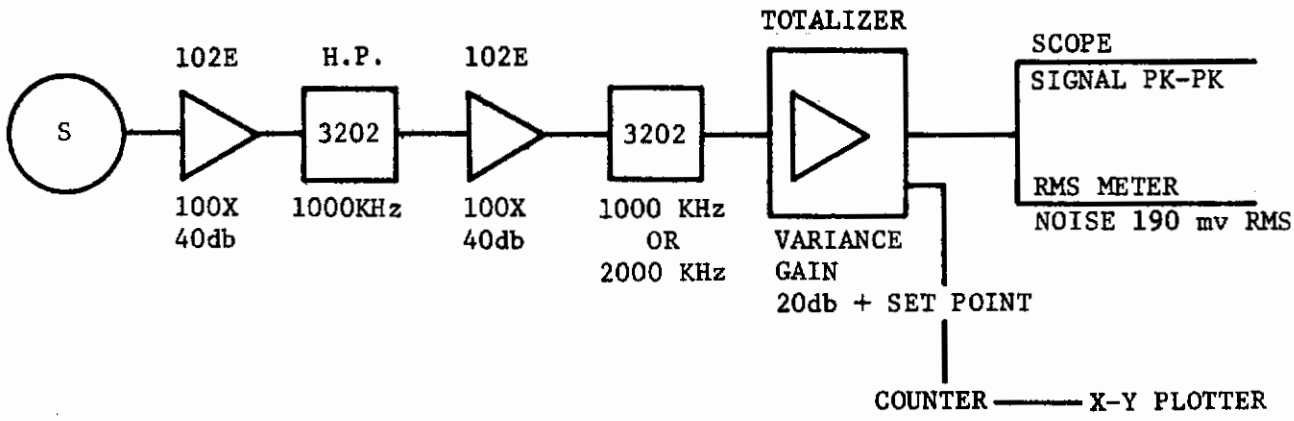

relationship between TSWE and crack growth size. The Compression P-15 and Dunegan sensors were found to give less voltage output for a given input signal but were essentially independent of pulse width.

(4) Sensor Response as Measured by TSWE

The measurement of voltage amplitude allows for a quick and concise method of determining the effect of the various variables on sensor response. The signal-to-noise ratios determined from voltage measurements were useful in that they defined the best system, from the components tested, for detecting the smallest stress-wave emission. The optimum instrumentation system was indicated to consist of Model 102E amplifiers, each at 40-db gain, and filtering in the band-pass mode. However, in the final analysis, it was considered necessary that data be obtained concerning the effect of system variables on sensor response as measured by stress-wave emission count.

Figure 37 is a plot of pulse width versus output voltage with the modified instrumentation system. Note that the results in Figure 37 do not show the grouping of sensors into two regions as was observed in Figure 36. A comparison between Figures 36 and 37 indicates that with the modified instrumentation there was from two to four times the output voltage even though the input voltage was half as great. The increased output voltage was due to the set-point adjustment which was required with the Dunegan totalizer system (NS-1A) to maintain a constant noise level for all sensors. The totalizer system triggers at a constant non-adjustable voltage of 0.707 v rms. This means that data are lost between the noise level and 0.707 v rms; therefore, it was the practice in this study to adjust the gain to a constant noise value just below the trigger level. If the trigger level of the Dunegan totalizer were adjustable to the noise level, it would be a more versatile piece of equipment. Another point of interest was that the sawtooth pattern observed in Figure 36 was not observed in Figure 37. A possible explanation for the absence of the sawtooth pattern in Figure 37 could simply be that the sharp increase occurred at a pulse width of 10μ sec in Figure 36 and the data was inadvertently missed for that collected for Figure 37. Additional possible explanations for the absence of the sawtooth pattern in Figure 37 could be the result of a difference in response due to a factor of 10 increase in gain or the change in input voltage from 1000 mv to 500 mv.

Figure 38 is a plot of TSWE (count) per pulse for the same system shown in Figure 37. The test results were generally independent of pulse width, with the exception of the 2213 and to a lesser extent, the Electra-Scientific sensor. The results in Figure 38 show that the Electra-Scientific and 2213 sensors had the highest TSWE per pulse. The relative relationships for the sensor output are valid only for the band-pass region of

200 to 2000 KHz and an input voltage of 500 mv, because of the observation in Figure 36 that the output voltage was affected considerably by the band-pass filter range. As the set points differed for each sensor, the total gain for each is recorded in Figure 38 where it can be noted the variation was less than a factor of two.

It was pointed out in the above that the set-point control defines the system gain; therefore, a short test series was run collecting the results for a constant set point and for a variable set point which would result in a constant background rms reading (665 mv). Table V shows the system, input voltage and lists the output voltage and TSWE per pulse for two set-point values for each sensor. A common set point of 5.0 and a constant input voltage of 250 mv were arbitrarily selected for the initial test. The Shear P-15 had the largest output voltage and TSWE per pulse. For a constant set point of 5.0, the P-15 sensors had the largest background noise reading and the 2213 the lowest. When the set point was adjusted so the background noise was constant at 665 mv rms the 2213 and Compression P-15 had the highest and the lowest output voltage, respectively; whereas, the Electra-Scientific and Compression P-15 had the highest and lowest TSWE per pulse, respectively. As the existing totalizer system has a constant trigger level, at 0.707 v rms, the results in Table V show that the Electra-Scientific and 2213 sensors would detect the smallest amounts of crack growth. As was noted previously, these results are valid only for an input signal of 250 mv with a pulse width of 10μ-sec and band-pass filtering of 200 to 2000 KHz.

A comparison of the band-pass and high-pass filter results can be made in Table IV. As was noted previously, the results in Table IV were not as clean as those in Figure 9 because of the desire to obtain TSWE data which required some changes in the set point. The stress wave count per pulse was greater for band-pass than for high-pass filtering. For two sensors, the shear P-15 and the 2213, the increase in TSWE per pulse was proportional to the change in voltage, but for the Electra-Scientific and the Compression P-15, the increase was not proportional.

(5) Sensor Response for a Different SWAT System

For this test sequence, a different amplifier-filter system was used as shown in Table VI, which shows the system, input signal, set point required for a noise level at 665 mv rms, output voltage and lists the TSWE per pulse. The Electra-Scientific required the maximum gain increase as noted by the set point of 4.4; whereas, the set points for the other four sensors ranged from 3.46 for the Dunegan sensor to 3.96 for the Endevco 2213. For the same input signal, the maximum voltage output was observed for the 2213 sensor and the Shear P-15 and 2213 sensors gave the largest value of TSWE per pulse. These observations are in general agreement with those observed in Table V. Again, it must be pointed out that these results are valid only for

TABLE V

OUTPUT VOLTAGE AND TSWE/PULSE AS A FUNCTION OF SET POINT (GAIN)

Sensor	Set Point	RMS Noise Level (mv)	Output Voltage	TSWE/ Pulse
Electra-Scientific				
ES-6016	5	280	7.6	162
	10	665	14.0	338
Endevco				
Shear	5	542	12.0	210
	5.3	665	10.0	221
Model 2213	5	255	11.5	180
	10	665	16.0	309
Compression	5	525	6.0	162
	5.3	665	6.0	167
Dunegan				
S-140B	5	315	5.0	72
	9	665	8.0	170

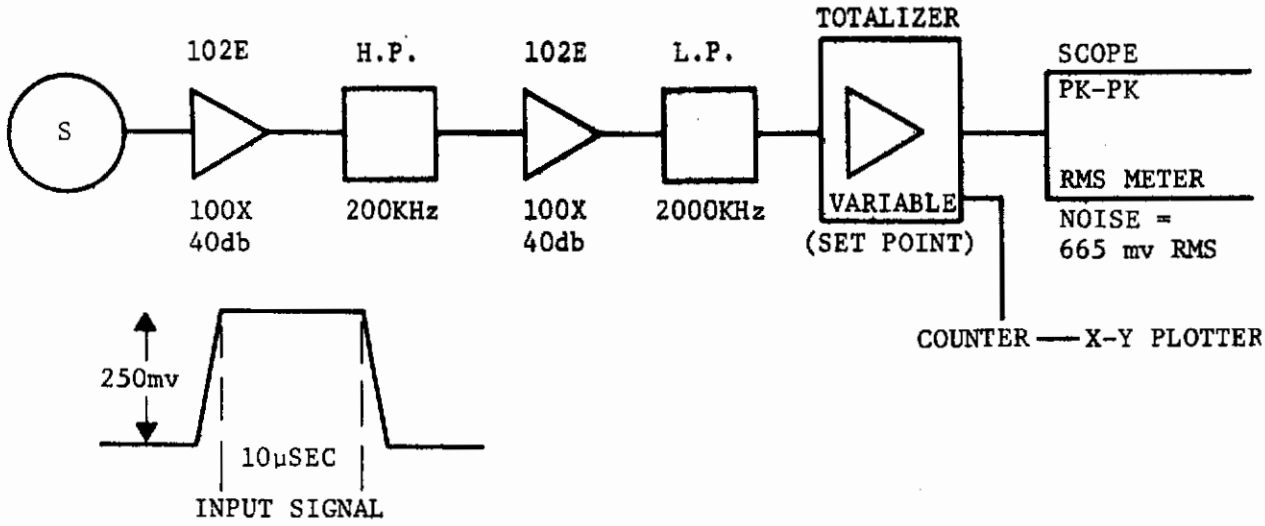

TABLE VI

OUTPUT VOLTAGE AND TSWE/PULSE FOR A SECOND AMPLIFIER-FILTER SYSTEM

Sensor	Set Point (a)	Output Voltage	TSWE/ Pulse
Electra-Scientific			
Model 6017	4.40	15.0	216
Endevco			
Shear P-15	3.74	17.5	306
Model 2213	3.96	18.4	303
Compression P-15	3.66	13.0	228
Dunegan			
S-140B	3.46	15.0	208

(a) Set point to get noise level to 665 mv rms

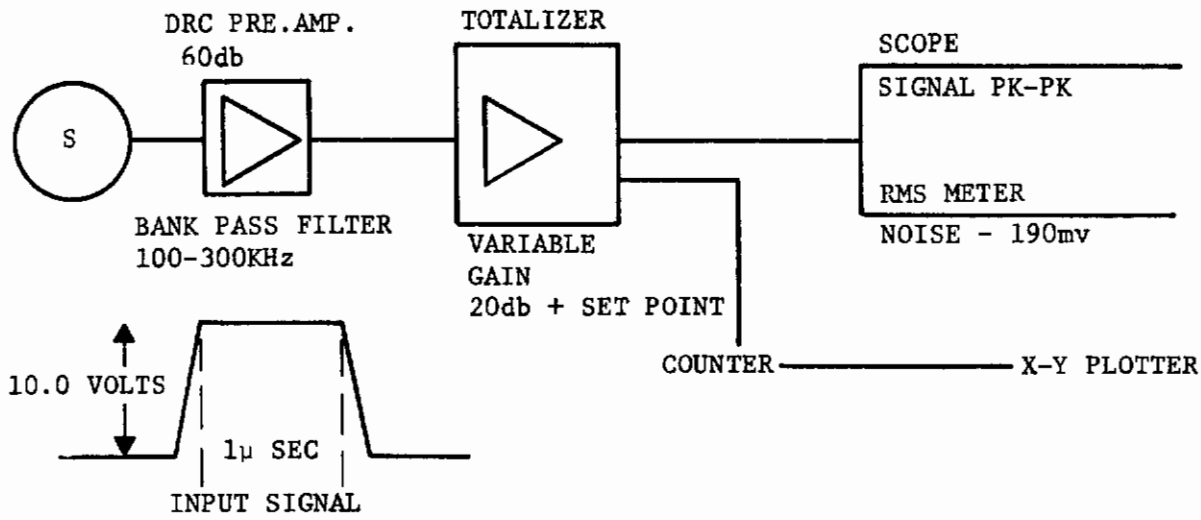

input signal of 100 volts, a pulse width of 1μ sec, and band passing at 100 to 300 KHz. It is interesting to note, however, that for the two widely different systems and input signal, shown in Tables V and VI that the relative sensor sensitivities were not affected.

B. INSTRUMENTATION SYSTEMS

1. Acoustic Emission for Nondestructive Inspection

An example of a real-time computer-based system is described in the following paragraphs. The operation of the system is relatively simple due to the inclusion of self-checking circuits in the digital analyzer and software. The sensor-preamplifier packages are located on the test vehicle at the test site using conventional surveying procedures. The number and arrangement of the sensors are determined by the size and shape of the test vehicle up to the maximum available in the system. The sensor packages are connected by coaxial cables to the patch panel of the main acoustic-emission-instrumentation consoles. These consoles contain all other components except the teletype and remote-video display. The teletype is a self-contained unit which can be located up to fifty feet from the main instrumentation consoles.

The major components are mounted in two consoles housing module racks, power supplies, computer systems and peripherals. These consoles incorporate such features as an anti-tilt base, cooling fans, filter covers and other features as required to permit convenient operation and transportation of the system. The overall system is shown as a schematic in Figure 39.

a. Acoustic Emission Acquisition

The acoustic-emission-aquisition subsystem consists of integrated sensor-preamplifier packages, sensor power supply, amplifiers and filters with associated interconnecting cables. In practice, the sensor-preamplifier packages are attached to the test article, while the power supply, amplifiers, and filters are mounted in central data-processing racks.

(1) Sensor Preamplifiers

The acoustic-emission-integrated sensor-preamplifier package utilizes a high-Q quartz sensing element coupled to a built-in impedance converter (preamplifier) through a high-pass filter. This subsystem responds to acoustic emission with a high-amplitude, short-duration ringing at its natural frequency and does not readily respond to extraneous low-frequency disturbances. The mounting base is electrically isolated from the housing.

(2) Sensor Power Supply

The sensor power supply provides constant current for powering the sensor channels. The unit operates the acoustic-emission sensors in a constant-current mode and supplies additional current for driving long cables. It also maintains constant sensitivity if the supply voltage fluctuates. A color-coded meter is used to selectively monitor each individual channel for normal system operation and indicates faults by monitoring the bias voltage on the signal/power lead.

(3) Filters

These units are all solid-state, variable, electronic filters with high-pass, low-pass, band-pass capabilities plus continuous tuning over the range of 20 Hz to 2 megahertz. The basic frequency-response characteristics of the filter closely approximates a fourth-order Butterworth with maximal flatness for cleanest filtering in the desired frequency domain. To meet the requirements of time domain, a switch changes the basic response to a simple R-C to provide superior pulse or complex (transient) signal filtering. Pass-band gain is unity and the single-channel attenuation slope is 24 db per octave. Each channel consists of four cascaded R-C elements coupled by isolating stages. A front-panel switch selects high-pass or low-pass filter functions.

(4) Amplifiers

The amplifiers accept the signal output from the sensor-preamplifier package and further amplifies the acoustic-emission signal. This system provides the capability of gain adjustment for 1000, 5000, 10,000, 50,000 and 100,000. The frequency response of the amplifiers ranges from 30 KHz to 300 KHz (-3 db at 300 KHz). The output of this system is routed to the filters and then to the graphic system, logic and processing system.

The amplifier system is a multi-channel, multi-stage transistorized feedback amplifier. The circuit is designed for maximum flatness and freedom from peaking. A 5-position rotary switch provides the 5 fixed-gain steps. These gain steps provide the versatility necessary to meet most test requirements.

b. Acoustic Emission Processing

The acoustic emission data processing system analyzes the signals detected by the data acquisition system and provides digital and analog outputs to the components of the data presentation system. The major output of the processing system relates to acoustic-emission rate, emission cumulative-count and emission-source location.

The major components of the data processing system include a logic module, digital analyzer and required programming.

(1) Digital Analyzer

The digital analyzer operates on the detected signal received from the filters and converts it to a form suitable for further processing by the computer. Initially, the signal is processed through a voltage comparator that detects a change in signal level, the output of which is routed to a series of flip-flops which senses arrival times and order of arrival of the acoustic-emission signal. Of the total number of channels, only the first four channels to receive the signal are recorded. The information is converted to a binary format and routed to the accumulator of the computer.

(2) Computer

The computer receives the signal from the digital analyzer. Within the computer, the detected signals are operated upon to provide the output for source location and data presentation by the various system components including the teletype, video and audio devices. Various computer models may be employed. A typical one would be a Model PDP-8/E which is a fast and compact general-purpose computer expanded to 8000 words in order to provide greater versatility. The computer is capable of further modular expansion to 32,000 words. This machine is quite flexible and has a high-capacity input/output capability that allows it to operate a variety of peripheral equipment besides the standard keyboard and paper-tape-punch-and-reader equipment.

(3) Computer Programming

The computer is programmed to operate on the acoustic-emission data. A main and a test subroutine triangulation program is employed. The triangulation program (main program) for a test vehicle is written so that location of the acoustic-emission sources can be automatically furnished as data output. Through this system, all data handling techniques can be automatically accomplished and displayed in real-time so that decisions or actions may be taken. The computer, functioning as process control, can also be programmed to make decisions and react to any pre-established situation such as continuous surveillance of critical components.

The main program provides real-time triangulation to the acoustic-emission source. This program locates the individual sources on a video display as an X-Y coordinate on a background representing the test article in flat pattern. The main program also services the time clock and

counters which show total counts for each sensor when it is the first sensor activated. These counts are transmitted to and tabulated by teletype at programmable clock intervals determined by the operator.

The subroutine test program provides the necessary instructions to post the first four sensor numbers that are activated, the corresponding three time differences and the test time in hundredths of hours. This information is posted by the teletype. The program also is used during the test calibration and posttest setup procedure in conjunction with the acoustic-emission simulator. This program also can be used for monitoring small, simple test articles where only a tabular format is desired. A typical teletype record for the subroutine program is shown below:

1st Channel	2nd Channel	T_1	3rd Channel	T_2	T_3	4th Channel	Test Time
10	2	41	5	70	90	6	0.03

The numbers listed under the channel headings are the channel numbers identified in the order of acoustic-emission arrival. The numbers presented under T_1, T_2 and T_3 headings represent arrival time in microseconds between the 1st and 2nd channels, 1st and 3rd channels and 1st and 4th channels, respectively. Readout time per pulse is 7-1/2 sec.

c. Acoustic-Emission Data Presentation

The acoustic-emission data are presented in real-time by audio, graphic, video (console) and tabular means. Each component is described below.

(1) Audio Monitor

The audio monitor is a subsystem of the totalizer system which is mounted in the main instrumentation racks. This monitor uses the heterodyning principle to convert high-frequency acoustic-emission signals to the audio frequency range. It makes use of a mixer, speaker, and local oscillator. The local oscillator frequency is adjustable to the resonant or a harmonic of the resonant of the acoustic-emission sensor.

(2) Graphic-Emission-Totalizer System

The acoustic-emission totalizer is mounted in the main instrumentation racks. This system consists of three basic units; i.e., the totalizer, an X-Y plotter and a ramp selector.

The emission totalizer further amplifies the acoustic-emission signals and digitally counts events which then exceed a 1-volt threshhold. Gain is adjustable from zero to 40 db. Integrated-circuit digital counters store the number of events. A precision digital-to-analog converter generates a proportional DC voltage to drive the panel meter and external plotters. Zero and full scale (10v dc) output voltages can be selected from a switch to facilitate calibration of an XY plotter. A monitor output is provided for an oscilloscope or recorder. The output is suitable for driving long cables. The totalizer power supply provides the physical mounting, electrical connections and regulated voltages required for acoustic emission totalizer subsystems such as the audio monitor, ramp generator and totalizer.

The X-Y recorder graphically presents the output from the acoustic-emission totalizer and the ramp generator or a pressure transducer.

The ramp generator provides a ramp voltage with both precision amplitude and time scale. The purpose of this unit is to drive the X axis of a plotter for cumulative acoustic-emission counts vs time.

(3) Video - Console Display Unit

The console display unit is mounted in the central instrumentation racks and provides the system operator with a video output display of the test data and/or calibration test data. It is possible to make a flat-pattern, transparent overlay of the test vehicle on the screen of this unit thereby providing a means of visually locating the signal source on the test vehicle. It is also possible to photograph the screen of the unit to provide a permanent record of the test.

(4) Remote viewing of the data is provided by a precision video display unit. The unit may be remotely located from the main instrumentation console to permit viewing of the test by interested parties without interrupting the test personnel. As with the console display unit, it is possible to superimpose a flat pattern layout of the test vehicle on the display screen in order to locate the signal source on the test vehicle.

(5) Tabular Teletype

A standard, automatic send-receive teletype is used to provide a tabular data output.

d. System Calibration

The calibration system provides a means for checkout and calibration of the overall system once the sensors have been installed on the test article. The major components of this system include a pulse generator, visual display (light panel) and four acoustic emission simulators which can be installed on the test vehicle. The pulse generator and visual display units are mounted in the instrumentation rack.

(1) Pulse Generator

This unit is a general-purpose pulse and square-wave generator for use in checking the overall response of the system.

(2) Visual Display

Visual display of the test signal is made on the video display units located in the master instrumentation system. These units include the console display and remove video screen. The data also are recorded by the teletype. In addition, a numerical digital indicator is provided on the master instrumentation console which indicates the four active sensor channels first detecting the test signal.

(3) The acoustic-emission similator is primarily a piezoelectric crystal encased in a shock-absorbent elastomer case which is mounted directly on the test vehicle. This unit converts the electrical input from the pulse generator to a mechanical pulse which is imparted to the test vehicle. The energy input and wave characteristics are controlled by the pulse generator.

(4) Calibration Light Panel

A calibration light panel is provided in the main console. The unit provides each channel with an adjustable signal detection threshhold, indicator light and ten-turn dial-reading potentiometer, as well as having a master signal-detection threshhold control that is adjustable. A 12-position switch and a digital voltmeter is incorporated in the panel which enables the operator to select and monitor the threshhold of each channel and power source.

2. Field Application

A system, similar to that described in the preceding section of this report, will permit not only the detection of crack growth but also location of the emitting sources. If the system reveals more than one location emitting multiple stress-wave emission, the most active of these should be thoroughly inspected with conventional nondestructive inspection methods.

If the defect cannot be located with conventional nondestructive inspection techniques because of geometrical complications and/or inherent sensitivity limitations in the conventional inspection technique, one practical solution is to use an array of sensors around the suspect area, and calibrate the array with a stress-wave simulator centered on the suspect area. Then, in a second proof test of the same pressure vessel, with the use of a computer and teletype printout, it is necessary only to monitor the suspect area(s). Likewise, when the subject pressure vessel is in service, only those areas indicated to have active defects need be placed under continuous surveillance.

a. Monitoring a Known Crack in a Steel Structure

The basic system used in monitoring a large steel structure under construction which contained a known crack is shown in the upper portion of Figure 40. The cracked girder consisted of 2-in.-thick, 30-in.-wide tension flange with a 7/8 in. thick web. While construction was shut down, it was possible to monitor the structure for subcritical crack growth using the basic system. When "noise" occurred in the structure it was necessary to utilize the Aerojet van. The lower portion of Figure 40 shows the computerized system for an array of four accelerometers to distinguish between signal generated by the known crack and those from elsewhere in the structure. With the computerized system it was possible to discount any stress wave emanating from a source other than the crack under investigation.

Isolation of the known defect from extaneous stress-wave sources was accomplished in the following manner: a pulser which simulates stress waves in the metal was placed in the immediate vicinity of the known crack. Then four sensors were positioned in an array around the crack and pulser so that sensor No. 1 received the pulser signal first, sensor No. 2 received the signal second, etc. With a computer logic system to determine that difference in time of arrival (Δt) between sensors, and a computer to receive, store and print the data by teletype, it was possible to distinguish between stress waves emanating from the known crack (or structural element) and extraneous "noise". Whenever the teletype printout showed a sensor sequence other than 1, 2, 3, 4, and with Δt values significantly different from those determined with the pulser, the data were rejected as not coming from the known crack.

An example of the data printout from the pulse, with the pulser positioned close to the known crack is shown in Table VII, Figure 39 shows the position of the sensors and pulser relative to the known crack. From Table VII note that the difference in time of arrival between sensors 1 and 2 was 80 microseconds, between sensors 1 and 3 was 170 microseconds and between sensors 1 and 4 was approximately 390 microseconds. The number in the first column of the teletype printout is the sensor that first receives the signal. When signals were generated by a source other than the known crack, columns (a),

TABLE VII

COMPUTER RESULTS FOR PULSER-GENERATED SIGNAL

SENSOR NO. (a)	SENSOR NO. (b)	TIME ΔT (c)	SENSOR NO. (d)	TIME ΔT (e)	TIME ΔT (f)	SENSOR NO. (g)	TEST TIME (h)
1	2	8	3	17	42	4	23.36
1	2	8	3	17	42	4	23.27
1	2	8	3	17	39	4	23.27
1	2	8	3	17	39	4	23.27
1	2	8	3	17	39	4	23.27
1	2	8	3	17	39	4	23.27
1	2	8	3	17	39	4	.00
1	2	8	3	17	39	4	.00
1	2	8	3	17	39	4	.00
1	2	8	3	17	39	4	.00
1	2	8	3	17	39	4	.01
1	2	8	3	17	39	4	.01
1	2	8	3	17	42	4	.01
1	2	8	3	17	42	4	.01
1	2	8	3	17	42	4	.01
1	2	8	3	17	42	4	.02
1	2	8	3	17	42	4	.02
1	2	8	3	17	42	4	.02
1	2	8	3	17	39	4	.02
1	2	8	3	17	39	4	.03

(a) number of the 1st sensor to receive signal
(b) number of the 2nd sensor to receive signal
(c) time differential between (a) and (b) in microseconds x 10
(d) number of the 3rd sensor to receive signal
(e) time differential between (a) and (d) in microseconds x 10
(f) time differential between (a) and (g) in microseconds x 10
(g) number of the 4th sensor to receive signal
(h) time at which signal was received

(b), (d) and (g) of the teletype printout indicated a sensor sequence different from 1, 2, 3, and 4, respectively.

Examples of the teletype printout for emissions from sources other than the known crack are shown in Table VIII. Note that stress-wave emission originating from locations other than the known crack resulted in a variety of sensor sequences. EEE on the teletype printout signifies a time differential in excess of a preset arbitrary maximum. The test-time printout (column h) is the time from the start of the data collection in hours. Thus, from Table II at 0.25 hours test time, sensor No. 1 first received a stress wave, sensor No. 4 received the signal 90 microseconds later, sensor No. 2 received the signal 1750 microseconds after sensor No. 1, and finally, sensor No. 3 received the signal but too late to be recorded. The sequence 1, 4, 2, 3 indicated a source other than the known crack. The difference in pulser time checks between Tables VII and VIII is the result of a small change in the pulser and sensor positioning.

b. F-111 Aircraft D6aC Fittings

Indications of low fracture toughness in F-111 aircraft D6aC steel wing-pivot-support structure aroused interest in the possible use of acoustic emission as a NDI method for F-111 aircraft. Aerojet was requested to instrument an F-111 D6aC wing-pivot fitting during fatigue test at the General Dynamics Fort Worth Structural Test Facility. The objective of the test was to (1) determine if acoustic emission could be detected and separated from the inherent noise of full-scale fatigue testing, and (2) demonstrate the location of stress-wave origins by sensor-zoning techniques. The Aerojet mobile laboratory was used for this purpose. The preselected "sphere of interest" was a taper-lock-fastened door in the wing carry-through structure. Sensors were positioned so as to monitor a sphere of interest of approximately 2-ft diam. Thus, sensors 1, 5, 8 and 9 established a circle in the horizontal plane, while 1, 3, 8 and 11 established a circle in the fore-and-aft vertical plane. The third plane was established by sensors 3, 5, 9 and 11. Sensor No. 2 was located at the center of the sphere.

Cracking within the zone of interest was defined by the time of stress-wave arrival at the various sensor positons. Stress waves originating at or near the center of the sphere of interest arrive first at the center sensor and later at the circumferential sensor locations. Conversely, stress waves or extraneous noise originating outside the sphere of interest arrive first at the circumferential sensor positions and later at the center. Equipment which automatically displays the sequence and time differentials clearly defined activity originating from the primary area of interest. The computerized SWAT system housed in the Aerojet van performed this function.

TABLE VIII

TYPICAL COMPUTER PRINTOUT RECORDING
STRESS WAVE EMISSION

SENSOR NO. (a)	SENSOR NO. (b)	TIME ΔT (c)	SENSOR NO. (d)	TIME ΔT (e)	TIME ΔT (f)	SENSOR NO. (g)	TEST TIME (h)
1	4	9	2	175	EEE	3	.25
3	1	1	4	3	EEE	2	.26
2	1	36	4	101	EEE	3	.37
1	4	14	2	91	EEE	3	.57
1	4	13	3	29	30	2	1.07
1	4	31	2	37	56	3	1.14
1	2	50	4	121	EEE	3	1.29
4	1	14	2	61	65	3	1.32
pulse check at location of known crack							
1	2	6	3	9	11	4	2.21
1	2	6	3	9	10	4	2.21
1	2	6	3	9	11	4	2.22

- - - - - - - - - - - - - - - - - -

(a) number of the 1st sensor to receive signal

(b) number of the 2nd sensor to receive signal

(c) time differential between (a) and (b) in microseconds x 10

(d) number of the 3rd sensor to receive signal

(e) time differential between (a) and (d) in microseconds x 10

(f) time differential between (a) and (g) in microseconds x 10

(g) number of the 4th sensor to receive signal

(h) time at which signal was received

Based on this early testing, the following conclusions were drawn: (a) stress-wave emission from crack growth in D6aC steel can be detected in selected areas during test; (b) test system noises can be accounted for and separated from crack growth by at least two means; viz., (1) spheres of interest are developed by preselected sensor arrays which serve to isolate specific areas of the test structure and (2) mechanical noises generally have a slower rise time than the transient stress-wave pulse which provides another means of discriminating noise from crack extension; and (c) automated control of the load-release mechanism may be used to avoid catastrophic failure from areas being monitored during structural testing of aircraft and components.

c. Pressure Vessel Monitoring

The Aerojet mobile laboratory has been used in the qualification testing of large pressure vessels. The typical location of sensors employed in such an application is shown in Figure 42. In addition to the sensors, four pulsers were located on the pressure vessel to provide a means of introducing an artificial stress wave into the vessel under load. The hydrotest procedure consisted of three cycles, with the pressure reduced to a low value between each cycle. The media was water; the material was 2219 aluminum with a nominal wall thickness of 0.190 in. The van and tank are shown in Figure 43.

The pulsers were used as an overall system check. An electrical signal was fed into the pulsers, which transformed the electrical signal into mechanical energy and then transmitted the energy to the wall of the pressure vessel. The simulated stress wave transmitted by the pulser propagated through the pressure vessel and was detected by the 15 sensors. Thus, the pulsers provided a check of the detection sensitivity and the reliability of the electronic components as well as an evaluation of the software of the computer. With pulsers located in different positions on the pressure vessel, the pulsers also provided a check of the system capability for detection and location of a stress-wave source. During test, when there is no crack growth, no solutions are posted by the computer and, therefore, without the pulsers, the operator has no way of knowing at any given time if the system is in peak operating condition. With the pulsers, on the other hand, the operator periodically can make an in-test, at load, overall system check.

The trigger level of the SWAT system was set 20 millivolts above the background noise level, and the signal amplification was set to provide a 60 db gain. The mechanical noise of the hydrotest system was sufficiently low that the filters were set at 30 KHz high-pass.

Data display was by visual and graphical means in real time during the test. The video display was on a television monitor which also showed the sensor locations on an overlay plan view of the pressure vessel. The sources of detected stress waves were posted on the screen of the monitor so that their location could be determined in relation to critical structural areas such as welds. Particular attention was paid to areas indicating multiple emissions since this can be indicative of subcritical crack growth. Video tape records of the monitor display also were made for posttest data analysis if required.

Analog records were made of the stress waves recorded by each of thirteen of the fourteen channels used to monitor the pressure vessel. These were recorded using a fourteen-channel Sangamo 3500 tape recorder operating in a direct mode. The fourteenth channel was used for tape synchronous control. In addition, a totalizer system was used to plot the cumulative stress-wave-emission count vs pressure for each hydrotest cycle. The output from channels 9, 10, 11 and 12 were mixed and plotted as a single output.

The hydrotest produced no significant increase in stress-wave rate during the pressure cycling. The background noise (amplitude and frequency) encountered during the hydrotest was very low with 30 KHz high-pass filtering. Multiple emissions were detected from two areas. These suspect areas were checked using other nondestructive inspection methods to ensure that no defects of significant size were present. Only random impulses were detected from the remainder of the pressure vessel.

d. Defects Too Small to be Verified by Conventional NDI

When acoustic-emission sources are located and then found by conventional nondestructive inspection (NDI) methods to be too small to require repair (or are too small to be located at all by the available NDI technique), the suspect location(s) can be monitored continuously using a simple, compact, non-computerized, data-conditioning system which utilizes a high-frequency transducer attached to the pressure vessel at the center of the suspect area. Because of the inherently high attenuation of stress waves in the megahertz range, only those signals emitting from the source in the immediate vicinity of the transducer will be recorded. This concept is an alternative to the technique of using an array of transducers, calibrated with a pulser

signal, and data processed by computer. Another alternative is a system based on two sensors which will accept only those signals that originate from sources that lie on a line between the two sensors. Thus, if a weld is indicated to contain the stress-wave-emission source, two sensors can be attached to the pressure vessel at an appropriate distance apart along the weld. The two-transducer system is currently under development by an acoustic-emission-systems manufacturer. The concept of selective monitoring with a high-frequency transducer is as yet untried.

SECTION III

ACOUSTIC-EMISSION AS A PRECURSOR OF FAILURE

Much of the acoustic-emission research done at Aerojet has been aimed at a better understanding of crack-growth mechanisms. These studies are summarized in Appendix A; the most noteworthy observations from all of these researches is that acoustic emission provides (1) a sensitivity to crack growth that is unequaled by any other known method, and (2) a recognizable, reproducible characteristic that can be used to predict the onset of crack instability. A variety of materials have been tested including aluminum alloys, HY-80, HY-100 and HY-150 steels, 6Al-4V titanium and D6aC steel. In each of the materials with useful toughness, stress-wave amplitude and rate of emission were found to provide precursors to crack instability. Thus, one can not only detect and locate flaw growth but also make judgment as to the severity of a flaw.

A. FRACTURE TESTING

1. Procedure

a. Test Machine

All specimens were tested in a Materials Test System (MTS) servo-hydraulic load frame model 301.02. This closed-loop system permitted rising-load-to-failure programming for all specimens at a nominal gross-stress loading rate of 50,000 psi/minute. Prior to specimen testing, a dead-headed run to maximum test-machine load capability (50,000 lb) provided data on the noise level of the test machine and test-specimen clevises. Since the test procedure called for two types of emission sensors on each specimen, an Endevco E2213 accelerometer and a Dunegan S-140A sensor were mounted on a test piece during the dead-headed run to full load. Figure 44 shows the noise level in millivolts, RMS, for the two sensors. All emission data were electronically filtered in a high-pass mode, 150 KHz for the two upper traces in Figure 44; these data represent the test machine noise level prior to wrapping each threaded joint with teflon pipe dope. The lower trace in Figure 44 shows the reduction in noise level obtained through the use of pipe dope on all threaded connections and high pass filtering at 180 KHz. Figure 44 also points up a difference in response to airborne acoustic signals between the mass-loaded and non-mass loaded sensor. The mass-loaded accelerometer has very low acoustic sensitivity while the non-mass loaded sensor displayed a much higher response to airborne acoustic energy. The latter can be minimized by acoustic shielding; however, this factor should be carefully evaluated whenever emission sensors are to be used in high ambient acoustical noise.

b. Instrumentation

The emission instrumentation is shown in Figure 45. This diagramatic representation shows two separate oscilloscopes; usually, however, one multitrace oscilloscope was more convenient. The counter system used to develop the rate and cumulative-emission totals has a frequency capability to 10 MHz; the overall counting-system response is down 3 db at 700 KHz. The data recorded on magnetic tape are limited in upper frequency to the tape recorder capability of 300 KHz.

The data obtained during each test were plotted versus applied load and consisted of rate of emission, cumulative-total count (TSWE), and emission signal-level in RMS volts. Selected specimens also were instrumented with a strain gage to permit observations regarding the degree of sensitivity of surface-deformation measurements and volumetric-deformation measurements. In addition, the single-edge-notch specimens were instrumented with a crack-opening displacement gage.

The emission sensors were preloaded against the specimen surface through the use of constant-force springs. These are springs which maintain a constant force, independent of extension. The contact side of each sensor was lightly coated with silicon vacuum grease to provide a good couplant between sensor and specimen. Prior to the beginning of each test and with all systems activated, the ambient noise level of the system was reconfirmed. This simple check is the key to assuring system performance. For any given test, deviation from the ambient noise level established at the beginning of the program was an indication that something was not operating properly in the system. For example, the low-noise battery-driven amplifiers were always a potential problem as the battery became discharged; however, the ambient-noise-level check always detected this condition. By this procedure, each test was conducted under identical conditions. Total system gain for these tests was set at 20,000:1.

c. Single-Edge-Notch Tension Test

Single-edge-notch (SEN) tension testing was done with 3 x 12-in. panels containing an electric-discharge-machined edge notch, extended and sharpened by tension-tension fatigue. The specimens, shown in Figure 46, were tested at a rate of approximately 50,000 psi/minute based on axial load with no adjustment for bending due to the asymmetry created by the edge notch. The stress intensity for the fatigue precracking operation was approximately one-half the estimated critical plane-strain stress intensity (K_{Ic}). For example, in 6Al-4V titanium and in D6aC 600°F-temper steel, the fatigue crack was extended in two increments; the first increment was an 0.05 to 0.08-in. extension at a load corresponding to approximately

20 ksi-in.$^{1/2}$, followed by a second increment of 0.03 to 0.05 in. at reduced load. Based on this procedure, the fatigue precracking was carried out as follows:

6Al-4V and D6aC (600 temper) assuming K_{Ic} = 40 ksi-in.$^{1/2}$

Thickness	Load	Crack Extension (ΔA) in.
0.10	1900	0.05 - 0.08
	1500	0.03 - 0.05
0.27	5000	0.05 - 0.08
	4200	0.03 - 0.05

D6aC (1100 temper) assuming K_{Ic} = 80 ksi-in.$^{1/2}$

0.10	3800	0.05 - 0.08
	3300	0.03 - 0.05
0.30	11000	0.05 - 0.08
	9000	0.02 - 0.05

Stress intensity was calculated from the expression published by ASTM Committee E24(46).

$$K_I = Y\ P\ a^{1/2}/BW$$

where $Y = 1.99 - 0.41\ (a/W) + 18.70\ (a/W)^2 - 38.48\ (a/W)^3 + 53.85\ (a/W)^4$, P = load, a = crack length, B = specimen thickness, and W = specimen width. The crack length at any particular load was calculated from crack-opening displacement (COD) measurements. The COD was measured between knife edges machined at the end of the specimen notch (see Figure 46). The measuring device consisted of a full bridge of electric-resistance strain gages mounted on a double-cantilever beam(47). This strain-gage device was balanced and amplified through an Endevco Signal Conditioner and dc amplifier system. The COD output was then recorded directly on an X-Y plotter (versus load) and on magnetic tape.

For purposes of in-test calibration, the COD-gage reading was adjusted to give the fatigue-precrack length as measured in the fractured test specimen. The calibration was made by reading COD values at low loads (generally less than 50 percent of the load corresponding to deviation from linearity in the load-COD plot) and determining a multiplying factor to give the measured fatigue precrack. For example, in 6Al-4V titanium specimen E1, the COD at 2.5, 5.0 and 7.5 kips was 3.5, 6.6 and 9.7 divisions, respectively (as read from the x-y plot of load vs COD). The measured fatigue precrack was 0.951 in. or a/W = 0.317. From the SEN-tension calibration curve (Figure 47), at a/W = 0.317:

$$vBE/P = 3.65$$

At 2.5 kips load, assuming no crack growth, for B = 0.268 in. and E = 16.5×10^6 psi,

$$v = 3.65 \times 2.5 \times 10^3 / 0.268 \times 16.5 \times 10^6$$

$$= 2.065 \times 10^{-3}$$

The COD multiplying factor to give an indicated crack length of 0.951 in. was

$$v1.MF = v$$

where v1 is the COD reading from the load-COD plot. At 2.5 kips load, v1 was 3.5 divisions, thus

$$3.5\ MF = 2.065 \times 10^{-3}$$

$$MF = 0.590 \times 10^{-3}$$

This procedure was repeated for the 5.0 and 7.5 kip loads, giving an average multiplying factor of 0.6179×10^{-3}.

All calculations were done by computer. The input to the computer for specimen E1, for example, was as follows:

Specimen No.	E1
Fatigue precrack (in.)	0.951
Specimen Width (in.)	3.005
Specimen Thickness (in.)	0.268
Young's Modulus (psi)	16.5×10^6
Yield Strength (ksi)	130.0

Load P1 (kips)	2.5
COD v1 (divisions)	3.5
Load P2 (kips)	5.0
COD v2 (divisions)	6.6
Load P3 (kips)	7.5
Load at the onset of crack instability P7 (kips)	26.2
COD at the onset of crack instability v7 (divisions)	49.0

The computer printout for specimen E1 was as follows:

Specimen No.	E1
MF 1	0.58981-03
MF 2	0.62555-03
MF 3	0.63845-03
MF (avg)	0.61794-03
P7 Load (kips)	26.20000
v7 COD (in.)	0.03028
A	1.12102
Y	3.48467
KI	120.030
RY	0.1357
$(KI/FTY)^2$	0.8525

Thus, at the load corresponding to the onset of crack instability as determined from stress wave emission (SWE), the calculated effective crack length was 1.121 in., the maximum (plane-stress) plastic-zone size

$$RY = (KQ/FTY)^2/2\pi$$

was 0.136 in. and the stress intensity factor was 120 ksi-in.$^{1/2}$

d. PTC-Tension Testing

The part-through-crack (PTC) tension specimen geometry is shown in Figure 48. The PTC was started by electric-discharge-machining (EDM) a triangular flaw in each specimen. This starter-flaw configuration

was used to control the shape of the fatigue precrack during cyclic bending. For 0.10 in.-thick sheet material, the EDM was done with an electrode having a triangular tip (base 0.20 in. and altitude 0.025 in.); thus, the EDM slot was 0.20 in. long by 0.025 in. deep. The cutting edge of the electrode was kept sharp so as to produce a radius in the bottom of the slot of not greater than 0.005 in. The 0.30 in.-thick sheet was machined to produce a triangular slot 0.30 in. long by 0.06 in. deep. The test pieces were cyclic loaded in cantilever bending with a maximum stress intensity at the bottom of the slot of one half the estimated critical stress intensity factor.

The stress intensity was calculated from the expression[48]

$$K_I = 1.1 \sqrt{\pi}\ F\ (a/Q)^{1/2}$$

where F is the gross stress perpendicular to the crack, a is the semi-minor axis of an ellipse (depth of crack), and Q is Irwin's plasticity correction (flaw shape parameter)

$$Q = \phi^2 - 0.212\ (F/FTY)^2$$

where ϕ is an elliptical integral of the second kind and FTY is the uniaxial yield strength of the material. Figure 49 is a plot of the flaw-shape parameter Q as a function of a/2c (ratio of crack depth to length).

The crack dimensions are obtained from the fractured test specimen. The critical stress intensity factor K_{Ic} usually is based on the dimensions of the fatigue precrack and the maximum (failure) load. If there is slow crack growth before the plane strain instability occurs, the calculation of K_{Ic} based on the fatigue precrack will give a fictitiously low value of critical stress intensity. If the crack growth is arrested after the plane-strain instability (pop-in) occurs, the calculation of K_{Ic} based on maximum load will give a fictitiously high value of K_{Ic}; and, if the crack is too deep with respect to the specimen thickness, the calculated value of stress intensity is fictitiously low. Kobayashi's solution[49]

$$K_I = 1.1\ F\ (\pi\ a/Q)^{1/2}\ .\ MK$$

for cracks between $0 < a/2C < 0.30$ provides an approximate correction for deep surface flaws. Table IX presents Kobayashi's magnification factors.

For a valid stress intensity measurement, it is generally accepted that in the PTC-tension test, the gross stress should not exceed the yield strength, and for Irwin's solution (without the Kobayashi correction) the crack depth should not exceed 50 percent of the specimen thickness. An additional even more stringent requirement is that the net-section stress should not exceed the yield strength of the material.

Brown and Srawley[50] have suggested that for valid K_{Ic} measurements the crack depth in the PTC-tension test should exceed 2.5 $(K_{Ic}/FTY)^2$ in., where FTY is the 0.2 percent offset yield strength. This is a severely limiting requirement. Consider, for example, the 0.25 in. thick plate used in this investigation. If the crack depth is held to approximately $a/B = 0.5$, for 0.25 in. thick 6Al-4V titanium at 155 ksi yield strength, the largest crack that can be tested is 0.125 in.; thus, the maximum toughness that can be tested according to the criteria suggested by Brown and Srawley is

$$2.5\ (K_{Ic}/FTY)^2 = 0.125 \text{ in.}$$

$$K_{Ic} = 35 \text{ ksi-in.}^{1/2}$$

Any stress intensity values greater than 35 ksi-in.$^{1/2}$ would require a crack depth greater than half the thickness of the test material. Thus, the critical stress intensity factors for many of the tests conducted in this investigation are <u>apparent</u> K_{Ic} values and therefore, are designated as KQ rather than K_{Ic}. Quantitative measurements of critical stress intensity factors were not required in this study since the primary objective was to determine the emission characteristics of crack growth.

All calculations were done by computer. The input to the computer for PTC-tension specimen E1, for example, was as follows:

Specimen No.	E1
Fatigue precrack depth (in.)	0.1300
Fatigue precrack length (in.)	0.5800
Specimen width (in.)	1.9780
Specimen Thickness (in.)	0.2690

TABLE IX

KOBAYASHI'S MAGNIFICATION FACTORS FOR FLAW DEPTH

Flaw Depth Thickness (a/B)	Mag. Factor Mk	Flaw Depth Thickness (a/B)	Mag. Factor Mk
0.025	1.00	0.525	1.18
0.050	1.00	0.550	1.20
0.075	1.00	0.575	1.22
0.100	1.01	0.600	1.24
0.125	1.01	0.625	1.26
0.150	1.01	0.650	1.28
0.175	1.02	0.675	1.30
0.200	1.02	0.700	1.33
0.225	1.02	0.725	1.36
0.250	1.03	0.750	1.39
0.275	1.04	0.775	1.42
0.300	1.05	0.800	1.45
0.325	1.06	0.825	1.51
0.350	1.07	0.850	1.51
0.375	1.08	0.875	1.53
0.400	1.09	0.900	1.55
0.450	1.12	0.925	1.57
0.475	1.14	0.950	1.58
0.500	1.16	0.975	1.59
		1.000	1.60

Yield Strength (ksi)	130.0000
Load (kips POP-IN)	29.7000
Load (kips FRACTURE)	35.4500

The computer printout for specimen E1 was as follows:

Specimen No.	E1
P (POP-IN load)	29.7000
FG (gross stress)	91.78
a/2C	0.2241
Q	1.2838
A/Q	0.1013
K_I (irwin)	56.9
A/B	0.4833
KI.MK (KOBAYASHI CORRECTED)	64.9
CA (crack area)	0.0592
FN (net stress)	112.3
FN/FTY	0.8641
FG/FTY	0.7060
RP/B (ratio plastic zone to thickness)	0.1058
(AO + RP)/B (ratio effective crack to thickness)	0.5891
$(KI/FTY)^2$	0.2495

In selected tests, an attempt was made to correlate fracture-surface markings and emission data by use of low-cycle fatigue. This was done by first subjecting the test specimen to a continuously rising load until a sufficient number of stress-wave bursts were observed to constitute a precursor to failure. The specimen was then subjected to low-cycle tension-tension fatigue on the MTS machine until the emissions indicated failure to be imminent. At this point, the specimen was unloaded and dye used in an attempt to determine the extent of crack growth. In other specimens, the low-cycle fatigue was not interrupted until fracture. The specimen

was then photographed under polarized[51] light in an attempt to distinguish between (1) the crack growth produced by the initial loading, (2) the crack growth produced by fatigue, and/or (3) the crack growth attending pop-in.

2. Fracture Mechanics Analysis

Under ONR Contract N00014-66-C0340, it was established from single-edge-notch (SEN) tensile tests of 7075-T6 aluminum, HY-80 and HY-150 constructional steels, D6aC low-alloy high-strength steel, and 6Al-4V titanium, that stress-wave amplitude and repetition rate are recognizable, reproducible stress-wave characteristics which can be used as precursors to crack instability[52][53]. In highly tough HY-80, HY-150, D6aC (austenitized at 1750°F and tempered at 1100°F), and 6Al-4V (aged at 1250°F) where there was no detectable pop-in by either crack-opening-displacement gage or stress-wave emission, the failure process was identified by an increasing stress-wave count, starting at approximately the load corresponding to deviation from linearity in the crack-opening-displacement plot. In the more brittle D6aC steel (austenitized at 1750°F and tempered at 600°F) and 7075-T6 aluminum where pop-in was readily detected, the plane-strain instability was identified by an order-of-magnitude increase in stress-wave amplitude and the final failure process was presaged by an increasing stress-wave count and amplitude, generally starting at approximately the plane-strain pop-in.

In the ONR study, the fact that the emission data did not provide a precursor of the plane-strain instability was considered to be a serious limitation from the standpoint of nondestructive inspection, particularly for applications where leak-before-burst can not be tolerated (as in a fuel tank) or in materials and material conditions where pop-in results in catastrophic failure (no crack arrest). In these situations, emission data are of little value if there is no precursor of the plane-strain instability. They can only be used to locate the flaw but will not indicate the precursor to instability.

In the investigation described in this report, a higher-sensitivity emission detection system was used. It was hypothesized that if the emission sensors would be capable of detecting crack growth before the plane-strain instability and, in particular, presaging the onset of plane-strain instability, then SWAT would be an important NDI method for those applications where a leak can not be tolerated or where material toughness is such that catastrophic failure results directly from plane-strain pop-in. For those applications where a leak-before-break situation can be tolerated or where the material is sufficiently tough that failure occurs by mixed-mode plane-stress fracture, it is well established that the concept of an emission-precursor is a useful, supplementary NDI method.

To determine the usefulness of emission data for detecting the onset of the plane-strain instability, it was necessary (1) to measure the critical stress intensity factor under plane-strain conditions and (2) to evaluate the stress-wave characteristics of each material at and before the plane-strain instability. In the SEN-tension test, the measurement of K_{Ic} is based on the load and crack length at pop-in in the COD-LOAD plot. If there is no detectable COD pop-in, then emission data must be used as a basis for determining the plane-strain instability. In the PTC-tension test, the usual basis for calculating K_{Ic} is simply maximum load and the dimensions of the fatigue pre-crack. If there is slow crack growth before plane-strain instability, the fatigue precrack dimensions will not be the correct crack dimensions to use in calculating the critical stress intensity. However, the calculated value will be a minimum; i.e., fictitiously low. If, on the other hand, there is a pop-in and then the crack is arrested, maximum load will not be the correct load to use with the fatigue precrack dimensions, i.e., pop-in will have occurred at a load less than maximum. In this case, the calculated value of K_{Ic} will be unconservative; i.e., fictitiously high. Thus, there can be ambiguity in the PTC-tension test result when the test involves either slow crack growth before pop-in or arrested pop-in.

With low-cycle fatigue it should be possible to determine the critical stress intensity without ambiguity if the semi-elliptical flat-fracture generated during the fatigue cycling can be measured exactly. In fatigue, the load at fracture is known and the semi-elliptical flaw growth prior to catastrophic propagation is easily and accurately measured up to the last few cycles. At that point, with the stress intensity almost at the critical value, the incremental growth becomes increasingly difficult to distinguish from the appearance of the fracture surface produced by catastrophic crack propagation. Figure 50 illustrates this situation.

Thus, the KQ value based on low-cycle fatigue experiments should be fictitiously low, i.e., consistently a conservative value. On the other hand, the KQ value as determined from continuously rising load test (conventional PTC-tension testing) and based on maximum load and the fatigue-precrack dimensions may be fictitiously high if semi-elliptical cracking beyond the fatigue precrack is the result of arrested pop-in, or fictitiously low if semi-elliptical cracking beyond the fatigue precrack is the result of slow crack growth prior to pop-in.

a. 6Al-4V Titanium

(1) Solution Treated and Aged

(a) SEN-Tension Test

Table X summarizes the single-edge-notch (SEN) tension test results. In the thinner sheet material (0.10 in.-thick heat 292796), there was no evidence of plane strain instability as manifested by a sudden increase in crack length (pop-in) in either the COD or the emission data until a stress intensity of

$$\text{Av(3)}\ \frac{57.0 - 59.4}{57.9\ \text{ksi-in.}^{1/2}}$$

Deviation from linearity in the COD-load plot occurred at approximately the same stress intensity

$$\text{Av(3)}\ \frac{52.4 - 61.8}{58.2\ \text{ksi-in.}^{1/2}}$$

thus, there was no significant crack growth prior to the emission-precursor stress intensity of 57.9 ksi-in.$^{1/2}$. The critical stress intensity based on COD occurred at

$$\text{Av(3)}\ \frac{63.3 - 79.2}{70.4\ \text{ksi-in.}^{1/2}}$$

a value significantly higher than the emission-precursor stress intensity. Thus, a system based on emission data such as SWAT would have provided ample warning of a growing crack before plane-strain instability. Failure of the test specimens occurred at

$$\text{Av(3)}\ \frac{86.7 - 101.0}{92.0\ \text{ksi-in.}^{1/2}}$$

In the thicker sheet material (0.27-in.-thick heat 293412), an emission pop-in was observed at approximately 45 ksi-in.$^{1/2}$. Deviation from linearity in the COD-load plots occurred at approximately the same or a somewhat higher stress intensity

$$\text{Av(3)}\ \frac{45.7 - 57.3}{52.3\ \text{ksi-in.}^{1/2}}$$

TABLE X

6Al-4V TITANIUM SOLUTION TREATED AND AGED (155 KSI YIELD STRENGTH)
SEN-TENSION TEST RESULTS

Specimen			Pre-Crack	COD Linearity		SWE Pop-in		SWE Precursor		Fracture	
No.	W	B	AO	Load	KQ	Load	KQ	Load	KQ	Load	KQ
S1	3.003	0.274	0.991	12.00	45.7	12.00	45.7(a)	18.40	74.0(b)	21.00	101.7
S2	3.002	0.272	0.968	13.85	53.9	10.95	42.4(a)	16.20	63.8(b)	16.95	78.7
S4	3.003	0.270	0.992	14.00	57.3	11.32	46.2(a)	16.50	71.2(b)	17.90	85.9
SS13	3.001	0.106	0.969	5.13	52.4	(c)	(c)	5.55	57.4(d)	6.82	88.4
SS14	2.996	0.105	0.987	5.62	61.8	(c)	(c)	5.30	57.0(e)	6.63	86.7
SS15	2.998	0.106	0.892	6.65	60.3	(c)	(c)	6.52	59.4(f)	6.86	101.0

(a) The plot of total stress wave emission count (TSWE) vs Load showed a succession of jumps in count starting at low stress intensity (13 to 21 ksi-in.$^{1/2}$); the particular jump listed was one of the last jumps before the onset of fracture;

(b) Also an abrupt increase in COD;

(c) no pop-in observed;

(d) abrupt increase in COD at 6.10 kips (68.7 ksi-in.$^{1/2}$);

(e) abrupt increase in COD at 6.52 kips (79.2 ksi-in.$^{1/2}$);

(f) abrupt increase in COD at 6.75 kips (63.3 ksi-in.$^{1/2}$).

and, therefore, there was no significant crack growth associated with the emission pop-in. The onset of crack instability as evidenced by a marked increase in stress-wave activity and an abrupt increase in COD occurred at

$$\begin{matrix} 63.8 - 74.0 \\ \text{Av}(3) \quad \underline{69.7 \text{ ksi-in.}^{1/2}} \end{matrix}$$

thus, the stress intensity at the plane-strain instability as determined by COD measurements and by the emission data was the same. Nevertheless, the emission data presaged instability in that the plot of total stress wave emission (TSWE) count vs load showed a succession of count jumps prior to COD pop-in; moreover, any one of these jumps would have provided ample data for triangulation in a structure. Failure of the test specimens occurred at

$$\begin{matrix} 78.7 - 101.7 \\ \text{Av}(3) \quad \underline{88.8 \text{ ksi-in.}^{1/2}} \end{matrix}$$

(b) PTC-Tension Tests

Table XI summarizes the part-through-crack (PTC) tension test results. Attention is invited to the extensive footnotes in connection with Table XI and other tables of tension test results; procedural details are provided that are important to the interpretation of the data. In the thinner material (0.10 in.-thick heat 292796), the plane-strain instability was manifested by a rapid and continuing progression of stress-wave activity rather than a discrete pop-in occurrence. The range and average value of the stress-intensity corresponding to the emission precursor was

$$\begin{matrix} 28.6 - 43.9 \\ \text{Av}(5) \quad \underline{36.3 \text{ ksi-in.}^{1/2}} \end{matrix}$$

The usual practice in calculating the plane-strain critical stress intensity is to use the dimensions of the fatigue precrack and the maximum (failure) load. If this is done here, the range and average value of the apparent K_{Ic} is

$$\begin{matrix} 55.2 - 69.6 \\ \text{Av}(5) \quad \underline{61.0 \text{ ksi-in.}^{1/2}} \end{matrix}$$

a value considerably higher than that calculated from the fatigue precrack and the load corresponding to the emission precursor. Whether the crack enlargement is a sudden occurrence (pop-in) or the result of slow crack growth, and when the crack growth occurs are basic questions in interpretation of the PTC-tension test results. Because of evidence of crack growth beyond the initial

TABLE XI

PTC-TENSION TEST RESULTS - HEAT 292796 SHEET 0.10 IN. THICK
6Al-4V TITANIUM, SOLUTION TREATED, AND AGED (155 KSI YIELD STRENGTH)

Specimen			Crack Dimensions (a)				SWE Precursor (b)		Maximum Load	
No.	W	B	A	2C	A/2C	A/B	Load	KQ	Load	KQ
SP 11	1.296	0.098	0.052	0.366	0.142	0.531	7.5	28.6(c)	14.00	55.2
	1.296	0.098	0.080	0.445	0.180	0.816	7.5	43.2	14.00	83.3
SP 12	1.298	0.100	0.046	0.340	0.135	0.460	-	-	16.60	59.0
	1.298	0.100	0.085	0.410	0.207	0.850	-	-	16.60	100.6
SP 13	1.296	0.099	0.053	0.348	0.152	0.535	9.70	37.4(c)	14.78	58.6
	1.296	0.099	0.080	0.435	0.184	0.808	9.70	55.2	14.78	86.5
SP 14	1.300	0.100	0.060	0.340	0.176	0.600	9.25	38.2(c)	16.22	69.6
	1.300	0.100	0.060	0.361	0.166	0.600	9.25	38.6	16.22	70.5
	1.300	0.100	0.085	0.460	0.185	0.850	9.25	55.1	16.22	100.5
SP 15	1.290	0.104	0.061	0.365	0.167	0.586	10.90	43.9(c)	15.18	62.6
	1.290	0.104	0.061	0.418	0.146	0.586	10.90	44.9	15.18	63.9
	1.290	0.104	0.085	0.530	0.160	0.817	10.90	62.7	15.18	89.5
SP 16	1.298	0.105	0.052	0.355	0.146	0.495	9.60	33.3(c)	9.88	34.3(d)
	1.298	0.105	0.095	0.460	0.206	0.905	-	-	9.88	59.9(e)
	1.298	0.105	0.095	0.610	0.156	0.905	-	-	9.88	63.0(f)

NOTES: (a) The first crack size listed for a given specimen is the ink-stained fatigue precrack. The other sizes correspond to semi-elliptical flat-fracture areas produced by crack growth during the test; (b) in general, the precursor obtained by the stress wave analysis technique (SWAT) is the onset of crack instability as evidenced by the start of a rapid and continuing progression of stress-wave activity; (c) the fatigue precrack dimensions are generally used in calculating the plane-strain fracture toughness. The high-sensitivity SWAT system used in these tests indicated no significant slow crack growth prior to the SWE precursor; therefore, the KQ value that reflects the plane-strain crack instability is based on the fatigue-precrack dimensions; (d) after initially loading to 11.1 kips (38.8 ksi-in.$^{1/2}$), specimen SP-16 was low-cycle fatigued at 9.88 kips maximum load (34.3 ksi-in.$^{1/2}$). The cycling rate was 74 cycles per minute; (e) after 2480 cycles, there was a marked increase in the crack growth rate attended by approximately 100 x 10^3 SWE count increase over a period of about 5 cycles, then fracture. The fracture surface corresponding to the intermediate crack dimensions (0.095 in. deep and 0.46 in. long) was associated with the fatigue up to the time of rapid growth; (f) although the exact shape of the semi-elliptical flaw in the final (fracture) cycle was not apparent, a close approximation of its length was made possible by the extension of flat fracture in the free surface.

fatigue precrack as shown in Figure 51, the use of maximum load and fatigue-precrack dimensions in calculating the critical stress-intensity factor is subject to question. If the enlarged crack is the result of pop-in and arrest, the use of maximum load would result in a fictitiously high critical stress intensity factor. If on the other hand, the enlarged crack is the result of slow crack growth culminating in pop-in, the use of the fatigue-precrack dimensions would result in a fictitiously low critical stress intensity factor. The emission precursor shows the crack growth to have started at 36 ksi-in.$^{1/2}$. Moreover, the emission data showed that the area of semi-elliptical crack extension observed in each test specimen was not the result of a discrete pop-in event. Thus the KQ value based on the fatigue precrack dimensions in these tests is a fictitiously low value. If plane-strain instability occurred after the slow crack growth, the range and average value of the stress intensity factor calculated on the basis of maximum load and the dimensions of the semi-elliptical crack growth observed in the broken test pieces was

$$\begin{array}{l} 83.3 - 100.6 \\ \text{Av(3)} \quad \underline{92.1 \text{ ksi-in.}^{1/2}} \end{array}$$

Thus, emission data appears to provide a conservative presage of the plane-strain instability.

In an attempt to obtain a quantitative measure of the plane-strain stability, specimen SP-16 was tested. The specimen was initially loaded to 11.1 kips (38.8 ksi-in.$^{1/2}$), a value just above the emission precursor stress intensity (9.6 kips, 33 ksi-in.$^{1/2}$). The specimen was then subjected to low-cycle tension-tension fatigue at a maximum load of 9.88 kips (34.3 ksi-in.$^{1/2}$) and a rate of 74 cycles per minute. After approximately 1700 cycles, there was a marked increase in the crack growth rate as evidenced by a jump of over 10 x 10^3 in the total stress-wave-emission (TSWE) count; this emission precursor in fatigue is shown in Figure 52. The increased rate of cracking occurred over a period of approximately 70 cycles. The cracking then continued at about the same rate as before the SWE precursor. After a total of approximately 2000 cycles there was a second SWE precursor during the low-cycle fatigue as evidenced by a jump of over 90 x 10^3 in the TSWE count. This final growth to critical crack size occurred over a period of about 5 cycles; the specimen then fractured. When the fracture surface was photographed under polarized light, as shown in Figure 53, a band of fatigue crack growth was clearly shown. During the last few cycles, the marked increase in stress-wave activity indicated a marked increase in the rate of crack growth as the critical crack size was approached. It is reasonable to assume that the fracture appearance associated with the last few cycles of load would not be significantly different from the fracture appearance associated with catastrophic propagation on reaching the critical

crack size. Therefore, it is difficult, if not impossible, to determine the exact shape and dimensions of the final crack. However, in this specimen the approximate dimensions of the critical crack were indicated by flat-fracture extension in the free surface of the piece (see Figure 53). The critical stress intensity, as calculated from this experiment, is considered to have physical significance because the load (maximum load in fatigue cycling) and the crack dimensions at the onset of rapid fracture are believed to be a close approximation. The stress intensity

based on:	dark, fatigue-crack area (Figure 53) and maximum load in fatigue is	59.9 ksi-in.$^{1/2}$
	bright, flat-fracture area (Figure 53) and maximum load in fatigue is	63.0 ksi-in.$^{1/2}$

from a comparison of these values and those determined from continuously rising load tests, it would appear that the combination of maximum load and the dimensions of the fatigue precrack provides a good approximation of the plane-strain fracture toughness K_{Ic} when testing PTC-tension specimens. However, agreement between KQ values based on (1) low-cycle, high-stress intensity fatigue tests (where the load and crack dimensions are reasonably accurately known) and (2) continuously rising-load tests (where maximum load and the fatigue precrack dimensions are physically incompatible) is believed to be fortuitous, particularly in those continuously rising load tests where slow crack growth is observed beyond the ink-stained fatigue precrack.

The plane-strain instability in the SEN-tension tests of the sheet material (0.1 in. thick heat 292796) occurred at 70 ksi-in.$^{1/2}$ which is somewhat higher than 61 ksi-in.$^{1/2}$ the critical stress intensity calculated from the PTC-tension test. The plane-strain stress-intensity value determined by the SEN-tension test was based on the load corresponding to an abrupt increase in the COD-load plot and the effective crack length as determined by COD gage. Thus, in the SEN-tension test there is little ambiguity with regard to the crack dimension at any particular load. It appears that the critical stress intensity values as determined in both the PTC-tension test and the PTC-low-cycle-fatigue test were somewhat low. It is possible that what appeared to be a fortuitous agreement between these tests may have been the result of approximately the same amount of unmeasured crack growth in the two kinds of tests. In both low-cycle fatigue and the continuously rising load PTC tests, near the critical stress intensity there is one or more large crack increments that are indistinguishable in appearance from the fracture surface produced by catastrophic propagation at the critical stress intensity.

However, from an engineering point of view, one can not disregard the lower value of stress intensity.

$$36.3\ \text{Av(5)}\ \text{ksi-in.}^{1/2}$$

calculated on the basis of the load at which stress-wave activity indicated a marked and continuing increase in crack growth in the PTC-tension test.

In the thicker sheet material (0.27 in. thick heat 293412), no pop-in was observed; the emission precursor was an abrupt, marked and continuing increase in stress-wave activity until failure. The range and average of the stress intensity values based on the emission precursor load and the fatigue crack dimensions was

$$\begin{array}{l} 57.1 - 71.8 \\ \text{Av(5)}\ \ \underline{61.2\ \text{ksi-in.}^{1/2}} \end{array}$$

This value is significantly below that based on maximum load and the dimensions of fatigue precrack; viz.,

$$\begin{array}{l} 79.7 - 82.4 \\ \text{Av(5)}\ \ \underline{80.6\ \text{ksi-in.}^{1/2}} \end{array}$$

From Table XII, there was no evidence of slow crack growth or arrested pop-in in the fracture surface; thus, there was no ambiguity in the critical stress intensity calculation. Nevertheless, specimen S-5 was tested in low-cycle fatigue until it fractured. There was excellent agreement between the K_{Ic} value determined in low cycle fatigue (79.7 ksi-in.$^{1/2}$) and the value determined by continuously rising load and using the fatigue precrack and maximum load as a basis of calculation (80.6 ksi-in.$^{1/2}$).

Figure 54 provides a comparison between typical tests of 0.1 in. and 0.27 in. thick STA titanium.

A comparison between the SEN- and PTC-tension tests based on emission-precursor and fracture showed the two tests to give approximately the same values with one exception as will be seen from the following summary:

Material Tested		Specimen	Critical Stress Intensity (ksi-in.$^{1/2}$)	
Heat	Thickness	Type	SWE Precursor	Fracture
292796	0.10	SEN	57.9	92.0
		PTC	36.3	92.1
293412	0.27	SEN	69.7	88.8
		PTC	61.2	80.6

TABLE XII

6Al-4V TITANIUM, SOLUTION TREATED AND AGED (155 KSI YIELD STRENGTH)
PTC-TENSION TEST RESULTS - HEAT 293412 SHEET 0.27 IN. THICK

Specimen			Crack Dimensions				Basis for Stress-Intensity Calculation			
							SWE Precursor		Maximum Load	
No.	W (in.)	B (in.)	A (in.)	2C (in.)	A/2C	A/B	Load (kips)	KQ (ksi-in.$^{1/2}$)	Load (kips)	KQ (ksi-in.$^{1/2}$)
S1	1.203	0.271	0.095	0.512	0.186	0.351	33.0	59.2	43.55	80.5
S2	1.203	0.272	0.130	0.560	0.232	0.478	28.5	60.2	37.56	80.4
S3	1.999	0.275	0.102	0.550	0.186	0.371	(a)	(a)	51.60	57.3 (a)
	1.203	0.275	0.102	0.550	0.186	0.371	31.0	57.1	43.30	82.4 (b)
S4	1.203	0.271	0.110	0.520	0.212	0.406	30.0	57.6	40.63	80.0
S5	1.200	0.271	0.120	0.530	0.226	0.443	35.37	71.8	(c)	(c)
	1.200	0.271	0.195	0.680	0.287	0.720	(d)	(d)	27.25	79.7 (d)

NOTES: (a) First loading of specimen S3 (specimen was not fractured); no precursor observed. (b) Second loading of specimen S3; specimen fractured. (c) After initial rising load to SWE precursor, specimen S5 was low-cycle fatigued at 27.25 kips (maximum load) until the specimen fractured. The applied stress intensity at the start of cycling was 54.4 ksi-in.$^{1/2}$. (d) No attempt was made to observe a SWE precursor during fatigue cycling. The stress-intensity value of 79.7 ksi-in.$^{1/2}$ was based on the fatigue-crack growth measured in the fracture surface.

The difference between the two thicknesses may be the result of a heat-to-heat difference. The difference between the PTC- and SEN-tension results based on the onset of crack instability in the thinner sheet (heat 292796) appears to be anomalous. However, the PTC-tension K_{Ic} value of 36.3 is in good agreement with the value measured in Minuteman 6Al-4V rocket motor case material; viz., 39.1 ksi-in.$^{1/2}$ with a standard deviation of 1.6 ksi-in.$^{1/2}$ (540 PTC-tension tests of 109 forgings).

(2) Extra-Low-Interstitial Annealed

(a) SEN-Tension Tests

Table XIII summarizes the single-edge-notch (SEN) tension test results. In the thinner sheet material (0.10 in. thick heat 302443) there was no evidence of plane-strain instability in the COD-load plots; however, there were sharply defined steps in the plots of total stress-wave-emission versus load, indicating crack growth. Based on the first jump, the stress-intensity values were

$$\begin{array}{l} 35.8 - 45.3 \\ \text{Av(3)} \quad \underline{42.0 \text{ ksi-in.}^{1/2}} \end{array}$$

Deviation from linearity in the COD-load plots occurred at a higher stress intensity

$$\begin{array}{l} 52.7 - 62.2 \\ \text{Av(3)} \quad \underline{56.5 \text{ ksi-in.}^{1/2}} \end{array}$$

indicating that the crack growth associated with the stress-wave emission jumps at 42 ksi-in.$^{1/2}$ was very small. The stress intensity corresponding to the onset of instability as determined by SWAT was

$$\begin{array}{l} 104.3 - 121.9 \\ \text{Av(2)} \quad \underline{111.2 \text{ ksi-in.}^{1/2}} \end{array}$$

Failure of the test specimens occurred at

$$\begin{array}{l} 150.7 - 203.4 \\ \text{Av(3)} \quad \underline{173.9 \text{ ksi-in.}^{1/2}} \end{array}$$

In the thicker sheet (0.27 in. thick heat 303109), pop-in was observed in three out of four tests in both the COD-load plots and the SWAT data.

$$\begin{array}{l} 59.5 - 69.3 \\ \text{Av(3)} \quad \underline{65.4 \text{ ksi-in.}^{1/2}} \end{array}$$

TABLE XIII

6Al-4V TITANIUM, ELI ANNEALED (130 KSI YIELD STRENGTH)
SEN-TENSION TEST RESULTS

Specimen No.	W	B	Pre-Crack AO	COD Linearity Load	COD Linearity KQ	SWE POP-IN Load	SWE POP-IN KQ	Onset of Instability Load	Onset of Instability KQ	Fracture Load	Fracture KQ
HEAT 303109											
E1	3.005	0.268	0.951	13.9	50.4	16.1	59.5(a)	26.2	120.0	27.1	155.4
E2	3.004	0.270	0.985	15.2	67.3	17.2	67.3(a)	25.6	123.7	27.4	160.2
E6	3.005	0.267	1.019	14.7	61.2	16.4	69.3(a)	24.5	123.0	26.8	154.1
E8	3.004	0.267	0.981	14.7	57.6	(b)	(b)	25.8	120.6	29.6	165.3
HEAT 302443											
ES 13	2.996	0.098	0.939	6.25	62.2	4.45	44.8(c)	11.8	107.5	12.1	167.5
ES 14	2.996	0.097	0.958	5.25	54.7	3.45	35.8(c)	10.2	121.9	12.8	203.4
ES 16	2.993	0.098	0.972	5.10	52.7	4.40	45.3(c)	9.2	104.3	11.2	150.7

(a) Pop-in: COD and SWE; (b) No pop-in by either COD or SWE; (c) No COD pop-in, 1st jump in SWE.

Deviation from linearity in the COD-load plots occurred at a somewhat lower stress intensity

$$\begin{matrix} 50.4 - 67.3 \\ \text{Av}(4) \quad \underline{59.1 \text{ ksi-in.}^{1/2}} \end{matrix}$$

and, therefore, there was significant crack growth and/or plastic-zone formation before pop-in. The onset of crack instability as evidenced by a marked increase in stress-wave activity occurred at

$$\begin{matrix} 120.0 - 123.7 \\ \text{Av}(4) \quad \underline{121.8 \text{ ksi-in.}^{1/2}} \end{matrix}$$

Failure of the test specimens occurred at

$$\begin{matrix} 154.1 - 165.3 \\ \text{Av}(4) \quad \underline{158.7 \text{ ksi-in.}^{1/2}} \end{matrix}$$

(b) PTC-Tension Tests

Table XIV summarizes the part-through-crack (PTC) tension test results. One of the tests of the thinner material (0.10 in. thick heat 302443) was anomalous in that there was no precursor to failure. The other tests produced pop-in or sharply defined steps in the plots of total stress-wave-emission versus load indicating crack growth. The emission-precursor stress intensity values were

$$\begin{matrix} 41.2 - 53.0 \\ \text{Av}(4) \quad \underline{45.8 \text{ ksi-in.}^{1/2}} \end{matrix}$$

In specimens EP 11, 12 and 13, subjected to continuously rising load, there was no evidence of slow crack growth in the fracture surfaces. Based on maximum load and the dimensions of the fatigue precrack, the critical stress intensity was

$$\begin{matrix} 60.0 - 63.4 \\ \text{Av}(3) \quad \underline{61.7 \text{ ksi-in.}^{1/2}} \end{matrix}$$

Specimen EP-14 was subjected to low-cycle fatigue. An unmistakable pop-in precursor occurred in fatigue after 1150 cycles, and again after 2192 cycles; the specimen was allowed to continue to failure (a total of 2200 cycles). Even the second precursor allowed more than ample time to unload the specimen before failure (approximately 8 sec). The crack had grown almost all the way through the thickness (A/B = 0.918 at the time of fracture). The stress intensity based on the crack growth produced in low-cycle fatigue was 83.6 ksi-in.$^{1/2}$. However, at this crack depth the net section was plastically deformed; from the computer printout:

TABLE XIV

6Al-4V TITANIUM, ELI ANNEALED (130 KSI YIELD STRENGTH)
PTC-TENSION TEST RESULTS

Specimen			Crack Dimensions				SWE Precursor		Maximum Load	
No.	W	B	A	2C	A/2c	A/B	Load	KQ	Load	KQ
HEAT 303109										
E1	1.978	0.269	0.130	0.580	0.224	0.483	-	-	51.85	69.0(a)
	1.203	0.269	0.130	0.580	0.224	0.483	29.70	64.5(b)	35.45	78.5
E2	1.203	0.270	0.137	0.575	0.238	0.507	32.60	73.5(c)	35.58	81.1
E3	1.203	0.269	0.132	0.575	0.230	0.491	27.5	60.0(d)	34.95	78.1
E4	1.203	0.272	0.134	0.585	0.229	0.493	27.5	59.9(e)	36.20	80.9
E5	1.203	0.272	0.150	0.580	0.259	0.552	32.50	77.6(f)	-	-
	1.203	0.272	0.180	0.660	0.273	0.662	27.50	74.9(g)	-	-
	1.203	0.272	0.180	0.735	0.245	0.662	-	-	27.50	78.3
HEAT 302443										
EP 11	1.307	0.097	0.050	0.342	0.146	0.516	(h)	(h)	15.38	61.6
EP 12	1.310	0.097	0.050	0.350	0.143	0.516	12.00	46.4(i)	15.72	63.4
EP 13	1.308	0.097	0.047	0.330	0.142	0.484	13.10	42.5(i)	15.76	60.0
EP 14	1.300	0.098	0.047	0.355	0.132	0.480	-	-	14.15	52.8(j)
			0.090	0.485	0.186	0.918	(k)	(k)	12.50	83.6(k)
EP 15	1.300	0.099	0.050	0.345	0.145	0.505	11.10	41.2(m)	15.35	59.4(p)
			0.060	0.360	0.167	0.606	12.50	54.1(n)	15.35	68.3(p)
EP 16	1.300	0.098	0.055	0.305	0.180	0.564	13.10	53.0(q)	14.75	60.6(p)
			0.070	0.350	0.200	0.718	12.50	63.2(r)	14.75	76.1(p)

Notes: (a) First loading of specimen E1, not fractured; no precursor observed; (b) second loading of specimen E1; pop-in precursor; (c) pop-in precursor; (d) inflection in total stress wave emission (TSWE)-load plot; (e) increase in TSWE; weak precursor; (f) first loading of specimen E5, sharp increase in slope of TSWE, not fractured; (g) low cycle fatigued at 1 cycle/sec. At start of cycling KQ = 63.5 ksi $in.^{1/2}$. After 357 cycles, sharp increase in slope of TSWE. Specimen failed during fatigue cycling; (h) no precursor observed; (i) pop-in precursor; (j) first loading of specimen EP 14, not fractured; load interrupted before precursor; (k) low-cycle fatigued at 1 cycle/sec., 12.50 kip max load. Unmistakable pop-in precursor occurred in fatigue after 1150 cycles. The test was continued; another unmistakable precursor occurred after 2192 cycles; specimen failed after a total of 2200 cycles; (m) first loading of specimen EP 15, not fractured; pop-in precursor; (n) low-cycle fatigued at 1 cycle/sec., 1250 kip max load After 710 cycles, specimen was unloaded based on a SWE precursor; (p) after fatigue cycling, continuously rising load to failure; (q) first loading of specimen EP 16, not fractured; pop-in precursor; (r) low-cycle fatigued at 1 cycle/sec., 12.50 kip max. load. After 802 cycles, specimen was unloaded based on a SWE precursor.

$$FG/FTY = 0.75$$
$$FN/FTY = 1.03$$
$$(KQ/FTY)^2 = 0.413$$
$$2.5\ (KQ/FTY)^2 = 1.03$$

Specimens EP 15 and 16 also were subjected to low-cycle fatigue. Both specimens were cycled until an emission precursor occurred and then unloaded. The specimens were then subjected to a continuously rising load until failure. If the crack growth produced in low-cycle fatigue is used as a basis for calculating the critical stress intensity, the range and average is

$$\begin{array}{ll} & 68.3 - 76.1 \\ \text{Av}(2) & \underline{72.2\ \text{ksi-in.}^{1/2}} \end{array}$$

This is a lower value than obtained from specimen EP-14; however, the emission data showed crack growth during the final rising-load cycle. If this crack growth was significant and undetected in the fracture surface, the calculated value of KQ would be fictitiously low.

In the thicker sheet material (0.27 in. thick heat 303109), the range and average of the stress intensity values based on the emission precursor was

$$\begin{array}{ll} & 59.9 - 77.6 \\ \text{Av}(6) & \underline{68.4\ \text{ksi-in.}^{1/2}} \end{array}$$

In specimens E-1, 2, 3 and 4 subjected to continuously rising load, there was no evidence of slow crack growth in the fracture surfaces. The critical stress intensity based on maximum load and the dimensions of the fatigue precrack was

$$\begin{array}{ll} & 78.1 - 81.1 \\ \text{Av}(4) & \underline{79.6\ \text{ksi-in.}^{1/2}} \end{array}$$

which is significantly higher than the emission-precursor stress intensity.

Specimen E-5 was failed in low-cycle fatigue. From a polarized-light photograph, the extent of the fatigue-crack growth was estimated at 0.180-in. deep and between 0.660 and 0.735-in. long; thus, at 27.5 kips load, the stress intensity at fracture was between 75 and 78 ksi-in.$^{1/2}$. The excellent agreement between this measurement and the calculation based on the fatigue-precrack dimension and maximum load indicates that in this series of tests there was little crack growth before fracture under continuously rising load. Examination of the fracture surfaces showed no slow crack growth.

A comparison between the SEN- and PTC-tension test results showed the two tests to be in excellent agreement based on the onset of crack instability as determined by stress wave emission.

Material Tested		Specimen	Critical Stress Intensity	
Heat	Thickness	Type	Instability	Failure
302443	0.10	SEN	42	174
		PTC	46	60
303109	0.30	SEN	65	159
		PTC	68	80

The difference between the 0.10 in. and 0.30 in. thick material may be the result of heat-to-heat differences. The difference between the SEN- and PTC-tension results based on failure load is attributed to a mixed-mode plane-stress condition in the SEN-tension test when the crack reached the critical size for fast fracture.

b. D6aC Low Alloy Steel

(1) Tempered at 600°F

(a) SEN-Tension Tests

Table XV summarizes the single edge-notch (SEN) tension test results. In the tests of the thinner sheet material (0.10 in. thick heat 3910262) two out of four exhibited clearcut pop-in in the COD-load plots at approximately 5.4 kips (57 ksi-in.$^{1/2}$); whereas, the emission precursor occurred at

$$\begin{array}{l} 36.2 - 43.7 \\ \text{Av(4)} \quad \underline{40.0 \text{ ksi-in.}^{1/2}} \end{array}$$

The emission precursor consisted of a rapid and nearly continuous succession of stress-wave activity. Deviation from linearity in the COD-load plots occurred at

$$\begin{array}{l} 49.6 - 55.6 \\ \text{Av(4)} \quad \underline{52.3 \text{ ksi-in.}^{1/2}} \end{array}$$

Thus, there was no significant crack growth prior to the emission-precursor stress intensity (40 ksi-in.$^{1/2}$). Failure of the test specimens occurred at

$$\begin{array}{l} 94.1 - 104.3 \\ \text{Av(4)} \quad \underline{99.5 \text{ ksi-in.}^{1/2}} \end{array}$$

TABLE XV

D6aC 600°F TEMPER (230 KSI YIELD STRENGTH)
SEN-TENSION TESTS

Specimen No.	W	B	Pre-Crack AO	COD Linearity Load	COD Linearity KQ	SWE/COD Pop-in Load	SWE/COD Pop-in KQ	Onset Instability Load	Onset Instability KQ	Fracture Load	Fracture KQ
S6	3.001	0.101	0.988	5.3	55.6	(a) 5.3	(a) 55.6	4.25	43.7	8.00	100.7
S7	3.004	0.100	0.980	4.8	49.6	(a) 5.5	(a) 57.6	3.50	36.2	7.87	104.3
S8	3.004	0.101	0.984	5.1	52.5	(a) (b)	(a) (b)	4.00	40.8	7.95	99.0
S9	3.003	0.101	1.002	4.9	51.4	(a) (b)	(a) (b)	3.77	39.5	7.35	94.1
S3-1	3.003	0.294	0.969	17.5	60.3	13.4 17.9	45.6(c) 62.8	15.65	53.0	20.2	92.6
S3-3	3.001	0.293	0.964	13.6	50.2	13.55 18.75	50.2(c) 70.9	17.2	63.9	21.07	99.6
S3-4	3.001	0.292	0.993	14.15	56.4	(a) 19.05	(a) 80.8	17.35	70.5	20.8	106.8

NOTES: (a) No SWE pop-in observed.
(b) No COD pop-in observed.
(c) Pop-in occurrences not as definite as in other materials and material condition investigated.

In the thicker sheet material (0.29 in. thick heat 3952092), a COD pop-in was observed in all three test specimens at

$$\text{Av(3)}\ \frac{62.8 - 80.8}{71.5\ \text{ksi-in.}^{1/2}}$$

whereas, the emission precursor occurred at

$$\text{Av(3)}\ \frac{53.0 - 70.5}{62.5\ \text{ksi-in.}^{1/2}}$$

Deviation from linearity in the COD-load plots occurred at

$$\text{Av(3)}\ \frac{50.2 - 60.3}{55.6\ \text{ksi-in.}^{1/2}}$$

The fact that the emission precursor came after deviation from linearity indicates that, in this case, there was a significant amount of crack growth and/or plastic-zone formation before the emission precursor stress intensity (62 ksi-in.$^{1/2}$); however, COD pop-in did not occur until 72 ksi-in.$^{1/2}$. Failure of the specimens occurred at

$$\text{Av(3)}\ \frac{92.6 - 106.8}{99.7\ \text{ksi-in.}^{1/2}}$$

Figure 55 shows the fracture-surface markings in specimen S3-3; the bands indicate alternating regions of slow crack growth (darker areas) and pop-in.

Specimen S3-5 was tested to failure in low-cycle fatigue. Initially the specimen was loaded (continuously rising load) until COD showed deviation from linearity (at approximately 20 kips); the specimen was then unloaded and reloaded in tension-tension fatigue (10 to 17.5 kips). The intent of this procedure was to mark the crack growth associated with COD deviation from linearity; the test results are shown in Figures 56, 57 and 58. After approximately 4000 cycles, the specimen was unloaded and then reloaded (continuously rising load) until the data indicated a marked increase in stress wave emission (at approximately 20 kips); there were about 30,000 stress waves counted in this 2nd loading. This procedure was repeated four times; i.e., after each of four loadings, the specimen was subjected to low-cycle fatigue in an attempt to mark the crack growth associated with the SWE attending each application of continuously rising load. The third and fourth loading was arbitrarily to 15 kips.

Figures 56 and 57 show the increase in COD during low-cycle fatigue after each loading. After the second loading, 2090 cycles produced approximately twice the COD that was produced with 4000 cycles after the first loading. Thus, the crack was growing but not to critical size until the 89th cycle after the fourth rising load. A calculation of the stress intensity based on the fatigue cracking load (18 kips) and the crack as measured in the broken specimen, with the plane-stress plastic-zone correction, gave

$$105 \text{ ksi-in.}^{1/2}$$

as the critical stress intensity at fracture. Specimens S3-1, 3 and 4 (Table XV) gave an average value of

$$99.7 \text{ ksi-in.}^{1/2}$$

From an NDI point of view, the important observation in this experiment was an unmistakable SWE precursor of failure during the low-cycle fatigue test. Figure 58 shows the progressive increase in total stress-wave emission (TSWE) count per cycle, giving ample warning of impending fracture.

(b) PTC-Tension Tests

Table XVI summarizes the part-through crack (PTC) tension test results. In the thinner material (0.1 in. thick heat 3910262), the plane-strain instability was manifested by a succession of pop-in like steps in the plot of total-stress-wave emission versus load and a marked increase in stress-wave activity as failure was approached. The range and average value of stress intensity corresponding to the emission-precursor was as follows:

$$\begin{array}{ll} & 30.7 - 42.3 \\ \text{Av(4)} & 39.2 \text{ ksi-in.}^{1/2} \end{array}$$

Based on the dimensions of the fatigue precrack and maximum load, the apparent critical stress-intensity was

$$\begin{array}{ll} & 57.6 - 66.3 \\ \text{Av(4)} & 63.1 \text{ ksi-in.}^{1/2} \end{array}$$

a value considerably higher than that calculated from the fatigue precrack and the emission-precursor load. When the fracture-surface marking indicated crack growth before maximum load as shown in Figure 59, the stress-intensity based on maximum load and the dimensions of semi-elliptical flaws grown beyond the ink-stained fatigue-crack envelope was

TABLE XVI

D6aC (600°F TEMPER) 230 KSI YIELD STRENGTH
PTC-TENSION TESTS

Specimen			Crack Dimensions				SWE Precursor		Maximum Load	
No.	W	B	A	2C	A/2C	A/B	Load	KQ	Load	KQ
P2	1.001	0.101	0.052	0.140	0.371	0.515	11.10	42.3(a)	15.11	57.6
			0.052	0.230	0.226	0.515	11.10	49.0	15.11	67.8
P3	0.998	0.101	0.080	0.505	0.158	0.792	4.25	30.7(b)	8.60	62.6
P4	1.000	0.101	0.050	0.215	0.233	0.495	10.00	42.3(c)	15.3	66.0
P5	0.994	0.100	0.050	0.180	0.278	0.500	10.00	41.4(d)	15.77	66.3
			0.055	0.210	0.262	0.550	10.00	45.7	15.77	73.2
P3-1	2.011	0.294	0.115	0.572	0.201	0.391	-	-	52.6	56.2(e)
	1.005	0.294	0.115	0.572	0.201	0.391	27.3	58.8(f)	29.65	63.5
			0.170	0.572	0.297	0.578	27.3	72.0	29.65	78.3
P3-2	1.005	0.277	0.114	0.521	0.219	0.412	28.8	64.6(g)	31.52	71.0
			0.170	0.521	0.326	0.614	28.8	80.5	31.52	88.2
P3-3	1.006	0.295	0.122	0.580	0.210	0.414	29.6	65.2(h)	31.47	69.4
			0.190	0.580	0.328	0.644	29.6	83.9	31.47	89.4
P3-4	1.004	0.294	0.121	0.521	0.232	0.412	30.5	65.7(i)	34.3	74.1
			0.175	0.521	0.336	0.595	30.5	79.8	34.3	90.0

NOTES: (a) SWE pop-in at 7.75 kips (29.1 ksi-in.$^{1/2}$). (b) SWE pop-in at 3.25 kips (13.0 ksi-in.$^{1/2}$); excessive precrack. (c) SWE pop-in at 8.75 kips (40.2 ksi-in.$^{1/2}$). (d) SWE pop-in at 6.65 kips (29.0 ksi-in.$^{1/2}$). (e) First loading of specimen P3-1, unloaded before SWAT precursor observed, not fractured. (f) Second loading of specimen P3-1; succession of SWE pop-in starting at 6.15 kips (13.0 ksi-in.$^{1/2}$). (g) Succession of SWE pop-in starting at 4.45 kips (9.85 ksi-in.$^{1/2}$). (h) Succession of SWE pop-in starting at 17.5 kips (38.0 ksi-in.$^{1/2}$). (i) Succession of SWE pop-in starting at 3.8 kips (8.54 ksi-in.$^{1/2}$).

$$\begin{matrix} 67.8 - 73.2 \\ \text{Av}(2) \quad \underline{70.5 \text{ ksi-in.}^{1/2}} \end{matrix}$$

In the thicker sheet material (0.29 in. thick heat 3952092), the emission precursor was clearly defined as an abrupt increase in the total stress wave count. The range and average value of the emission-precursor stress intensity was

$$\begin{matrix} 58.8 - 65.7 \\ \text{Av}(4) \quad \underline{63.6 \text{ ksi-in.}^{1/2}} \end{matrix}$$

Based on the dimensions of the fatigue precrack and maximum load, the range and average stress intensity was

$$\begin{matrix} 63.5 - 74.1 \\ \text{Av}(4) \quad \underline{69.5 \text{ ksi-in.}^{1/2}} \end{matrix}$$

a value which is probably fictitiously low considering the evidence of slow crack growth as shown on Figure 60, that appeared in all the fracture surfaces. When the dimensions of the semi-elliptical flat fracture surface were used in lieu of the ink-stained fatigue precrack dimensions, the stress intensity values were

$$\begin{matrix} 78.3 - 90.0 \\ \text{Av}(4) \quad \underline{86.5 \text{ ksi-in.}^{1/2}} \end{matrix}$$

which is an appreciably higher value than that calculated based on the fatigue precrack. Figure 60 contradicts the concept that slow crack growth in the PTC-tension test is the result of plastic deformation. Consider the case of specimen P3-1, for example. At a load of 27.3 kips, the stress intensity corresponding to the enlarged crack was

$$72 \text{ ksi-in.}^{1/2}$$

while the criteria for elastic behavior, again based on the enlarged crack, were

$$\begin{aligned} \text{FG/FTY} &= 0.402 \\ \text{FN/FTY} &= 0.543 \\ (\text{KQ/FTY})^2 &= 0.098 \text{ in.} \\ 2.5\ (\text{KQ/FTY})^2 &= 0.245 \text{ in.} \\ \text{A} &= 0.170 \\ \text{A/B} &= 0.578 \end{aligned}$$

With the net-section stress approximately half the yield strength, one might expect elastic behavior, particularly in view of the predominatly flat fracture developed in this series of test specimens.

(2) Tempered at 1100°F

(a) SEN-Tension Tests

Table XVII summarizes the single-edge notch (SEN) tension test results. In the tests of the thinner sheet material (0.1 in. thick heat 3910262), while there was no evidence of COD pop-in, there were indications of pop-in in the emission data. The range and average stress-intensity values corresponding to the emission pop-in were

$$\begin{matrix} 55.0 - 87.6 \\ \text{Av(3)} \quad \underline{69.9 \text{ ksi-in.}^{1/2}} \end{matrix}$$

Deviation from linearity in the COD-load plots occurred at

$$\begin{matrix} 95.4 - 107.7 \\ \text{Av(3)} \quad \underline{101.4 \text{ ksi-in.}^{1/2}} \end{matrix}$$

a stress intensity higher than that corresponding to the emission data pop-in; thus, there was no significant crack growth prior to the emission data pop-in. An unmistakable emission precursor was observed in each test at stress intensities ranging from

$$\begin{matrix} 124.1 - 139.2 \\ \text{Av(3)} \quad \underline{130.4 \text{ ksi-in.}^{1/2}} \end{matrix}$$

corresponding to the start of rapid and continuing stress wave activity. Failure of the test specimens occurred at

$$\begin{matrix} 274.6 - 294.0 \\ \text{Av(3)} \quad \underline{285.1 \text{ ksi-in.}^{1/2}} \end{matrix}$$

In the thicker sheet material (0.29 in. thick heat 3952092), again there was little evidence of COD pop-in. The emission data pop-in occurred at stress intensities ranging from

$$\begin{matrix} 82.1 - 96.4 \\ \text{Av(3)} \quad \underline{90.4 \text{ ksi-in.}^{1/2}} \end{matrix}$$

and deviation from linearity in the COD-load plots occurred at

$$\begin{matrix} 74.4 - 99.2 \\ \text{Av(3)} \quad \underline{87.0 \text{ ksi-in.}^{1/2}} \end{matrix}$$

TABLE XVII

D6aC (1100°F TEMPER) 200 KSI YIELD STRENGTH SEN-TENSION TESTS

Specimen				COD Linearity		SWE Pop-in		SWE Precursor		Fracture	
No.	W	B	A0	Load	KQ	Load	KQ	Load	KQ	Load	KQ
S2	3.000	0.101	1.002	9.0	95.4	5.30	55.0(a)	11.55	127.9	16.9	274.6
S5	2.999	0.101	1.009	9.4	101.1	6.30	67.1(a)	11.30	124.1	17.1	294.0
S12	3.004	0.101	1.011	10.0	107.7	8.20	87.6(a)	12.50	139.2	17.1	286.8
S3-7	3.002	0.292	0.959	19.5	74.4(b)	24.8	96.4	29.45	116.8	43.6	251.4
S3-8	2.999	0.293	0.993	26.0	99.2(c)	24.3	92.6	29.7	116.1	41.5	224.3
S3-9	3.000	0.293	0.965	24.5	87.3(d)	23.2	82.1	30.0	110.2	40.3	204.3

NOTES:
(a) First of a succession of jumps in total stress wave count.
(b) COD pop-in at 33.25 kips (139 ksi-in.$^{1/2}$).
(c) Inflection in COD-LOAD curve at 31.5 kips (126 ksi-in.$^{1/2}$).
(d) Inflection in COD-LOAD curve at 30.2 kips (111 ksi-in.$^{1/2}$).

thus, there was some crack growth prior to emission data pop-in. An unmistakable emission precursor was observed in each test at stress intensities ranging from

$$\begin{array}{ll} 110.2 & - \quad 116.8 \\ \text{Av}(3) & \underline{\quad 114.4 \text{ ksi-in.}^{1/2} \quad} \end{array}$$

A comparison between this and the intensity at deviation from linearity in the COD-load plots (at 87 ksi-in.$^{1/2}$), indicates that considerable crack growth and/or plastic-zone formation had occurred before the emission precursor. COD pop-in, on the other hand, occurred in Specimen S3-7 at 139 ksi-in.$^{1/2}$; whereas, in Specimens S3-8 and S3-9 there was not clear-cut pop-in but a distinct inflection in the COD-LOAD plot which indicated crack instability at 126 and 111 ksi-in.$^{1/2}$, respectively. Thus, the plane-strain instability occurred at

$$\begin{array}{ll} 111 & - \quad 139 \\ \text{Av}(3) & \underline{\quad 125 \text{ ksi-in.}^{1/2} \quad} \end{array}$$

Failure of the test specimens occurred at

$$\begin{array}{ll} 204.3 & - \quad 251.4 \\ \text{Av}(3) & \underline{\quad 226.7 \text{ ksi-in.}^{1/2} \quad} \end{array}$$

(b) PTC-Tension Tests

Table XVIII summarizes the part-through-crack (PTC) tension test results. In the thinner sheet material (0.1 in. thick heat 3910262), the plots of total-stress-wave count versus load showed a succession of steps starting at very low load making it impossible to select a stress-wave precursor. This is shown in Figures 61 and 62 for 0.1 in. thick Specimen P-11; the behavior of this specimen was typical of all of this series. Note, at 14 ksi, the unmistakable increase in the RMS plot - the stress-wave precursor for Specimen P-11. The emission precursor for this series of tests ranged from

$$\begin{array}{ll} 49.5 & - \quad 54.8 \\ \text{Av}(4) & \underline{\quad 52.6 \text{ ksi-in.}^{1/2} \quad} \end{array}$$

Based on the usual practice of using the fatigue-precrack dimensions and maximum load for calculating critical stress intensity

$$\begin{array}{ll} 64.7 & - \quad 79.2 \\ \text{Av}(4) & \underline{\quad 71.6 \text{ ksi-in.}^{1/2} \quad} \end{array}$$

TABLE XVIII

D6aC (1100°F TEMPER) 200 KSI YIELD STRENGTH
PTC-TENSION TESTS

Specimen			Crack Dimensions				SWE Precursor		Maximum Load	
No.	W	B	A	2C	A/2C	A/B	Load	KQ	Load	KQ
P8	0.999	0.100	0.035	0.175	0.200	0.350	15.0	54.8(a)	19.38	71.0
			0.045	0.220	0.204	0.450	15.0	64.1	19.38	83.9
P9	0.999	0.100	0.040	0.180	0.222	0.400	14.5	54.8(b)	20.12	79.2
P10	1.998	0.101	0.035	0.140	0.250	0.346	18.8	30.4(c)	26.5	42.6
	1.003	0.101	0.035	0.140	0.250	0.346	14.75	49.5(d)	19.06	64.7
			0.050	0.230	0.217	0.495	14.75	65.4	19.06	87.0
P11	0.999	0.101	0.040	0.150	0.267	0.396	14.0	51.2(e)	19.55	71.7
			0.047	0.198	0.237	0.465	14.0	57.3	19.55	83.1
P12	0.999	0.101	0.028	0.145	Defective Precrack					
			0.063	0.233	0.271	0.624	(f)	(f)	13.50	69.5(g)
P3-7	0.790	0.294	0.120	0.533	0.225	0.408	(f)	(f)	34.28	95.3
			0.180	0.533	0.338	0.612	(f)	(f)	34.28	123.0
P3-8	0.790	0.292	0.133	0.598	0.222	0.456	(f)	(f)	30.55	91.8
			0.180	0.598	0.301	0.616	(f)	(f)	30.55	109.5
P3-9	0.790	0.295	0.120	0.550	0.218	0.407	(f)	(f)	33.92	94.8
			0.165	0.550	0.300	0.559	(f)	(f)	33.92	110.8
P3-10	0.790	0.293	0.124	0.507	0.243	0.423	(f)	(f)	34.78	94.8
			0.170	0.507	0.335	0.580	(f)	(f)	34.78	114.0
P3-11	0.790	0.293	0.130	0.600	0.217	0.444	(f)	(f)	23.00	77.0(h)
			0.200	0.650	0.308	0.683	(f)	(f)	23.00	103.0

NOTES: (a) Succession of SWE pop-in starting at 4.5 kips (15 ksi-in.$^{1/2}$). (b) Succession of SWE pop-in starting at 4.4 kips (15 ksi-in.$^{1/2}$). (c) First loading of Specimen P10. Succession of SWE pop-in starting at 3.6 kips (6 ksi-in.$^{1/2}$). No SWAT precursor, not fractured. (d) Second loading of Specimen P10. Succession of SWE pop-in starting at 4.3 kips (14 ksi/in$^{1/2}$). (e) Succession of SWE pop-in starting at 3.9 kips (13 ksi-in.$^{1/2}$). (f) Nearly continuous stress-wave activity, starting at very low load. (g) Specimen P12, initially loaded to 17.5 kips, was subjected to low-cycle tension-tension fatigue. After approximately 2400 cycles, under a maximum load of 13.50 kips, there was an unmistakable SWAT-precursor; about 70 cycles later the specimen fractured. (h) Specimen P3-11, initially loaded to 28.75, was subjected to low-cycle tension-tension fatigue, under a maximum load of 23 kips (77 ksi-in.$^{1/2}$). After approximately 470 cycles, the specimen failed; the critical stress intensity based on the semi-elliptical fatigue-crack growth was 103 ksi-in.$^{1/2}$.

However, as shown in Figure 63, three out of four specimens tested contained flat, semi-elliptical flaw growth beyond the ink-stained fatigue precrack. The stress intensities based on these crack dimensions were

$$\begin{matrix} 83.1 & - & 87.0 \\ \text{Av}(3) & & \underline{84.7 \text{ ksi-in.}^{1/2}} \end{matrix}$$

Specimen P-12, 0.10-in.-thick, was initially loaded to 17.5 kips; approximately 230,000 stress waves were recorded. On a second loading, there were fewer than 2500 stress waves. This indication of the Kaiser effect (i.e., irreversible nature of emissions[54] suggests that the triggering level was set at too high a sensitivity for these tests and was recording plastic deformation. The specimen was then subjected to tension-tension low-cycle fatigue at a rate of 50 cycles per minute. After 805 cycles at 14.65 kips maximum load, the specimen was unloaded, and an unsuccessful attempt was made to ink stain the fatigue crack. The low-cycle fatigue was then resumed, this time at a somewhat lower maximum load, 13.50 kips. After approximately 1585 additional cycles, an unmistakable emission precursor was observed in the plot of total stress-wave emission versus time. After approximately 70 additional cycles, the specimen fractured.

The fracture surface clearly showed two areas of low-cycle fatigue growth associated with the ink-stained fatigue precrack*. This explained a very large count during fatigue cycling. Beyond the two separate areas there was an additional area of fatigue-crack growth that could be seen in the fractured test piece but could not be photographed without polarized light.

A calculation of critical stress intensity based on the known load (13.5 kips) and the outer limit of the semi-elliptical fatigue crack shown in the polarized photograph, gave a value of

$$69.5 \text{ ksi-in.}^{1/2}$$

From Table XVIII it will be seen that this is somewhat higher than the emission precursor stress intensity (53 ksi-in.$^{1/2}$), and in good agreement with the KQ value based on maximum load and fatigue-precrack dimensions (72 ksi-in.$^{1/2}$). However, based on the evidence of slow crack growth in the fracture surfaces of the continuously rising load test specimens, this correlation is believed to be fortuitous. The plane-strain critical stress intensity is probably higher than these values.

* Several specimens in this series were improperly electric-discharge machined. A triangular elox slot was supposed to be cut 0.025 in. deep (Altitude) and 0.20 in. long (base of triangle). Instead, a circular cut was made which led to the defective fatigue precrack. A triangular slot has been found to be a superior starting notch for fatigue precracking.

In the thicker sheet material (0.29 in. thick heat 3952092), there was a large amount of stress-wave activity starting at low load which continued at a more or less constant level of activity until fracture (see Figures 61 and 62). Thus, there were no discrete events that could be identified as an emission precursor of the failure. However, if this behavior were encountered in a structure instrumented for triangulation, the defect source could have been located at a low load, long before fracture. The stress intensities calculated on the basis of maximum load and the dimensions of the fatigue precrack ranged from

$$\begin{matrix} 91.8 & - & 95.3 \\ Av(4) & & \underline{94.2 \text{ ksi-in.}^{1/2}} \end{matrix}$$

As shown in Figure 64, each specimen contained flat, semi-elliptical flaw growth, beyond the ink-stained fatigue precrack. The corresponding stress intensities were

$$\begin{matrix} 109.5 & - & 123.0 \\ Av(4) & & \underline{114.3 \text{ ksi-in.}^{1/2}} \end{matrix}$$

Specimens P3-11 was initially subjected to a continuously rising load to 28.75 kips and then unloaded before a precursor was observed. The specimen was then subjected to two cycles of 20 kips maximum load using the same rate as in the initial loading. The stress-wave count in these cycles was markedly lower than that at 20 kips in the first cycle, again attributed to the Kaiser effect (see Figure 65).

Cycle	Count
1	940,000
2	60,000
3	22,000

The evidence of the Kaiser effect suggests that at the triggering level used for these tests plastic deformation and crack growth were both sensed. Specimen P3-11 was then subjected to a low-cycle high-stress-intensity (77 ksi-in.$^{1/2}$) fatigue. After 354 cycles, there was a clearly defined emission precursor (pop-in) (see Figure 66). The load was dumped before the specimen fractured; the specimen was then reloaded for continued low-cycle, tension--tension fatigue at 23 kips maximum load. After 117 additional cycles, there was another emission precursor; the specimen was allowed to fail. After approximately 10 additional cycles and 50,000 stress-wave counts, the specimen fractured. A calculation of the stress intensity at fracture based on the semi-elliptical flat-fracture produced by the low-cycle-fatigue crack growth and the maximum load used in the fatigue cycling gave a value of 103 ksi-in.$^{1/2}$ for KQ. A comparison between this and the values obtained from the conventional,

continuously rising load tests (P3-7, 8, 9, 10) based on the fatigue precrack (94 ksi-in.$^{1/2}$) and the clearly delineated semi-elliptical, flat-fracture areas in each test specimen (114 ksi-in.$^{1/2}$) showed good agreement by either method of calculation. The incremental crack growth could be getting larger with each cycle just before fracture and, therefore, the surface appearance associated with the last 2 or 3 cycles might not be significantly different from the fracture appearance associated with catastrophic propagation after the critical crack was developed. Thus, the critical crack could be larger than the apparent crack size. If the dimensions of the critical crack could be measured, the calculated value of stress intensity would be higher than 103 ksi-in.$^{1/2}$ and, thus, closer to 114 ksi-in.$^{1/2}$.

A comparison between the SEN- and PTC-tension test results from the D6aC-600 and D6aC-1100 heat-treat conditions showed the two test methods to be in good agreement based on the emission precursor. In the 0.1 in. thick D6aC-1100 sheet material, the tests did not agree if the onset of instability was used as the basis of calculating the SEN-KQ value (130 ksi-in.$^{1/2}$); however, if emission pop-in was used as the basis for calculation, the agreement was fair (70 versus 53 ksi-in.$^{1/2}$). The fact that the emission instability KQ values were consistently lower for the 0.10 in. thick material as compared to the 0.29-in.-thick material may be the result of heat-to-heat differences.

Material	Specimen		Critical Stress Intensity (ksi-in.$^{1/2}$)		
	Thick	Type	Emission Instability	KQ	Fracture
D6aC-600	0.10	SEN	40	57	100
		PTC	39	63	70
	0.29	SEN	62	72	100
		PTC	64	70	86
D6aC-1100	0.10	SEN	70	108	285
		PTC	53	72	85
	0.29	SEN	90	125	227
		PTC	-	94	114

Figure 67 illustrates the differences in fracture behavior resulting from tempering at 600 and 1100°F. The fracture surfaces in the 600°F tempered material consistently developed bands which were interpreted to be alternating slow growth and pop-in. An attempt to correlate the band positions with crack depth corresponding to discontinuities in the COD-LOAD plot indicated that deviation from COD linearity corresponded to the first dark band (calculated crack depth 1.017 in. based on COD at the point of deviation from linearity, less a plastic-zone correction). The first dark

band also corresponded in position to the first five bursts of stress-wave activity (at 12.5, 13.9, 15.8, 17.2 and 18.0 kips). Table XIX shows details of the correlation of fracture-surface markings and fracture-testing events. The dark bands are presumed to be slow crack growth followed in each case by pop-in. Thus, the fifth SWE burst corresponding to the first dark band was the pop-in event producing the following bright band. The count (TSWE) and stress-wave activity (RMS) associated with each of these five bursts confirms this in that the counts became progressively larger (Figures 68 and 69).

	SWE Activity	
LOAD (kips)	TSWE (Counts)	RMS ($X10^{-3}V$)
12.50	4,300	0.5
13.90	5,900	0.8
15.75	7,500	3.0
17.20	8,000	5.0
18.00	10,000	100
19.50	36,000	100
20.50	60,000	100

3. Quantitative Prediction of Crack Growth

Potentially one of the most important observations derived from acoustic-emission technology is that the emission characteristics of flawed specimens are highly dependent upon the stress intensity of the flaw present. The first evidence obtained at Aerojet of a relationship between stress-wave emission and stress intensity factor came from a study of fatigue cracking in 1/8 x 8 x 24 in. D6aC through-cracked, center-notched panels*. As shown in Figure 70, the crack growth rate in low-cycle high-stress-intensity fatigue was shown to be directly proportional to the summation of stress-wave amplitude in each cycle.

At about the same time, Dunegan, Harris and Tatro at the University of California Lawrence Radiation Laboratory (LRL) showed that with the counter trigger level set to record plastic deformation (dislocation activity), most of the emission occurs during and shortly after yielding,

*C. E. Hartbower, W. W. Gerberich and P.P. Crimmins, "Characterization of Fatigue Crack Growth by Stress Wave Emission", Final Report CR-66303 on NASA (Langley Research Center Contract NAS 1-4902, June 1966. See also International Journal of Fracture Mechanics, Vol. 3, p. 185, Sept. 1967.

TABLE XIX

CORRELATION OF FRACTURE-SURFACE MARKINGS AND FRACTURE-TESTING EVENTS

Fracture Bands[a]		SWE Bursts[b]		COD Events[b]	
Color	Depth (in.)	Load (kips)	Crack (in.)	Load (kips)	Crack (in.)
Ink Stained	0.964	-	-	-	-
Light	0.964-0.978	-	-	-	-
Dark	0.978-1.020	12.50	1.011		
		-	-	13.60	1.017[c]
		13.90	1.016	-	-
		15.75	1.014	-	-
		17.20	1.020	-	-
		18.00	1.020	-	-
Light	1.020-1.056	-	-	18.75	1.032
		-	-	18.88	1.050
Dark	1.056-1.092	19.50	1.082	-	-
Light	1.092-1.117	-	-	-	-
Dark	1.117-1.136	-	-	20.12	1.126
		20.50	1.127	-	-
		-	-	20.75	1.131
Light	1.136-1.187	-	-	-	-
Dark	1.187-1.248	Continuous (d)		21.07	1.202
Light	1.248-1.306	Continuous (d)		Continuous (d)	
Dark	1.306-1.338	Continuous (d)		Continuous (d)	
Light	1.338-3.001	Continuous (d)		Continuous (d)	

(a) Average of three 1/4-point measurements
(b) Crack depth based on COD at that load
(c) COD-LOAD deviation from linearity
(d) Succession of fracture-testing events so rapid as to be indistinguishable.

then decreases as further straining takes place. Based on the volume of metal being strained in the plastic zone at the tip of a crack, Dunegan assumed that the acoustic emission count rate would be proportional to the rate of increase of the volume of metal producing the acoustic emission. This led to the prediction that if all the acoustic-emission pulses are added up as the test proceeds, then at any time the total number of counts will be proportional to the fourth power of the stress-intensity factor associated with the flaw at the time. Figure 71 from the work of Dunegan and Harris, shows the relationship between stress-intensity factor and acoustic emission cumulative count in rising-load-to-failure tests of 7075-T6 aluminum. Note that data obtained from four initial crack lengths grouped into a single curve fitting the theoretical fourth-power curve. Unfortunately the plots of such data did not always conform to a 4th power curve; in another study, Dunegan and Harris reported the exponent to vary between the 6th and 8th power. Later studies at Aerojet[14] indicated a direct proportionality between stress-intensity factor and cumulative stress-wave count in single-edge-notch tension specimens (Figure 72). It was hypothesized that the difference between the LRL and Aerojet test results could be the result of a difference in trigger level. At LRL the counter trigger level was set to include the continuous emission produced by plastic deformation; whereas, in most Aerojet studies, the trigger level was set above the continuous emission, focusing on the burst-type stress-wave emission associated with incremental crack growth. However, differences from test to test, even with a supposedly constant data-acquisition system, have been encountered and as yet not explained.

The importance of the relationship between stress intensity factor and acoustic emission lies in the possibility of estimating flaw sizes and failure load based on in-service, real-time, nondestructive inspection of a flawed structure utilizing acoustic emission. However, before this can be realized, much has to be learned about the variables affecting the count-versus-K relationship. To facilitate comparisons between results obtained in the various studies at Aerojet, a computer program was used to calculate stress-intensity values from empirically determined values of load and COD, and to plot various relationships. These relationships were based on the following fracture-mechanics parameters*:

$$G = K^2/E$$

$$(COD)E/(1-\nu^2) = \frac{2K}{\pi}(2\pi r)^{1/2}$$

$$r = \frac{1}{2\pi}\left(\frac{K}{FTY}\right)^2$$

*Irwin, ENGINEERING FRACTURE MECHANICS, Vol. 1, No. 2, pp. 241-257, 1968.

where G is the stress-field energy release rate (in.-lb/in.^{2}), K is the stress intensity factor (ksi-in.^{2}), E is the modulus (psi), COD is crack-opening displacement (in.), v is Poisson's ratio, r is the plastic-zone size (in.) and FTY is the 0.2 percent offset yield strength (psi).

It was hypothesized that if the electronic counter integrates size and number of the stress-wave emission, the count can be assumed to be proportional to the stress-field energy release rate, G. Based on this assumption, it can be shown that the above fracture-mechanics parameters should provide a proportionality between TSWE and K^2/E and between COD and $(1-v^2)$ TSWE/FTY, where TSWE is the cumulative stress-wave emission count.

A computer program was used to calculate the stress-intensity values from empirically determined values of load and COD, and to plot the semi-empirical relationships. The relationship K versus TSWE was also plotted as a basis of comparison. An example of the computer printout is shown in Table XX.

To obtain a better understanding of how the acoustic-emission data-acquisition system affects the plot of count versus K, the data collected in AFML Contract AF 33(615)-2788 were re-evaluated by computer program, as well as those obtained in an early phase of the present contract. The data from Contract 2788 were primarily sustained-load tests with hydrogenation and tested in water at 65 and 165°F. In AFML Contract 2788, the stress-wave system involved a single transducer (ENDEVCO 2213 accelerometer) with 100X amplification followed by 30 KHz high-pass filtering and 1000X amplification. Figure 73 is a schematic of the system. The method for setting and maintaining the trigger of the counter at a constant level was relatively crude compared with the Dunegan system used in the current ARPA study. Figures 74-76 are computer printout from Contract 2788. Note that all of the data indicated relationships between the various parameters, but there was considerable displacement from curve to curve in any one series, as might be expected with a variable counter level.

A single heat of Grade-250 maraging steel, split to provide part as air-melt and part as vacuum-arc-remelt provided encouraging results as will be seen from Figures 77-79 The contrasting D6aC test results are summarized in Figure 80 in a semilog plot.

Figure 81 shows the system used in obtaining data in an early phase of the current contract. Note that the sequence of amplification was changed and the filter level was markedly increased as a result of noise in the Research Incorporated testing system.

TABLE XX

SINGLE-EDGE-NOTCH TENSION TEST PROGRAM, S82 MAY 19

PROGRAM NUMBER SA015, DEPT 4350, 5/18/71 BY COMPUTER

MF(AVE)= .54305-04 MF... .53066-04 .55543-04

V	VBE/P	P KIPS	AO	Y	KI KSI-IN-1/2	RY IN.	(KI/FTY)**2
.01009	1.48847	26.03000	.54489	2.35977	117.959	.0565	.3549
.01352	1.96082	26.47000	.65254	2.50912	139.577	.0791	.4969
.01389	2.00304	26.62000	.66187	2.52312	142.157	.0820	.5155
.01529	2.20681	26.60000	.70565	2.59112	150.625	.0921	.5787
.01576	2.27067	26.66000	.71882	2.61235	153.616	.0958	.6019
.01642	2.36532	26.66000	.73791	2.64377	157.514	.1007	.6329
.01737	2.50220	26.66000	.76487	2.68951	163.141	.1080	.6789
.01775	2.55695	26.66000	.77541	2.70784	165.380	.1110	.6976
.01830	2.63517	26.66000	.79019	2.73397	168.560	.1153	.7247
.01976	2.85273	26.60000	.82938	2.80583	176.829	.1269	.7976
.02014	2.90765	26.60000	.83876	2.82359	178.952	.1300	.8169
.02383	3.44074	26.60000	.92098	2.98953	198.538	.1600	1.0054

V	K**2/E	(1-NU**2)/FTY*TSWE	DEL(AREA)	DEL(TSWE)*E/K**2	TSWE
.01009	463.81	.00000	.014	22.50714	1.
.01352	649.39	.06718	.001	3.96365	14617.
.01389	673.62	.07945	.006	15.39800	17287.
.01529	756.27	.13297	.002	2.58964	28932.
.01576	786.59	.14233	.002	12.27288	30969.
.01642	827.03	.18898	.003	9.99255	41119.
.01737	887.16	.22972	.001	5.19809	49984.
.01775	911.68	.25150	.002	9.71615	54723.
.01830	947.08	.29380	.005	2.35540	63925.
.01976	1042.28	.30508	.001	4.62312	66380.
.02014	1067.46	.32776	.011	15.45836	71315.
.02383	1313.92	.42111	.000	.00000	91626.

Figure 82 presents data from three tests of D6aC material of the same thickness and heat treatment as used in obtaining the data of Figure 80. With an increase in thickness, the relationship between G and acoustic-emission count was appreciably changed as will be seen from Figure 83. Again, from Figure 84-85, with a higher-strength, lower-toughness condition (600°F temper), D6aC provided a fairly consistent relationship but with considerable variation between individual tests. Figure 86, is the computer printout for K^2/E versus count plotted on a uniform scale rather than semilog; Figure 87 is a plot of K versus count. Two thicknesses of material are included in these plots. When D6aC was tempered at 1100°F, the effect of thickness was more pronounced as will be seen in Figure 88.

B. SUBCRITICAL CRACK GROWTH IN LOW-CYCLE HIGH-STRESS INTENSITY FATIGUE

1. Background

One of the first studies at Aerojet based on stress-wave emission was sponsored by NASA Langley Research Center to characterize fatigue-crack growth by stress wave emission[9]. The study conclusively demonstrated the feasibility of using SWAT for monitoring fatigue cracking cycle by cycle (see Figure 70).

Electron fractography has provided much information on how fatigue cracks grow. However, the expense of electron fractography both in terms of equipment and skill required, severely limits the use of this tool. The use of stress-wave emission promises to be much cheaper and provides a dynamic real-time measurement of crack growth. Coupling the two techniques, electron fractography and stress-wave emission, will greatly enhance both methods.

The need for more detailed information on the fatigue cracking process has been recognized for at least a decade. Weibull[55] in 1961 discussed this subject. "In any fatigue damaging process, continued until final rupture, various stages of quite different characters can be distinguished. From an engineering aspect, it may be convenient to divide the process into an initiation period, ending with the appearance of a visible crack, and a propagation period, ending with the final rupture".

Studies of crack growth based on the appearance of fracture surfaces also were discussed by Christensen[56] in 1961. Findings from such study "...support the general conclusion that the crack-propagation phase of fatigue damage is more predictable and less subject to scatter than the crack nucleation phase. Most scatter in fatigue data results from scatter in the micro-crack nucleation period... The transition from crack nucleation to the crack propagation phase is a rather difficult and complex stage for which limits should be defined. Although this has been recognized and discussed by many

researchers, the point of view taken here is based on field experiences where it has been found that a crack one-fourth inch to one-half inch long is about the smallest flaw that can be readily detected in working structures. This is reasonable for structures composed of many members and alternate load paths. Moreover, it may be fortunate that most metals research programs have taken this practical viewpoint of assuming the existence of cracked members. In the later stages of cracking which the designer encounters he is far more concerned with crack growth and fracture characteristics in structures than with the crack nucleating period. On the other hand, the designer must also focus his attention on crack nucleation in his efforts to design fatigue resistant structures. Nevertheless, it is well to separate the two phenomenon for study. Unless fatigue data are properly evaluated and separated in these respects, it becomes too diluted, and gives rise to more speculation than understanding.*

Much has been said about sporadic crack growth in fatigue. For example, with programmed loading, it has been observed that in certain instances, when stepwise loading is decreasing, there is a delay before the crack propagation resumes, and when the stepwise loading is increasing, cracks propagate immediately and apparently at a greater rate than would be otherwise expected. Also, periods of constant load at elevated temperature may be attended by creep which, on resumption of cyclic loading, sometimes causes a pronounced decrease in the rate of crack growth for a short period of time. These phenomena can be studied using stress-wave emission in greater detail than heretofore possible on a cycle-to-cycle basis.

---

*Christensen was one of the first to use stress-wave emission in the study of cracking. At the Cranfield Symposium in 1961, Christensen described his setup for measuring microsounds that accompany microcracking in stressed metal as follows: "As the microcrack occurs, it sets up a vibrational wave that propagates through the metal. A crystal accelerometer, cemented to the test panel in a direction perpendicular to the loading, picks up this component of the wave motion traversing the panel in the same manner as a seismograph in recording earthquakes. The magnitude of the early microcracks that were recorded in this particular test were in the order of 0.004 g's. These micro metal quakes can be converted into sound pressures and received on conventional headsets. If a value of zero db is considered as the threshhold of unaided hearing and 80 db the level of normal conversation then this will represent a measurement latitude from 1 to 10,000. The micro sounds that have been recorded in experiments are believed to be far below this threshhold value and therefore the magnification has been many times more than 10,000. The physical significance of these observations is that the occurrence and generation of heretofore undetected cracks were probably formed very early in the useful life of structures. The growth and extension of such cracks then will increase with the continued use of randomly loaded parts or members. To date these studies have indicated that microcracking can occur on the application of a load as low as 25% of the load that would normally fracture the part. Of equal significance is the fact that this was observed in the relatively notch-resistant material, RENE' 41. (continued on next page)

Moreover, in the presence of a stress-corrosion environment, crack growth will be a complex interplay of stress-corrosion cracking and fatigue. Study of the cycle-to-cycle crack growth produced by environmentally assisted fatigue based on stress-wave emission as a function of stress level, load wave-shape, temperature, and/or programmed loading should contribute greatly to an understanding of the crack-growth process.

In several researches at Aerojet, there has been occasion to subject fracture-mechanics test specimens to low-cycle fatigue. The results have confirmed the feasibility of SWAT as a nondestructive test method for predicting the onset of fracture in single-edge-notch (SEN) tension specimens tested in low-cycle fatigue where SWAT was used as a monitoring system (see Figure 58). From a nondestructive inspection point of view, the important observation in these experiments was an unmistakable SWE precursor of failure during the low-cycle fatigue test.

2. Procedures

The SWAT system used in this phase of the investigation is shown in Figure 89. The test specimen was the precracked single-edge-notch tension specimen (see Figure 46). Gross cracking was monitored by means of the crack-opening-displacement (COD) gage, while microcracking, cycle-by-cycle, was monitored with acoustic-emission sensors. The sensors were bonded to the test specimen using quartz wax. The gain was increased at the totalizer until the background noise level was within a few millivolts of the threshhold acoustic-emission level. The output signals of the totalizer and the COD gage were recorded on a strip chart. The COD gage had a sensitivity of 0.0013-in. when recorded on the 10-in. wide strip chart. With a dual-pen strip-chart, it was a simple matter to determine where in the load cycle the bursts of stress-wave emission occurred. This is illustrated in Figure 90 using data from D6aC (600°F tempered) specimen 6S42. Note that the pen recording the COD was 0.1 in. behind the pen recording the stress-wave emission count. The arrows indicate the position on the COD record where cracking started in each cycle.

---

*Note: "It is possible that with the aid of more sensitive equipment, micro-cracking can be detected at much earlier stages than reported here. It may also be practical to use this technique to prove the existence of an early crack formation period in elevated temperature fatigue. This technique also suggests a method for detecting and evaluating microcracking during proof loading of manufactured parts. For example, from the frequency of the microcrack sounds that occur during the loading to destruction of a few typical flash-welded parts it may be possible to classify marginal parts for service use. Having established a level of reliability in this manner, all subsequent proof-tested parts then will have far greater degrees of confidence for prolonged service use.

All specimens were tested in a Materials Test System (MTS) servo-hydraulic load frame model 301.02. This closed-loop system was used to cyclic load (sine wave) at six (6) cycles per minute. Each specimen was first step loaded to provide in-test calibration of the COD gage and to determine the noise level at load; the in-test calibration was accomplished as described on page 39 of this report. The set point (gain) of the emission totalizer was determined at the maximum load for cyclic testing. The specimen was then unloaded to the mean cyclic load, all instrumentation checked, and then the cyclic loading started. In general, the choice of maximum load was based on COD deviation-from-linearity.

3. Fracture-Mechanics Calculations

All calculations were done by computer. The program described on page 39 was utilized with the following additions:

INPUT TO COMPUTER

1. LOAD: P_{max} and P_{min}.
2. STRESS-WAVE COUNT: increase in count with each cycle (Δ SWE)

PRINTOUT

1. LOAD: P_{max} and P_{min}.
2. CRACK DEPTH: cumulative and increase per cycle (da/dN).
3. STRESS-INTENSITY FACTOR: K_{max} and ΔK for each cycle.
4. STRESS-WAVE EMISSION: cumulative count for each cycle.
5. AVERAGE VALUES FOR OVERALL TEST: K_{max} average
   K_{min} average
   ΔK average
   da/dN average

PLOTTING OF DATA

1. Cumulative crack depth versus cumulative stress-wave count (TSWE).
2. K_{max} versus cumulative stress-wave count (TSWE).
3. Cumulative stress-wave count (TSWE) versus cycle number.

4. Discussion of Results

a. D6aC Steel

Specimens of D6aC steel in two thicknesses and two tempering conditions were tested in low-cycle high-stress intensity fatigue. Table XXI summarizes the tests and stress-intensity factors at fracture. Note that the critical stress intensity values calculated from fatigue testing were approximately the same as those obtained from a single cycle, i.e., rising load to failure.

Figure 91 is a plot of the cumulative stress-wave count (TSWE) versus cycle number for specimen 6S26; the computer-plotted curve shows the stress-wave count for each cycle. Note the marked increase in count during the last 20 cycles. At the cycling rate of 6 cpm there was more than ample time to unload the test specimen if one wished to avoid fracture. Figure 92 shows plots of crack length (a) and stress-intensity factor (K_{max}) versus cumulative stress-wave count for each successive cycle. Note that K_{max} - TSWE is approximately a linear relationship.

Specimen 6S27 was tested in the same manner as 6S26 except that the notch of the single-edge-notch (SEN) tension specimen was filled with water after the specimen had been cycling for some time. The specimen went 500 cycles after the water was added, before it failed; only the data from the last 90 cycles (15 min) of test were analyzed. Figure 93 is the plot of TSWE versus cycle number for Specimen 6S27. Note the unmistakeable precursor of failure in the last ten cycles. Because of the very large count recorded in the last twenty cycles, it was necessary to plot Figure 93 with TSWE x 10^4; thus, the large stress-wave activity in the last three minutes of the test was somewhat masked by this plot. Figure 94 is a plot of the COD data obtained in the last 60 cycles of the test, with the stress-wave-count per cycle superimposed. Note the excellent correlation between the two measurements, and the unmistakeable precursor starting 20 to 30 cycles before failure. Figure 95 shows the plots of crack length (a) and stress-intensity factor (K_{max}) versus cumulative stress-wave count (TSWE) for each successive cycle. Again, the relationship between K_{max} and TSWE is shown to be approximately linear.

Figure 96 is a plot of the cumulative stress-wave count (TSWE) versus cycle number for Specimen 6S46. Note that the unmistakeable precursor of failure occurring in the last 15 to 20 cycles. Figure 97 shows the relationship between crack length (A) and cumulative stress-wave count. Note that in this thicker material, the relationship is exponential rather than the linear relationship found for the thinner material.

Specimen 6S47 was tested initially in the same manner as the preceding specimens; i.e., in a low-humidity air-conditioned laboratory.

TABLE XXI

CRITICAL STRESS-INTENSITY IN FATIGUE

Material	Test Specimen Number	Test Specimen Thickness	Critical Stress Intensity Rising Load	Critical Stress Intensity Fatigue
1100 D6aC	6S46	0.294	204 - 251 Avg(3)227	222
	6S47	0.292		265(a)
	6S26	0.101	275 - 287 Avg(3)285	240
	6S27	0.100		265(b)
600 D6aC	6S42	0.293	92 - 107 Avg(3)100	65
	6S22	0.104	94 - 104 Avg(4)100	116
	6S23	0.101		112(c)

- - - - - - - - - - - - -

(a) last 290 cycles with water in the notch; because the COD in the last cycle was lost, the K_c value is for one cycle before failure.

(b) water in the notch; the K_c value is for one cycle before failure.

(c) last 188 cycles with water in the notch; the K_c value is for one cycle before failure.

However, after 178 cycles, the edge notch was filled with water. After 290 additional cycles with water in the notch, the specimen failed. Figure 98, the plot of TSWE versus K_{max}, appears to be very similar to Figure 97 for the specimen tested in air. Likewise, Figure 99 showing the plot of TSWE versus cycle number was very similar to Figure 96, with both showing a marked precursor of failure. Figure 100 is a plot of the same data as in Figure 99 except that the data before adding water (X) are plotted for TSWE x 10^2; whereas, after adding water, the data (0) are plotted for TSWE x 10^4. The difference in scale was necessary because of the very large count measured as the specimen approached failure. Note that the count rate appeared to be slowing after approximately 100 cycles; after adding water, 290 additional cycles were required to fracture the test piece.

Specimen 6S23 was cut from 600°F tempered D6aC steel; this specimen was tested in the same manner as the specimen described above, with water inserted in the notch after 163 cycles in low-humidity air. In the 600°F tempered material, the water was extremely detrimental. Figure 101 is a plot of TSWE versus cycle number. Note that at the point where water was added, 163 cycles, there was an increase in the stress-wave count rate. A comparison between Figures 99 and 101 shows the marked difference in behavior between the 600 and 1100°F tempered material; recall that in obtaining the data of Figure 99, water was added after 178 cycles with little, if any, effect. In Figure 102, note the short periods of dormancy in the plot of data taken before adding water, followed by great and nearly continuous activity after adding the water.

Specimen 6S22 was first subjected to a maximum load of 3010 lb (630 lb minimum), tested in a low-humidity air-conditioned laboratory. There were occasional small bursts of stress-wave emission around maximum load. A sample of these data are shown in the following tabulation (only the cycles producing stress-wave data are tabulated):

Cycle Number	Stress-Wave Count/Cycle
13	100
16	600
22	1100
27	2700
29	1650
31	950
32	170
37	200
71	200
73	750

Cycle Number	Stress-Wave Count/Cycle
75	200
77	100
79	370
94	2500
95	4400
96	2300
109	150
110	420

Thus, there were periods of dormancy interspersed with varying sizes of bursts. However, the crack-opening displacement did not increase significantly in these 100 cycles and, therefore, the crack growth was very small.

After 388 cycles, the notch was filled with water and cycling continued at 3.0 kips maximum load. There was some increase in stress-wave activity but still no significant increase in crack-opening displacement. The following tabulation shows the stress-wave activity recorded in the first twenty five cycles after adding the water:

Cycle Number	Stress-Wave Count/Cycle	Cycle Number	Stress-Wave Count/Cycle
1	2220	13	2300
2	1400	14	600
3	280	15	400
4	2100	16	0
5	0	17	1050
6	500	18	3200
7	830	19	2000
8	600	20	2500
9	0	21	0
10	200	22	0
11	150	23	0
12	100	24	0
		25	2400

The average count per cycle for the data sample tabulated for dry air was 171 counts per cycle; after adding water the average count per cycle based on the data sample tabulated above was 913 counts per cycle. Thus it appears that stress corrosion cracking was taking place.

After a total of 815 cycles (427 cycles after adding water), the maximum load was raised to 3260 lb (450 lb minimum). With no significant increase in COD after 40 cycles, the load again was raised (3520 lb maximum, 428 lb minimum). The specimen was subjected to a total of 1155 cycles (340 cycles at the increased load of 3520 lb) before the specimen fractured. The stress intensity at the start of the last 300 cycles was 43 ksi-in.$^{1/2}$. Thus, the K_{Iscc} in fatigue for the 600°F tempered D6aC steel is below 43 ksi-in.$^{1/2}$. Fracture of Specimen 6S22 occurred at a stress intensity of 116 ksi-in.$^{1/2}$. Note that Specimen 6S23 which started to fail immediately after water was added, was started at a stress-intensity of 56 ksi-in.$^{1/2}$. Figure 103a shows the stress-corrosion cracking which occurred in 600°F tempered Specimen 6S22; Specimen 6S23 had a similar appearance. Thus, the crack growth in both 6S22 and 6S23 involved stress corrosion. Figure 103b shows the fracture surface in 1100°F tempered Specimen 6S27. Although this specimen was also exposed to water, it appears to have been immune to stress corrosion cracking even at the high stress intensity associated with the last few fracture cycles. The stress intensity in the cycle before fracture was 265 ksi-in.$^{1/2}$.

Figure 104 is a plot of TSWE versus K_{max} for Specimen 6S22; again a linear relationship is indicated.

b. 6Al-4V Titanium

Specimens of 6Al-4V titanium in two thicknesses and two heat-treat conditions were tested in low-cycle, high-stress-intensity fatigue. Table XXII summarizes the tests and stress-intensity factors at fracture. Note that the critical stress intensity values calculated from the fatigue testing varied somewhat from those obtained from conventional rising-load-to-failure tests. Note also that in fatigue testing the two thicknesses of material gave a significantly higher value for the thinner material as would be expected.

Figure 105 is a plot of the cumulative stress-wave count (TSWE) versus cycle number for Specimen SS21; the computer plotted curve shows the stress-wave count for each cycle. Note the marked increase in count during the last 20 cycles before failure, indicating an unmistakeable precursor. Note that the crack-opening-displacement (COD) gage also showed that failure was eminent in the SEN tension specimen.

Figure 106 is the computer plot of stress-intensity factor (K_{max}) versus cumulative stress-wave count (TSWE) for each successive cycle. Note that after the crack had begun to grow significantly and up to the last cycle, a linear relationship was indicated; the last cycle generated a very large count.

TABLE XXII

CRITICAL STRESS-INTENSITY IN FATIGUE OF 6A1-4V TITANIUM

Material Condition	Test Specimen Number	Test Specimen Thickness	Critical Stress Intensity Rising Load	Critical Stress Intensity Fatigue
Solution treated and aged (155 ksi yield	SS32	0.265	79 - 102 Avg(3) 89	78
	SS21	0.108	87 - 101 Avg(3) 92	139
Annealed (130 ksi yield)	E5	0.270	154 - 165 Avg(4) 159	171
	ES23	0.098	151 - 203 Avg(3) 174	189

Figure 107 is the TSWE versus cycle plot for Specimen ES23, cut from the annealed ELI heat of titanium. Note the unmistakeable precursor approximately 15 cycles before fracture. Figure 108 is the K_{max} versus TSWE plot; note the indication of a linear relationship.

The preceding tests were both of 0.10 in. sheet. Figure 109, a plot of K_{max} versus TSWE, indicates an exponential relationship for the 0.26 in. sheet.

c. 7075-T6 Aluminum

Specimen BS-1 was tested in the same manner and with the same system as in the steel and titanium testing. After approximately 200 cycles in an air-conditioned low-humidity laboratory, a 3 percent NaCl solution was placed in the notch of the SEN tension specimen. The stress intensity at the time of adding the solution was 28.5 ksi-in.$^{1/2}$ (ΔK was 26.3 ksi-in.$^{1/2}$). In 216 additional cycles the specimen fractured; the stress intensity at fracture was 52.1 ksi-in.$^{1/2}$. The cumulative stress-wave count before and after adding the 3% NaCl solution is shown in Figure 110. Note the two-orders-of-magnitude change of scale in plotting the count after stress-corrosion cracking was initiated. Data were tabulated for a total of 58 cycles before adding the solution; note the unmistakeable change after 58 cycles. Table XXIII is a tabulation of the average count rate and the average crack growth in each successive 10 cycles before and after adding the 3% NaCl. Note that there was an order of magnitude increase in stress-wave count rate after adding the salt solution. The increase in crack growth rate was not as dramatic but nevertheless unmistakeable after adding the salt solution. Note that approximately 50 cycles before failure occurred, there was a marked increase in the count rate and in the crack growth rate. In Figure 110, the change of slope would serve as the precursor of failure (approximately 50 cycles before fracture). From Figure 111, note the linear relationship between TSWE and K_{max}.

d. Sensor Response

In several of the tests described above, two sensors were mounted on the test specimen using quartz wax. The signals from each sensor were conditioned by identical systems, as shown in Figure 89. The only difference in conditioning the data from the two sensors was in the "set-point" of the Dunegan totalizer; i.e., in the gain provided by the totalizer itself. The totalizer set-point was used to adjust the gain as necessary to bring the background noise level to just below the fixed trigger level of the Dunegan system (0.707 volt RMS). Thus, the procedure was to amplify the signal from both sensors to 40 db (preamplifier 102E), high-pass filter (400 KHz), amplify again to 40 db, then low-pass filter (1000 KHz) and finally record by means of the Dunegan totalizers. The set-point of the totalizer was adjusted until the

TABLE XXIII

AVERAGE COUNT AND CRACK-GROWTH RATES, 7075-T6

Cycle Range	Average Count Rate SWE per Cycle	Average Crack Growth in. per Cycle x 10^{-3}
50 - 40	563	0.142
40 - 30	316	0.141
30 - 20	186	0.141
20 - 10	583	0.000
10 - 0	269	0.000
	3% NaCl ADDED	
0 - 10	2057	0.973
10 - 20	3191	0.948
20 - 30	1182	0.794
30 - 40	3676	1.784
40 - 50	1760	0.494
50 - 60	2230	1.089
60 - 70	2060	1.174
70 - 80	4410	0.913
80 - 90	5270	1.221
90 - 100	2550	0.651
100 - 110	4350	0.849
110 - 120	4820	1.037
120 - 130	3050	1.011
130 - 140	5520	1.472
140 - 150	2020	1.709
150 - 160	5510	1.277
160 - 170	4980	1.234
170 - 180	9400	2.606
180 - 190	6490	4.056
190 - 200	9560	3.088
200 - 210	11820	5.426
210 - 217	26360	14.53

maximum-load background noise recorded by each sensor began to show counts at a 10^3 scale setting; the set-point was then backed off (gain reduced) until there were no counts observed at 10^3. This procedure was followed for each sensor investigated, with the set-point adjustment made at maximum load before cycling. Three sensors were compared with the Endevco 2213E accelerometer; viz., Endevco's P-15 Shear (experimental), Electra-Scientific's ES-6017 and Dunegan's S-140B.

In test BS-1 (7075-T6 aluminum) the Electra-Scientific ES-6017 was compared with the 2213E accelerometer. Figure 112 shows the count in the last 25 cycles as plotted by dual-pen recorder, with one line the 2213E accelerometer and the other line the ES-6017 sensor. Note that the ES-6017 sensor gave somewhat higher counts than the 2213E accelerometer. The following tabulation shows the counts corresponding to Figure 112:

Cycle Number	Electra Scientific	Endevco 2213E
25	7500	3000
24	12500	7700
23	11000	7900
22	19800	12500
21	18500	11000
20	26900	19000
19	17300	9300
18	24500	15500
17	11500	7300
16	16000	8900
15	13000	7900
14	25200	17600
13	19000	11800
12	15500	8800
11	16800	10900
10	24900	16400
9	42700	25000
8	70700	50500
7	32400	20400
6	45000	28300
5	34500	23500
4	28000	17000
3	14700	8200
2	50000	26300
1	185800	141000
	FAILURE	

Figure 113 shows the output of the two sensors 90 cycles before fracture. At this stage of the failure process, the ES-6017 sensor was still recording somewhat larger counts than the 2213E accelerometer. The corresponding points on each record are indexed alphabetically. Figure 114 shows the output at 180 cycles before fracture. Note that the ES-6017 sensor tended to record many more distinct events in a given cycle than the accelerometer. Generally, the accelerometer indicated a distinct stair-step increase in count with each cycle; whereas, the ES-6017 sensor produced many small steps along with the larger steps; e.g., note the count in cycles, b-c, f-g, j-k and n-o.

In test 6S27 (1100D6aC) the Endevco P-15 Shear (experimental) sensor was compared with the 2213E accelerometer. From Figure 115 it will be seen that the two sensors gave very nearly the same count in the last few cycles before fracture. However, earlier in the failure process, the experimental sensor was variable in its output; at times the count was so low in each cycle, it appeared to be continuous noise with no correlation to load in the cycle. Figure 116 illustrates this condition 200 cycles before fracture. The variable output of the transducer suggests that the stress wave was changing during the failure process. If a transducer were to produce a change such as shown in Figures 115 and 116 just before failure this would provide additional warning of imminent failure. It should be noted that the P-15 experimental sensor inherently has a high noise level when conditioned by the Aerojet SWAT system and, therefore, required less set-point gain to achieve the totalizer trigger-level voltage.

In test 6S23 (600 D6aC) the Dunegan S-140B sensor was compared with the Endevco 2213E accelerometer. Figure 117 is a plot of cumulative count (TSWE) versus cycle number as obtained from the two sensors. Note that they gave almost identical results. Figure 118 shows the dual-pen recording of the two sensors in the last 15 cycles before failure; the excellent correlation is apparent. Figure 119 shows the same result immediately after adding water 188 cycles before fracture; in 20 cycles after adding water, the accelerometer gave a count of 47,500 and the S-140B sensor gave a count of 46,650.

In test 6S47 (1100 D6aC), the Dunegan S-140B sensor was compared with the Endevco 2213E accelerometer using the same set-point gain for both (set-point 10 on 0-20 db range). In the last 10 cycles before the failure cycle, the count was as follows:

2213E	S-140B
1,940,000	1,399,000

Failure occurred after a total of 648 cycles. After a total of 555 cycles, a comparison of the two sensors showed the following average count rate in 20 cycles:

2213E	S-140B
845	875

Figure 120 shows the dual-pen recordings of the two sensors in the last several cycles before failure and for several cycles immediately after adding water; the quantitative correlation is apparent.

SECTION IV

SUMMARY DISCUSSION OF RESULTS

Tests of a variety of materials and material-toughness levels confirmed the reality of the stress-wave-emission precursor to failure. Ample warning was obtained both with surface, part-through-crack (plane-strain) and with single-edge-notched (plane stress) specimens. Thus, the stress-wave-analysis technique (SWAT) provides both the means to locate a growing crack and an assessment of its criticality. As a crack approaches critical size (the critical stress intensity), the stress-wave amplitude and rate of occurrence markedly increase, serving as precursors of failure.

SWAT in the present stage of development is not capable of determining the size of a source defect except at the onset of crack instability and then only if the fracture toughness (critical stress intensity) is known. Thus, SWAT must be used in conjunction with conventional nondestructive inspection to determine the size and orientation of the source defect. Relationships between cumulative stress-wave count and applied stress-intensity factor have been observed previously and confirmed in this study. However, the work has been done with laboratory test specimens; application of the relationship to prototype structures remains as one of the most important objectives of future R&D. If the relationship can be applied to actual structures and tankage, then it will be possible to calculate the crack size from the cumulative stress-wave count and the known stress.

Various techniques are discussed for utilizing acoustic emission as a nondestructive inspection method. With the most advanced systems available at the time of this reporting, one can continuously, in real time, monitor between 15 and 20 sensors, with signal gain of approximately 10,000X and band-pass filtering anywhere between 50 and 500 KHz, to locate and evaluate one or more defects which are actively growing.

Investigation of the continuous-wave response of several sensors showed that any one of them, including an accelerometer with a mounted first mechanical resonance at 30 KHz, can be used to detect acoustic emission at filter frequencies above 100 KHz.

Use of a pulser designed to simulate stress-wave emission is a highly effective and useful tool for establishing and maintaining reliability in the acoustic-emission system. Signals from the pulser can be (1) varied in pulse height and width to simulate different sizes of stress-wave, (2) used to test the sensitivity of a given sensor or the relative sensitivity of a series of sensors, (3) used to simulate a stress-wave source in calibrating an array of sensors in sphere-of-interest inspections, (4) used to evaluate signal attenuation as a function of geometry and distance, and (5) used to check the detection sensitivity of the overall system and reliability of the electronic components and software of the computer. In particular, during an inspection or proof test, the pulser permits the acoustic-system operator periodically to make an in-test overall system reliability check.

When defects are detected by an acoustic-emission system, and conventional nondestructive inspection is incapable of detecting the source because of either insufficient sensitivity or geometrical complications, the suspect location can be continuously or periodically inspected by SWAT using the sphere-of-interest principle where a calibrated array of sensors are used to zero-in on the suspect area.

In low-cycle high-stress-intensity fatigue, acoustic emission was demonstrated to be highly effective as a nondestructive test method for following crack growth. Moreover, the process of stress-corrosion cracking started during low-cycle, high-stress-intensity fatigue, was readily detected by an early, marked increase in the stress-wave count rate.

The use of acoustic emission as a precursor of imminant failure was demonstrated for low-cycle, high-stress-intensity fatigue as well as for the case of environmentally assisted fatigue. Plots of cumulative stress-wave count versus cycle number consistently showed a marked increase in count rate several (10-20 or more) cycles before fracture.

Plots of K_{max} versus cumulative stress-wave count in low-cycle high-stress-intensity fatigue confirmed the existence of a relationship between acoustic emission and crack growth. Generally, the relationship was linear; in a few tests it was exponential.

Comparisons based on two sensors attached to the same test specimen loaded in low-cycle, high-stress-intensity fatigue, showed that all of the transducers investigated were capable of detecting the precursor. With the same amplification (except for minor adjustments in gain for each transducer to set the trigger level) and the same filtering for each type of sensor investigated, the Dunegan S-140B, Electra Scientific ES-6017, Endevco P-15 Shear (experimental) and Endevco 2213E accelerometer all gave nearly the same high count in the precursor range; i.e., in the last several cycles before failure. However, earlier in the failure process, there sometimes were inconsistencies, particularly in the P-15 experimental sensor. Nevertheless, all showed the cycle-by-cycle failure process.

Acoustic emission confirmed the existence of periods of dormancy punctuated with periods of active crack growth in low-cycle, high-stress-intensity fatigue. Using a suitable, dual-pen, strip-chart recorder displaying both crack-opening-displacement and stress-wave count on the same chart, it was a simple matter not only to observe whether or not there was crack growth in each individual cycle but also where in the cycle it occurred. The cycle rate in this investigation was 6 cycles per minute.

In some tests there was "noise" at or near minimum load in each cycle. A dual filter system was used in all fatigue testing, with the first filter high-pass at 400 KHz and the second filter low-pass at 1000 KHz. This particular "window" was dictated by noise in the MTS loading system used in all the fatigue testing. The "noise" that was observed around minimum load in some of the tests was assumed to be metal-to-metal contact as the yawning crack closed; these signals were disregarded in tabulating the cumulative stress-wave count.

SECTION V

CONCLUSIONS

Acoustic emission is the basis for a highly sensitive nondestructive inspection method, capable of detecting growing defects at least an order of magnitude smaller than any other known NDI method and, with a computerized system, capable of locating one or more defects in real time. Thus, the stress-wave-analysis technique (SWAT) can be used for in-service continuous, NDI. When defects emit stress-waves and yet are too small to be confirmed by conventional nondestructive inspection, the suspect area is placed under surveillance using an array of transducers. When the defect approaches critical crack size, the acoustic-emission count rate increases markedly, providing a precursor of crack instability and failure.

REFERENCES

1. J. Kaiser, "Untersuchungen uber das Auftreten Gerauschen Beim Sugversuch," PhD. Thesis, Techn. Hochsch., Munchen, (1950), and Arkiv Fur das Eisenhuttenwesen, 24, 43-45, (1953).

2. B. H. Schofield, R. A. Bareis, and A. A. Kyrala, "Acoustic Emission Under Applied Stress," WADC Technical Report 58-194, (April 1958).

3. B. H. Schofield, "Acoustic Emission from Metals, Its Detection, Characteristics, and Source," Proceedings of the Symposium on Physics and Nondestructive Testing, Southwest Research Institute, San Antonio, Texas, (October 1963).

4. B. H. Schofield, "Acoustic Emission Under Applied Stress," ASD-TR-53-509, Part I, (April 1963), Part II, (May 1964).

5. A. T. Green, C. S. Lockman, and R. K. Steele, "Acoustic Verification of Structural Integrity of Polaris Chambers," Modern Plastics, 41, 137-139, (July 1964).

6. A. T. Green, C. E. Hartbower, and C. S. Lockman, "Feasibility Study of Acoustic Depressurization System," Report NAS 7-310, Aerojet-General Corporation, (February 1965).

7. C. E. Hartbower, W. W. Gerberich, and P. P. Crimmins, "Monitoring Sub-Critical Crack Growth by an Acoustic Technique," Weld Imperfections Symposium, Lockheed Research, Palo Alto, California, (September 1966). Published in WELD IMPERFECTIONS, Addison-Wesley, Menlo Park, California.

8. C. S. Lockman, A. T. Green, and R. K. Steele, "Acoustic Monitoring During Proof Testing," Weld Imperfections Symposium, Lockheed Research, Palo Alto, California, (September 1966). Loc cit.

9. C. E. Hartbower, W. W. Gerberich and P. P. Crimmins, "Characterization of Fatigue-Crack Growth by Stress-Wave Emission," NAS 1-4902, (June 1966). Available from NASA, P. O. Box 5700, Bethesda, Maryland 20014.

10. A. T. Green, C. S. Lockman, S. J. Brown, and R. K. Steele, "Feasibility Study of Acoustic Depressurization System," NASA CR-55472, (March 1966).

11. A. T. Green, Stress-Wave Detection, Saturn S-II, NASA CR-61161, (December 1966).

12. W. W. Gerberich and C. E. Hartbower, "Some Observations on Stress-Wave Emission as a Measure of Crack Growth," International Journal of Fracture Mechanics, 3, 3, (September 1967).

13. W. W. Gerberich and C. E. Hartbower, "Monitoring Crack Growth of Hydrogen Embrittlement and Stress Corrosion Cracking by Acoustic Emission, "Conference on Fundamental Aspects of Stress Corrosion Cracking, Ohio State University, (September 1967).

14. C. E. Hartbower, W. W. Gerberich, and P. P. Crimmins, "Mechanisms of Slow Crack Growth in High-Strength Steels," AFML-TR-67-26, Vol. 1, Aerojet-General Corp., (February 1967). Also "Monitoring Subcritical Crack Growth by Detection of Elastic Stress-Waves," American Welding Society Meeting, Houston, Texas, (October 1967). THE WELDING JOURNAL, Vol. 47(1), p. 1-s, Jan 1968. Received the Spraragen Award as best research paper published in the WELDING JOURNAL in the year 1968.

15. A. T. Green, "Testing of 10-inch Glass Hemispheres Using Stress-Wave Analysis Technique," N00014-67-C-0333, Naval Ship Research and Development Center, (September 1967).

16. A. T. Green and C. E. Hartbower, "Stress-Wave Analysis Technique for Detection of Incipient Failure," Aerojet-General Corp., Presented at ORNL Conference on Incipient Failure Diagnosis for Assuring Safety and Availability of Nuclear Power Plants, Gatlinburg, Tennessee, (October 1967). Published in the PROCEEDINGS of the AEC Conference.

17. W. G. Reuter, A. T. Green, C. E. Hartbower and P. P. Crimmins, "Monitoring of Crack Growth in Ti-6Al-4V Alloy by the Stress Wave Analysis Technique," Report on NASA Houston Contract NAS 9-7759, Dec. 1968.

18. C. E. Hartbower, W. W. Gerberich, and P. P. Crimmins, "Spontaneous Strain Aging as a Mechanism of Slow Crack Growth," Presented at the American Welding Society Annual Conference, Chicago, Illinois, (April 1968). The WELDING JOURNAL, Vol. 47(10), Oct. 1968.

19. C. E. Hartbower, W. W. Gerberich, and H. Liebowitz, "Investigation of Crack-Growth Stress-Wave Relationships," Engineering Fracture Mechanics, Vol. I(2), p. 291, August 1968. Also C. E. Hartbower, W. W. Gerberich, W. G. Reuter, and P. P. Crimmins, "Stress-Wave Characteristics of Fracture Instability in Constructional Alloys," AD-674-881, Aerojet-General Corp., (July 1968). Copy of ONR Final in NCEL Library.

20. G. S. Baker, "Acoustic Emission and Prefracture Processes in High-Strength Steels," AFML-TR-67-266, Aerojet-General Corporation, Wright-Patterson AFB, (March 1968).

21. C. E. Hartbower and P. P. Crimmins, "Fracture of Structural Metals as Related to Pressure-Vessel Integrity and In-Service Monitoring," presented at the ICRPG/AIAA 3rd Solid Propulsion Conference (AIAA Paper 68-501), Atlantic City, June 1968.

22. W. W. Gerberich and W. G. Reuter, "Theoretical Model of Ductile Fracture Instability Based on Stress-Wave Emission," ONR Contract Report N00014-66-C0340, Aerojet-General Corp., Sacramento, California (February 1969).

23. C. E. Hartbower, W. G. Reuter and P. P. Crimmins, "Mechanisms of Slow Crack Growth in High-Strength Steels and Titanium," Final Technical Report AFML-TR-67-26, Vol. II, June 1969 on Contract AF 33(615)-2788 for the period April 1967 - April 1969, 199 pages.

24. A. T. Green, Development of a Nondestructive Testing Technique to Determine Flaw Criticality, ARPA Contract F33615-68-C-1705, Aerojet-General Corp., Sacramento, California, (August 1969).

25. C. E. Hartbower, Application of SWAT to the Nondestructive Inspection of Welds, Technical Note, Aerojet-General Corp., Sacramento, California, (September 1969). The WELDING JOURNAL, Vol. 35(2), Feb. 1970.

26. C. E. Hartbower, F. J. Climent, C. Morais, and P. P. Crimmins, Stress-Wave-Analysis Technique Study of Thick-Walled Type A302-B Steel Pressure Vessels, NASA NAS9-7759, Aerojet-General Corp., (July 1969).

27. A. T. Green, "Detection of Incipient Failures in Pressure Vessels by Stress-Wave Emission," Nuclear Safety, 10, 4-18, (January-February 1969).

28. A. T. Green and C. E. Hartbower, "Development of a Nondestructive Testing Technique to Determine Flaw Criticality," Interim Technical Report on ARPA Contract F33615-68-C-1705 (ARPA Order No. 1244, Code 8D10), May 1970.

29. H. L. Dunegan, D. O. Harris, and C. A. Tatro, "Acoustic Emission Research Status Report, December 1963-August 1964," UCID-4868 Rev. 1, Lawrence Radiation Laboratory, (November 1964).

30. H. L. Dunegan and C. A. Tatro, "Passive Pressure Transducer Utilizing Acoustic Emission," Review of Scientific Instruments, 38, 8, (August 1967).

31. H. L. Dunegan, D. O. Harris, and C. A. Tatro, "Fracture Analysis by Use of Acoustic Emission," Engineering Fracture Mechanics, 1, 105-122, (June 1968).

32. H. Dunegan and D. Harris, "Acoustic Emission-A New Nondestructive Testing Tool," Ultrasonics, 7, 160-166, (July 1969).

MICHIGAN STATE UNIVERSITY

33. C. A. Tatro, "Sonic Techniques in the Detection of Crystal in Metals," Progress Report, Division of Engineering Research, Michigan State University, East Lansing, Michigan, (January 1959).

34. C. A. Tatro and R. G. Liptai, "Acoustic Emission from Crystalline Substances," Proceedings of the Symposium on Physics and Nondestructive Testing, Southwest Research Institute, San Antonio, Texas, 145-174, (October 1962).

35. R. G. Liptai, "An Investigation of the Acoustic Emission Phenomenon," Ph.D. Thesis, Michigan State University, East Lansing, Michigan, (1963).

36. R. B. Engle, "Acoustic Emission and Related Displacements in Lithium Fluoride Single Crystals," Ph.D. Thesis, Michigan State University, East Lansing, Michigan (1966).

37. L. D. Mitchell, "An Investigation of the Correlation of the Acoustic Emission Phenominon with the Scatter in Fatigue Data," Ph.D. Thesis, University of Michigan, Ann Arbor, Michigan (1965).

38. J. N. Kerawalla, "An Investigation of the Acoustic Emission from Commercial Ferrous Materials Subjected to Cyclic Tensile Loading," Ph.D. Thesis, University of Michigan, Ann Arbor, Michigan (1965).

39. A. B. L. Argarwall, "An Investigation of the Behavior of the Acoustic Emission from Metals and a Proposed Mechanism for its Generation," Ph.D. Thesis, The University of Michigan, Ann Arbor, Michigan (1968).

40. J. R. Frederick, "Use of Acoustic in Nondestructive Testing," Semi-Annual Report 01971-2-T, March-August 1969, University of Michigan, Ann Arbor, Michigan (November 1969).

41. N. G. Sankar, "Unload Emission Behavior of Material and Its Relation to the Bauschinger Effect," Ph.D. Thesis, University of Michigan, Ann Arbor, Michigan (1969).

42. D. M. Egle, "A Comprehensive Analysis of an Acoustic Emission Detection System," Ph.D. Thesis, Tulane University, New Orleans, Louisiana (1965).

43. R. H. Chambers, "New Techniques in Nondestructive Testing by Acoustical and Exo-electron Emission," AD-691-230, Arizona University, Tuscon, Arizona (July 1969).

44. C. K. Day, "An Investigation of the Plastic Bursts of Microstrain in Zinc as Sources for Acoustic Emission," M.S. Thesis, Washington State University, Pullman, Washington (1969).

45. J. C. Spanner, "A Selective Review on the Utilization of Acoustic Emission Techniques for Materials Research and Structural Integrity Analysis," M.S. Thesis, Washington State University, Pullman, Washington (1970).

46. Brown, W. F., Jr., and Srawley, J. E., "Plane-Strain Crack Toughness Testing of High-Strength Metallic Materials," ASTM STP 410, p.12.

47. Fisher, D. M., Bubsey, R. T., and Srawley, J. E., "Design and Use of Displacement Gage for Crack Extension Measurements," Technical Note D-3724, NASA, Nov 1966.

48. G. R. Irwin, "Crack Extension Force for a Part-Through Crack in a Plate," J. of Applied Mechanics, Vol. 84E No. 4, Dec 1962.

49. A. S. Kobayashi, "On the Magnification Factors of Deep Surface Flaws," Structural Development Research Memo No. 16, Boeing Co., December 1965.

50. Brown and Srawley loc cit., p. 32

51. Dr. Earl C. Roberts, Boeing Company, P.O. Box 3999, Mail Stop 88-07, Seattle 98124, Private Communication, 15 April 1970.

52. C. E. Hartbower, W. W. Gerberich and Dr. Harold Liebowitz, "Investigation of Crack-Growth Stress-Wave Relationships," Journal of Engineering Fracture Mechanics, Vol 1 (2), Aug 1968.

53. C. E. Hartbower, W. W. Gerberich, W. G. Reuter, and P. P. Crimmins, "Stress Wave Characteristics of Fracture Instability in Constructional Alloys," Final Report on ONR Contract N00014-66-C0340, July 1968.

54. Kaiser, J., "Untersuchungen über das Austreten Gerauschen Beim Zugversuch," Ph.D. Thesis, Technische Huchschole, Munich, 1950.

55. W. Weibull, "The Effect of Size and Stress History on Fatigue Crack Initiation and Propagation," PROCEEDINGS OF THE CRACK PROPAGATION SYMPOSIUM, CRANFIELD, ENGLAND, September 1961, Vol 2, p. 271.

56. R. H. Christensen, "Cracking and Fracture in Metals and Structures," Ibid. p. 326.

APPENDIX A

AEROJET STRESS-WAVE-EMISSION RESEARCH AND DEVELOPMENT

NASA sponsored Contract NAS 7-310 to establish the feasibility of using SWAT"...to detect and locate a growing flaw, monitor its growth, and then to initiate a system that would arrest the flaw growth and thus prevent the accidental destruction of a 260-in.-dia rocket motor case during its proof pressure test"(1). In this contract, the feasibility of the SWAT system and concept was established.

NASA sponsored Contract NAS 1-4902 to "...determine the characteristics of the stress wave emission (SWE) attending fatigue crack growth as a means for monitoring increment-by-increment crack growth in fatigue, as well as to evaluate its potential for investigating the mechanisms of fatigue crack growth in selected alloys"(2). Fatigue crack growth was verified to be a discontinuous process with marked differences between the materials and material conditions investigated. Relationships were established between the SWE associated with fatigue crack growth and several metallurgical and loading variables.

The Navy sponsored Contract N600(167)-64934(X)(FBM) to "...determine the feasibility of monitoring incremental fatigue crack growth on HY-80 weld and heat-affected base metal using the Aerojet stress wave detection system to monitor the elastic waves emanating from the propagating fatigue crack front"(3). The feasibility of using SWAT was demonstrated.

The Air Force (AFML) sponsored Contract AF 33(615)-2788 to "...investigate the metallurgical nature of slow crack growth in 18% nickel maraging steel, 6Al-4V titanium and D6aC low-alloy steel using the stress-wave-analysis technique (SWAT) as a new tool for monitoring incremental crack growth". The

(1) A. T. Green, C. E. Hartbower and C. S. Lockman, "Feasibility Study of Acoustic Depressurization System", Report NAS 7-310, February 1965; A. T. Green, C. S. Lockman, J. J. Brown and R. K. Steele, Final Report NASA CR-55472, March 1966.

(2) C. E. Hartbower, W. W. Gerberich and P. P. Crimmins, "Characterization of Fatigue-Crack Growth by Stress Wave Emission", Report CR 66303, June 1966. Available from NASA, P.O. Box 5700, Bethesda, Maryland, 20014.

(3) W. W. Gerberich and C. E. Hartbower, "Feasibility Study for Measuring Fatigue Crack Growth Rate on Welded HY-80 Steel Using Stress Wave Emission", Final Report, 15 July 1966.

findings of the research were published in two parts[4]. The subcritical-crack-growth process was revealed in far greater detail than heretofore possible; SWAT provided at least an order of magnitude greater sensitivity than any other known method. The mechanisms of subcritical crack growth investigated included hydrogen embrittlement, stress-corrosion cracking (distilled water at 65 and 165°F), the combined effect of interstitial-solid-solution hydrogen and water, and strain aging.

The Office of Naval Research sponsored Contract N00014-66-C0340 to "...determine (1) if there is some recognizable, reproducible stress-wave characteristic(s) which can be used to predict the onset of crack instability under both plane-strain (K_{Ic}) and plane-stress (K_c) conditions, (2) if such a characteristic varies from one material to another, and (3) if such a characteristic is affected by specimen configuration"[5]. Five material types were investigated, including 7075-T6 aluminum, HY-80 and HY-150 steel, 6Al-4V titanium and D6aC Q&T steel; marked differences in stress-wave characteristics were observed (primarily as a function of material toughness). Moreover, stress-wave amplitude and repetition rate were found to be recognizable, reproducible stress-wave characteristics serving as precursors to crack instability.

The Air Force (AFML) sponsored Contract AF 33(615)-5027 to "...investigate the factors affecting the applicability to stress-wave monitoring techniques to the detection of crack initiation and/or growth in high-strength structures. Particular emphasis was placed on determining, by metallurgical investigation, the nature and sources of prefracture emissions on high-strength steel alloys, and correlating the acoustic emission characteristics (amplitude and rate of emission) from these sources with discontinuous crack growth"[6]. With a standard accelerometer, it was found that nucleation or growth of a crack greater than 10^{-5} in.^{2} was readily detected at a sensitivity level of

(4) C. E. Hartbower, W. W. Gerberich and P.P. Crimmins, "Monitoring Subcritical Crack Growth by Detection of Elastic Stress Waves", AFML-TR-67-26, Vol. 1, (163 pages), February 1967. Also the WELDING JOURNAL, Vol. 47(1) p. 1-s, January 1968 (received the SPRARAGEN AWARD as the best research paper published in the WELDING JOURNAL in the year (1968). See also "Spontaneous Strain Aging as a Mechanism of Slow Crack Growth," Ibid. Vol. 47(10), October 1968. See also Final Technical Report AFML-TR-67-26 Vol. II, June 1969 on Contract AF 33(615)-2788 for the period April 1967 - April 1969, 199 pages.

(5) C. E. Hartbower, W. W. Gerberich, W. G. Reuter, and P. P. Crimmins, "Stress-Wave Characteristics of Fracture Instability in Constructional Alloys", Final Report July 1968. Also see ENGINEERING FRACTURE MECHANICS, Vol. 1(2), p. 291, August 1968.

(6) Dr. G. S. Baker, "Acoustic Emission and Prefracture Processes in High-Strength Steels", Final Report, August 1967.

0.01 g. It was concluded that the technique provides a means of nondestructively detecting and locating propagating flaws in structures under stress, permitting test or service termination prior to catastrophic failure.

The Navy sponsored Contract N00014-67-C0333 to apply SWAT to "...the hydrostatic compression testing of 10-in.-dia, hollow, glass hemispheres to provide further knowledge regarding failure mechanisms in this structure and to determine characteristics of stress wave emission"(7). The tests confirmed the ability of SWAT to detect failure in the glass hemispheres under external pressure; at least one characteristic of impending failure, the rate of stress wave emission, was demonstrated and used as a criterion to reduce pressure and prevent specimen failure. Time differences between stress wave arrival at each sensor location was used in conjunction with seismic triangulation techniques to determine the origin of the stress-wave emission.

The Navy sponsored Contract N600(61533)-65927 to "...investigate the feasibility of monitoring crack growth in titanium alloys by the use of stress-wave emission"(8). The materials investigated included Ti-6Al-4V sheet (0.125-in. thick) in the annealed and duplex-heat-treated conditions, and Ti-7Al-2Cb-1Ta plate (0.4-in. thick). Stress wave emission was detected in both air and 3% MaCl solution environments. The stress-wave data were successfully employed to monitor crack growth and demonstrated that stress-corrosion cracking was at least partially by a jump process and not entirely a disolution mechanism.

NASA sponsored Contract NAS 9-7759 to "...(1) demonstrate improved SWAT transducer attachment techniques, (2) determine stress-wave characteristics associated with part-through-flaw growth in the titanium 6Al-4V alloy exposed to air, distilled water inhibited with sodium dichromate, and methyl alcohol environments; (3) define the system sensitivity required to detect the stress-wave emission activity associated with flaw growth; and (4) compare and correlate such characteristics with data obtained from the Apollo SPS tankage hydroburst previously performed"(9). Sensor attachment techniques were successfully developed which overcame previous bonding-agent cracking encountered during hydrotest of the SPS tank. The system sensitivity required to detect stress-wave emissions from subcritical crack growth in thin walled (0.030 and 0.060-in.) 6Al-4V titanium was successfully achieved and demonstrated in air,

(7) A. T. Green, "Testing of Glass Hemispheres Using the Aerojet Stress-Wave Analysis Technique", Interim Technical Report, September 1967; "Stress-Wave Emission Generated During the Hydrostatic Compression Testing of Glass Spheres", Final Report, April 1969.

(8) W. W. Gerberich, et al., "Evaluation of Selected Titanium Alloys as a Function of Environment and Heat Treatment", Final Report, August 1967.

(9) W. G. Reuter, A. T. Green, C. E. Hartbower and P. P. Crimmins, "Monitoring of Crack Growth in Ti-6Al-4V Alloy by the Stress Wave Analysis Technique", Final Report, December 1968.

inhibited water, and methyl alcohol environments. Verification of adequate SWAT-system sensitivity was made through analysis of stress-wave emission data from a previous Apollo SPS-tank hydroburst. The stress-wave emission characteristics which were determined as precursors of failure were the same for all environments investigated; viz., (1) the rate of occurrence, (2) the cumulative count, and (3) the amplitude of stress-wave emissions, all of which increased significantly as failure approached. In methyl alcohol, stress wave emission was observed during the holding periods and increased both in rate of occurrence and amplitude as failure approached. The interval between the onset of detectable crack growth as shown by the stress-wave emission data and actual failure, varied as a function of environment and applied stress intensity; in all instances, this time interval was sufficient to terminate the pressurizing cycle in a hydrotest prior to failure.

The Navy sponsored Contract N00600-C-0308 to design a SWAT system for detecting and locating incipient flaws by the use of stress-wave emission(10). A real-time-system design was completed and presented to the U.S. Navy Ship R&D Center, Carderock for evaluation.

NASA sponsored Contract NAS 9-7759 (Mod. 1) to "...(1) develop relationships between subcritical crack growth and stress-wave-emission characteristics in Type A302, Grade B alloy steel, (2) characterize background noise existing in typical bottle fields at the Kennedy Space Center, and (3) determine the feasibility of monitoring subcritical crack growth in pressure vessels in bottle fields at Kennedy Space Center by correlating the results of the background noise characterization and signal attenuation tests with those obtained through laboratory tests relating stress-wave characteristics and subcritical crack growth"(11). When the material was tested in an environment of 3% NaCl, continuous stress wave emission was observed, whereas, when the material was hydrogenated and tested in air, the stress wave emission was discontinuous. The combination of prior hydrogenation and testing in 3% NaCl solution was indicated to produce a synergistic effect. Measurements of background noise in the bottle fields at Kennedy Space Flight Center indicated that SWAT can be used as a fail-safe nondestructive inspection system.

The Navy sponsored Contract N00024-70-C-5215 to determine (1) the feasibility of detecting weld cracking in submarine hull construction and (2) the duration of such cracking by stress-wave (acoustic) emission. The findings showed that stress wave emission can be employed as a highly sensitive nondestructive inspection technique. Bursts of stress-wave emission

(10) R. K. Steel, C. F. Morais, H. P. Briar, and J. Stanfield, "Design of a System to Detect and Locate the Incipient Development of Flaws in Materials", Milestone Report No. 2, March 1969; Final Report, May 1969.

(11) C. E. Hartbower, F. J. Climent, C. Morais and P. P. Crimmins, "Stress-Wave Analysis Technique Study on Thick Walled, Type A302B Steel Pressure Vessels", Final Report, July 1969.

indicative of delayed cracking were found to occur intermittently in some weldments for over 400 hours after welding was completed. Two of the 33 weldments tested were sectioned and examined metallographically; the extent of cracking was found to correlate with cumulative stress-wave count. Thus, it appears that the present shipyard practice of a 7-day interval between welding and nondestructive inspection is unconservative(12).

NASA sponsored Contract NAS 8-21405 to investigate the correlation of stress-wave emission characteristics with fracture in aluminum alloys, and to prove the feasibility and practicality of using stress-wave emission to predict failure in components fabricated from selected aluminum alloys. The latter objective involved hydrotesting subscale pressure vessels at room and cryogenic (-320°F) temperatures. Testing was done with the computerized SWAT system housed in the Aerojet van. The final report on this study was in preparation at the time of this reporting.

(12) C. E. Hartbower, C. F. Morais, W. G. Reuter, and P.P. Crimmins, "Detection of Weld Cracking in HY-80, HY-100 and HY-130 Steels by Stress Wave Emission" Final Report on Contract N00024-70-C-5215, March 1971.

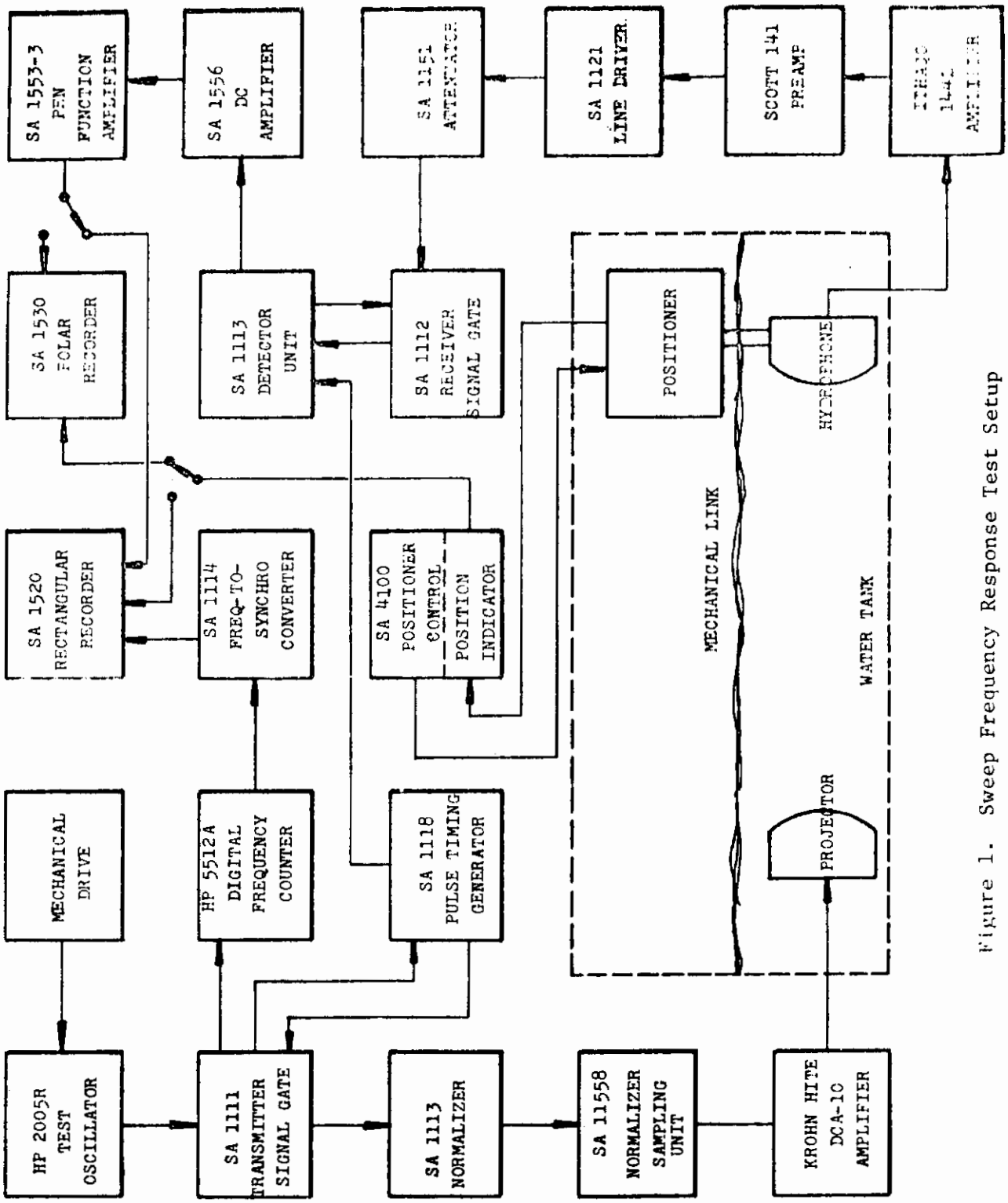

Figure 1. Sweep Frequency Response Test Setup

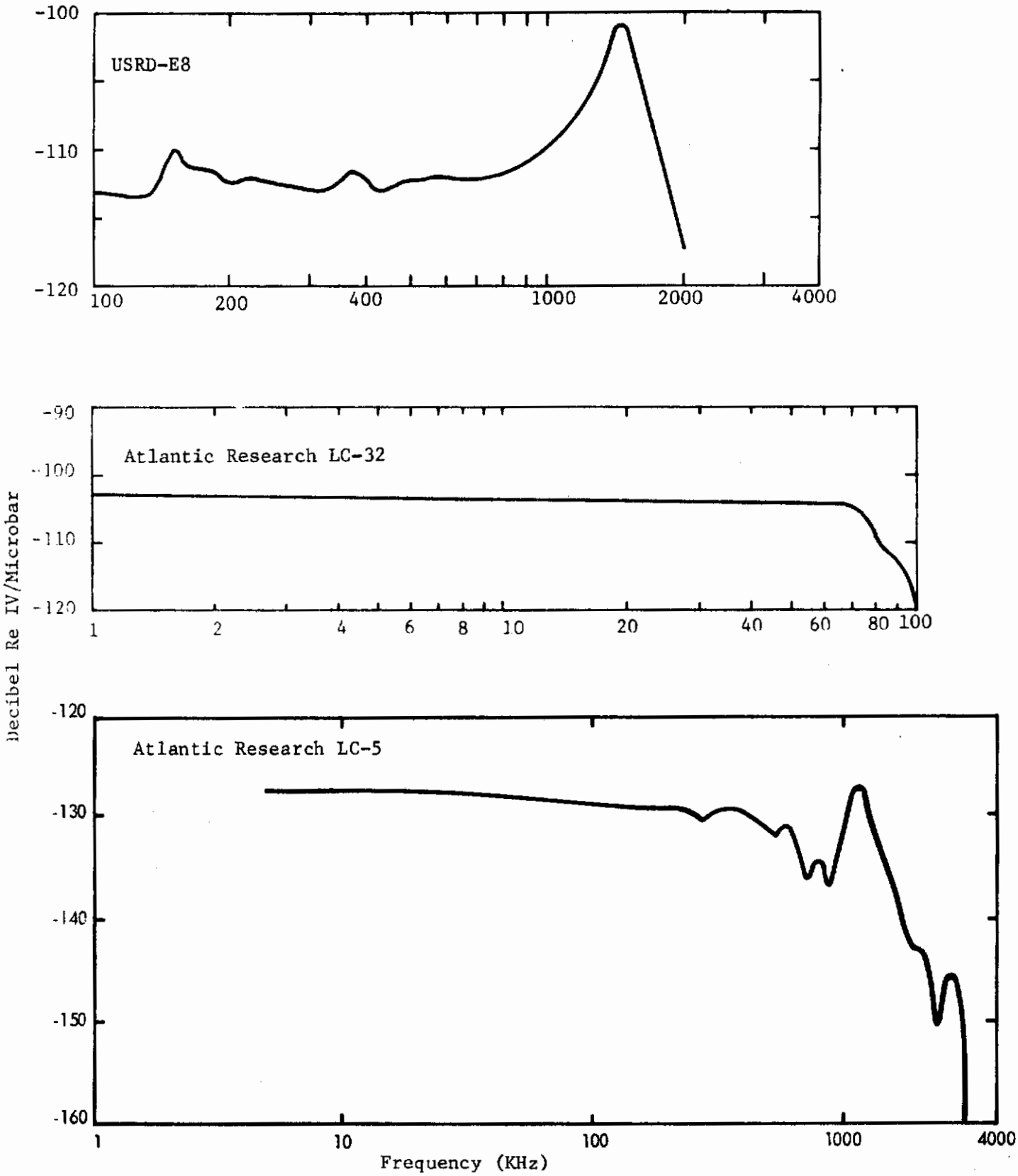

Figure 2. Free Field Frequency Response for the Hydrophone Standards

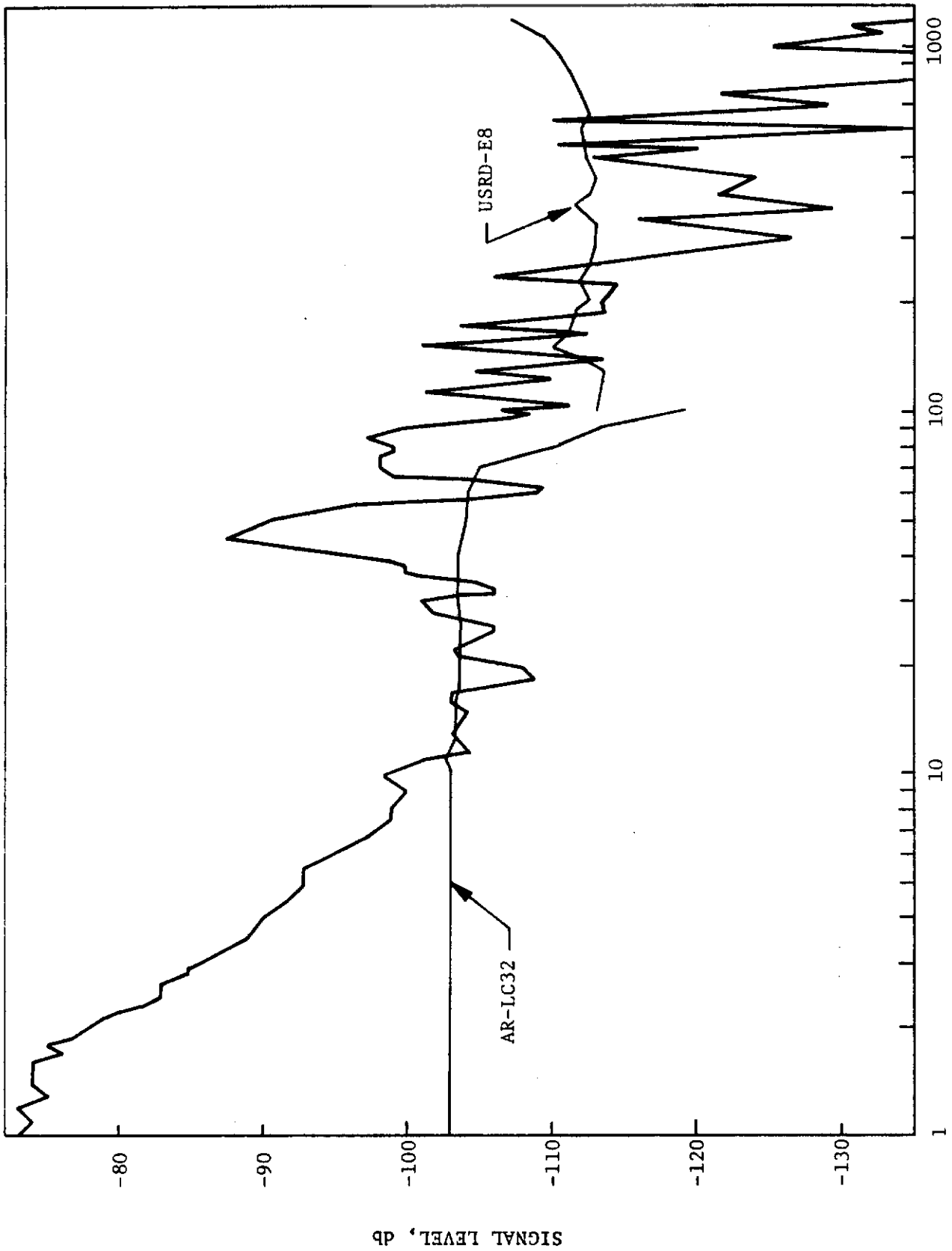

Figure 3. Sweep Frequency Response for Endevco 2213E

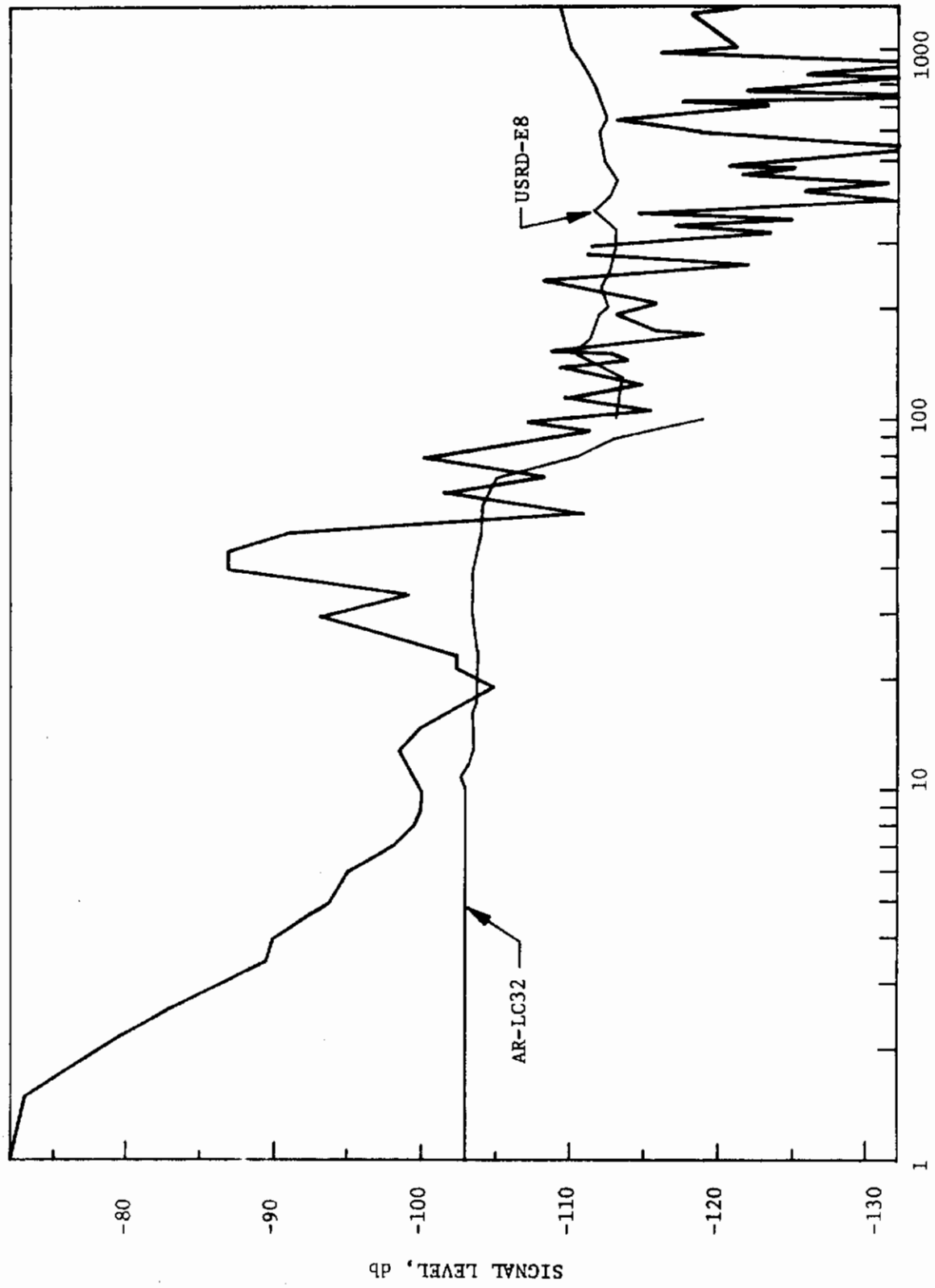

Figure 4. Sweep Frequency Response for Endevco 2217E

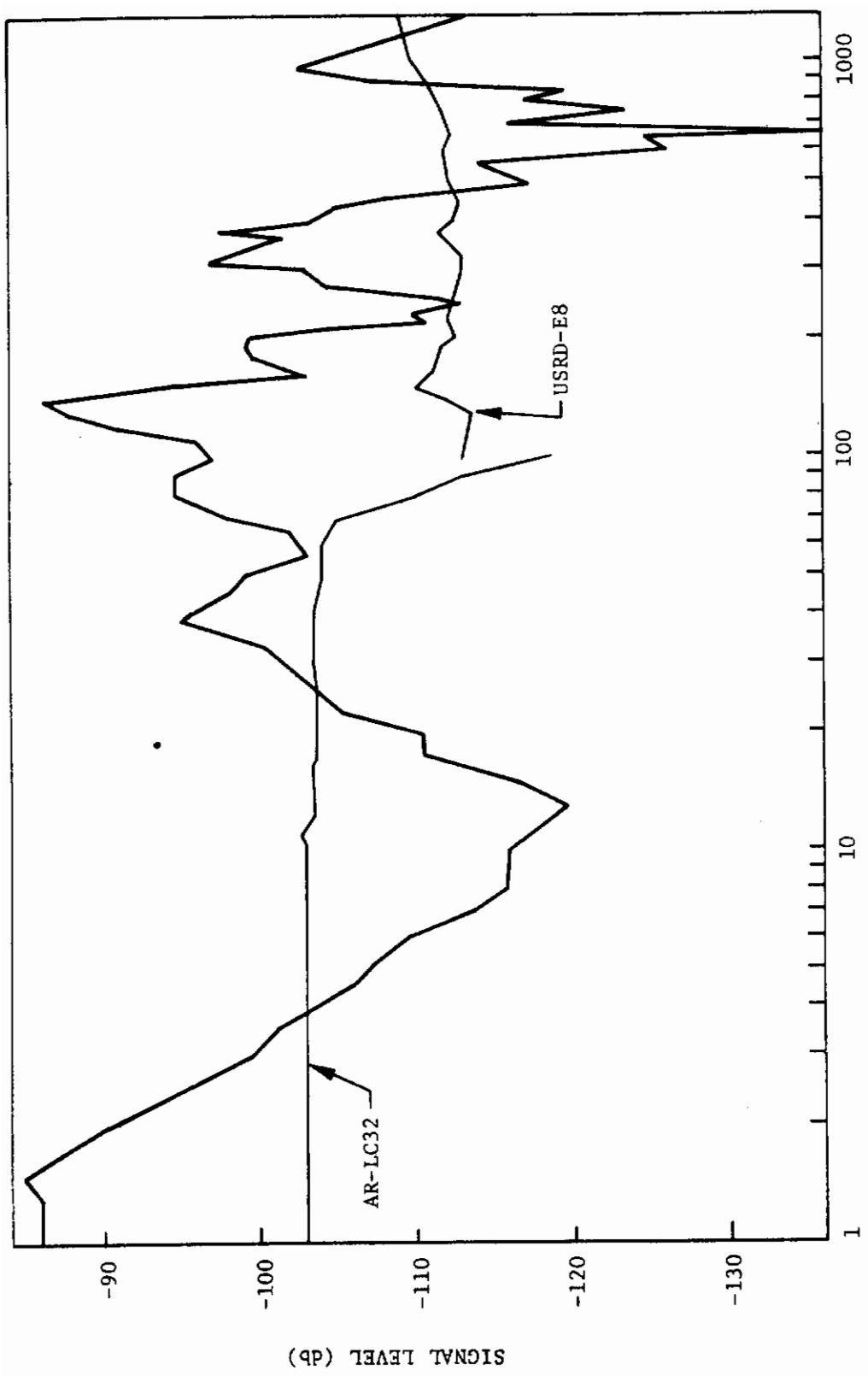

Figure 5. Sweep Frequency Response for Dunegan S-140A

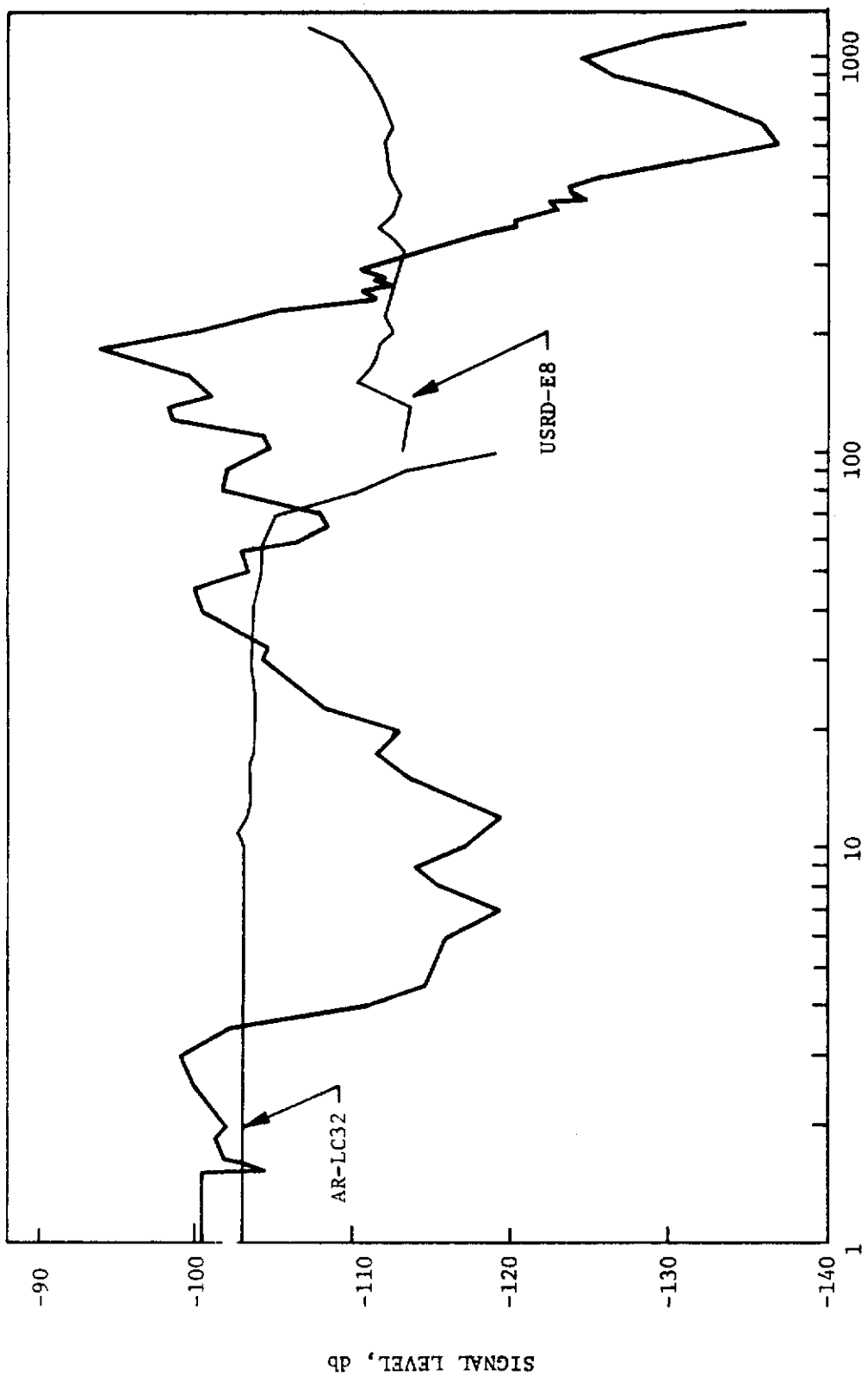

Figure 6. Sweep Frequency Response for Dunegan D-140A

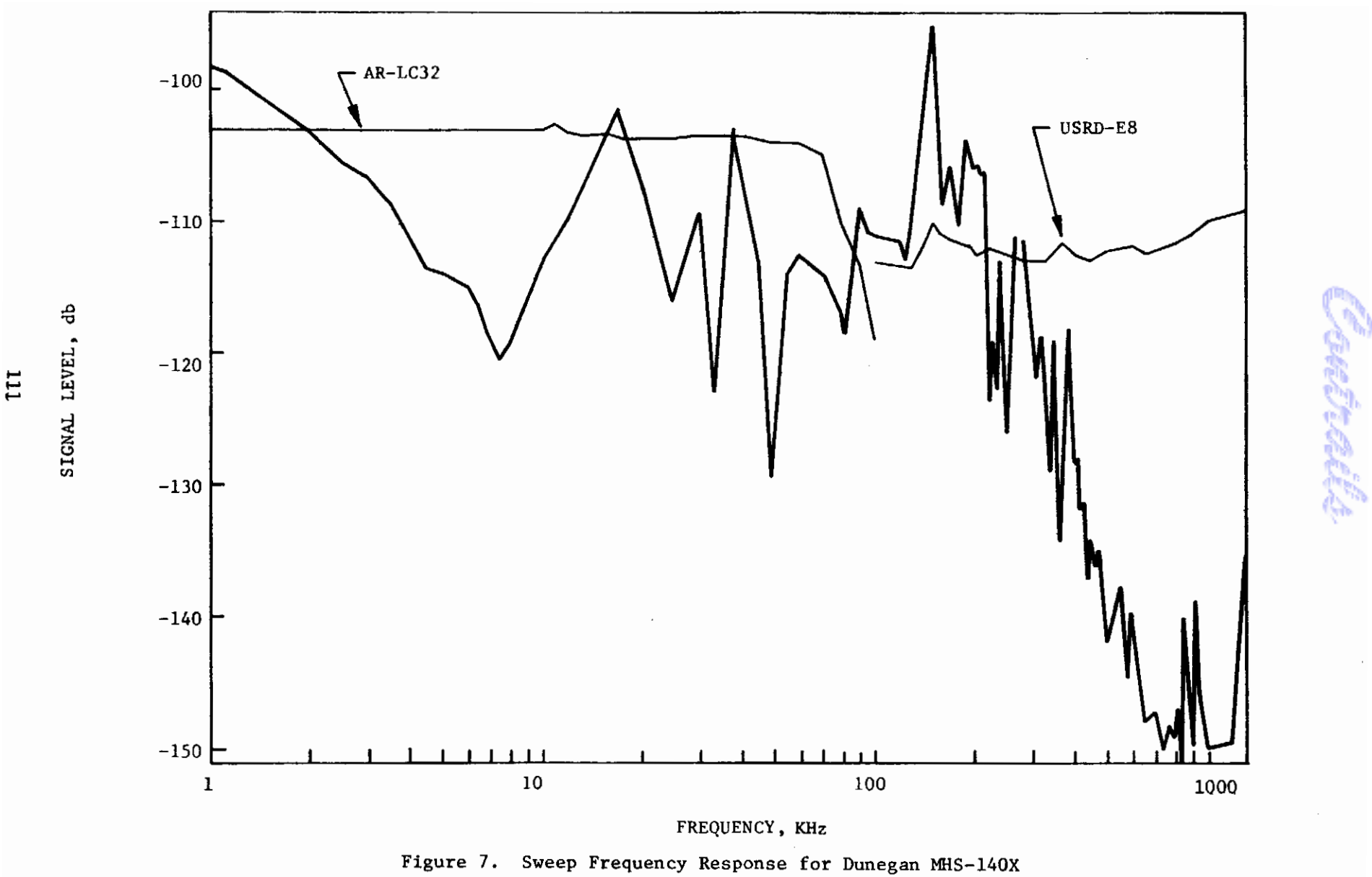

Figure 7. Sweep Frequency Response for Dunegan MHS-140X

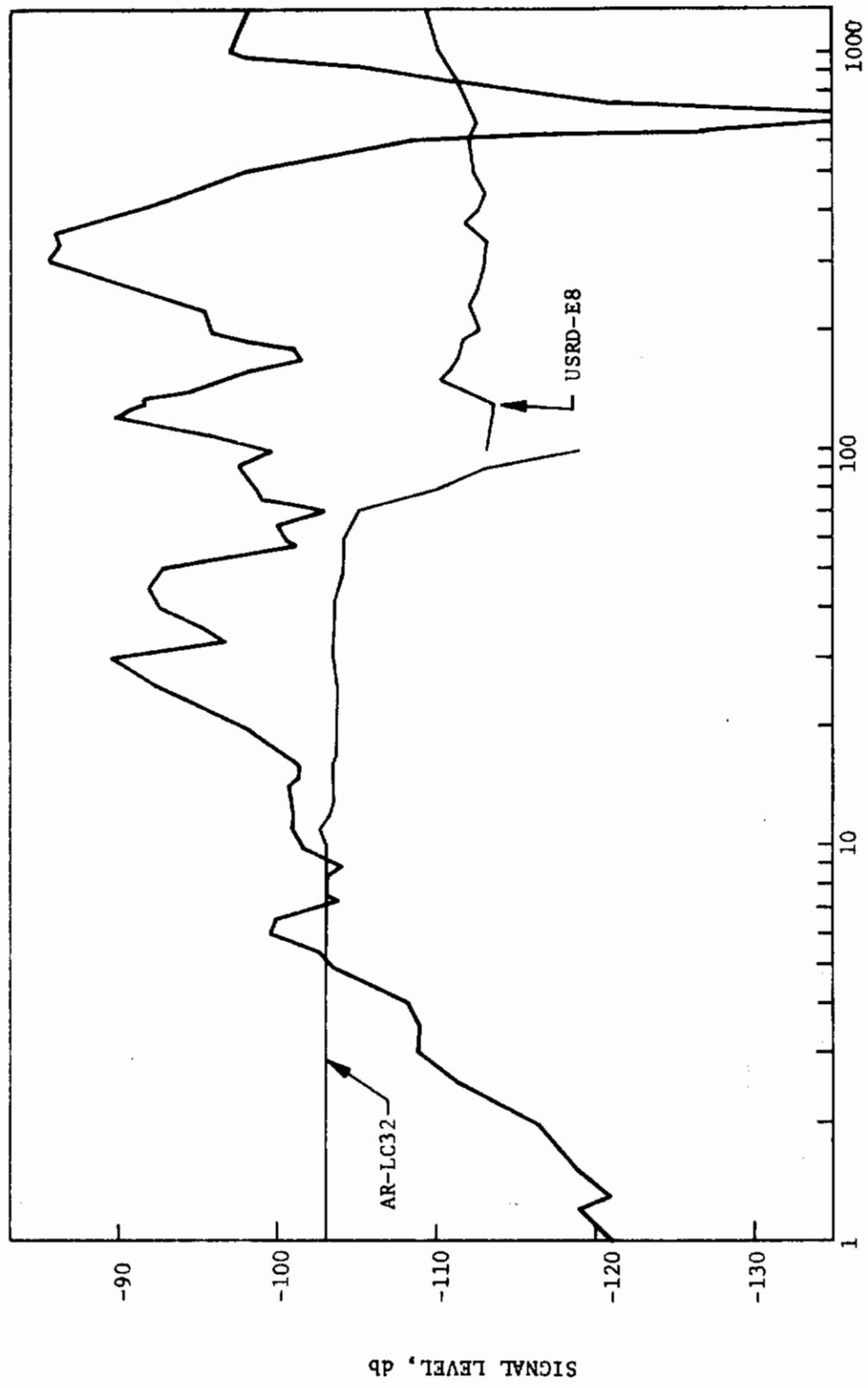

Figure 8. Sweep Frequency Response for Branson X-271A D00103

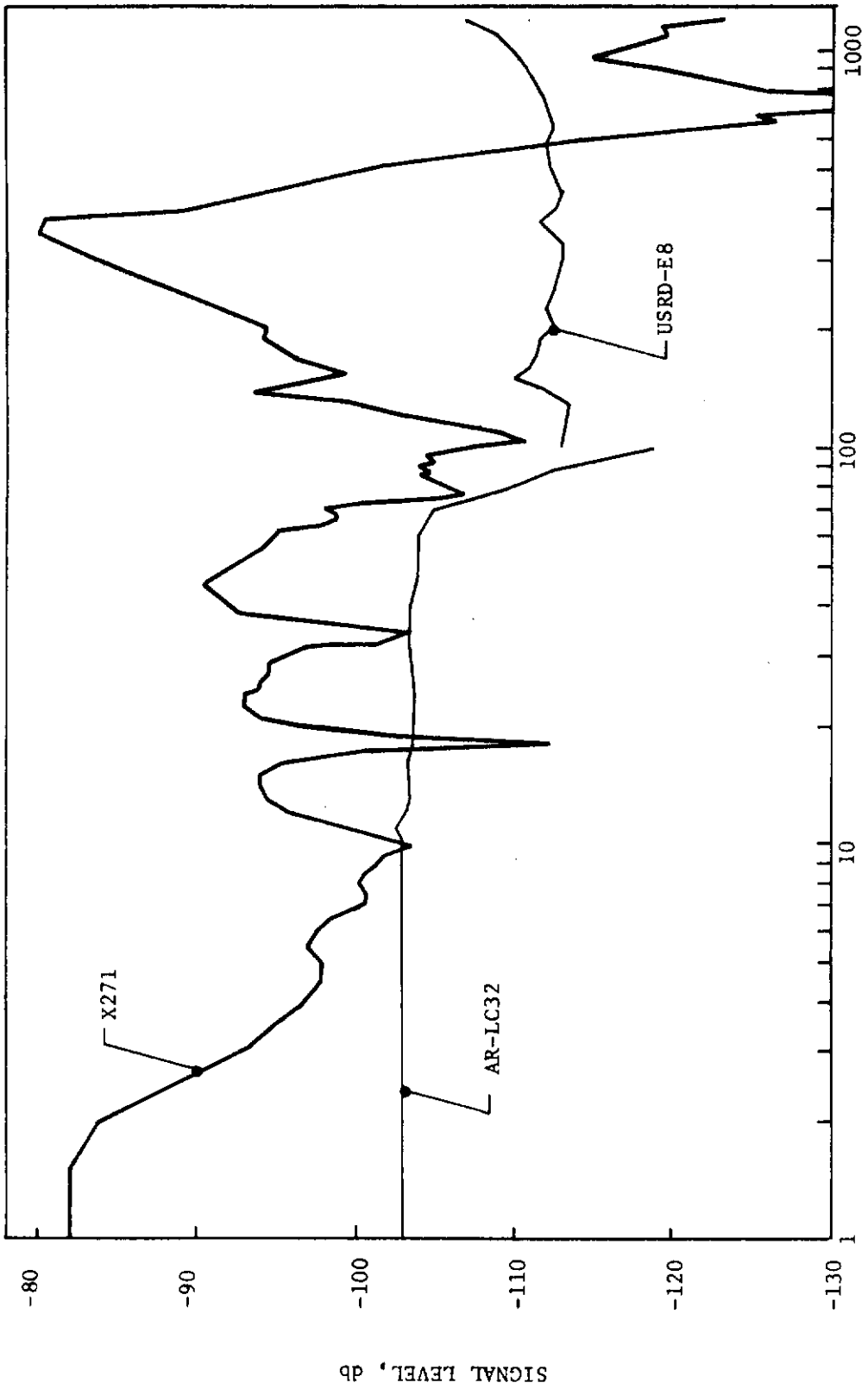

Figure 9. Sweep Frequency Response for Branson X-271A D02490

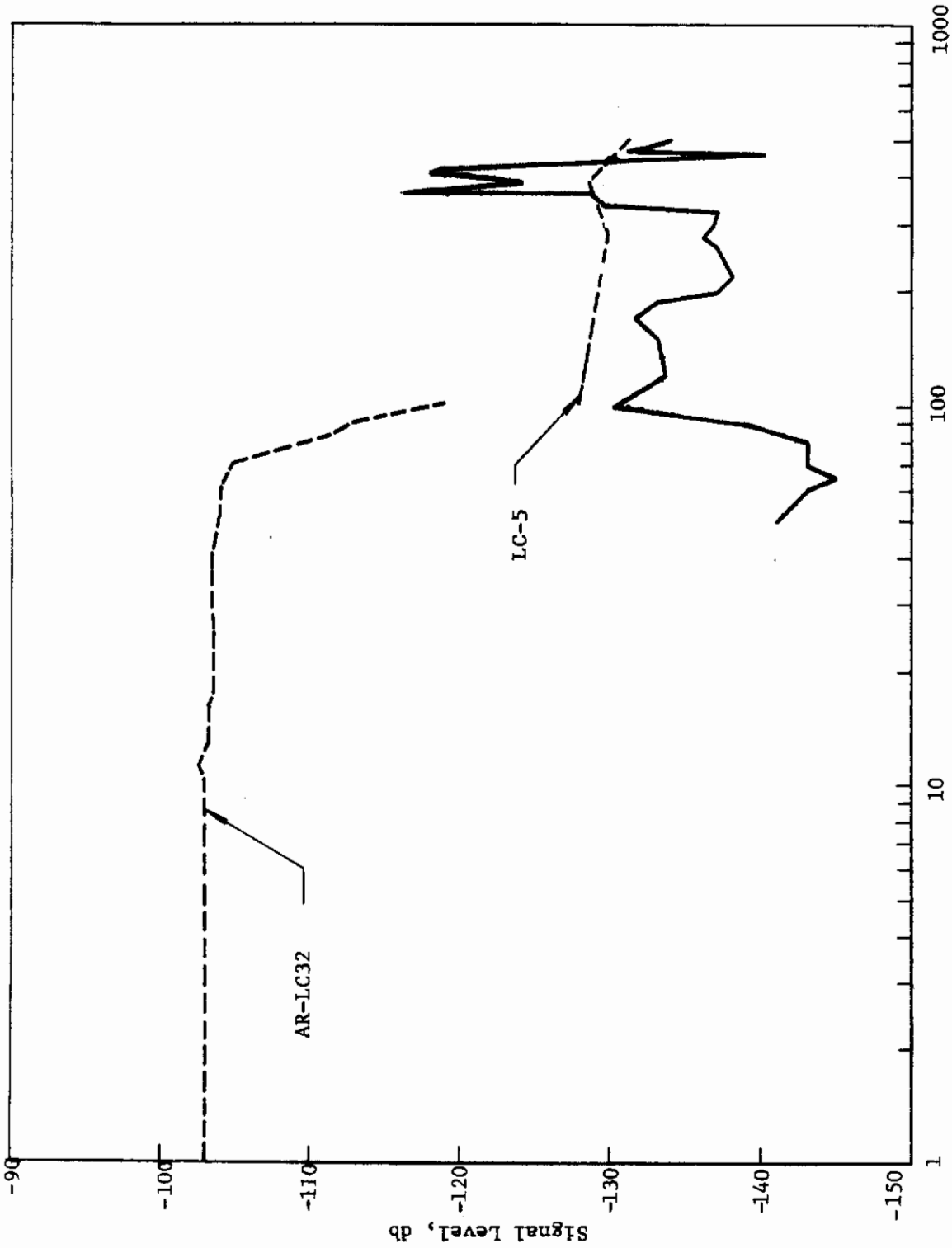

Figure 10. Sweep Frequency Response for Panametrics PZT-5

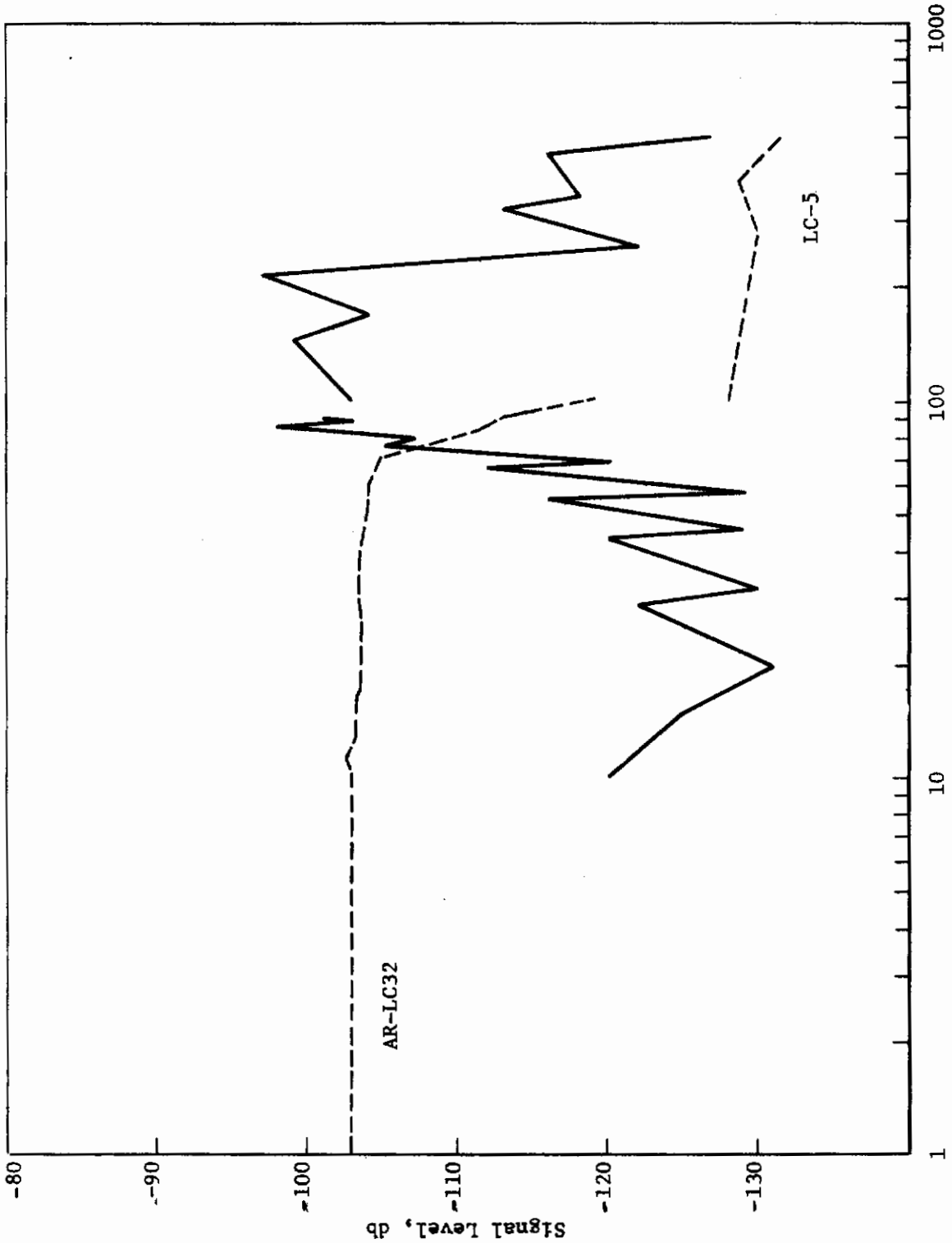

Figure 11. Sweep Frequency Response for Aerojet Experimental

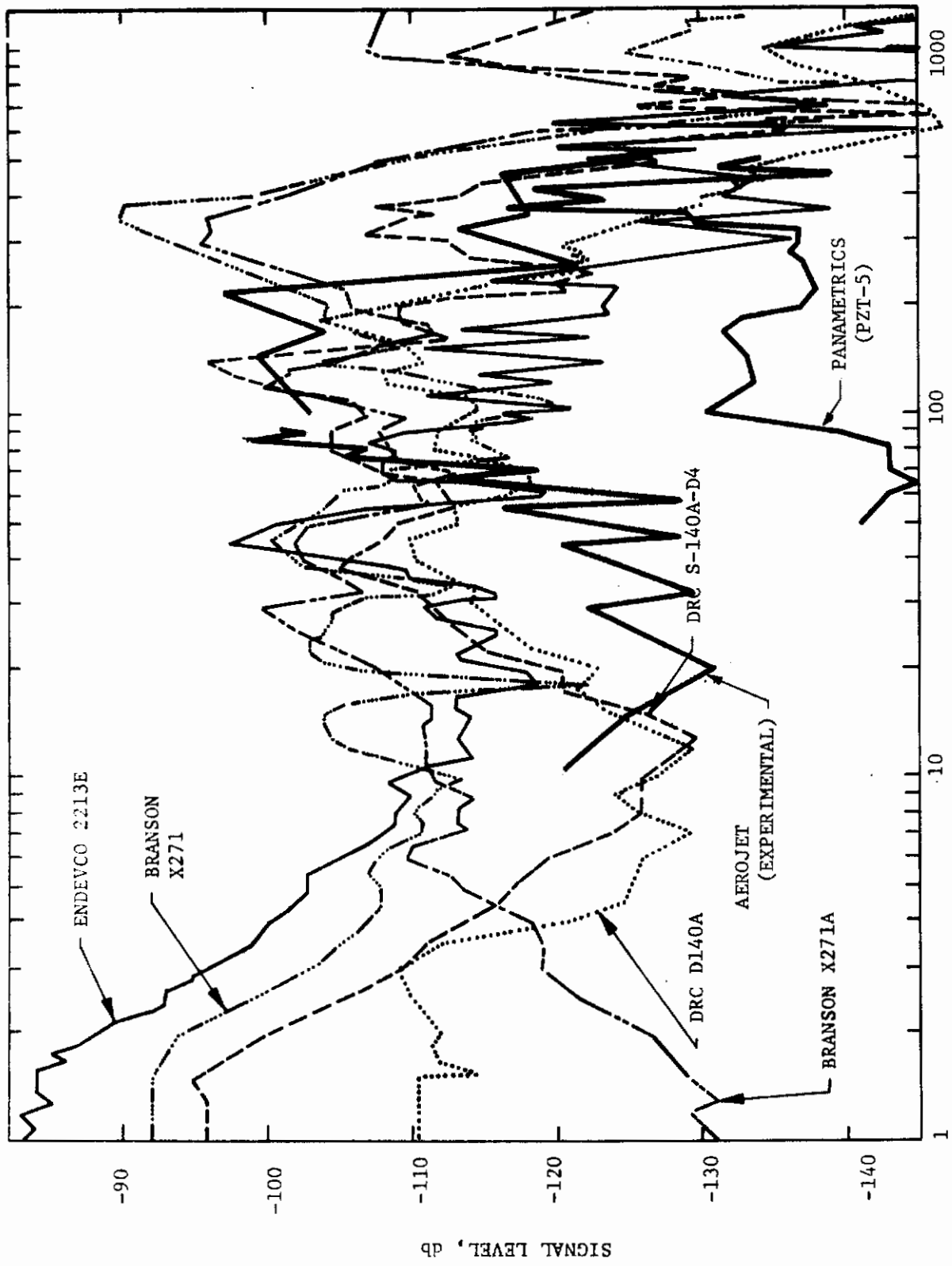

Figure 12. Comparative Frequency Responses

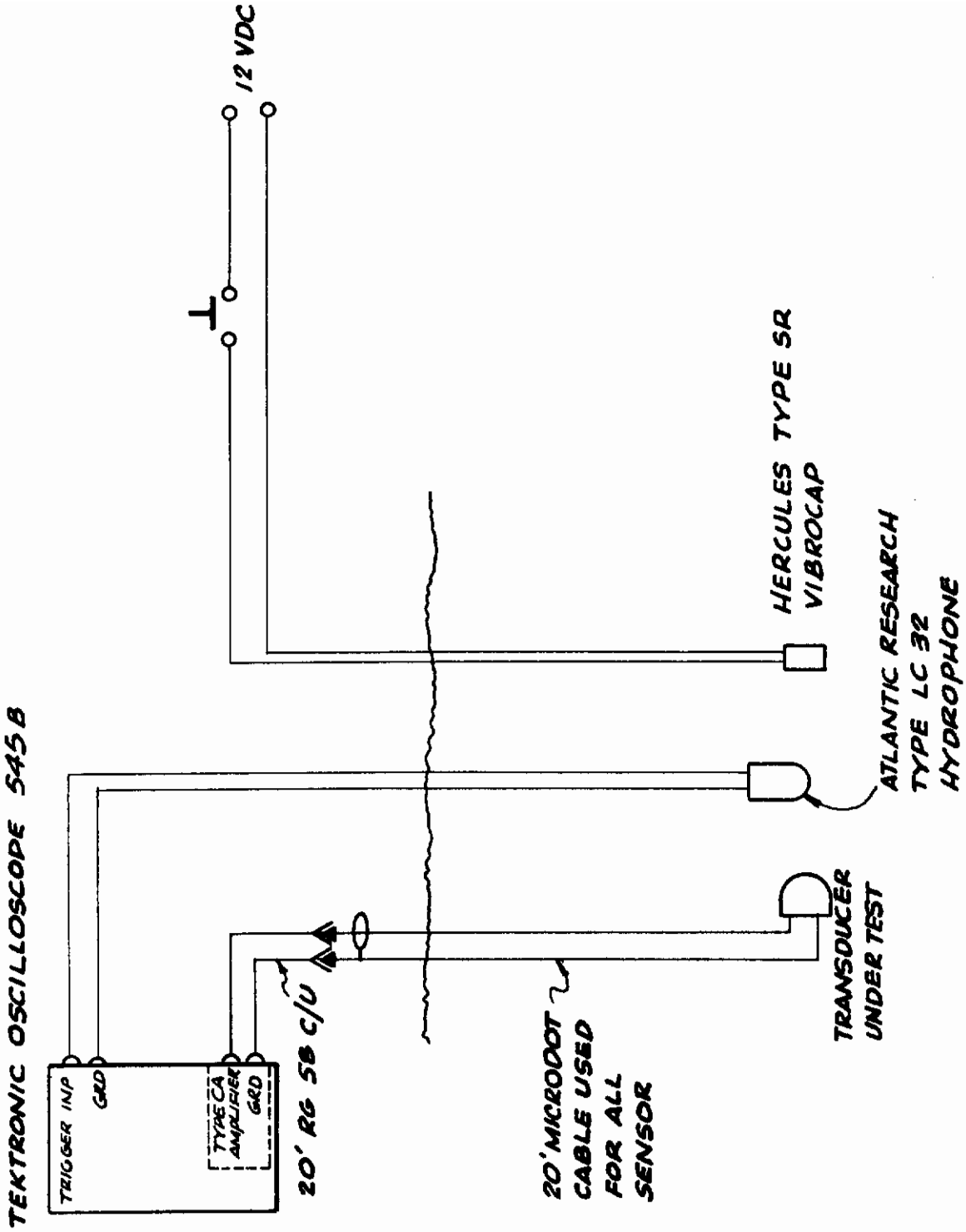

Figure 13. Pulse Response Test Setup

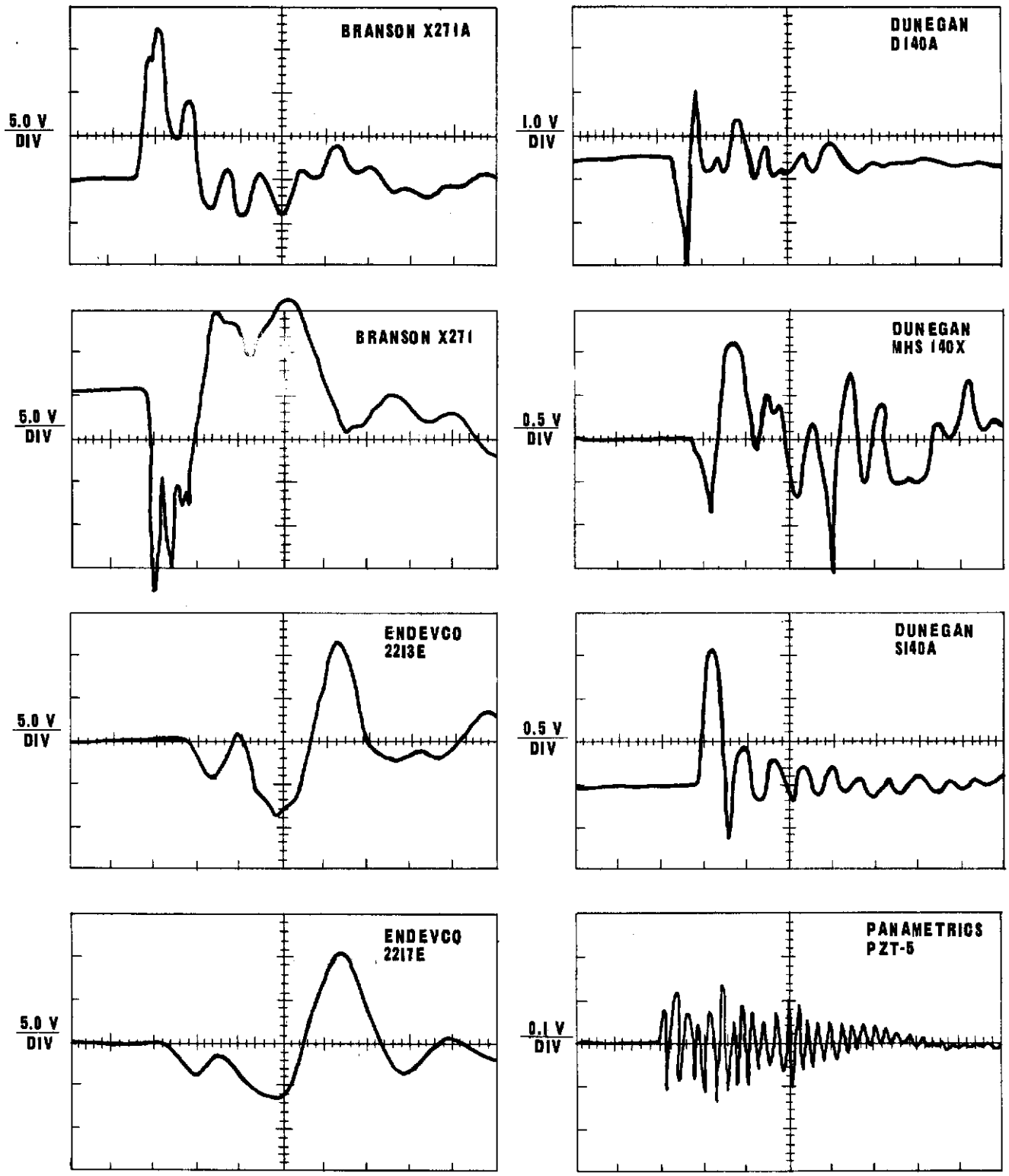

Figure 14. Pulse Response of Eight Commercial Transducers

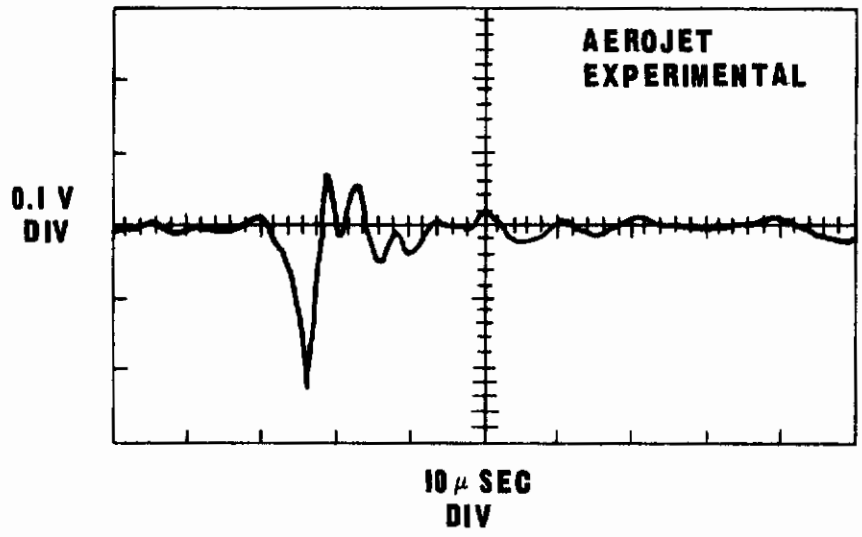

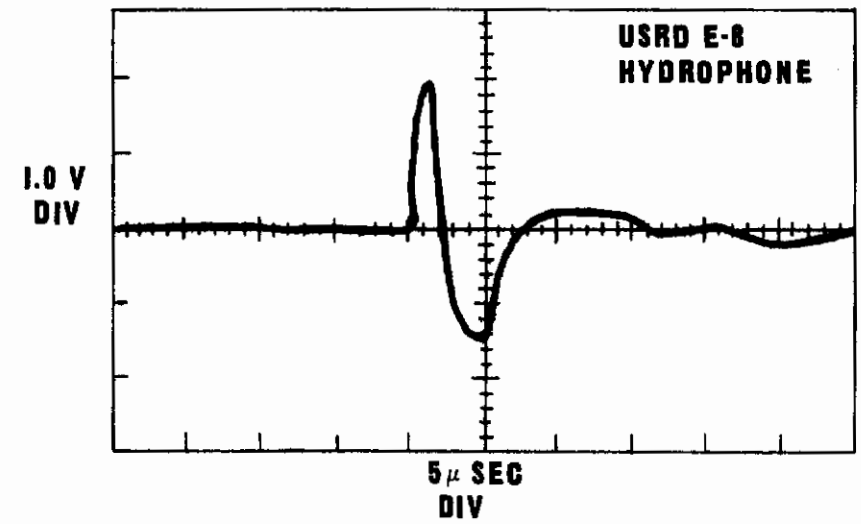

Figure 15. Pulse Response of the USRD E-8 Hydrophone and an Aerojet Experimental Transducer

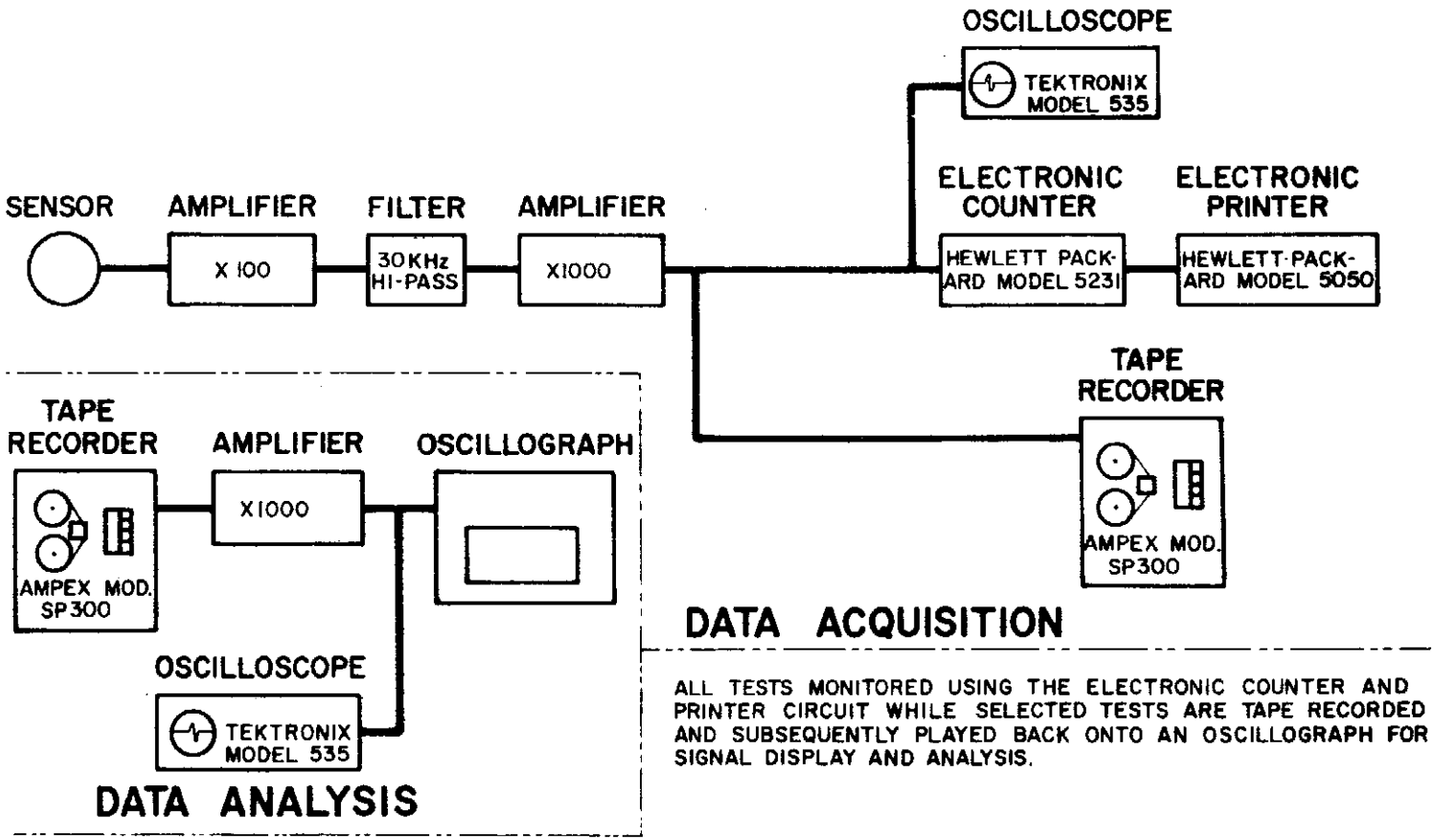

Figure 16. Schematic of Laboratory Data Acquisition-and-Analysis Instrumentation

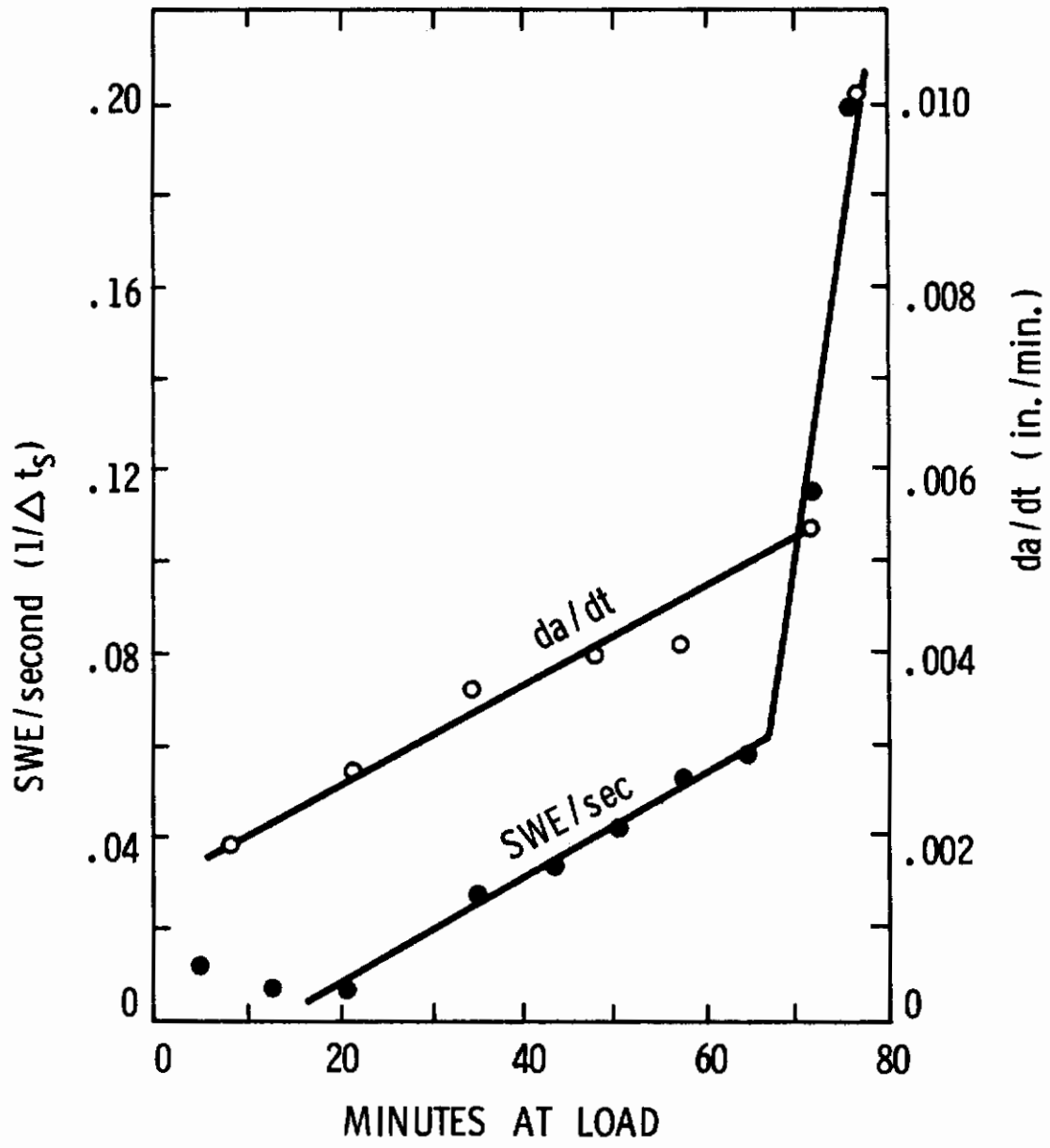

Figure 17. Correlation of Stress Wave Emission and Crack Growth in D6aC Under Constant Load in Water

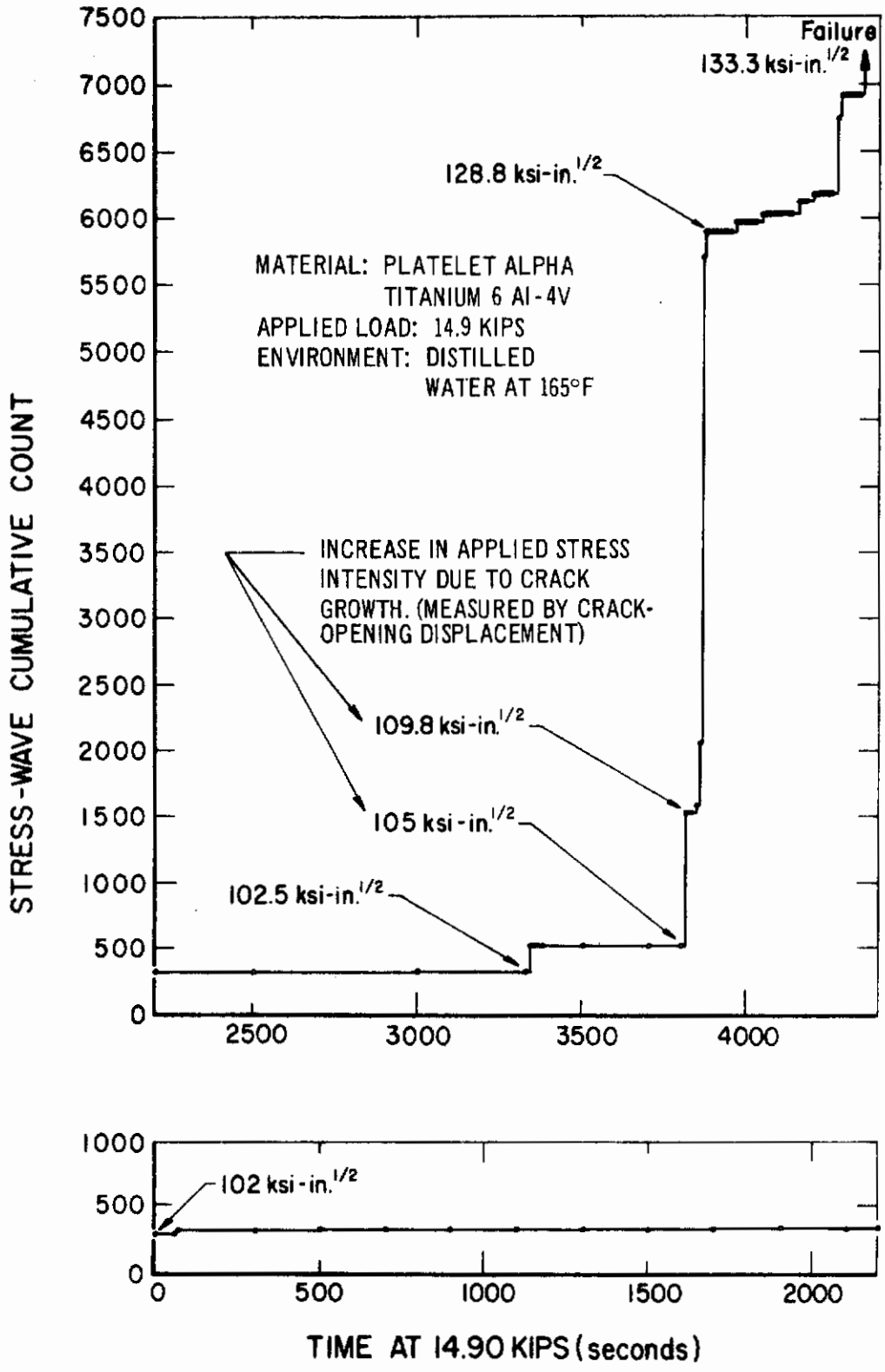

Figure 18. Details of Crack Growth Process in 6Al-4V Titanium Under Constant Load in Water at 165°F

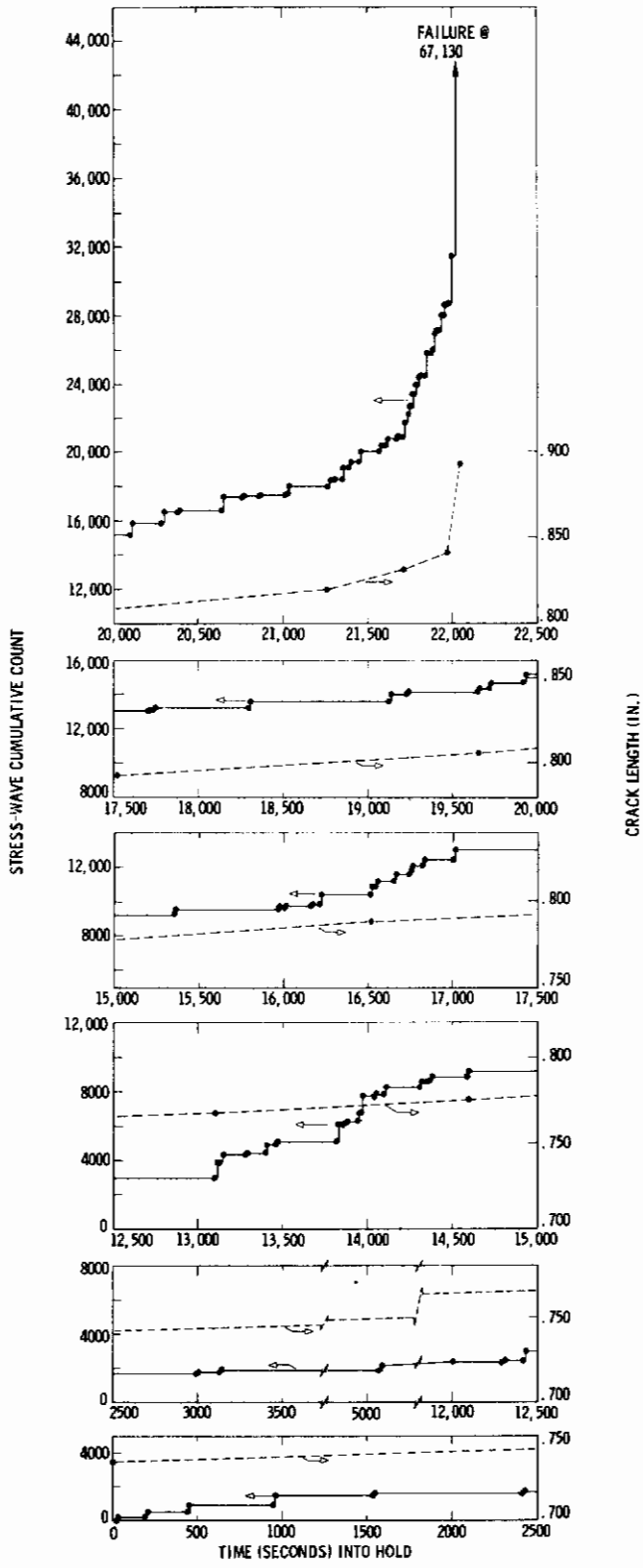

Figure 19. Details of Subcritical Crack Growth in 18% Nickel Maraging Steel Under Constant Load in Water at 70°F

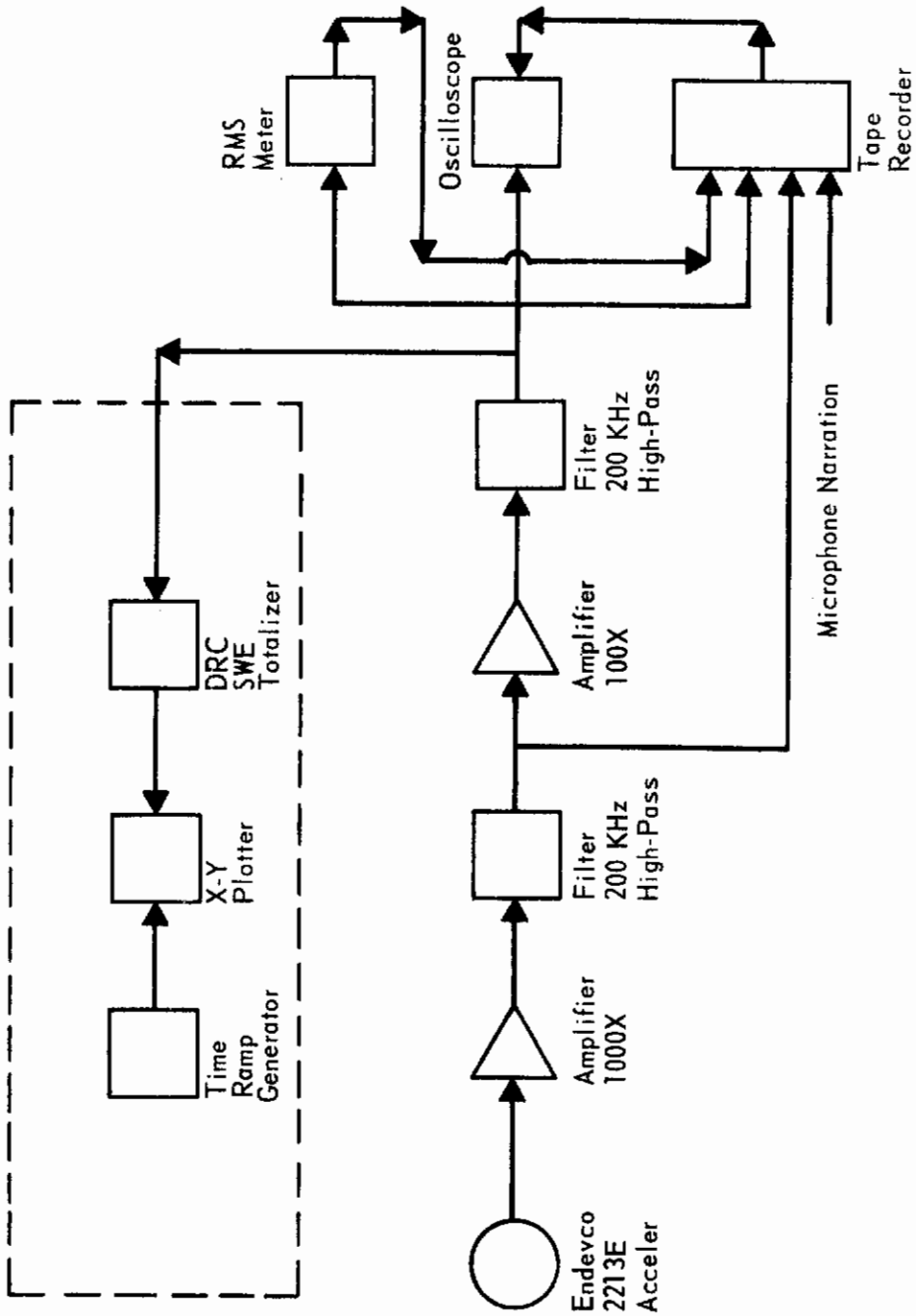

Figure 20. Instrumentation Used in Monitoring Weld Cracking

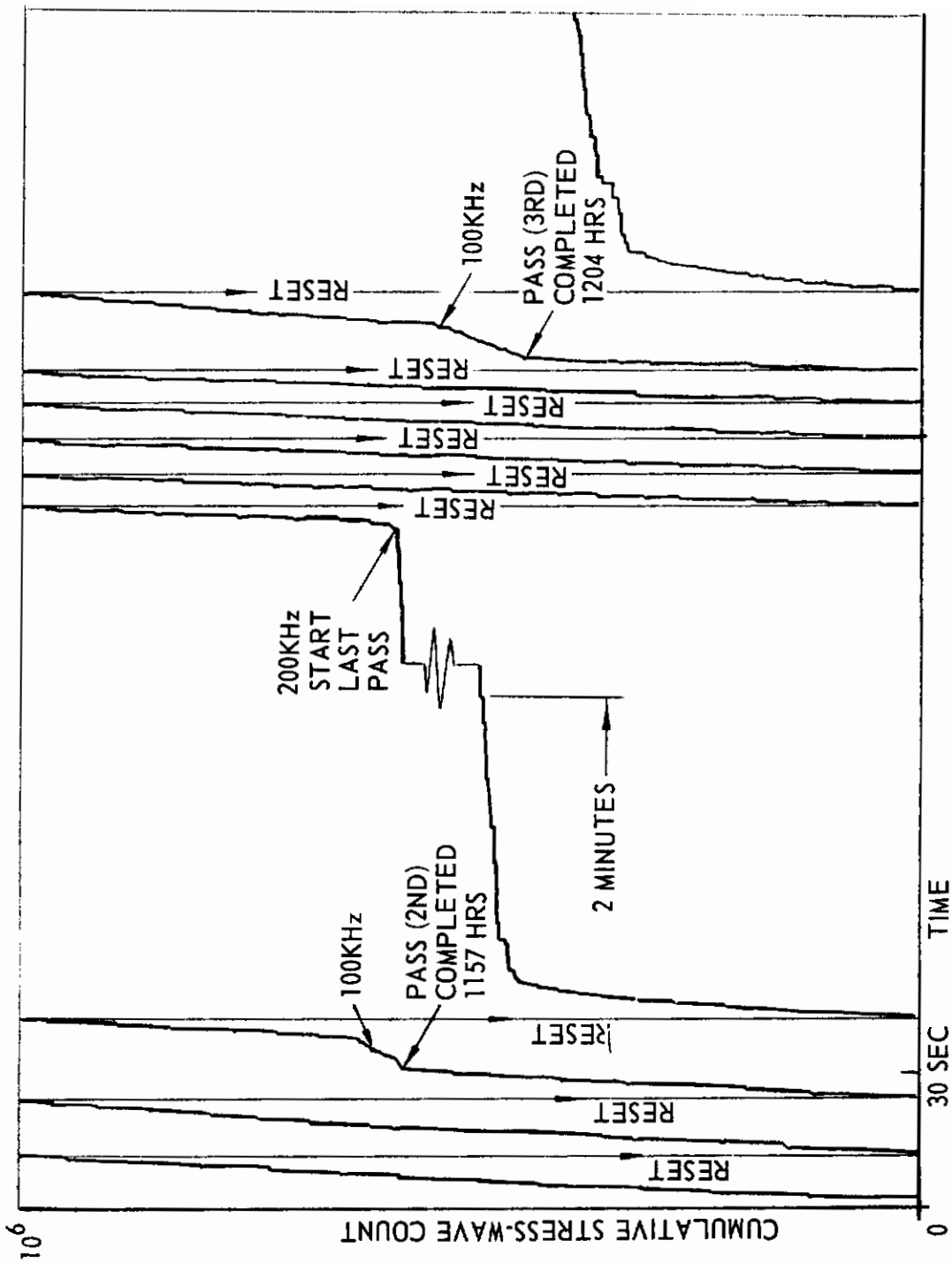

Figure 21. Cumulative Stress-Wave Count During and Immediately After MIG Welding HY-100

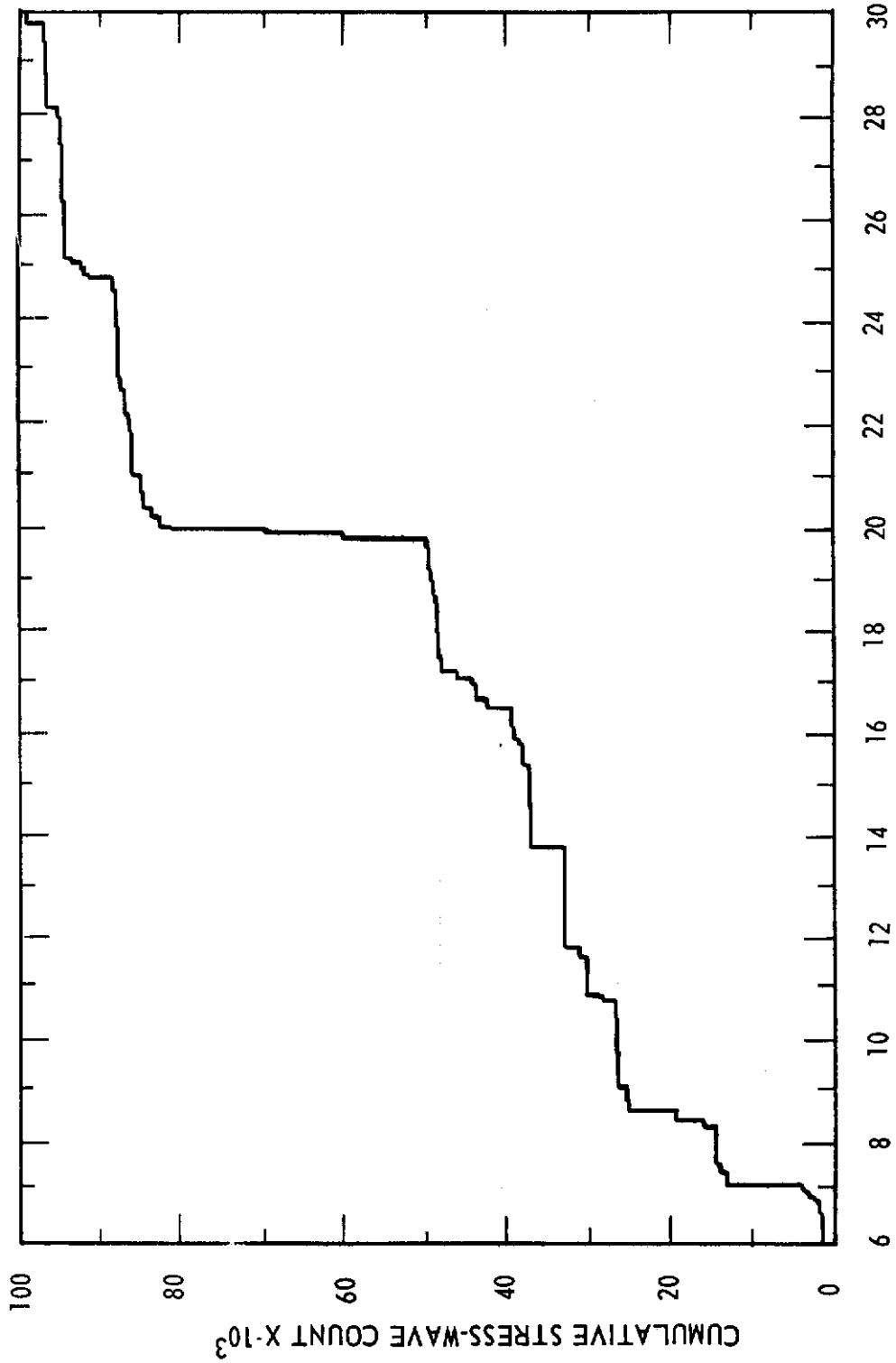

Figure 22. Cumulative Stress-Wave Count from 6 to 30 Hours After Welding HY-100 with a Covered Electrode

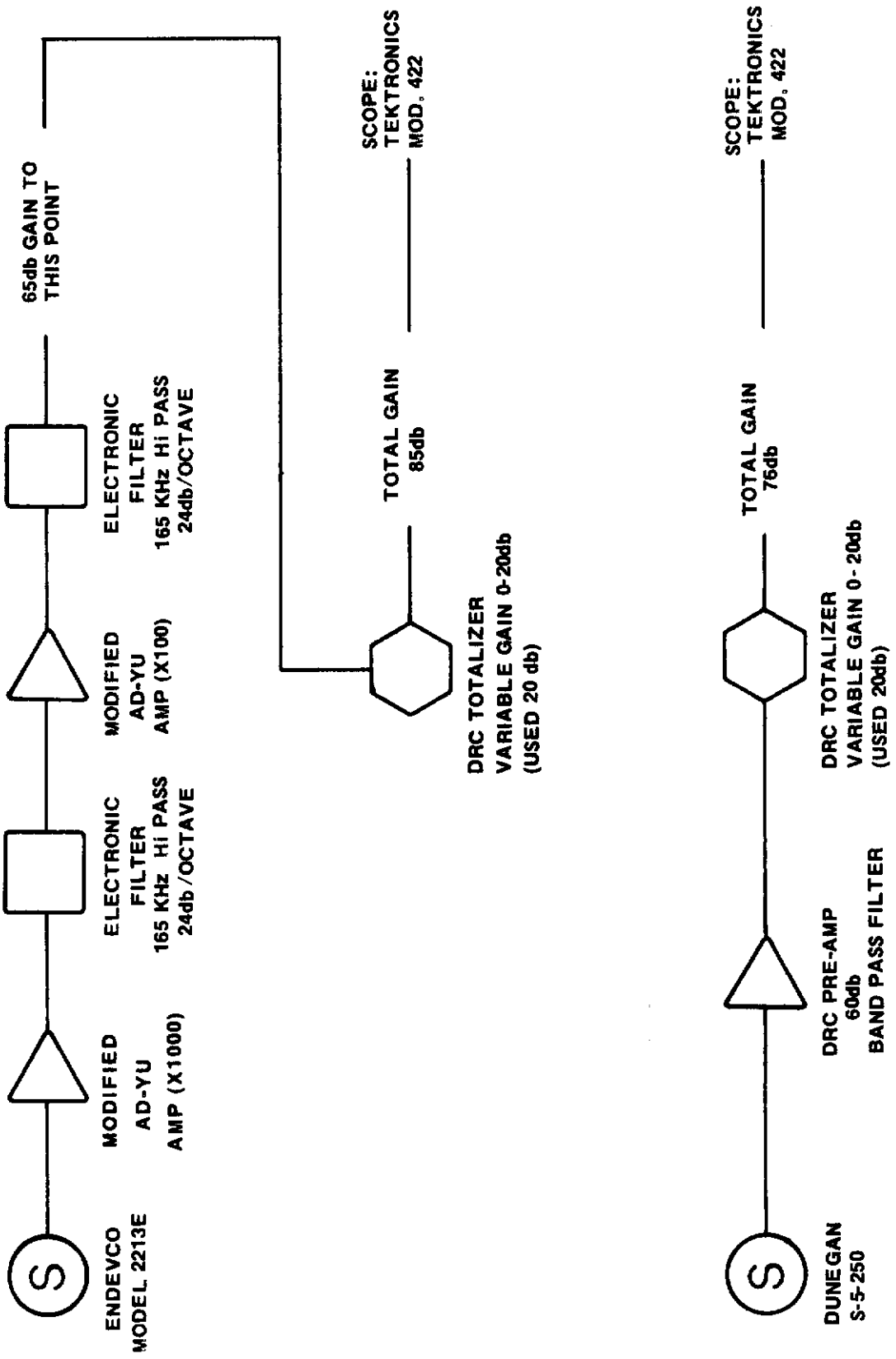

Figure 23. Schematic of the Instrumentation Systems Receiving the Pulser Signal

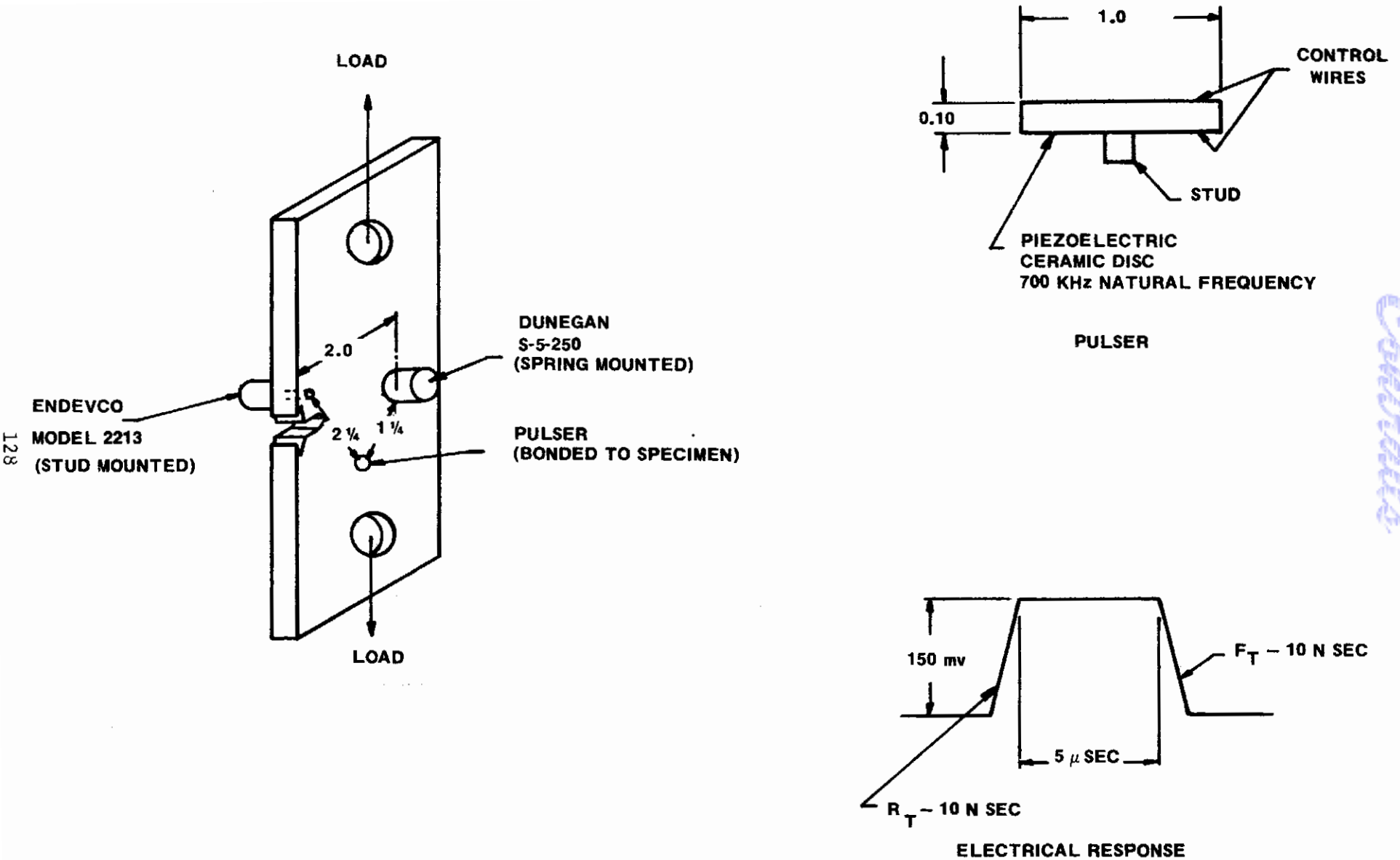

Figure 24. Location and Mounting of Pulses and Sensors

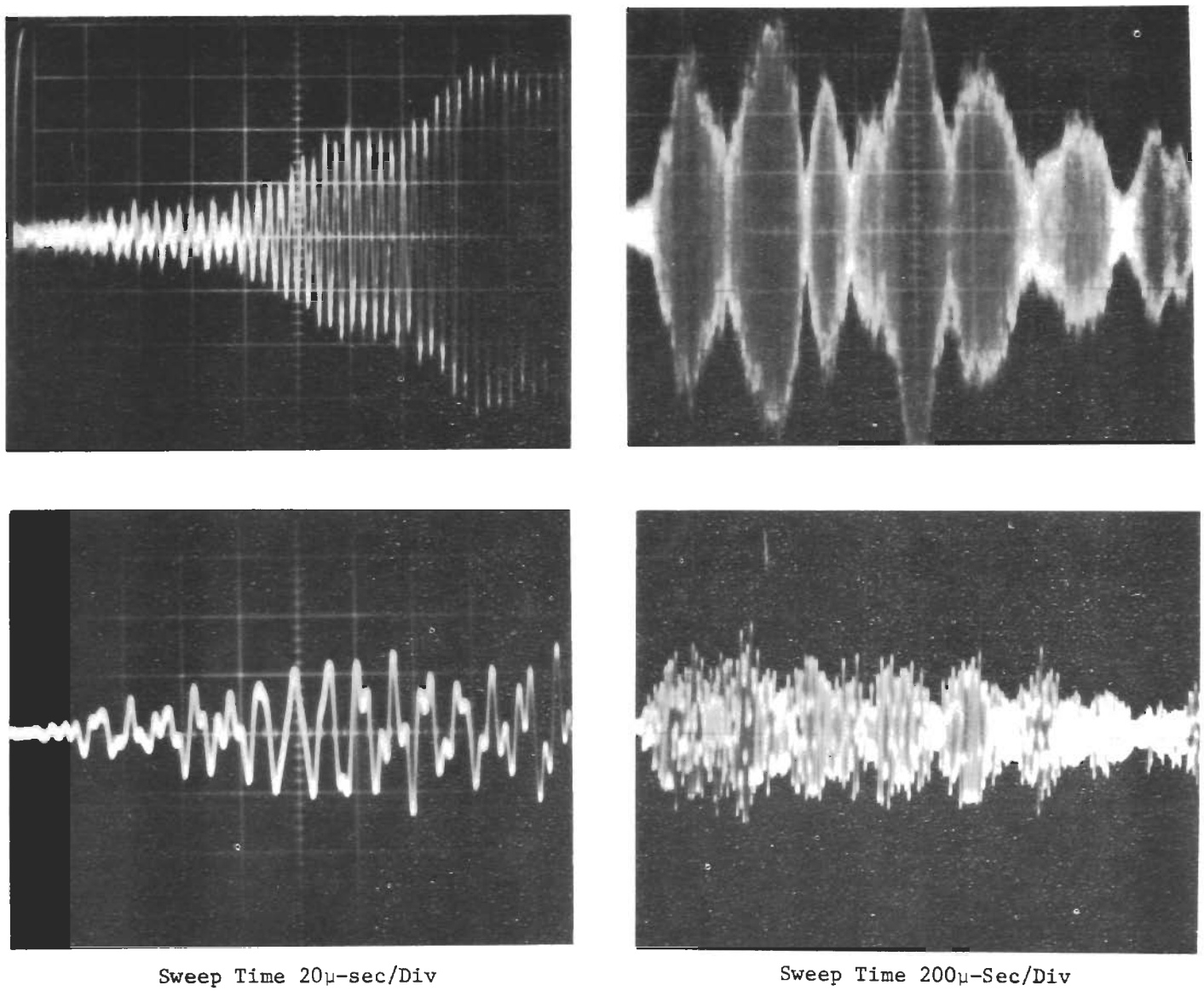

Figure 25. Output of the Endevco 2213E and Dunegan S-5-250 Transducers at Zero Load

10 Kip Load

Endevco
Model 2213E
0.5v/div.

DRC
S-5-250
0.5v/div.

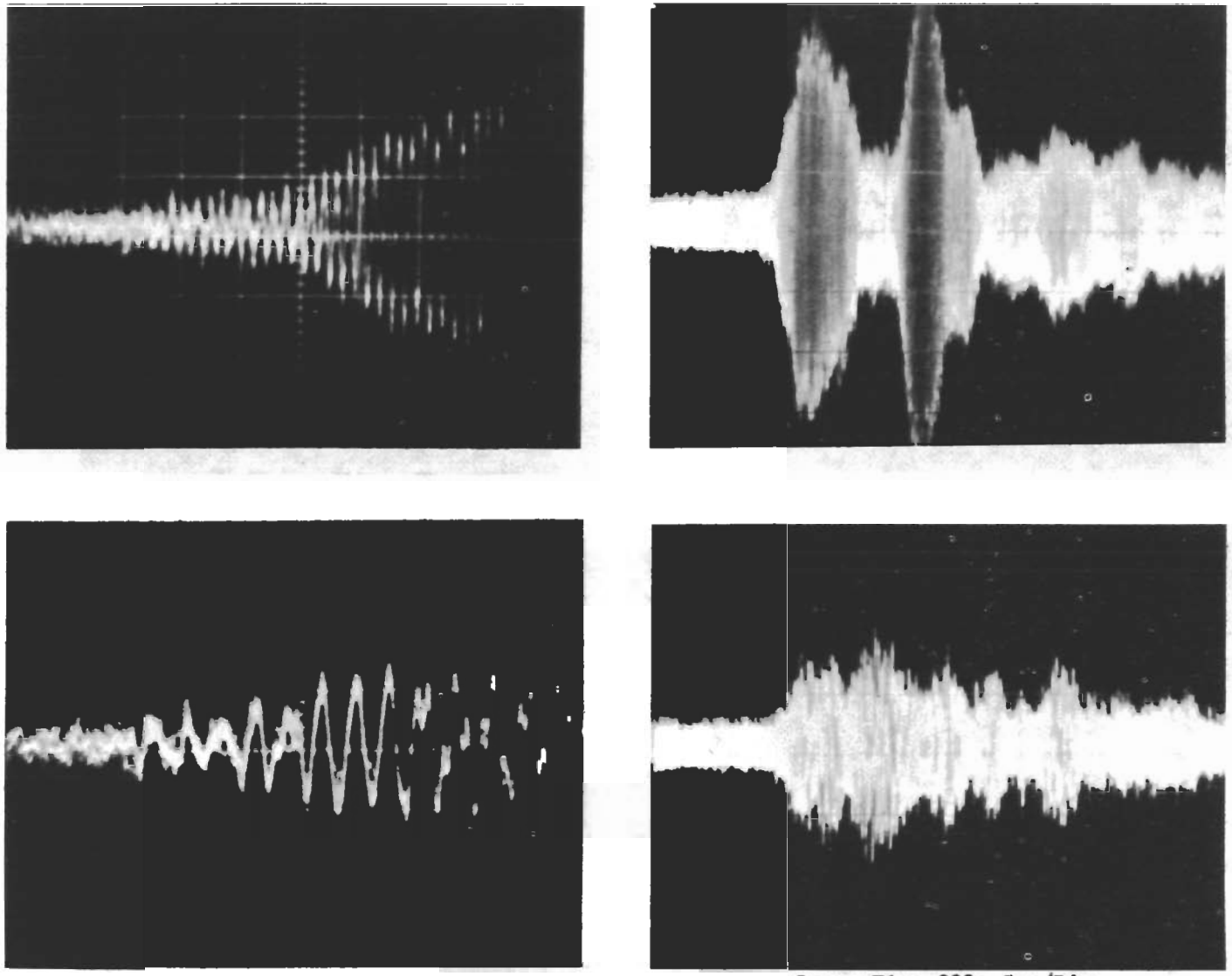

Sweep Time 20μ-Sec/Div

Sweep Time 200μ-Sec/Div

Figure 26. Output of the Endevco 2213E and Dunegan S-5-250 Transducers at 10-kips Load

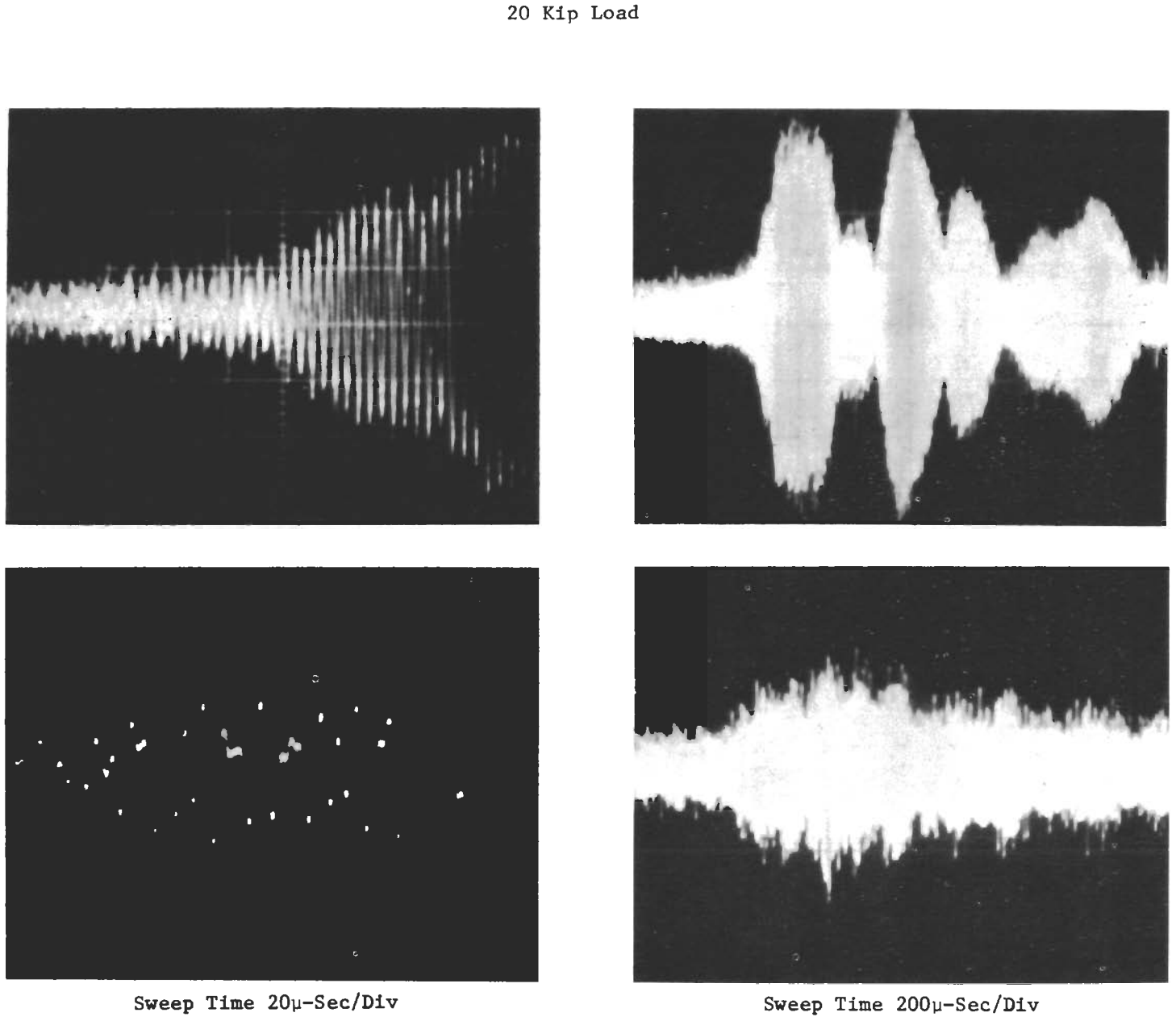

Figure 27. Output of the Endevco 2213E and Dunegan S-5-250 Transducers at 20-kips Load

30 Kip Load

Endevco
Model 2213E
0.5v/div.

DRC
S-5-250
0.5 v/div.

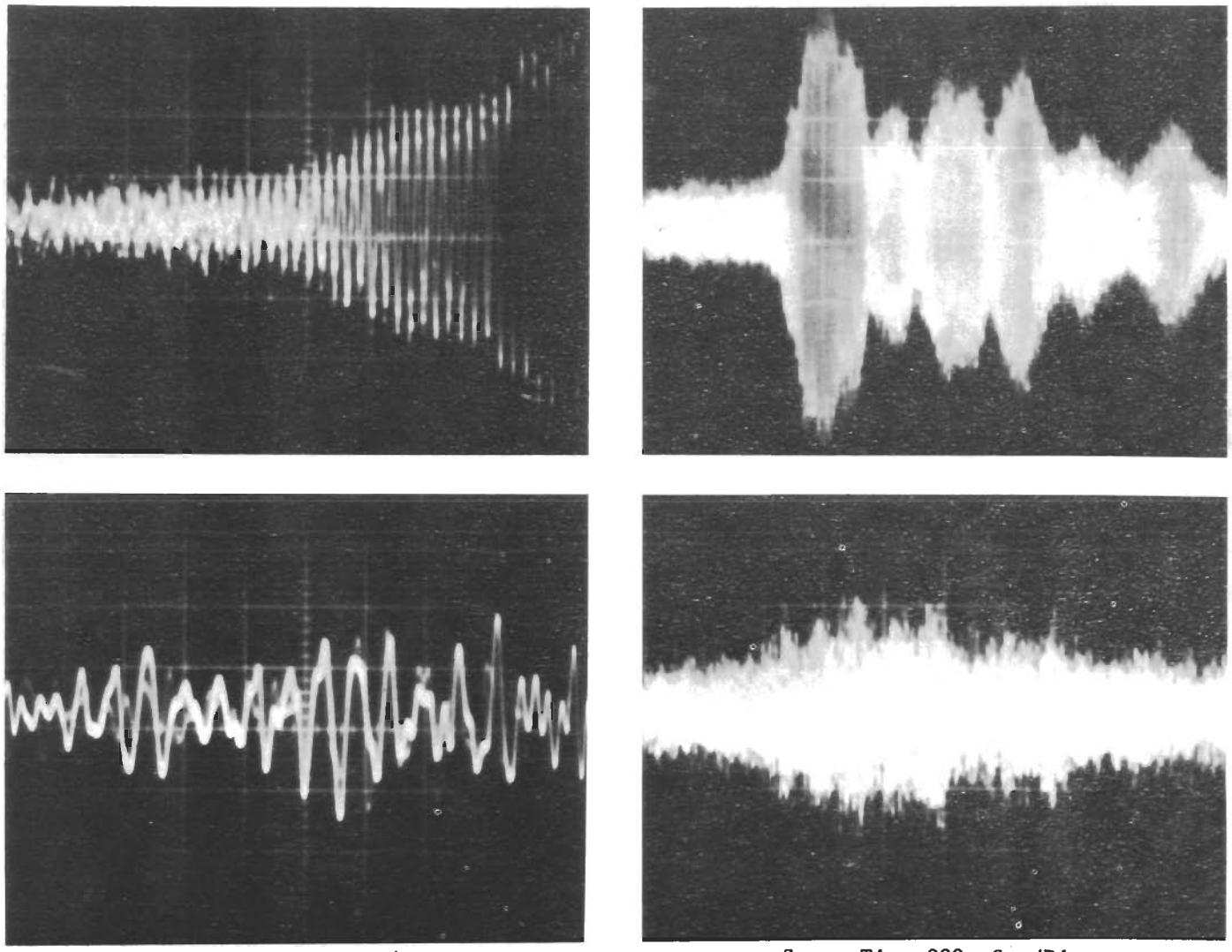

Sweep Time 20μ-Sec/Div

Sweep Time 200μ-Sec/Div

Figure 28. Output of the Endevco 2213E and Dunegan S-5-250 Transducers at 30-kips Load

40 Kip Load

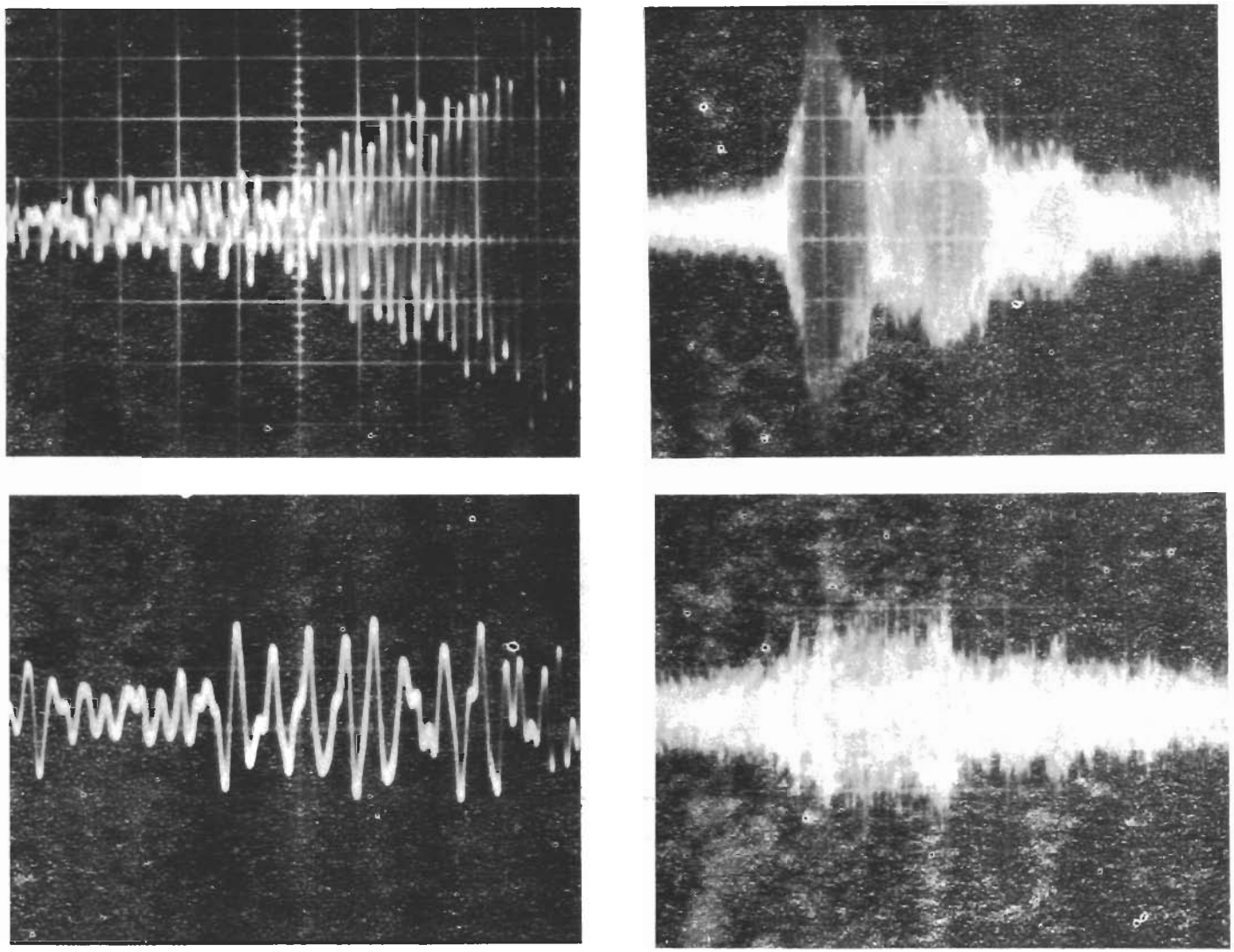

Figure 29. Output of the Endevco 2213E and Dunegan S-5-250 Transducers at 40-kips Load

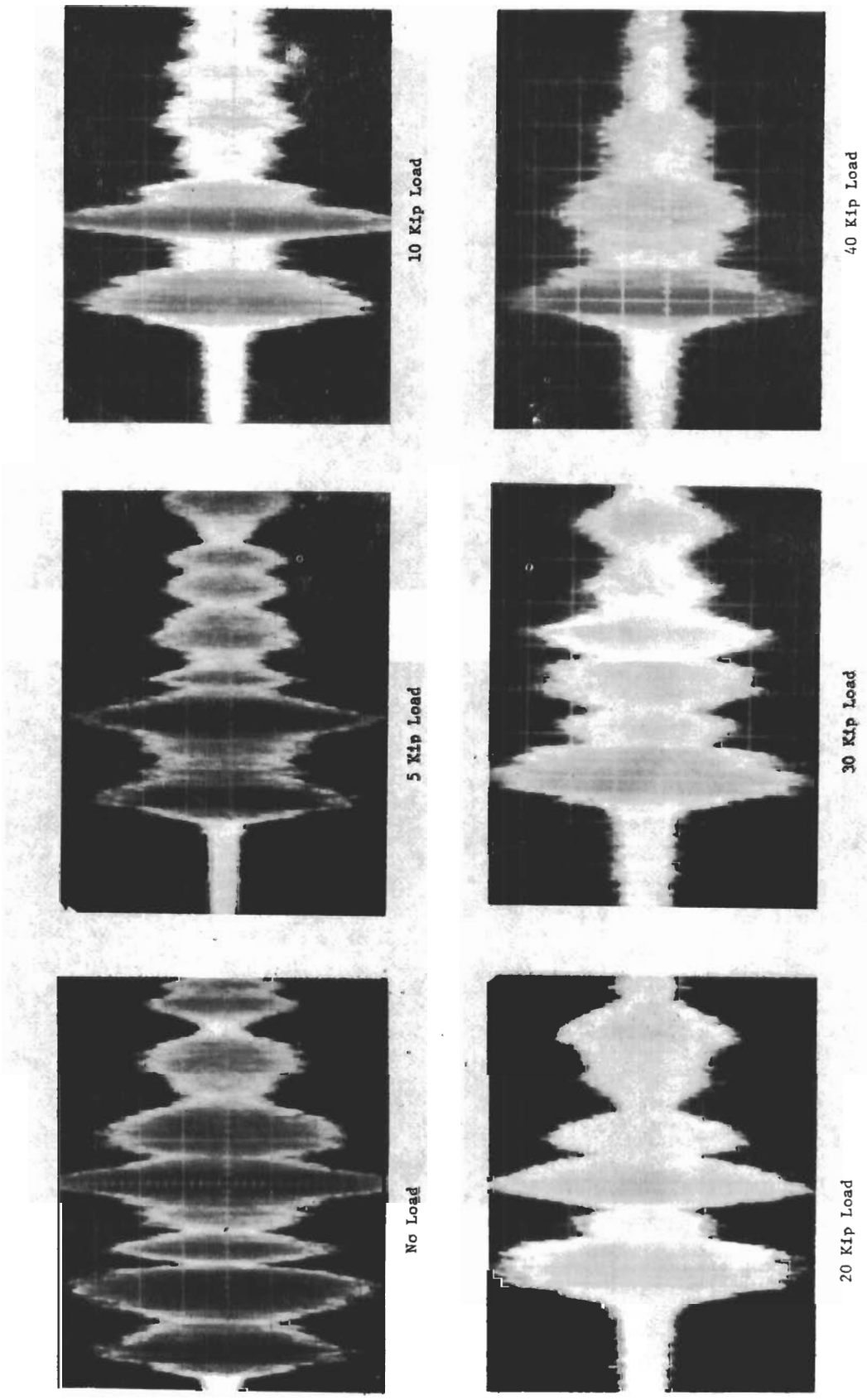

Figure 30. Variation in Endevco 2213E Output as a Function of Load

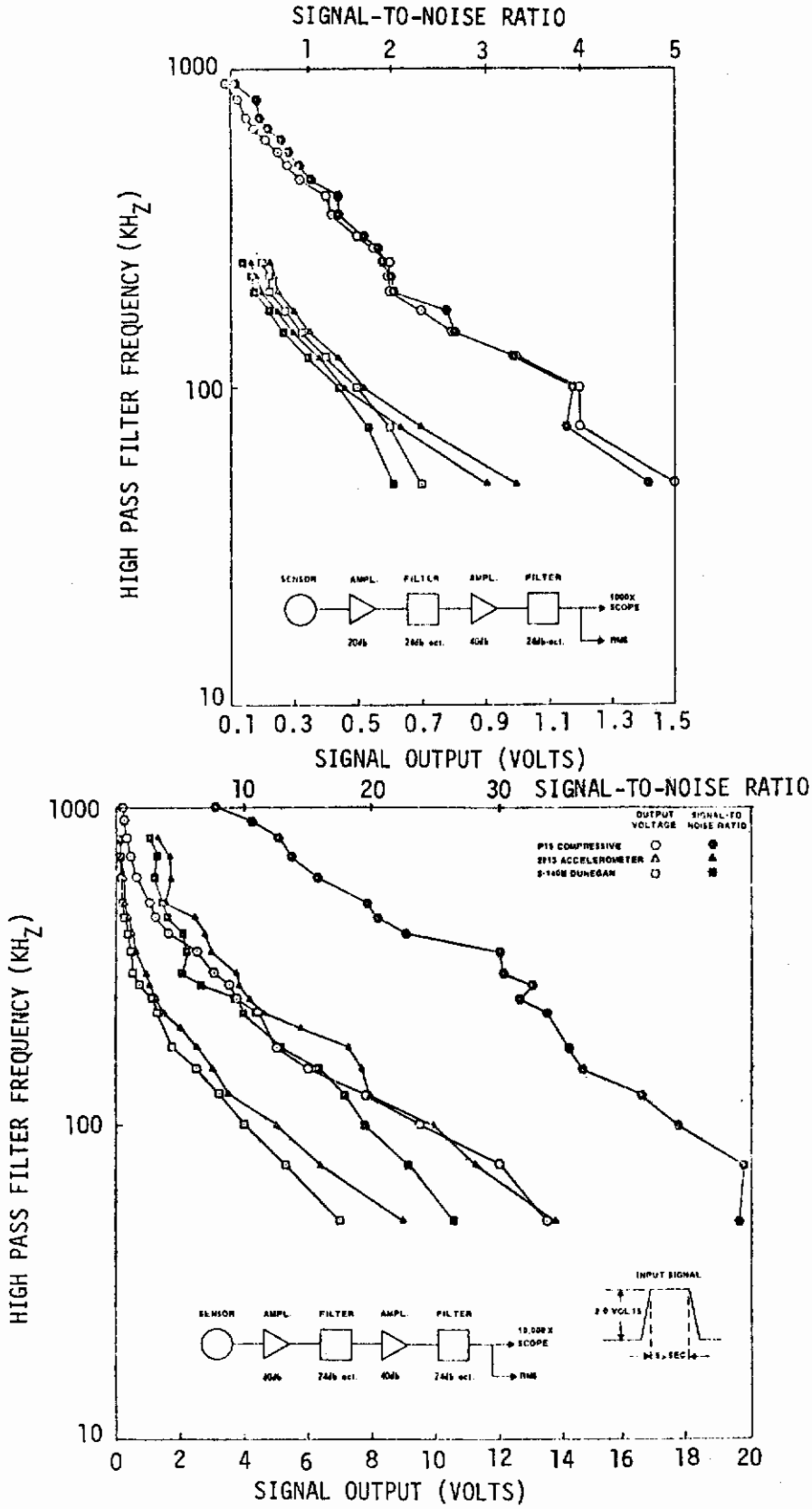

Figure 31. Sensor Output as a Function of High-Pass Filter Frequency and Gain

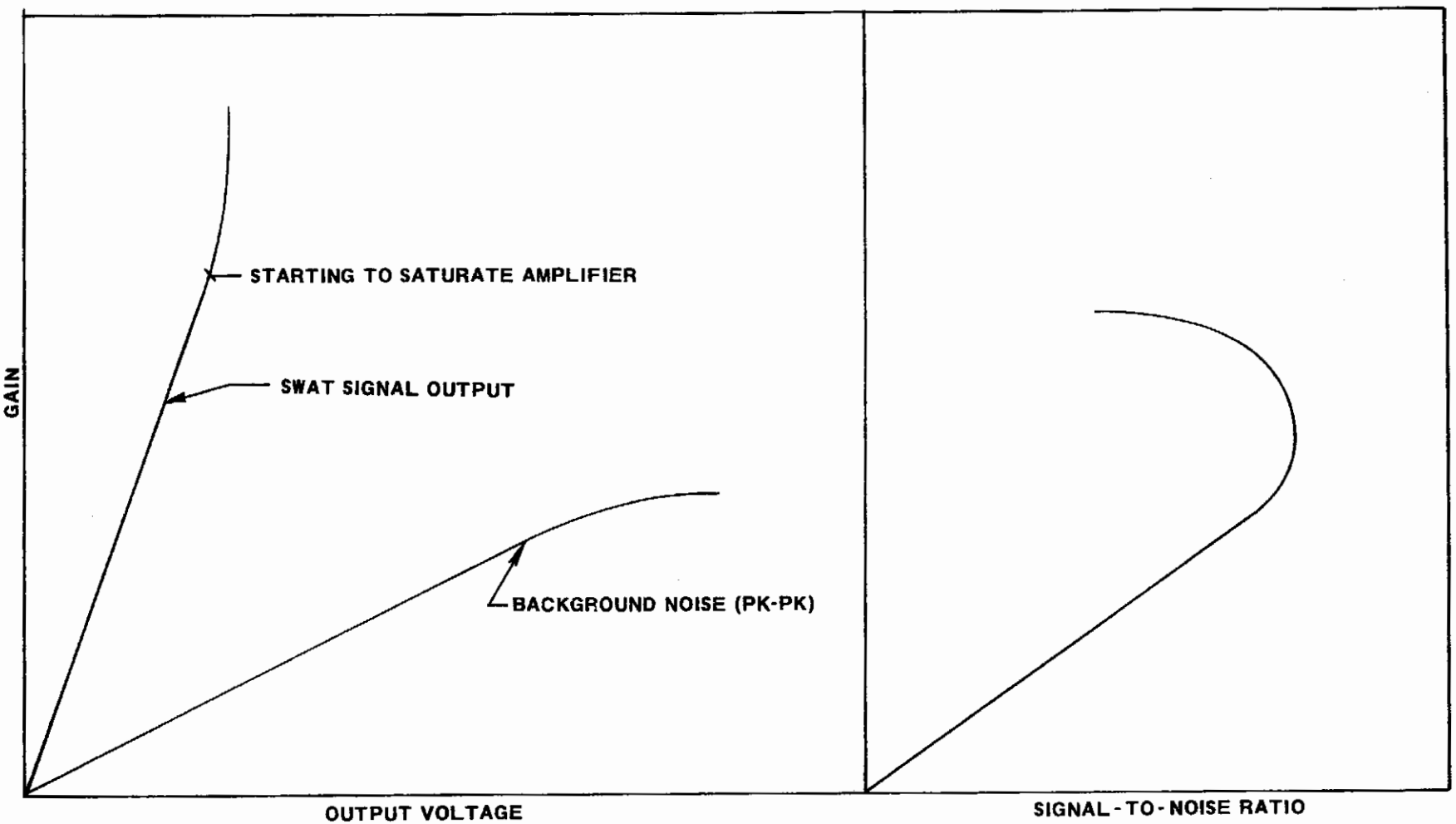

Figure 32. Schematic Showing the Effect of Gain on Output Voltage and Signal-to-Noise Ratio

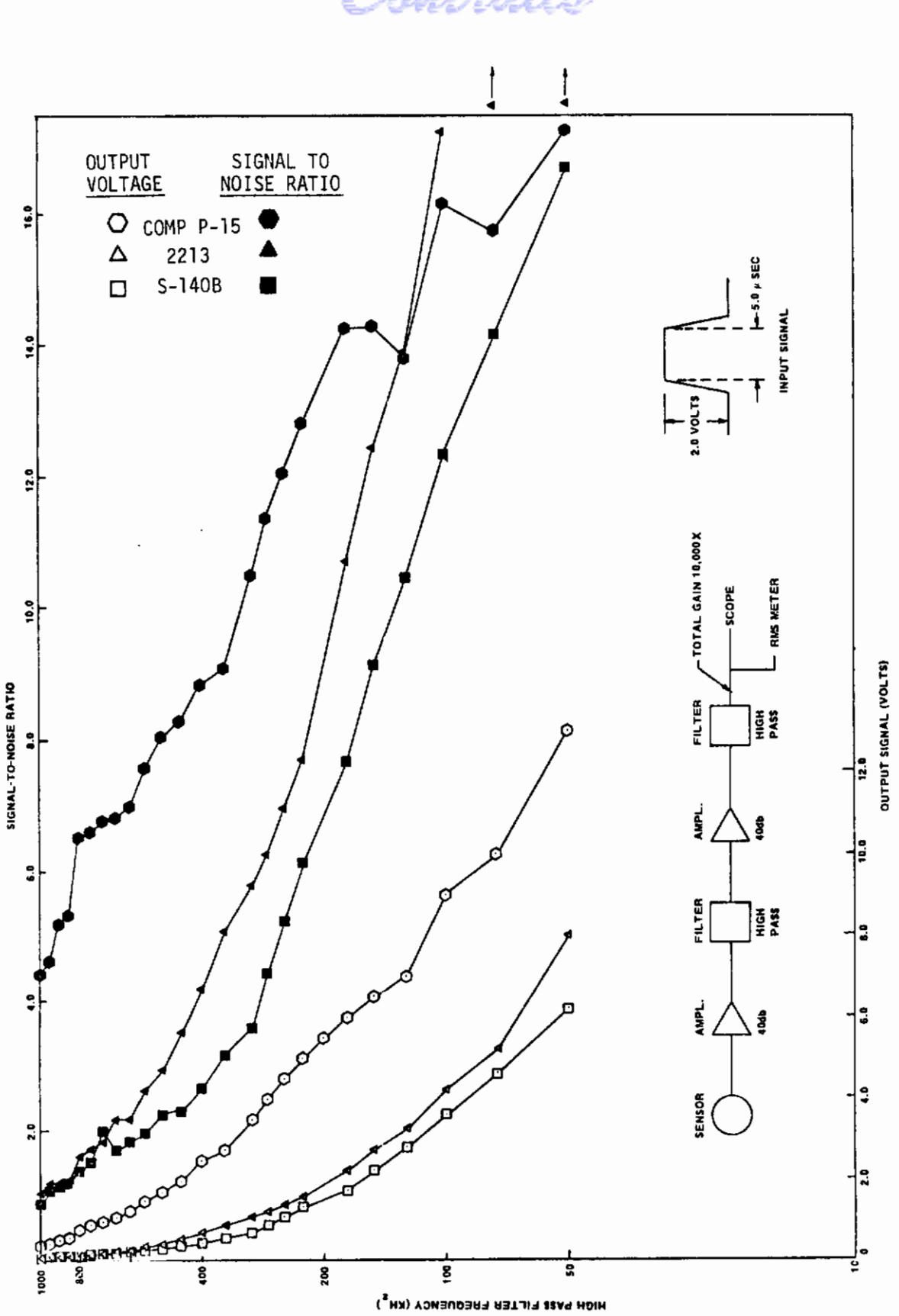

Figure 33. Sensor Output and Signal-to-Noise Ratio as a Function of High-Pass Filter Frequency for Three Sensors

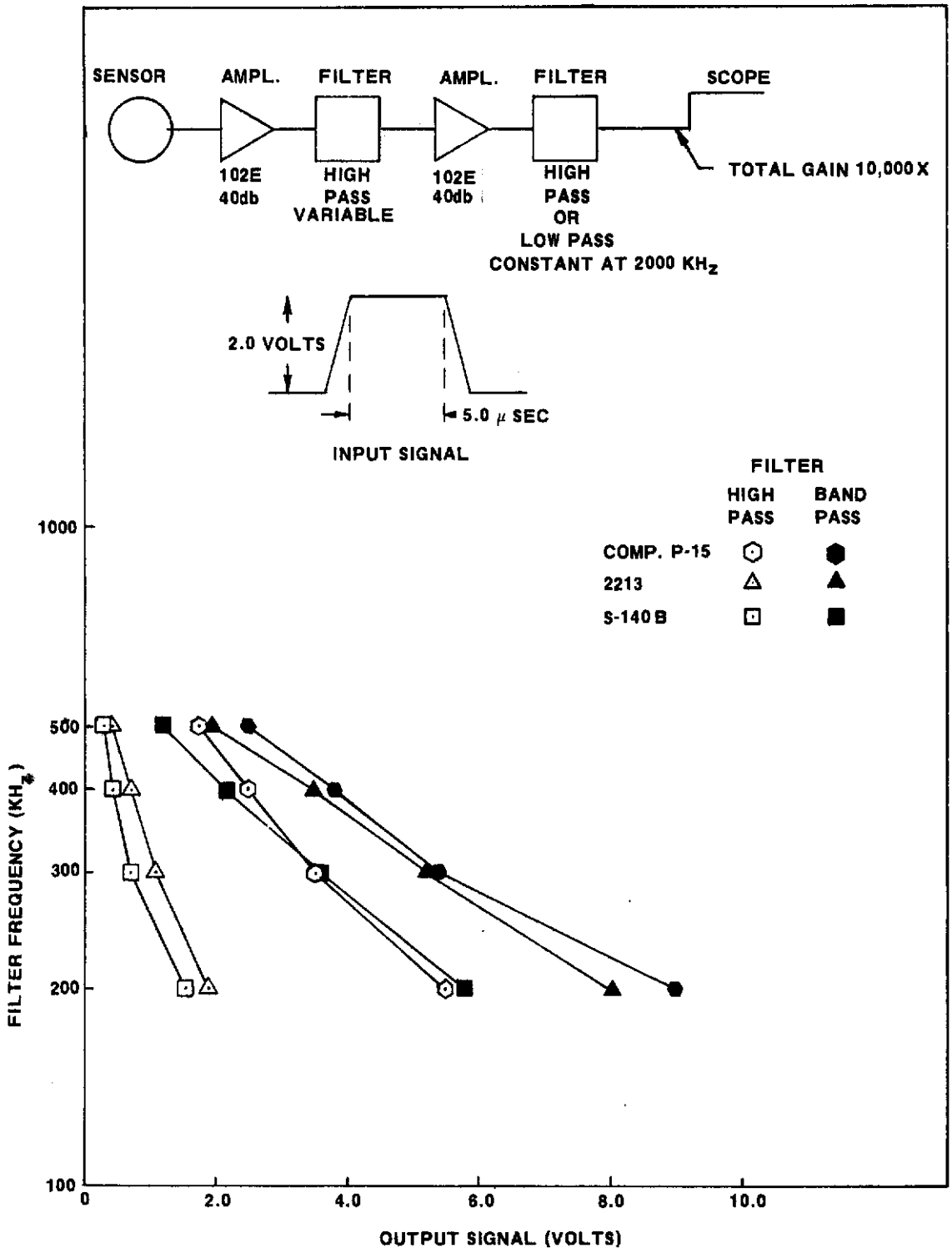

Figure 34. Sensor Output as a Function of Filter Mode for Three Sensors

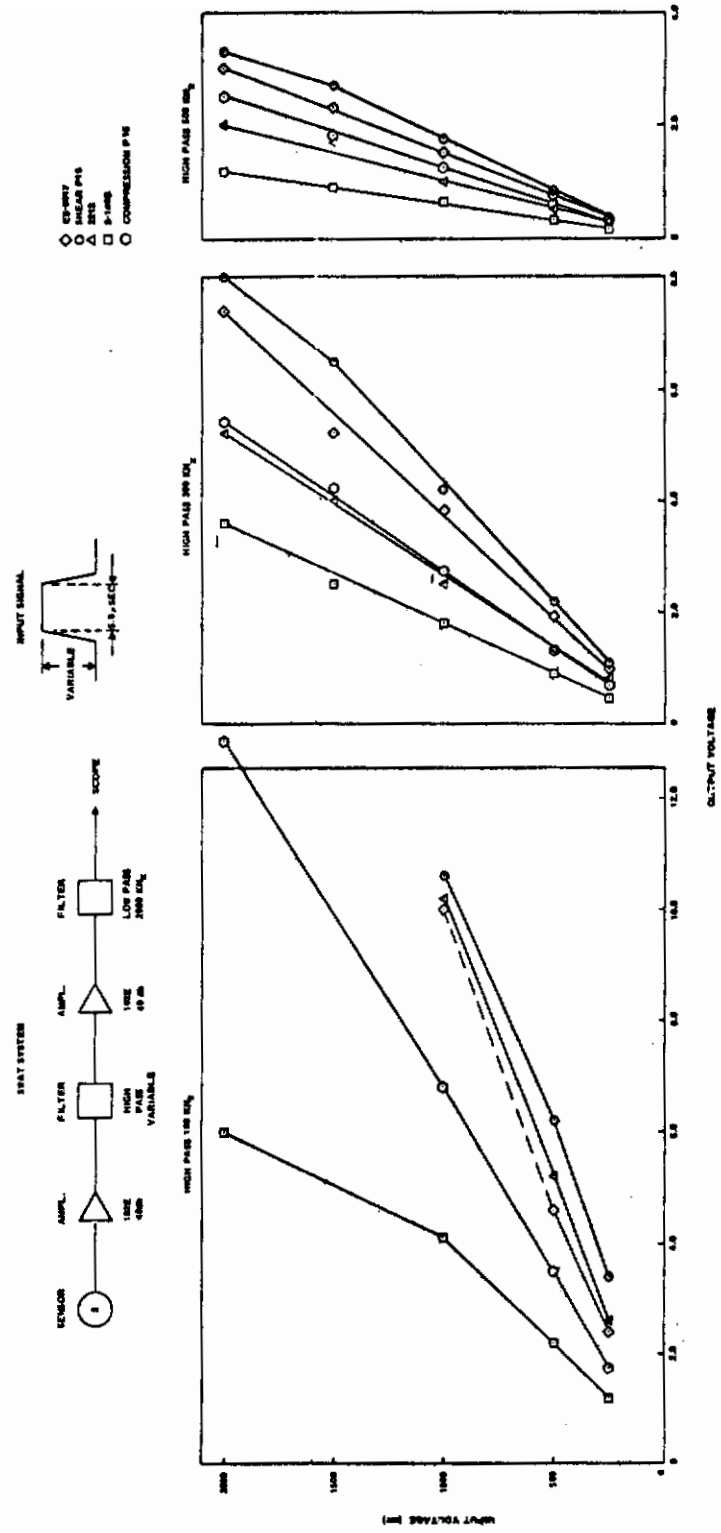

Figure 35. Sensor Output as a Function of Input Voltage and Filter Frequency for Five Sensors

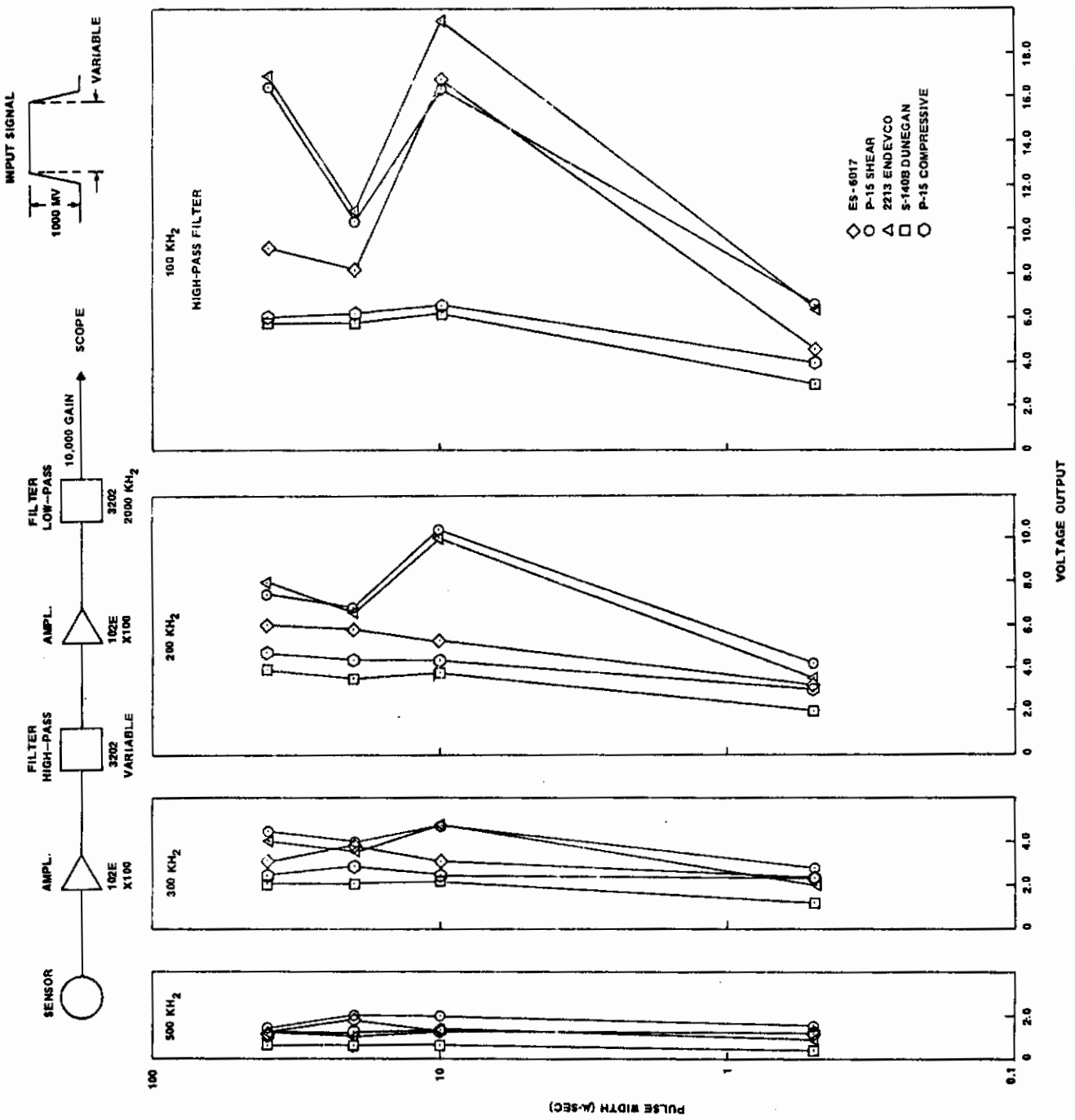

Figure 36. Sensor Output as a Function of Pulse Width and Filter Frequency

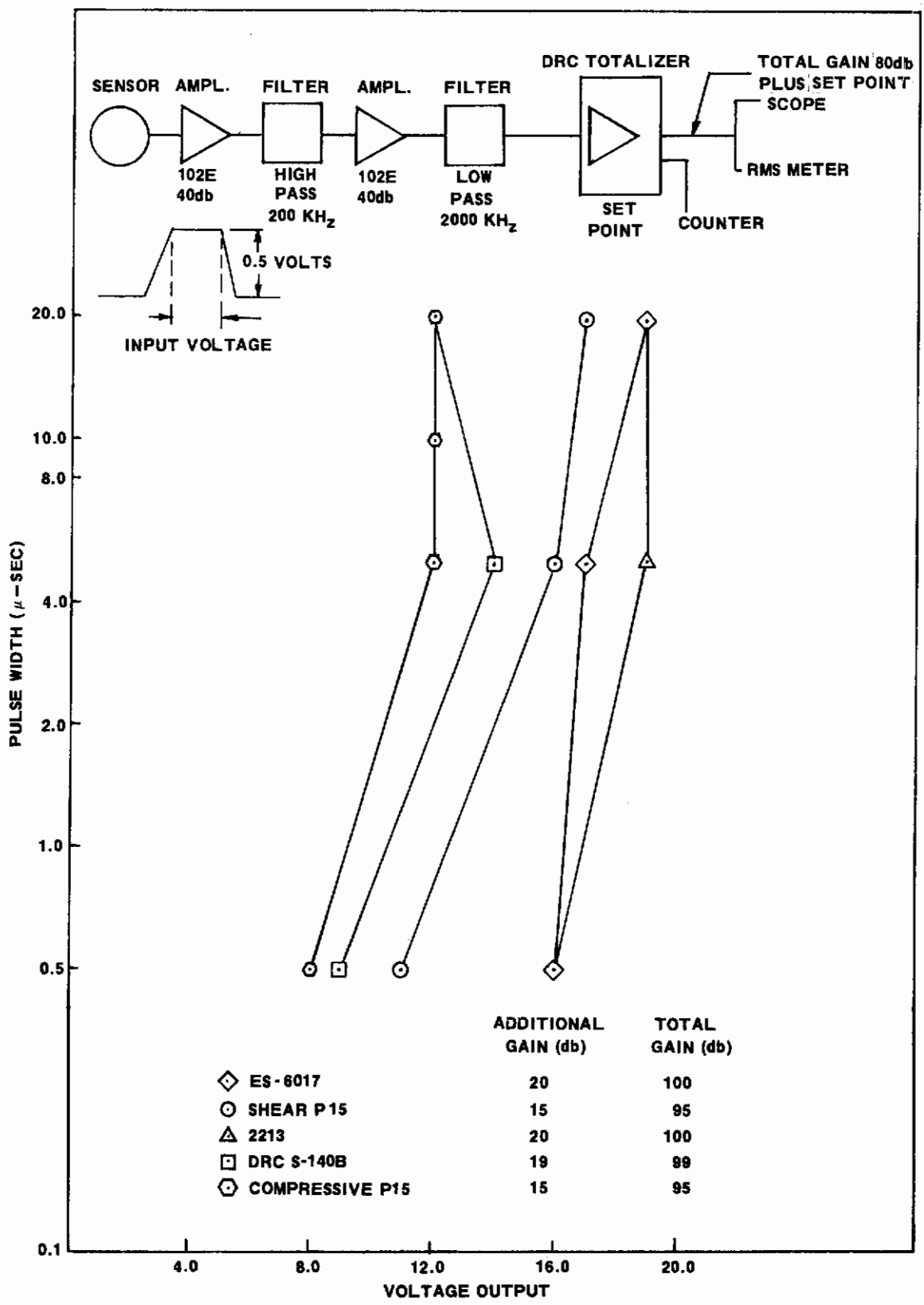

Figure 37. Sensor Output Voltage as a Function of Pulse Width for Five Sensors

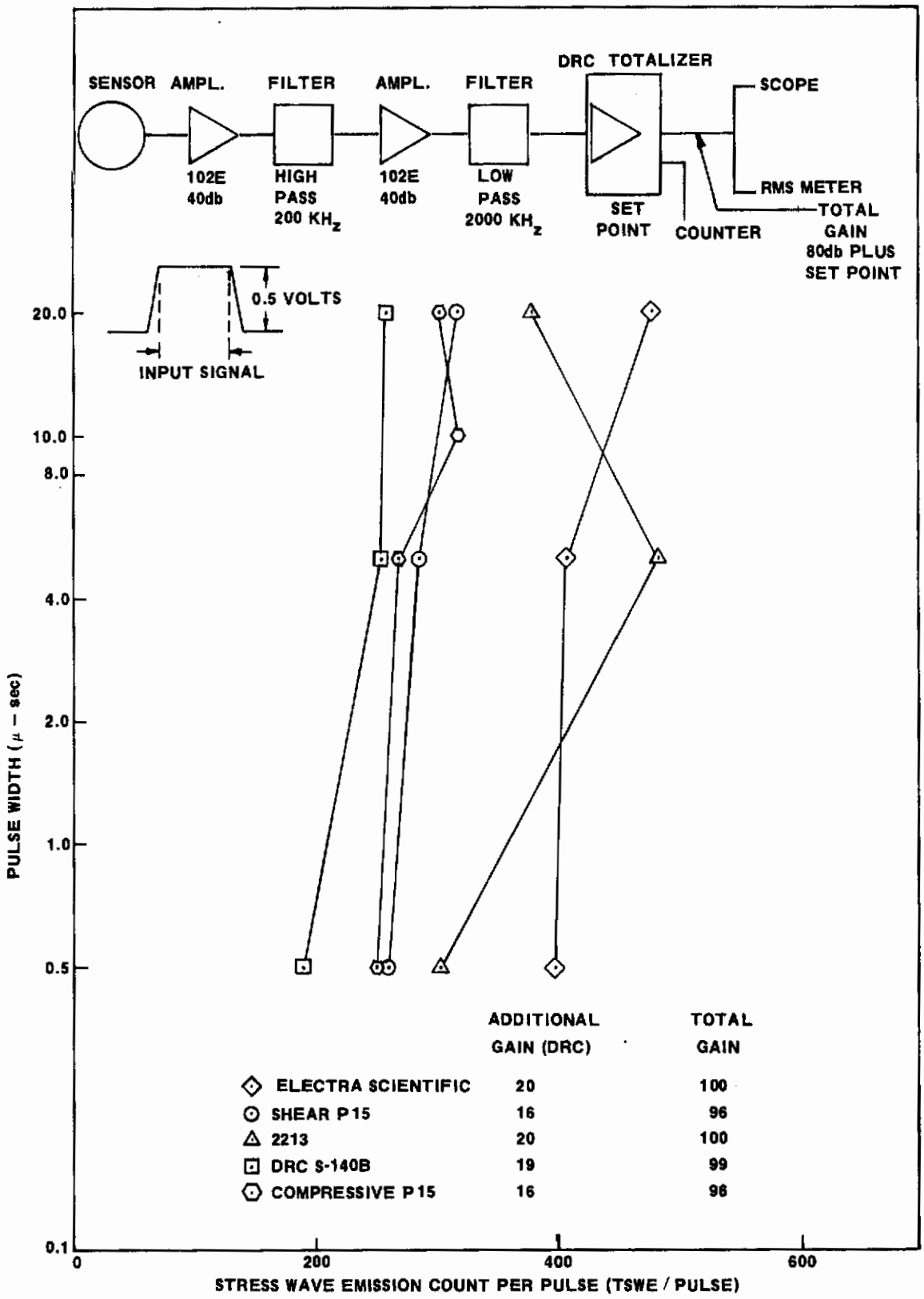

Figure 38. Acoustic Emission Count per Pulse as a Function of Pulse Width for Five Sensors

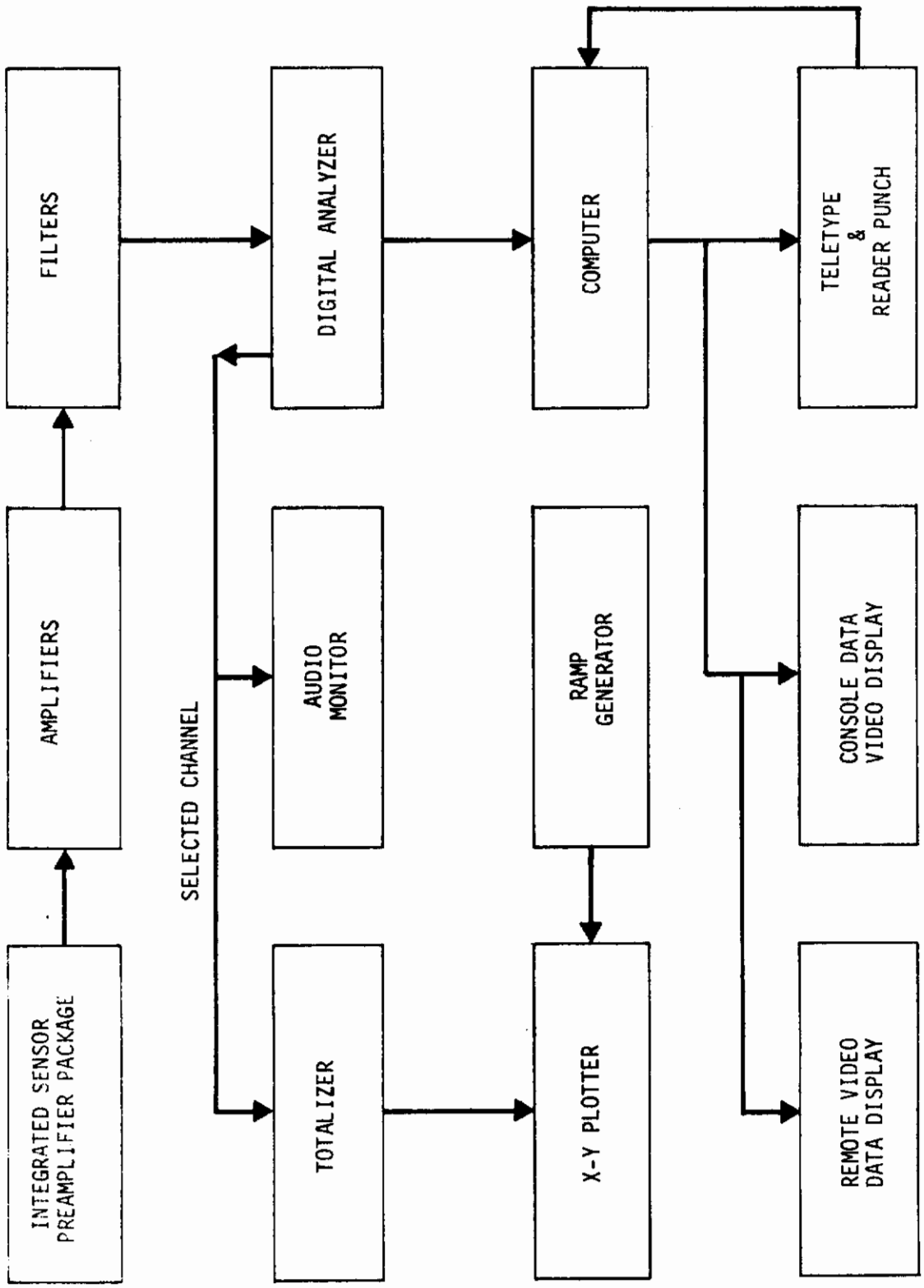

Figure 39. Schematic Diagram - Real Time Acoustic Emission Analysis and Triangulation System

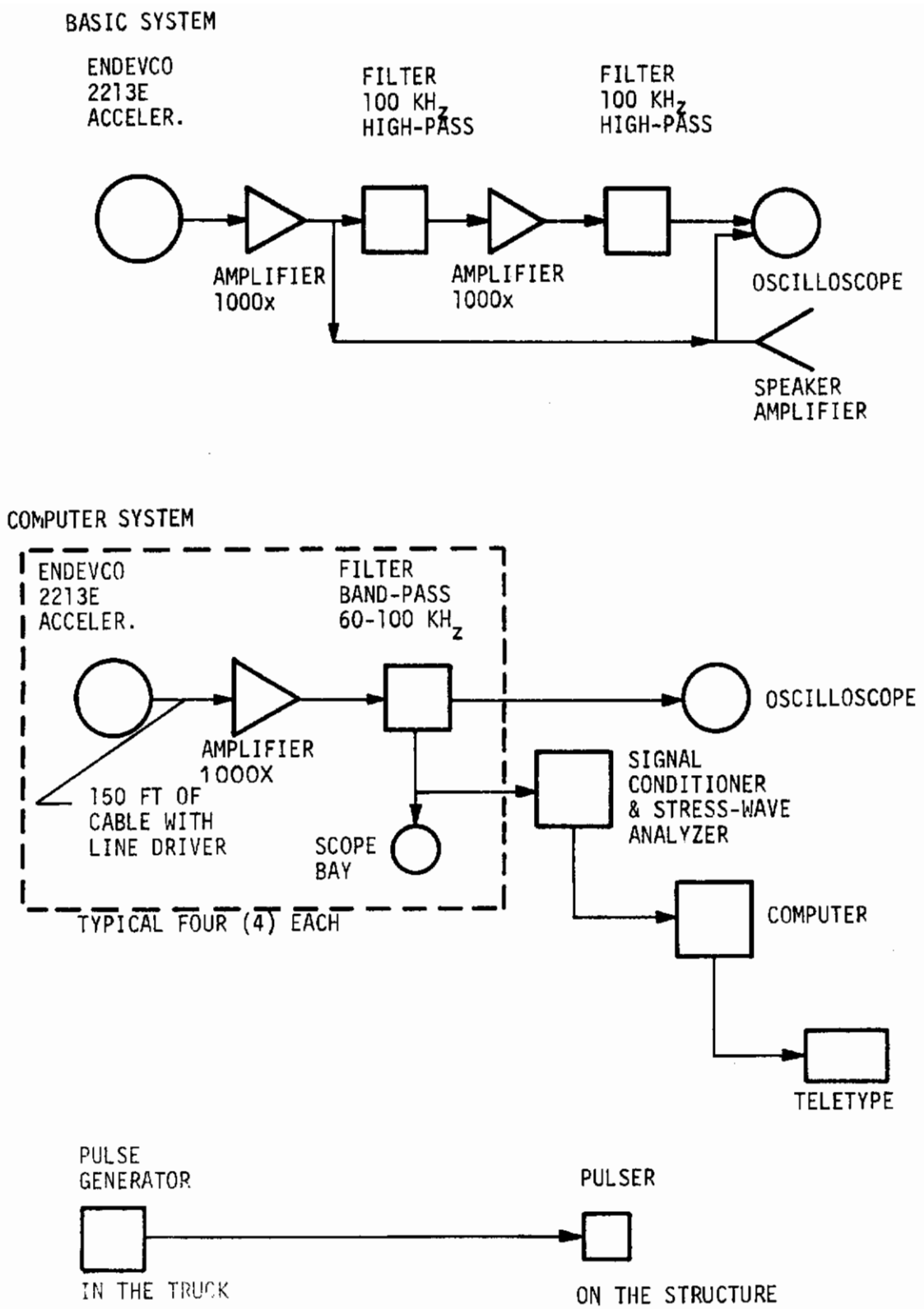

Figure 40. Schematic of the Systems Used in Monitoring a Cracked Girder in a Large Steel Structure

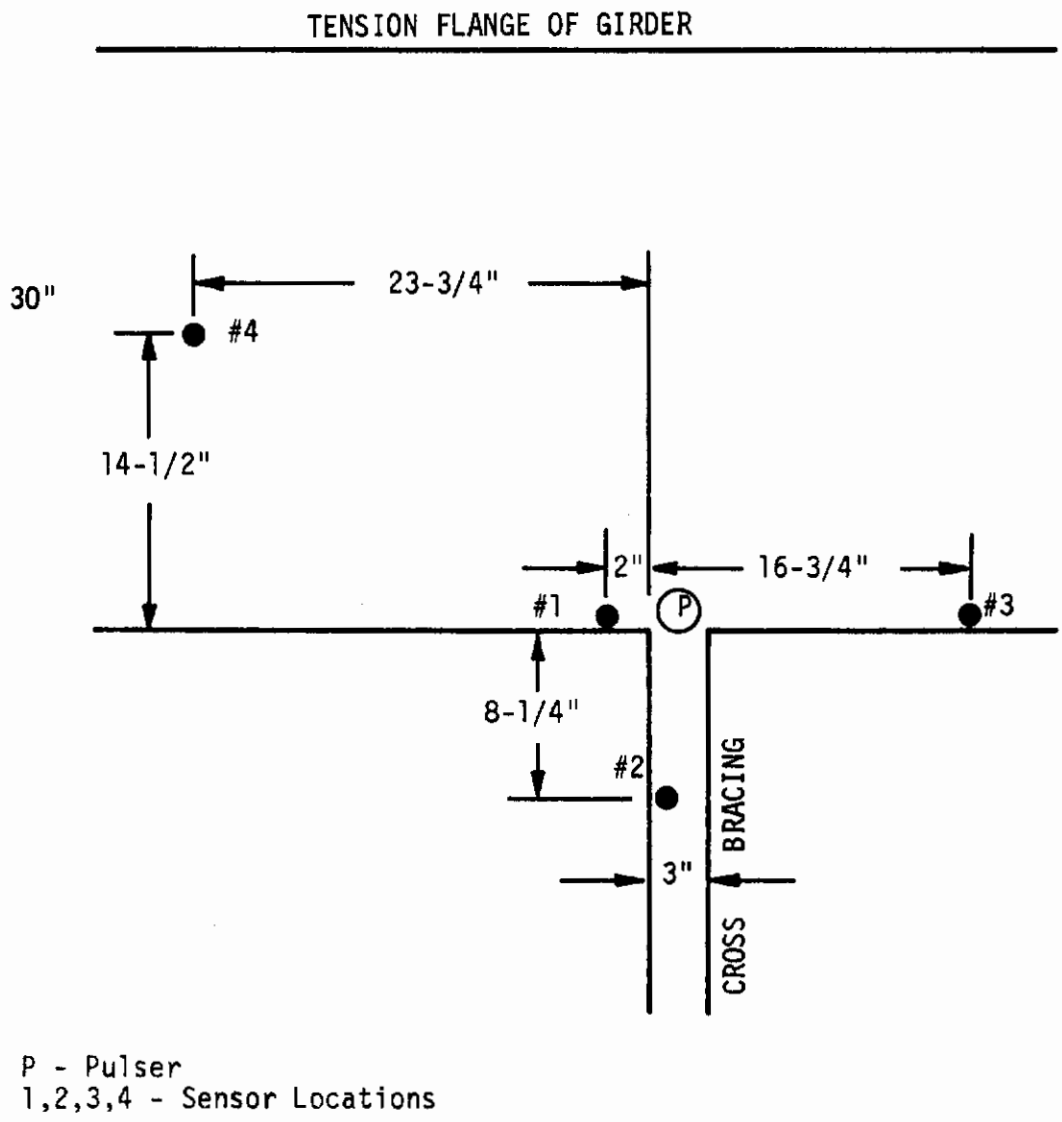

Figure 41. Location of Sensors on a Girder Element Containing a Known Flaw

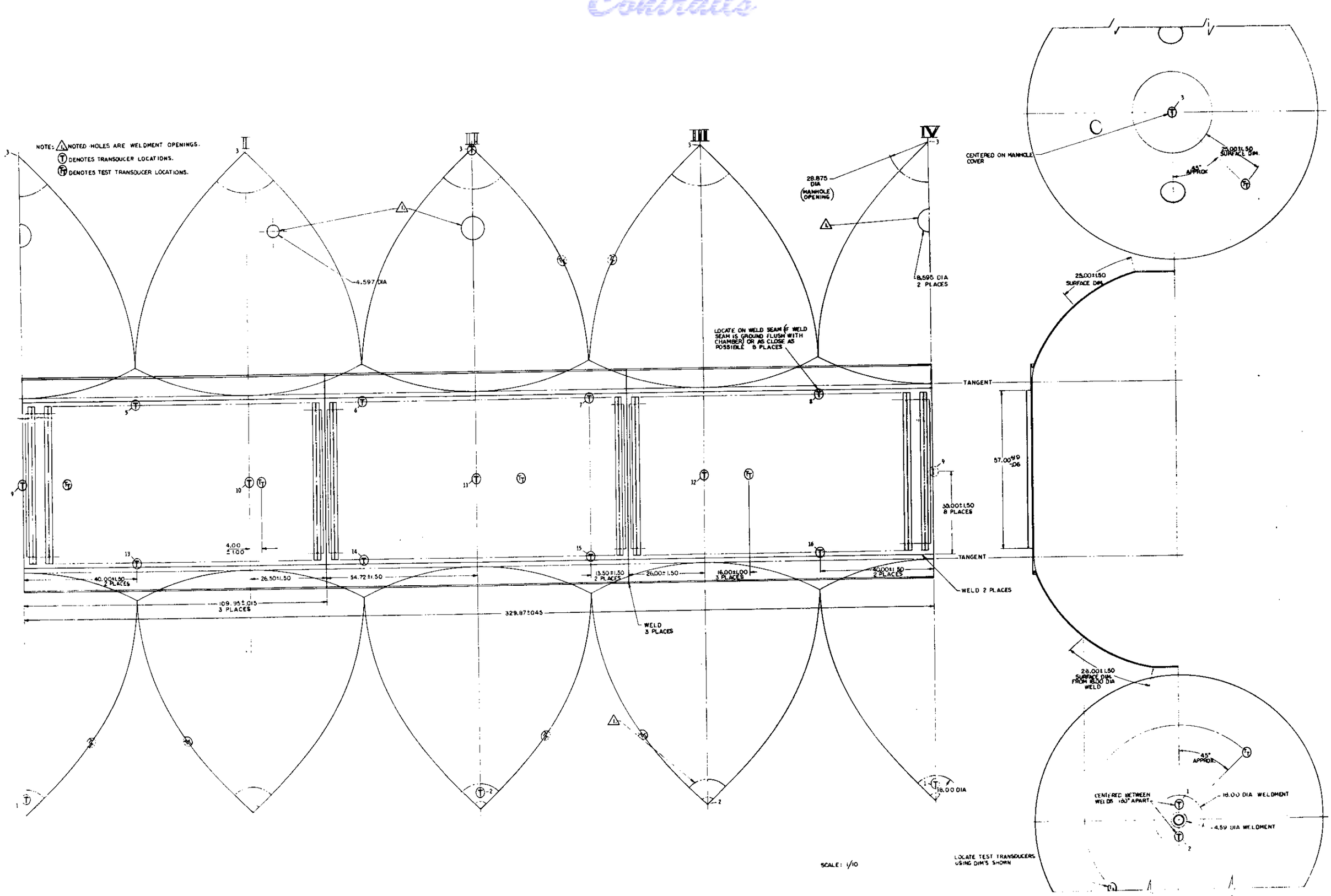

Figure 42. Transducer Locations and Video Display for Hydrogen Fuel Tank

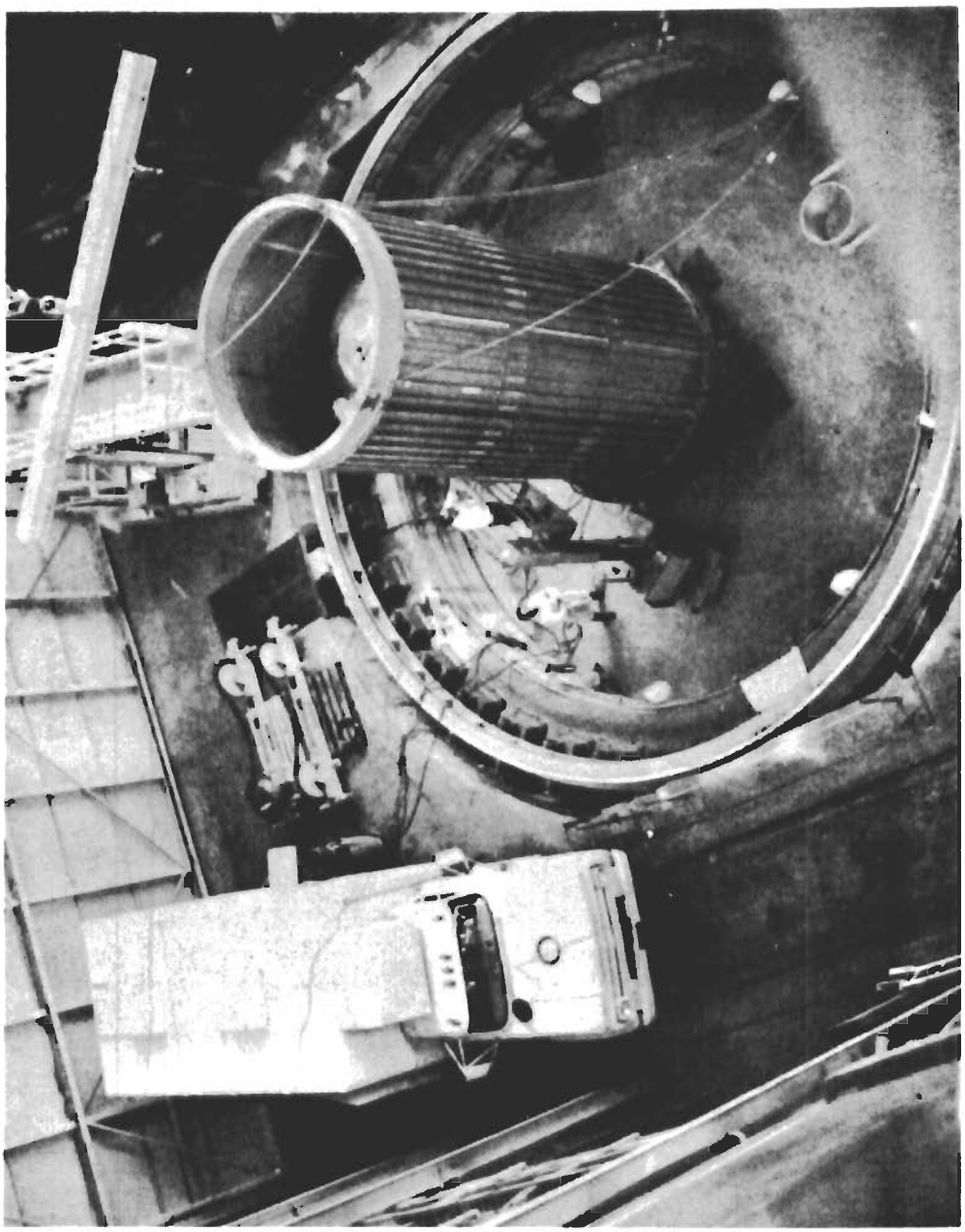

Figure 43. Van and Pressure Vessel Prior to Test

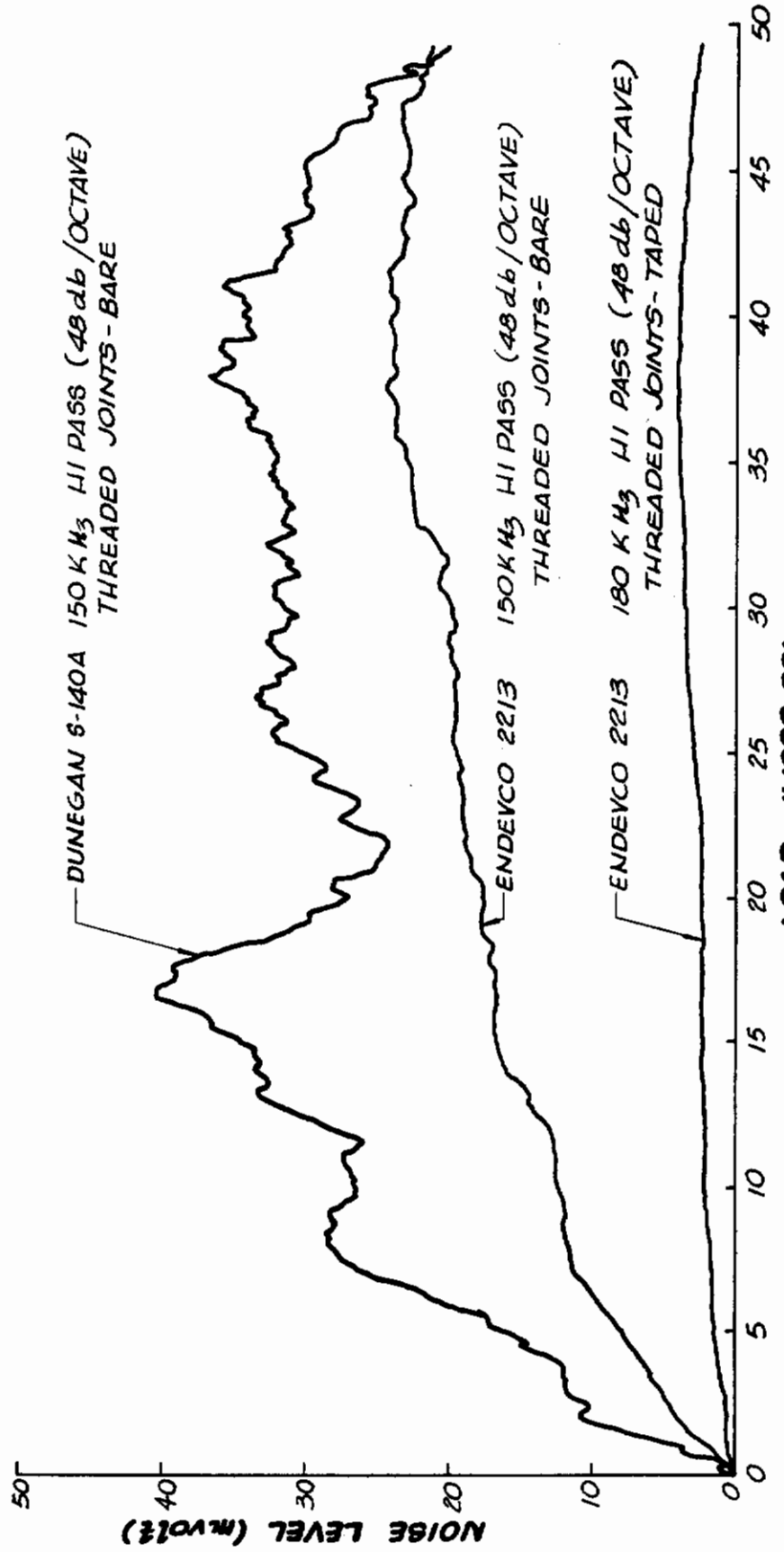

Figure 44. Test Machine Noise Versus Load

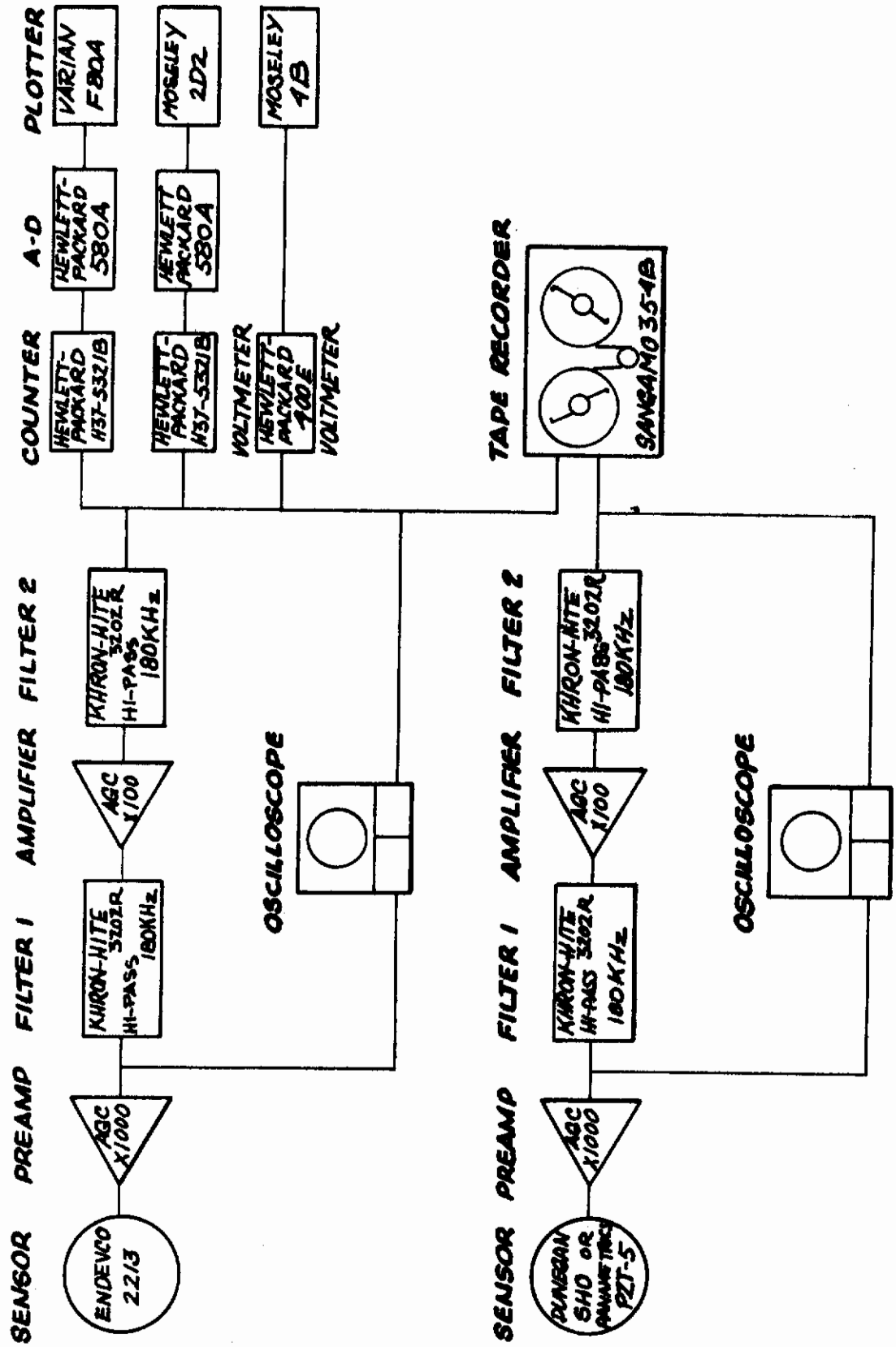

Figure 45. Instrumentation System for Fracture Testing

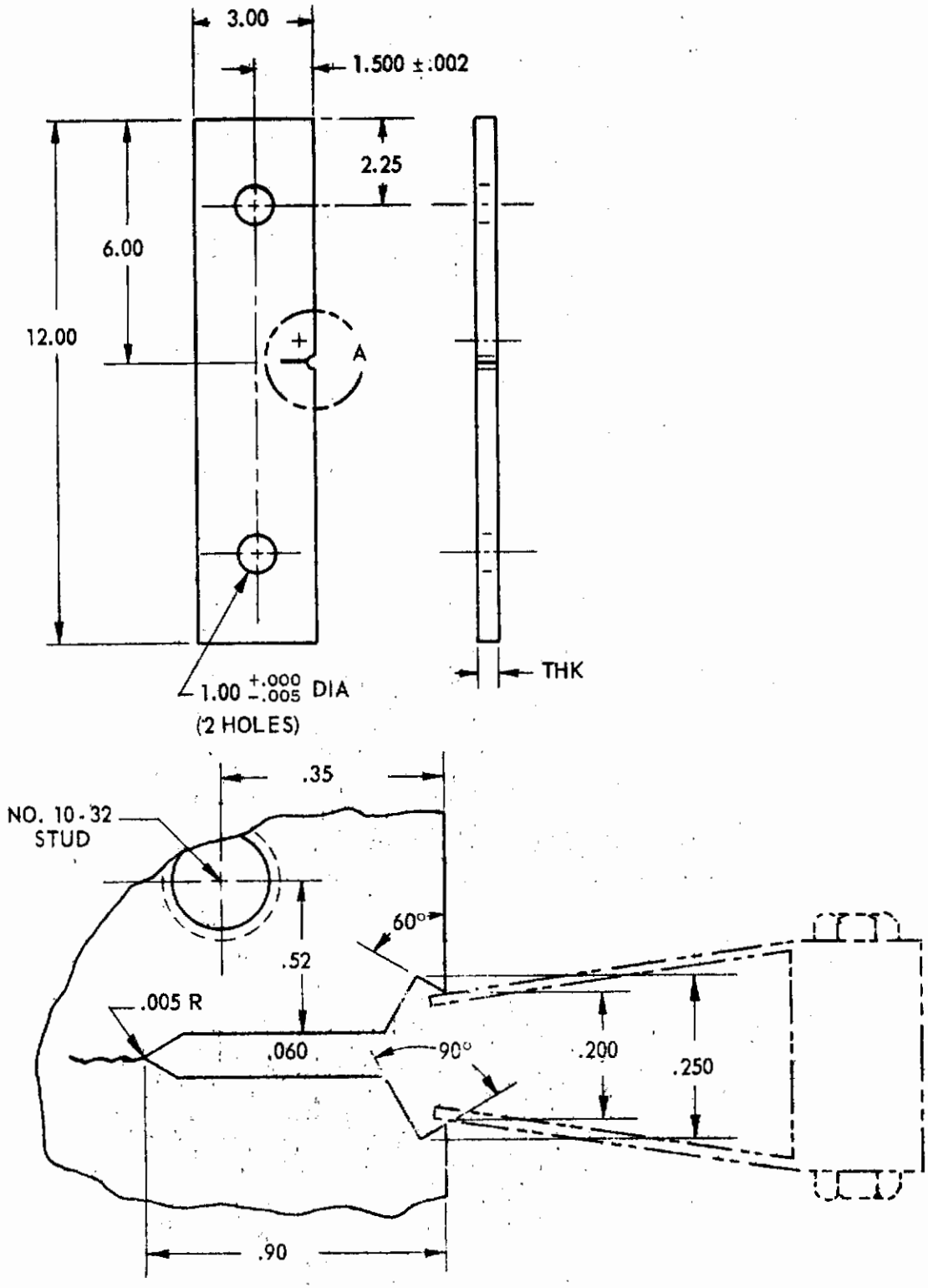

Figure 46. Single-Edge-Notch Specimen and Crack Opening Displacement Gage

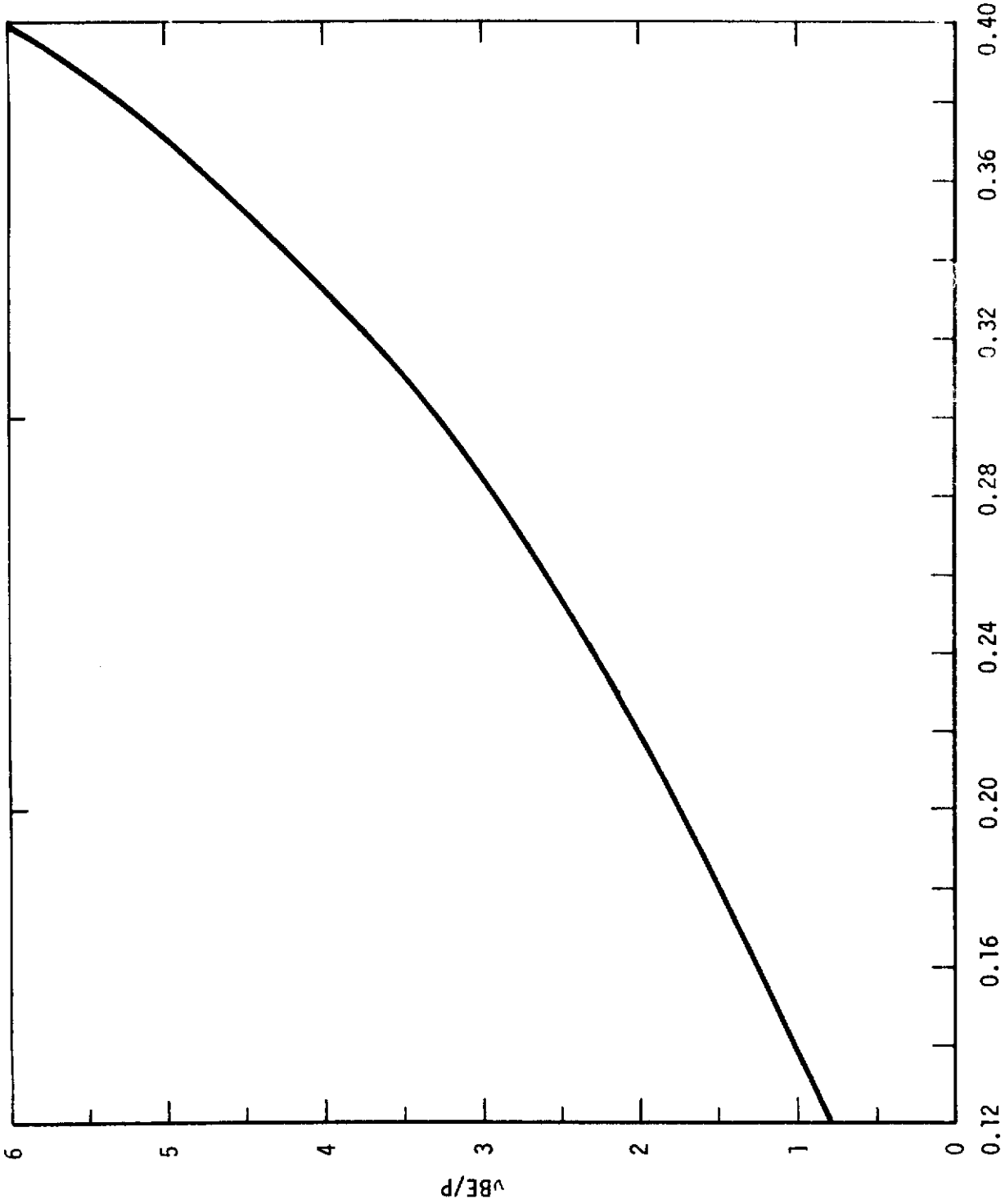

Figure 47. Calibration Curve for Crack-Opening Displacement Gage Mounted on SEN Tensile Specimen

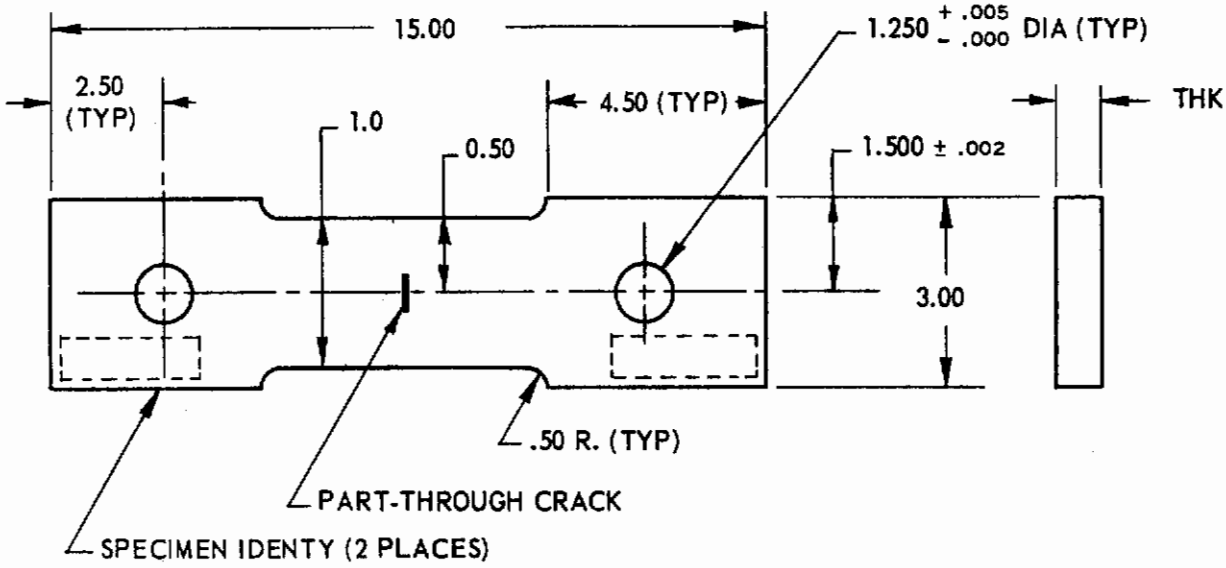

Figure 48. Part-Through-Crack (PTC) Tension Specimen

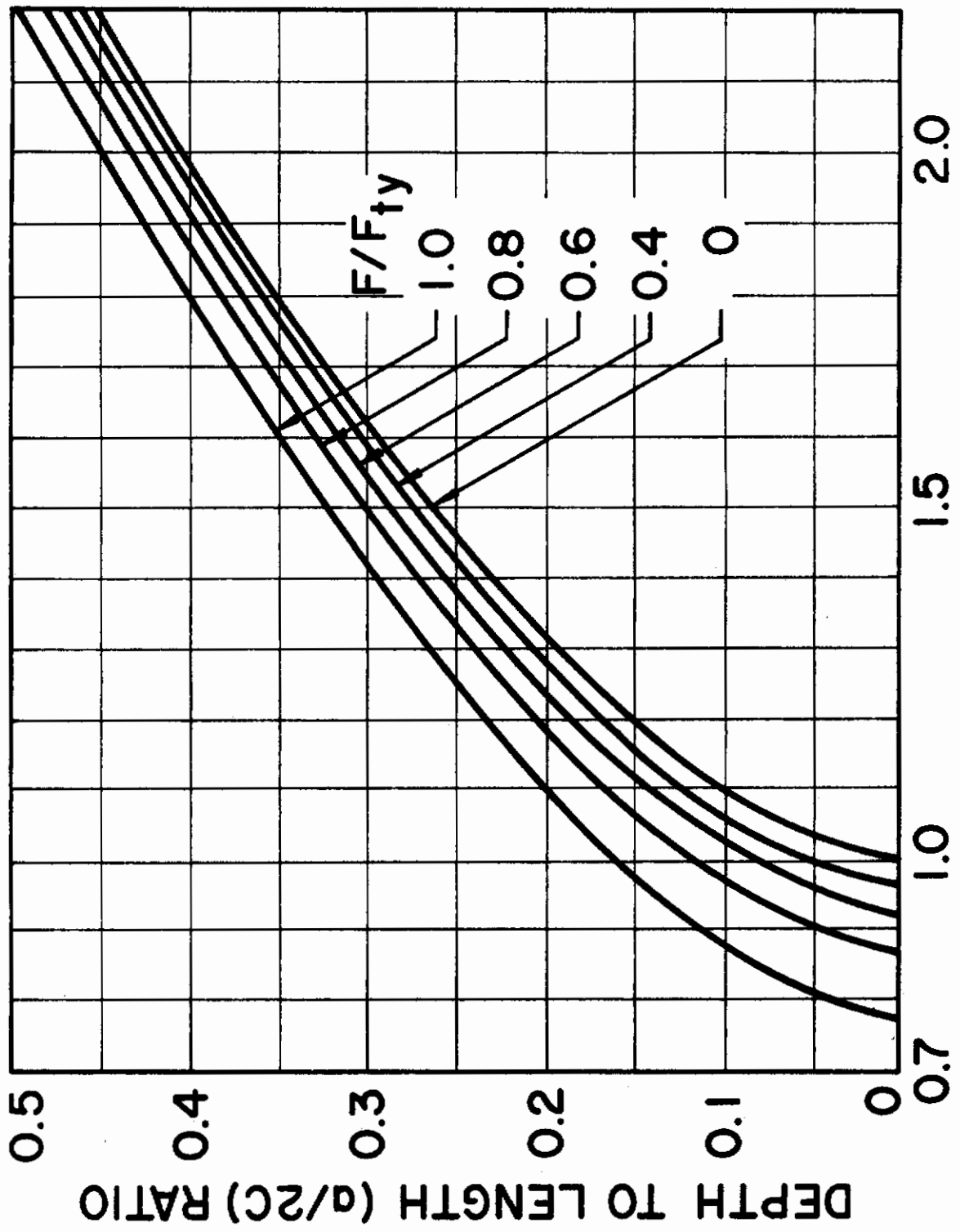

Figure 49. Flaw Shape Parameters, Q, for Surface and Embedded Flaws

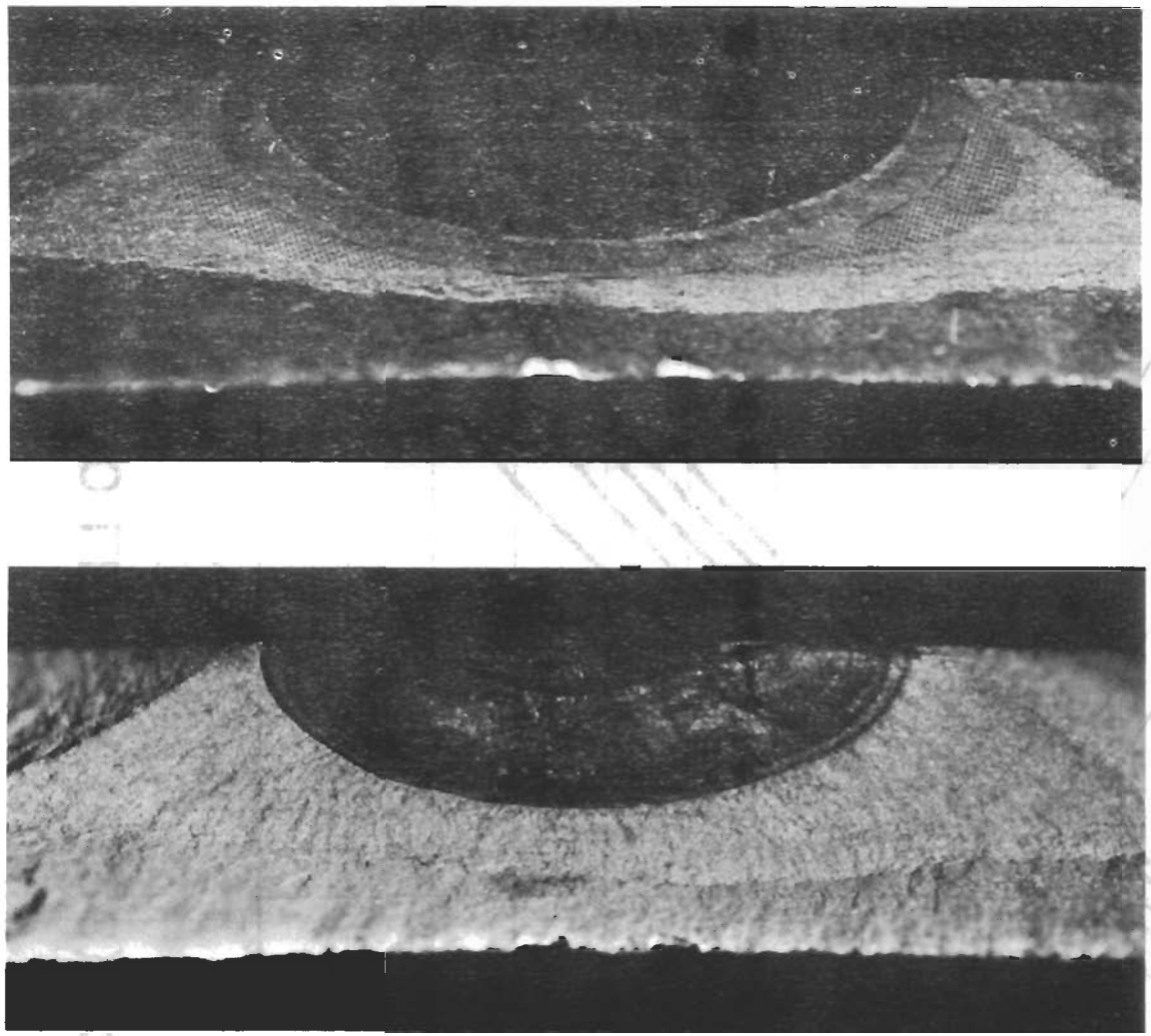

POLARIZED LIGHT:

Black Area,
Fatigue Precrack

Dark Area,
Fatigue Crack Growth

Stippled Area,
Suspected Crack Growth

PHOTOGRAPHED WITHOUT
POLARIZED LIGHT.

Figure 50. Low Cycle Fatigue Crack Growth - 6Al-4V Titanium PTC Specimen E-5

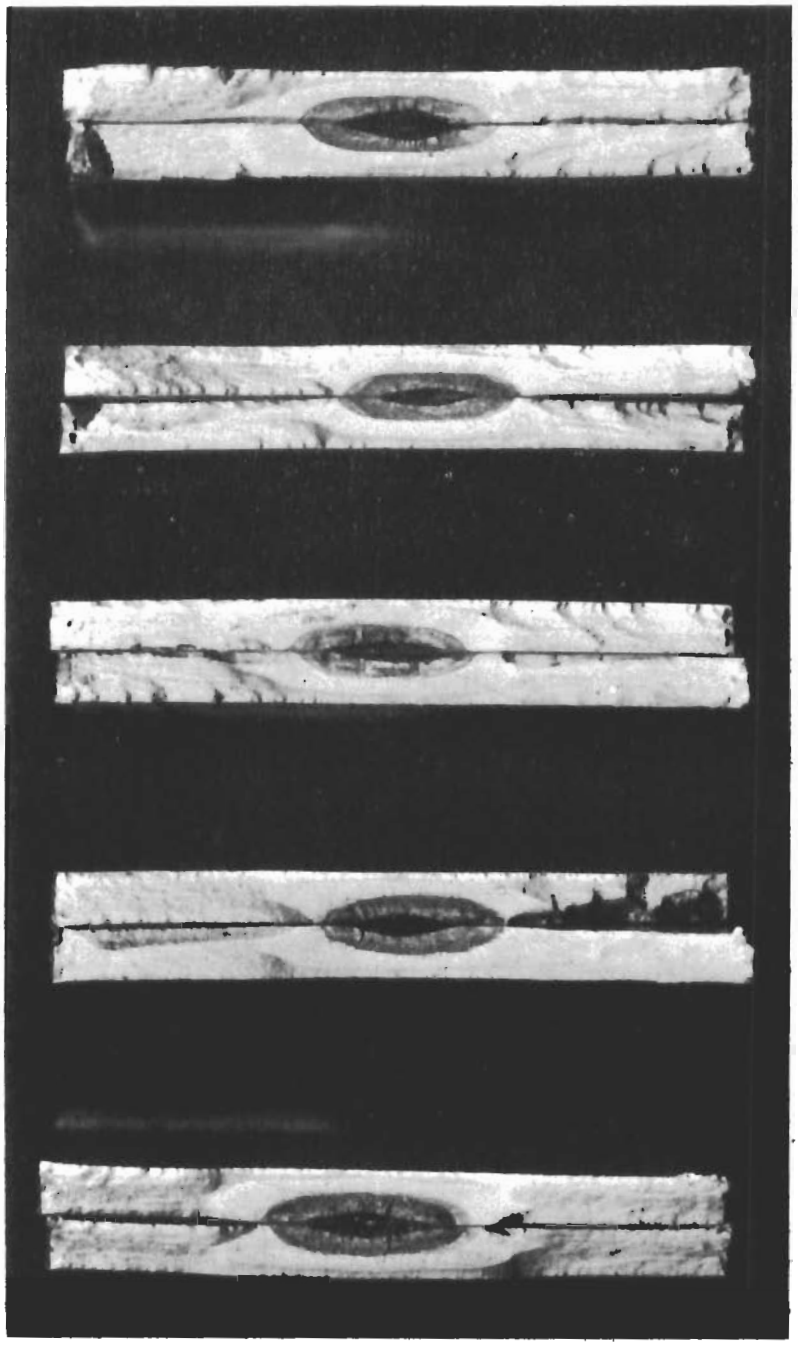

Figure 51. Part-Through-Crack Fracture Surfaces - Illustrating Crack Growth Beyond Fatigue Starter Flaw - Titanium STA 0.1 in.

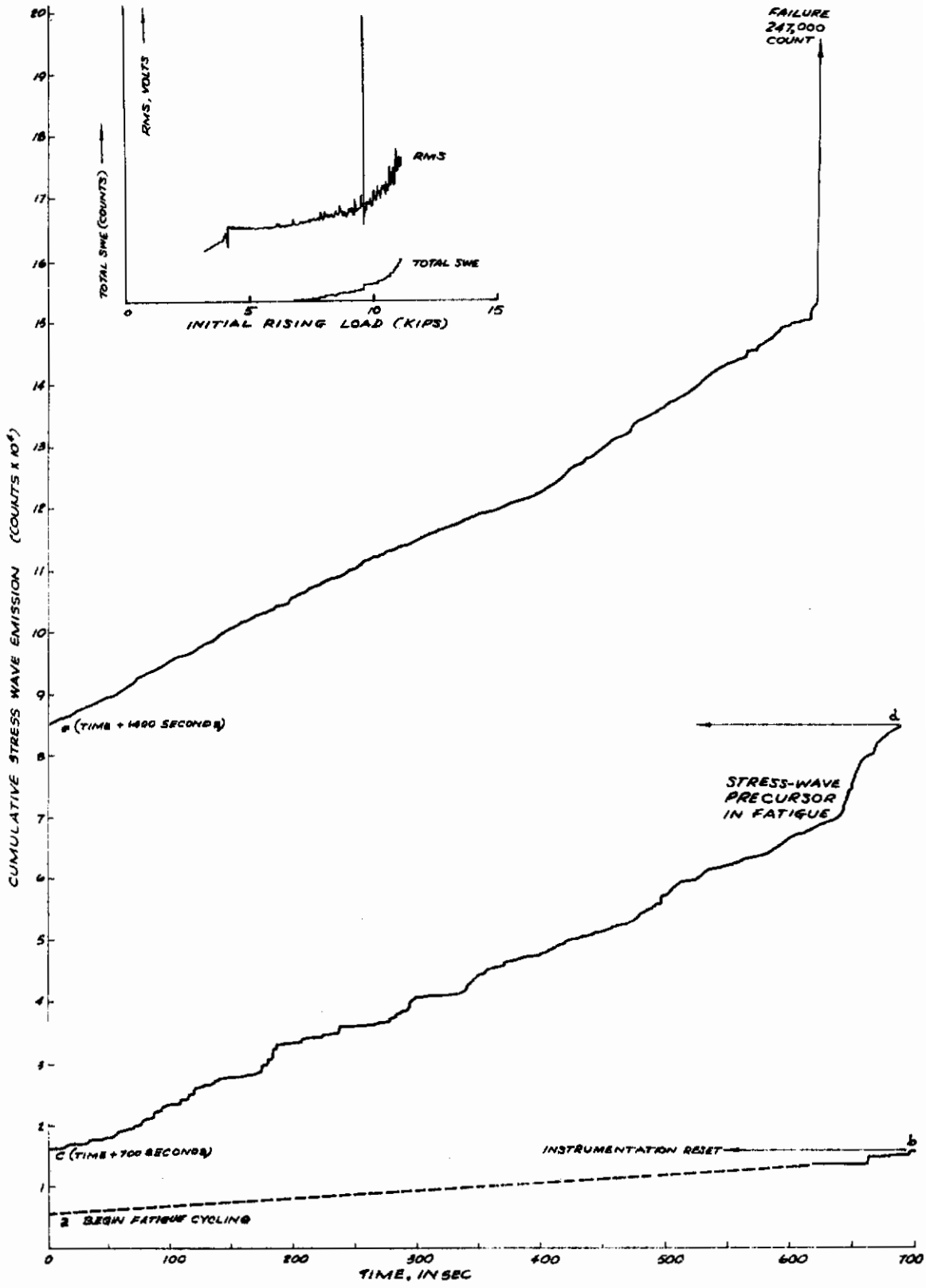

Figure 52. Total Stress Wave Emission - Fatigue Cycling PTC Specimen SP-16 6Al-4V Titanium STA 0.1 in.

Unpolarized Light

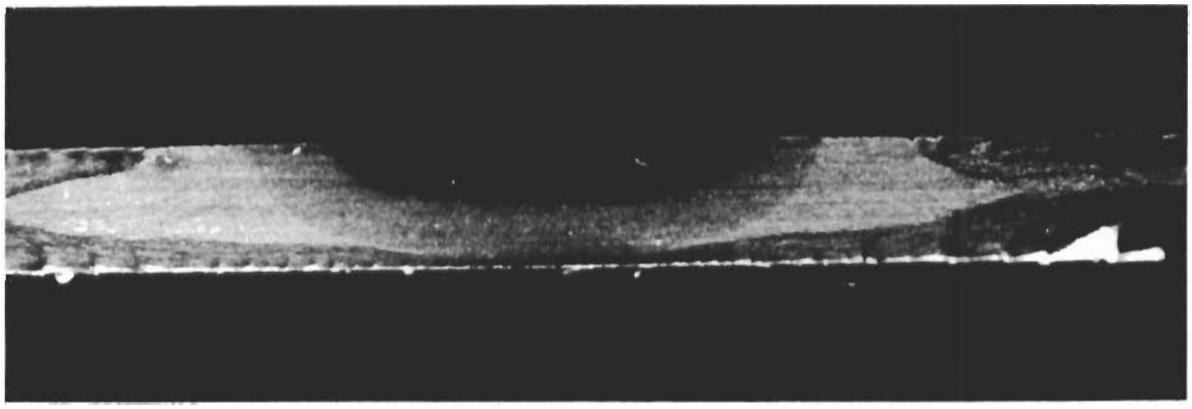

Polarized Light

Figure 53. Low Cycle Fatigue Crack Growth in STA 6Al-4V Titanium PTC Specimen SP-16

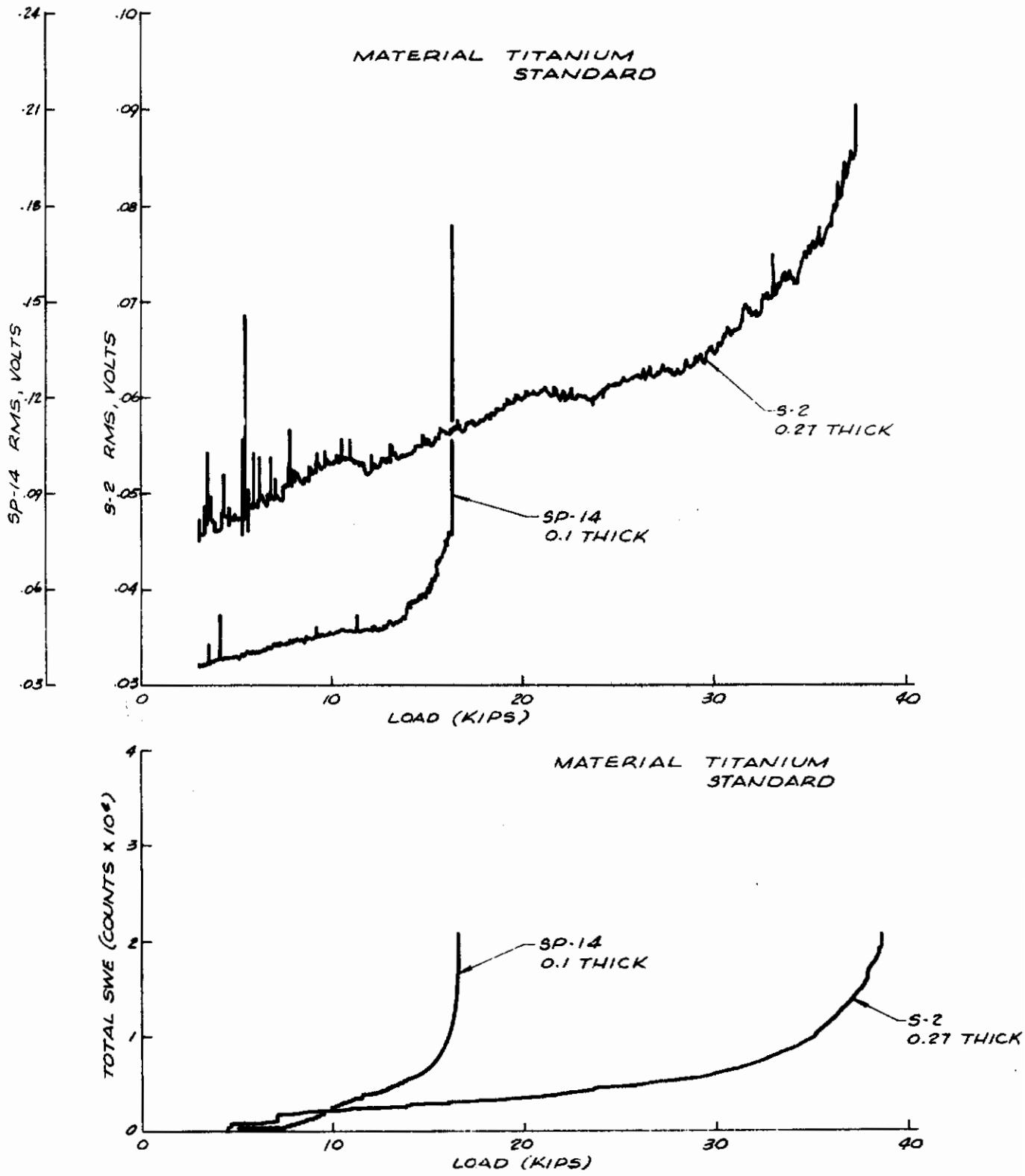

Figure 54. Signal Level and Total Stress Wave Emission - Titanium STA - PTC Specimen

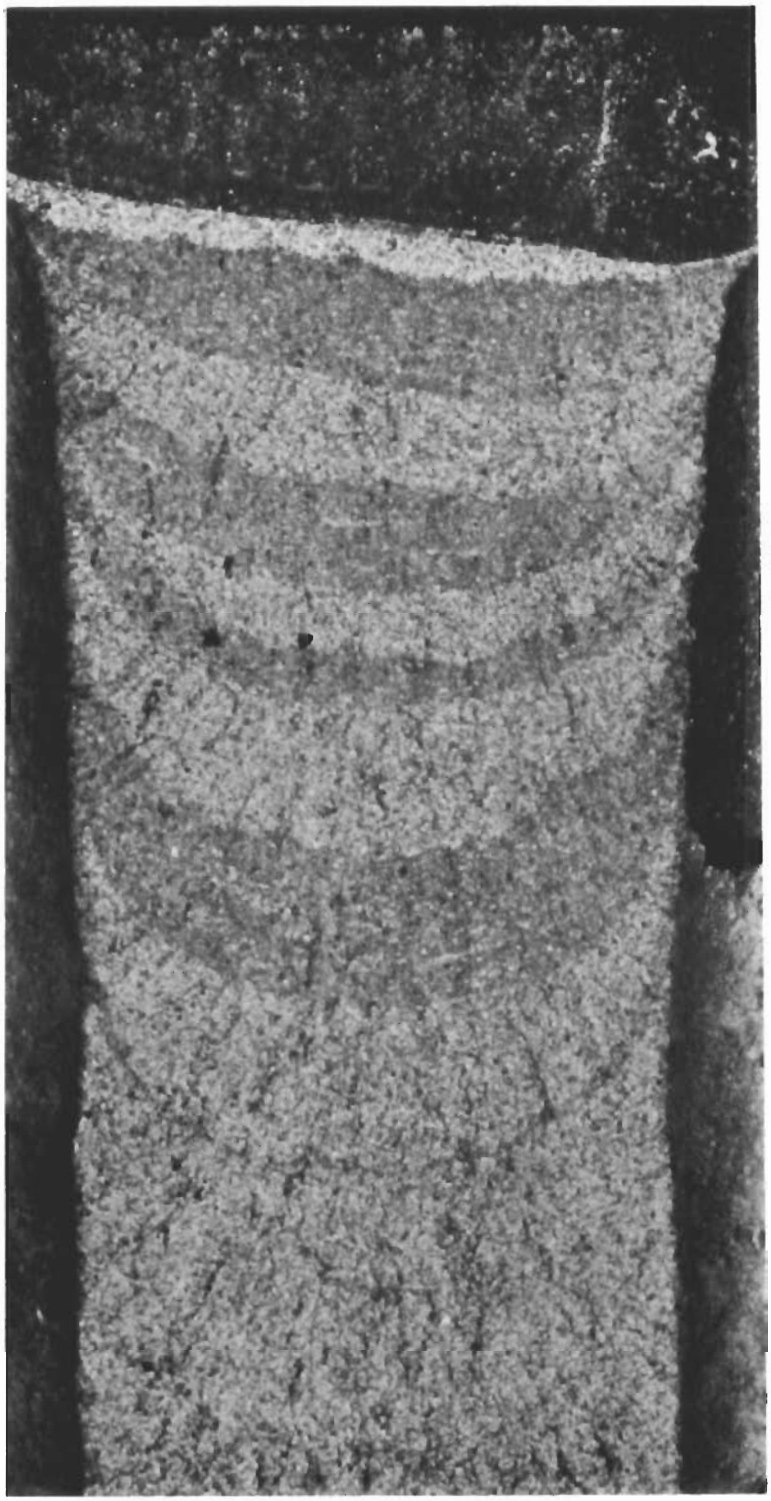

Figure 55. Fracture Markings in SEN-Tension Specimen S3-3 Showing Regions of Slow Crack Growth and Pop-in

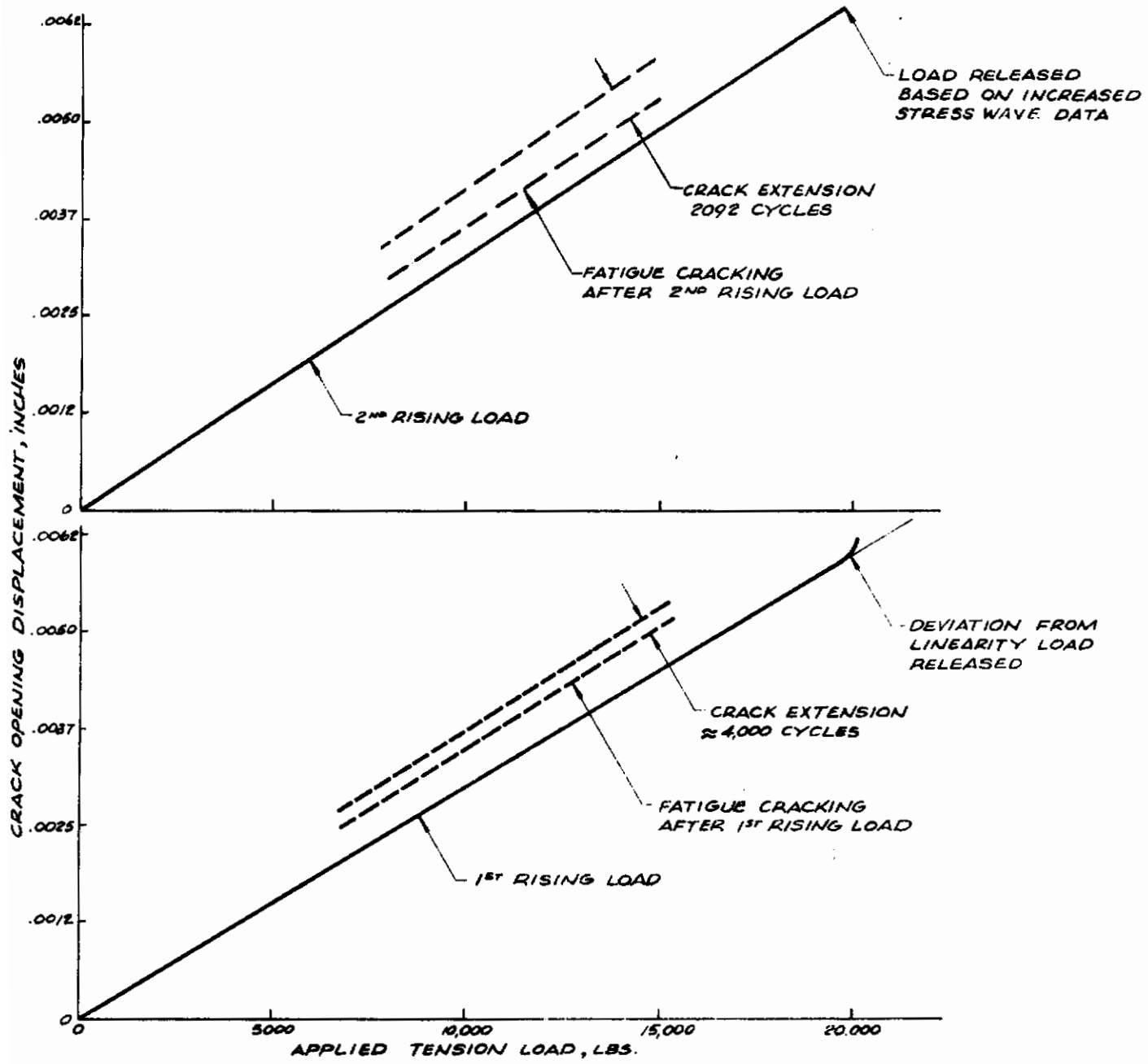

Figure 56. Crack Opening Displacement 1st and 2nd Cycle Rising Load and Intermediate Fatigue Cycling - SEN Specimen S3-5 D6aC 600°F 0.29 in.

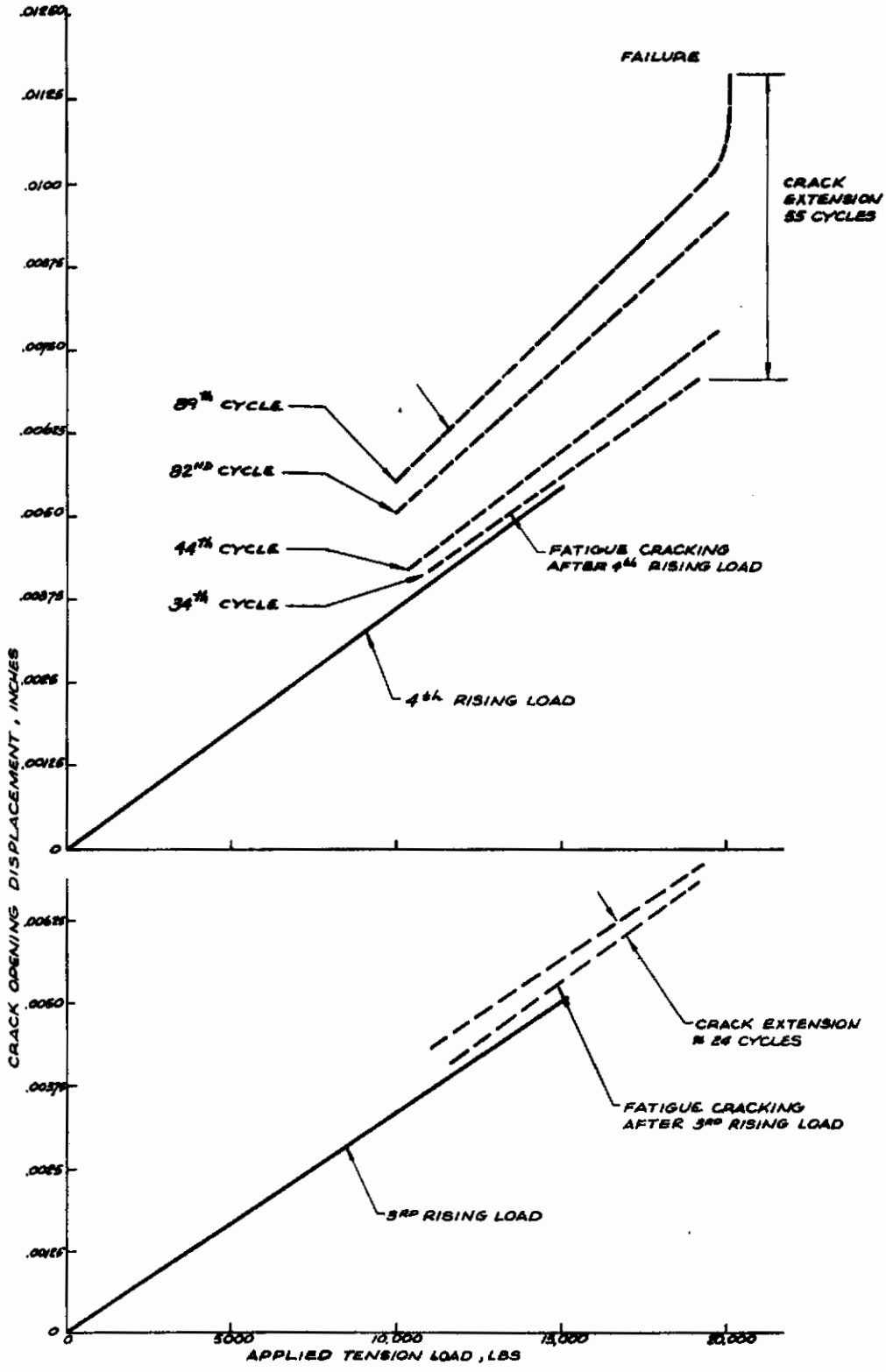

Figure 57. Crack Opening Displacement 3rd and 4th Cycle Rising Load and Intermediate Fatigue Cycles - SEN Specimen S3-5 D6aC 600°F 0.29 in.

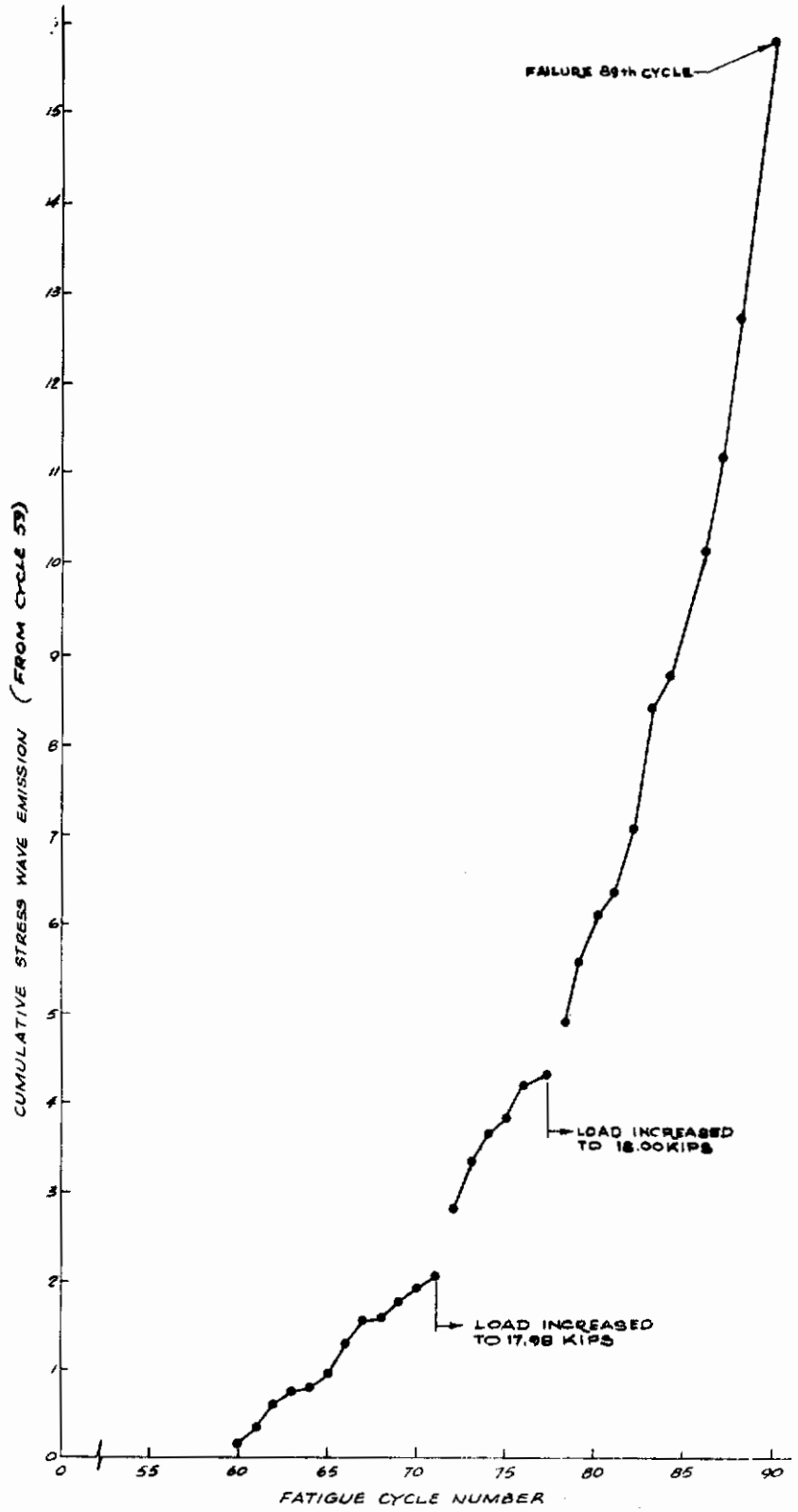

Figure 58. Total Stress Wave Emission vs Fatigue Cycling (D6aC 600°F 0.29 in. - SEN Specimen S3-5

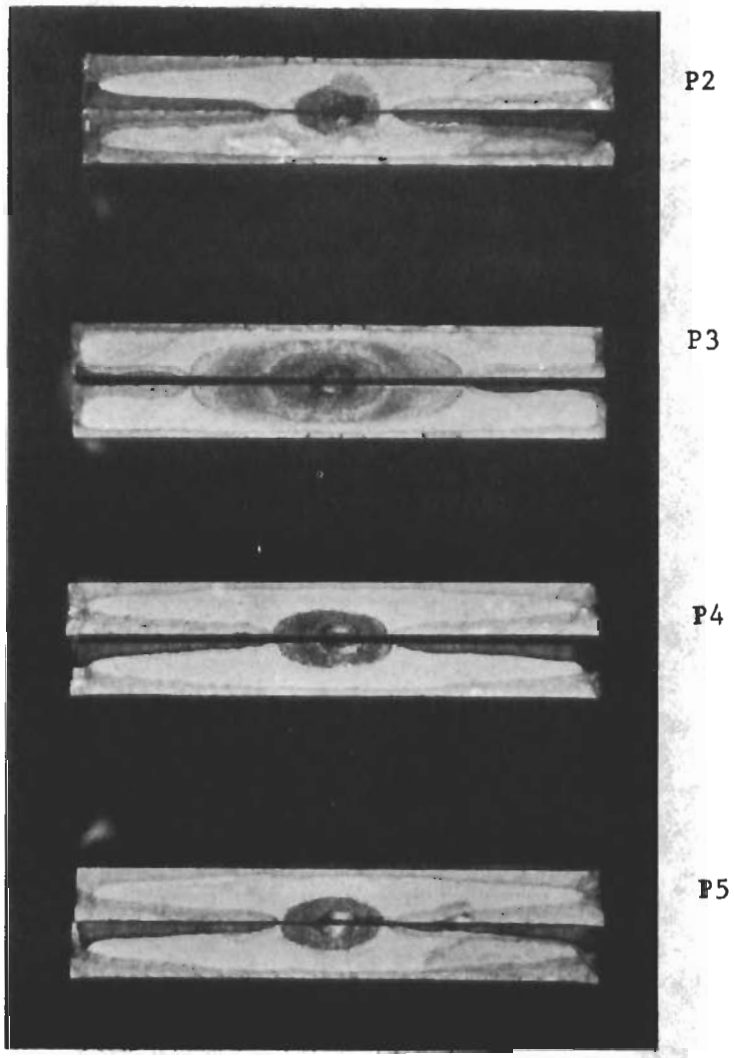

Figure 59. Part-Through-Crack Fracture Surfaces - D6aC 600°F 0.1 in.

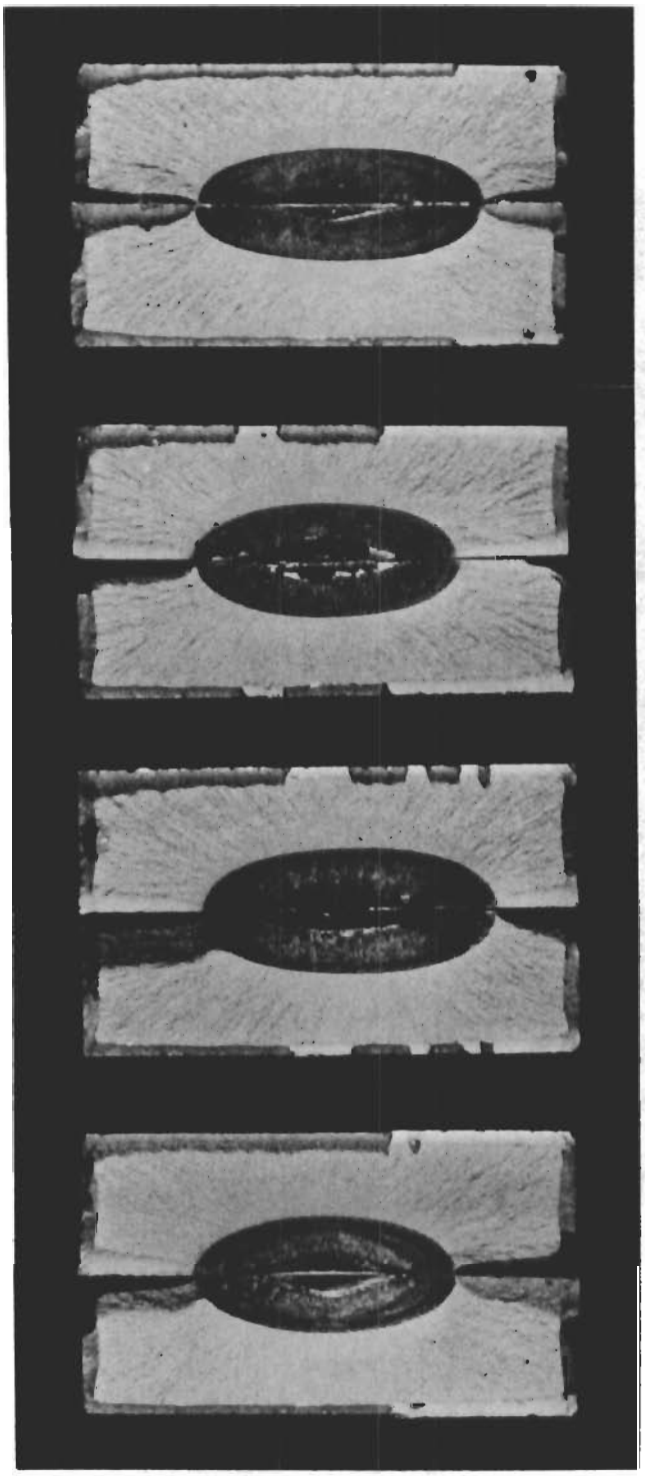

Figure 60. Part-Through-Crack Fracture Surfaces - D6aC 600°F 0.29 in.

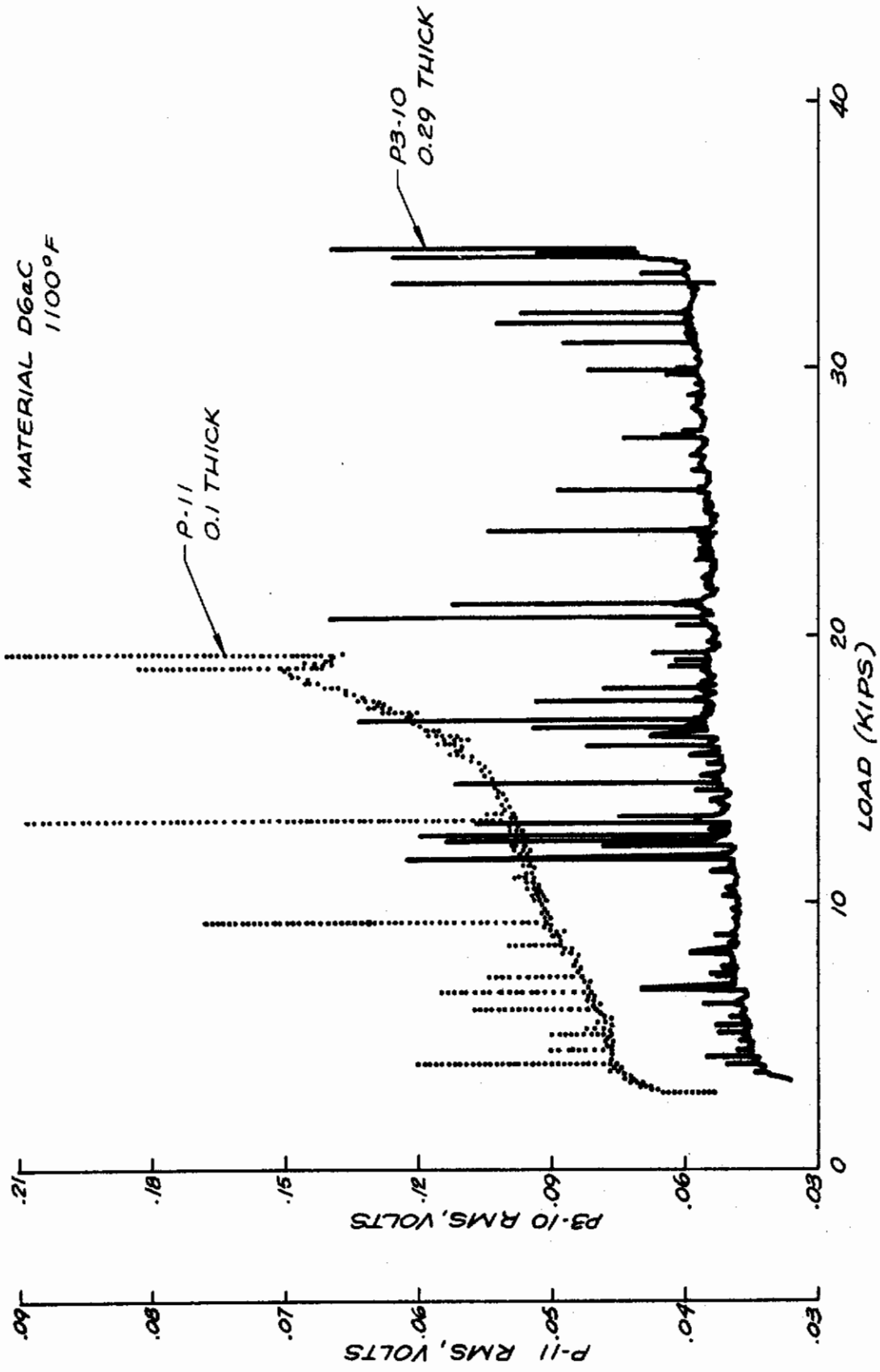

Figure 61. Emission Signal Level - D6aC 1100°F - PTC Specimens

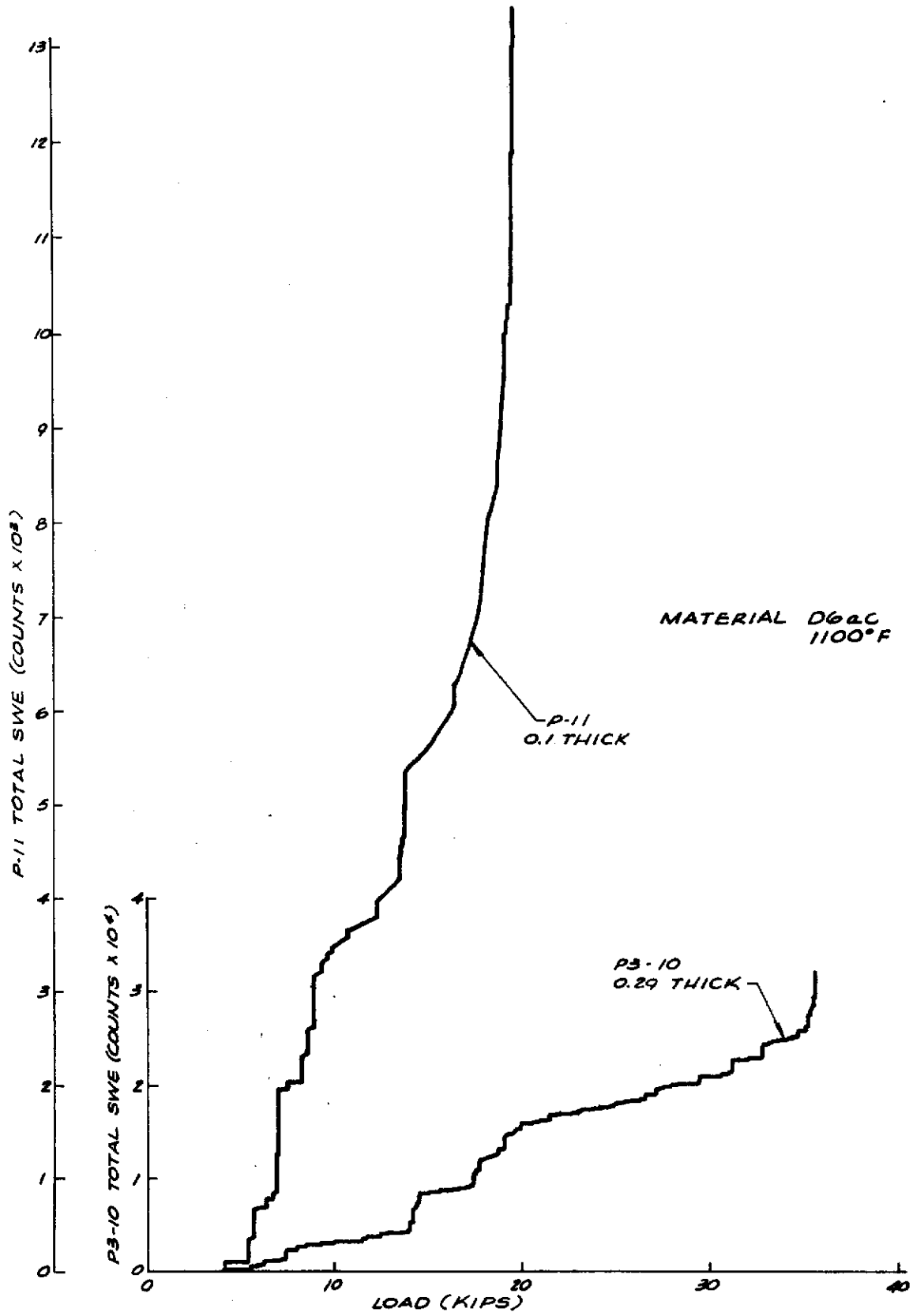

Figure 62. Total Stress Wave Emission

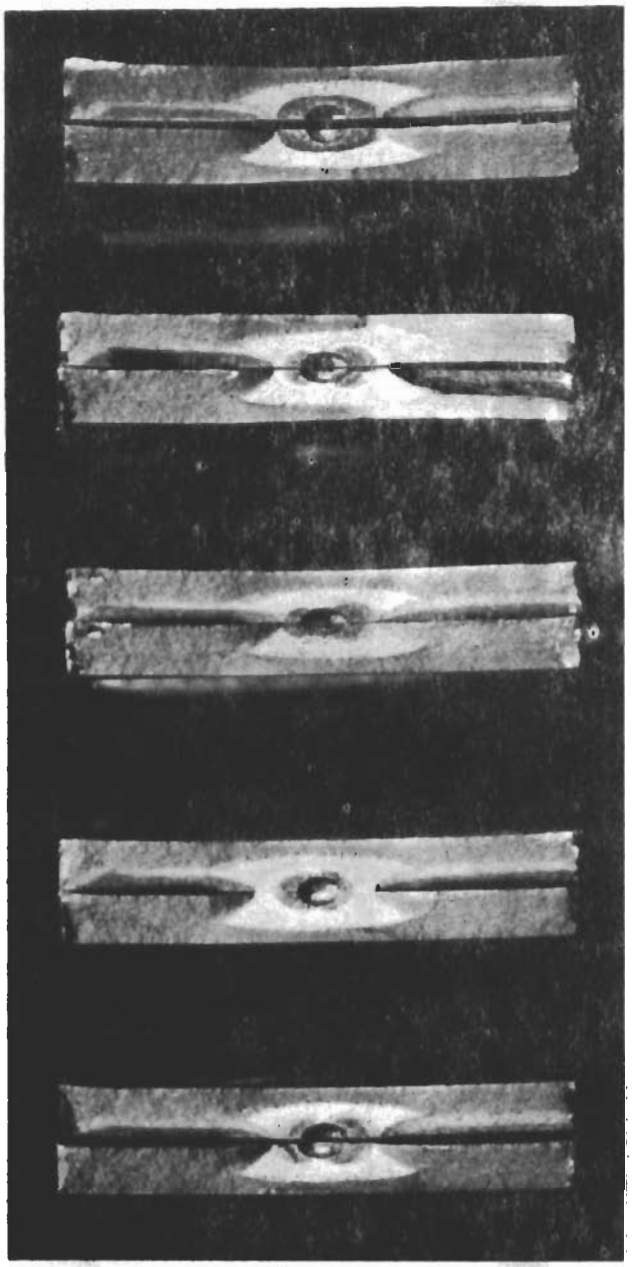

Figure 63. Part-Through-Crack Fracture Surfaces - D6aC 1100°F 0.1 in.

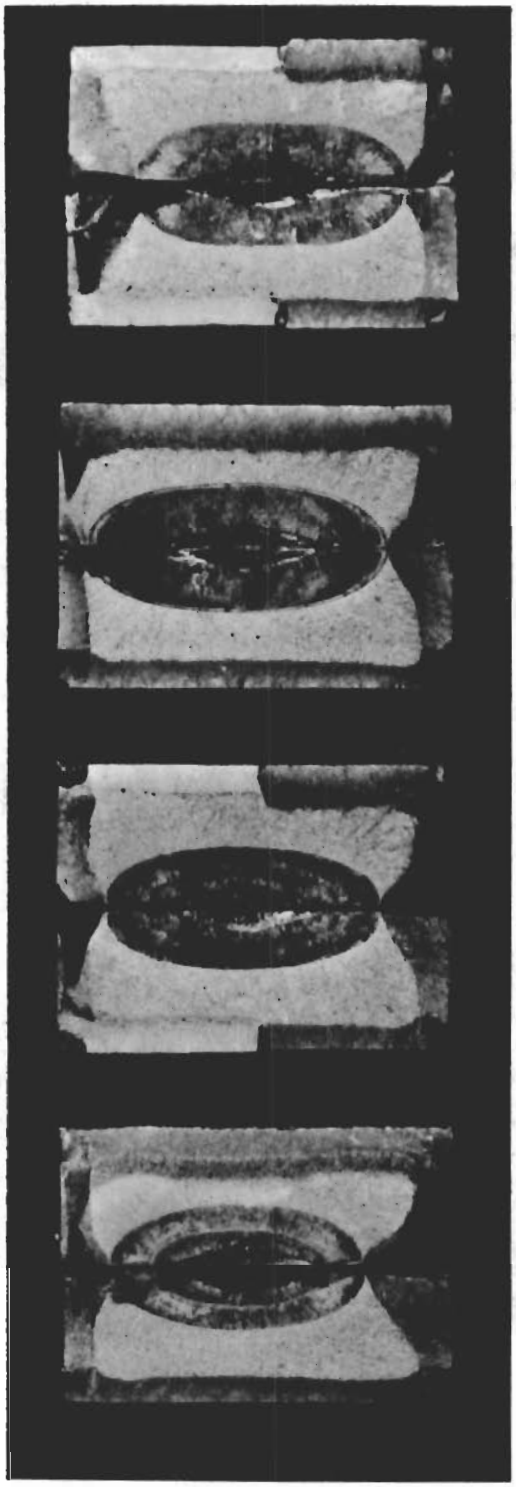

P3-7

P3-8

P3-9

P3-10

Figure 64. Part-Through-Crack Fracture Surfaces - D6aC 1100°F 0.29 in.

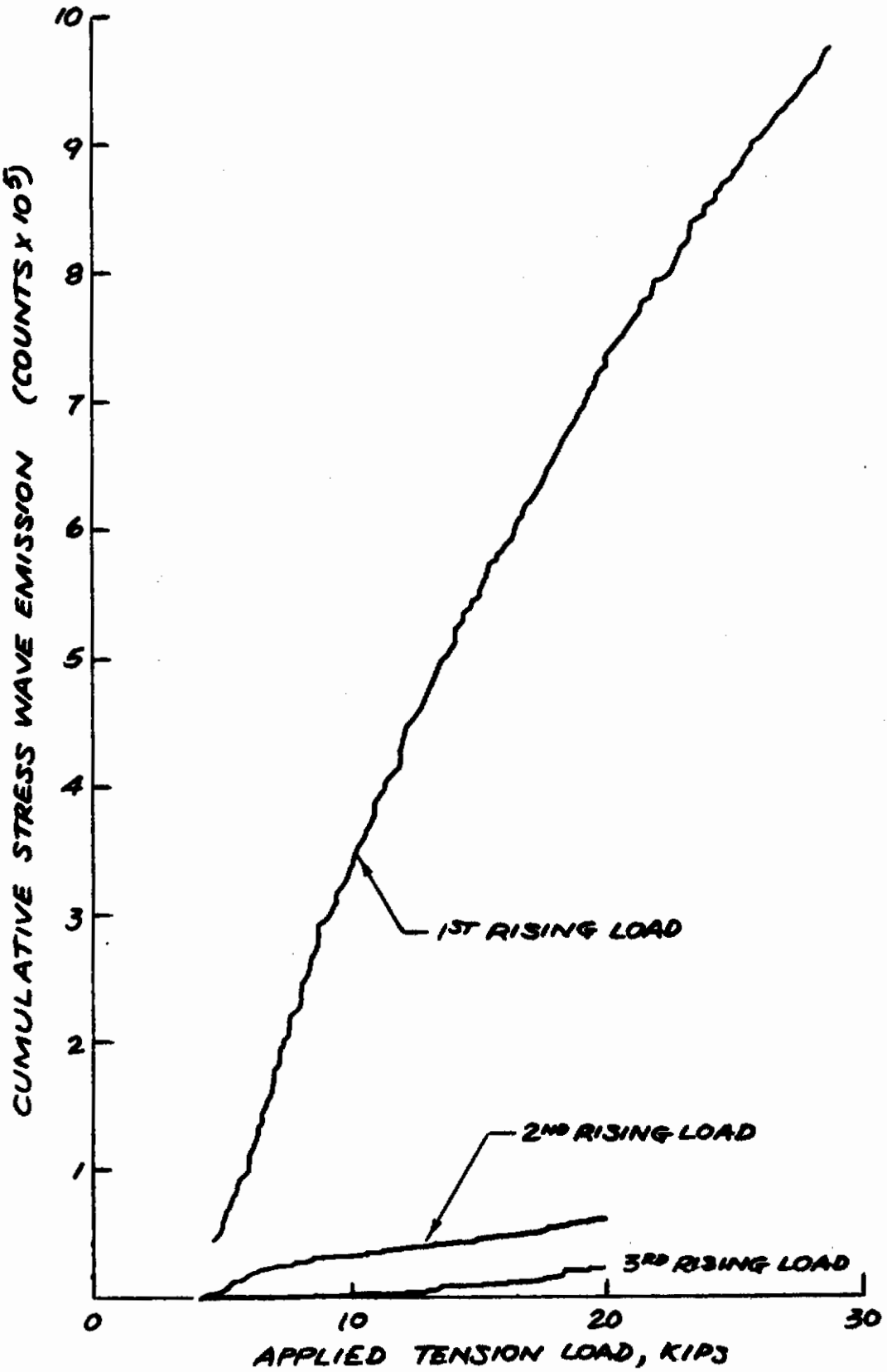

Figure 65. Total Stress Wave Emission 1st Three Rising Load Cycles - D6aC 1100°F - 0.29 in. PTC Specimen P3-11

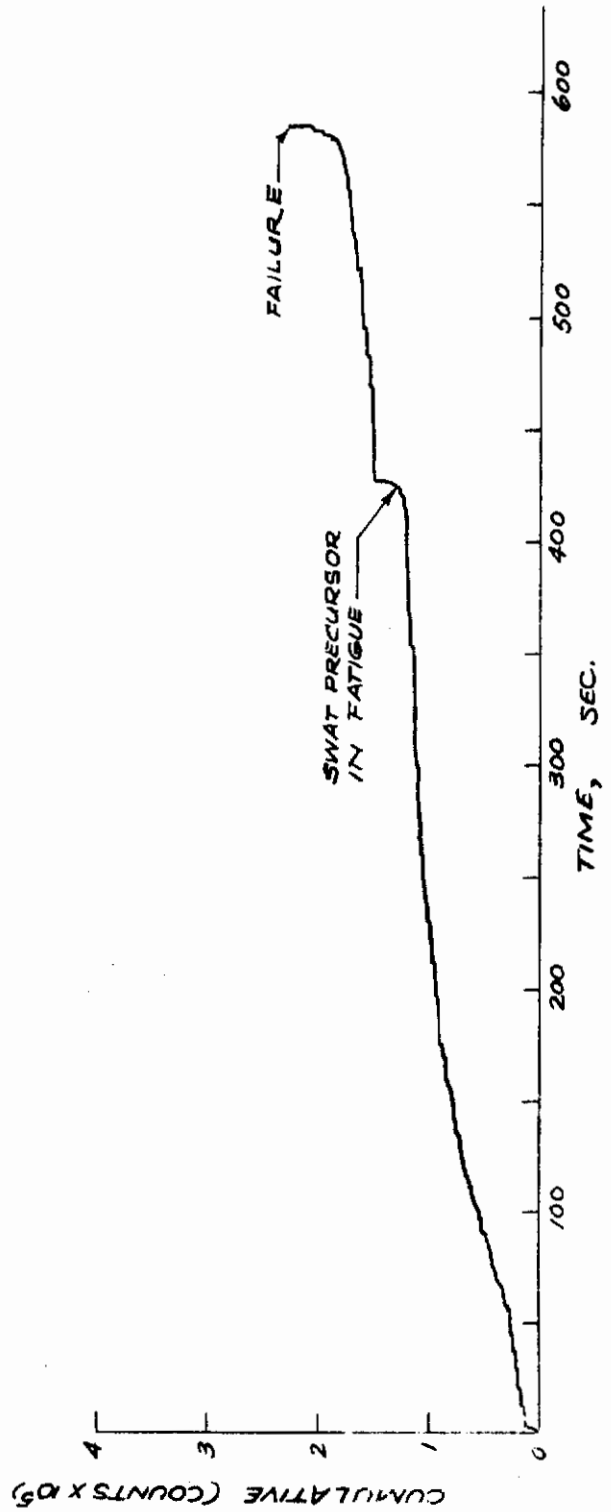

Figure 66. Total Stress Wave Emission - Fatigue Cycling - PTC Specimen P3-11 D6aC 1100°F 0.29 in.

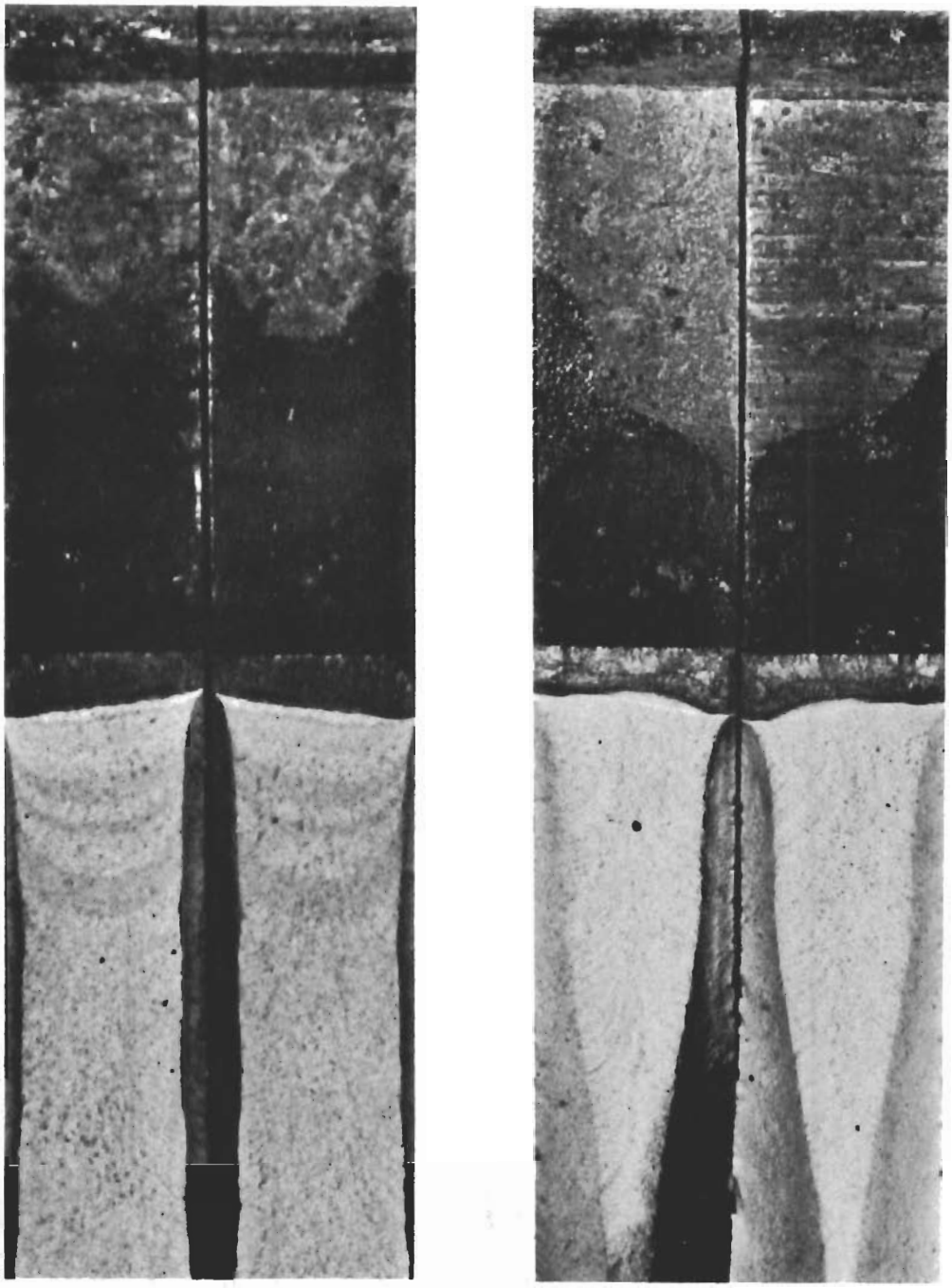

S3-3
600°F Temper

S3-9
1100°F Temper

Figure 67. Fracture Initiation and Propagation in 0.29-in. Thick SEN Tension Specimens

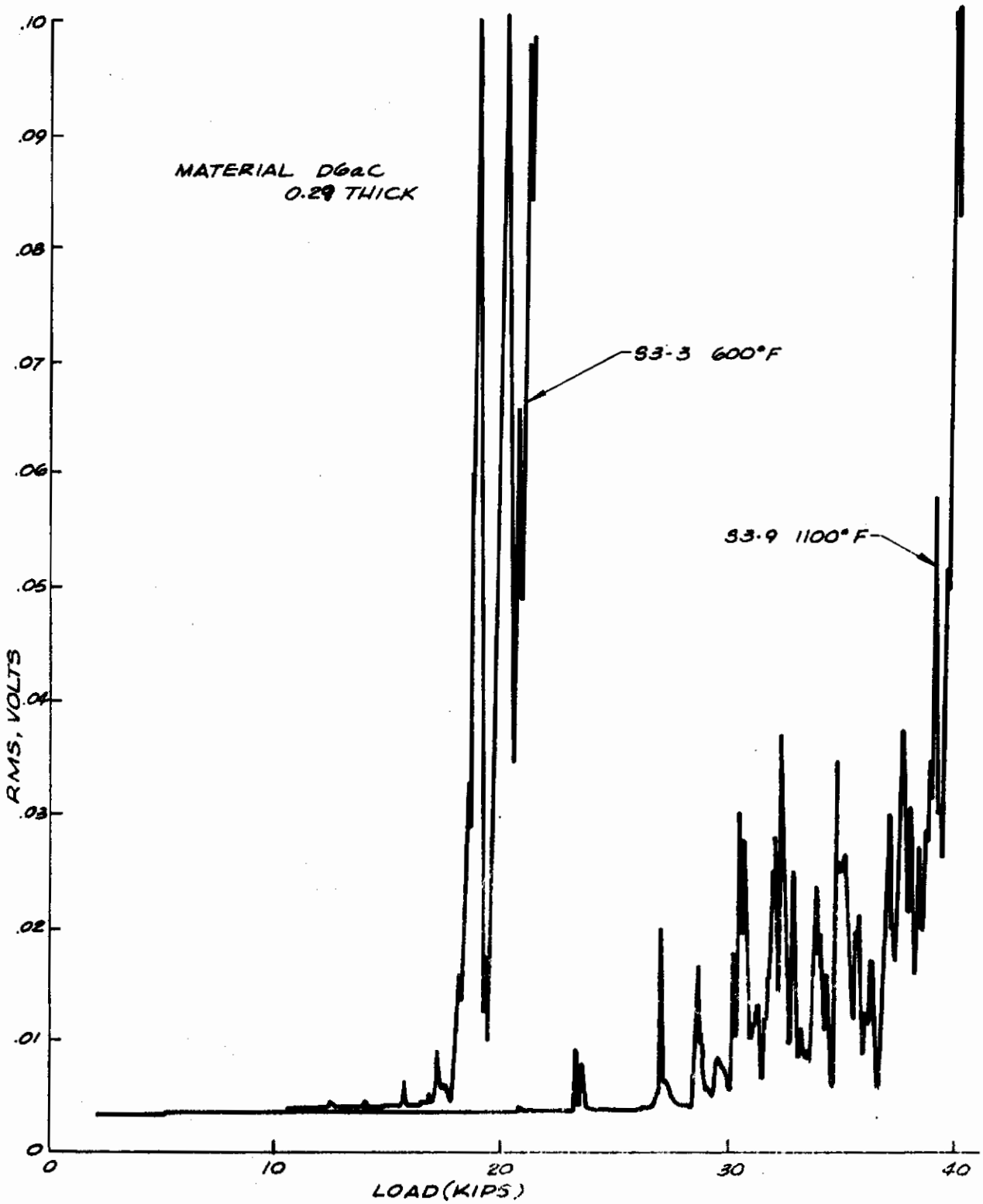

Figure 68. Emission Signal Level - SEN Specimens S3-3 and S3-9 D6aC 0.29 in.

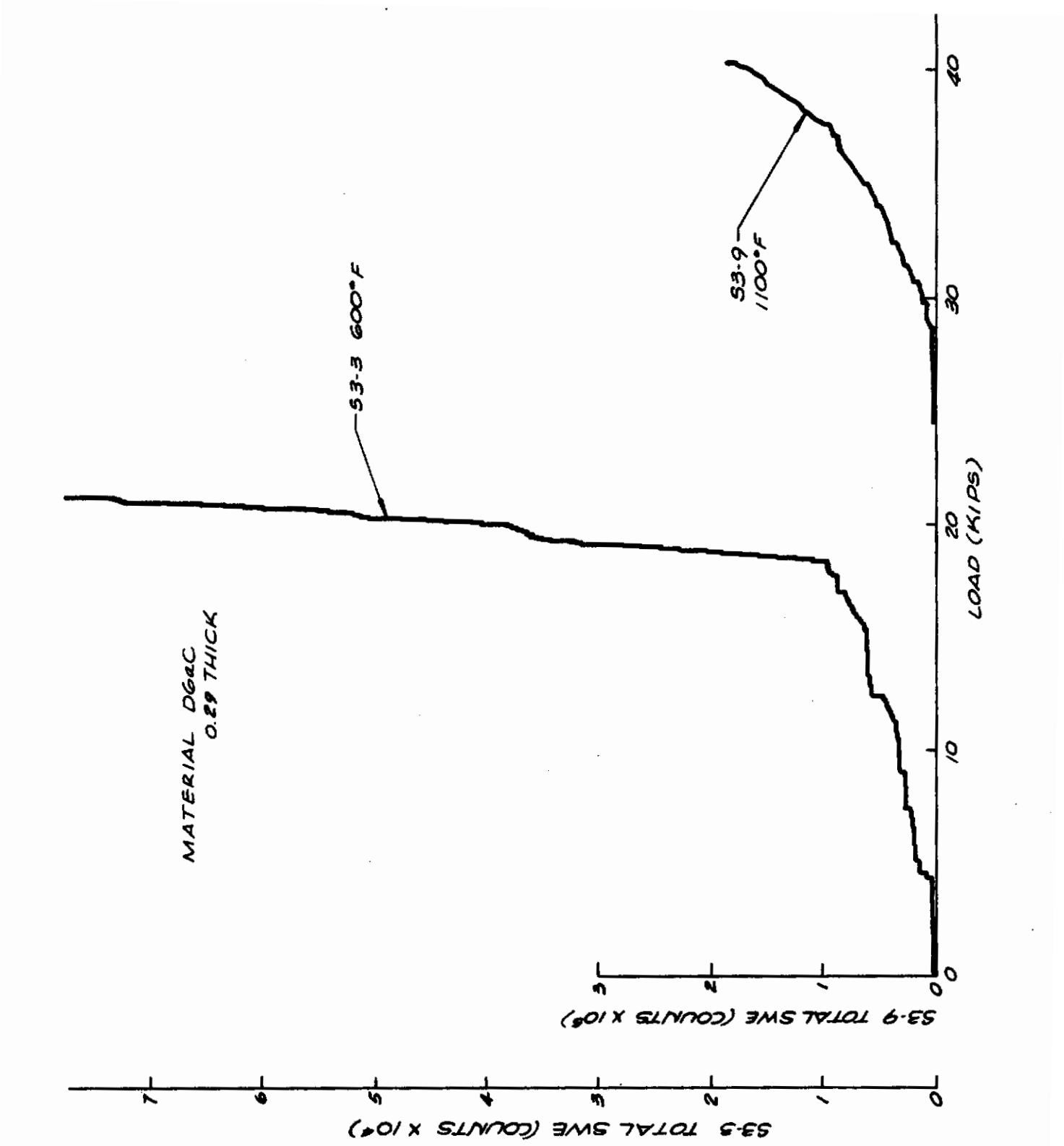

Figure 69. Total Stress Wave Emission - SEN Specimens S3-3 and S3-9 D6aC 0.29 in.

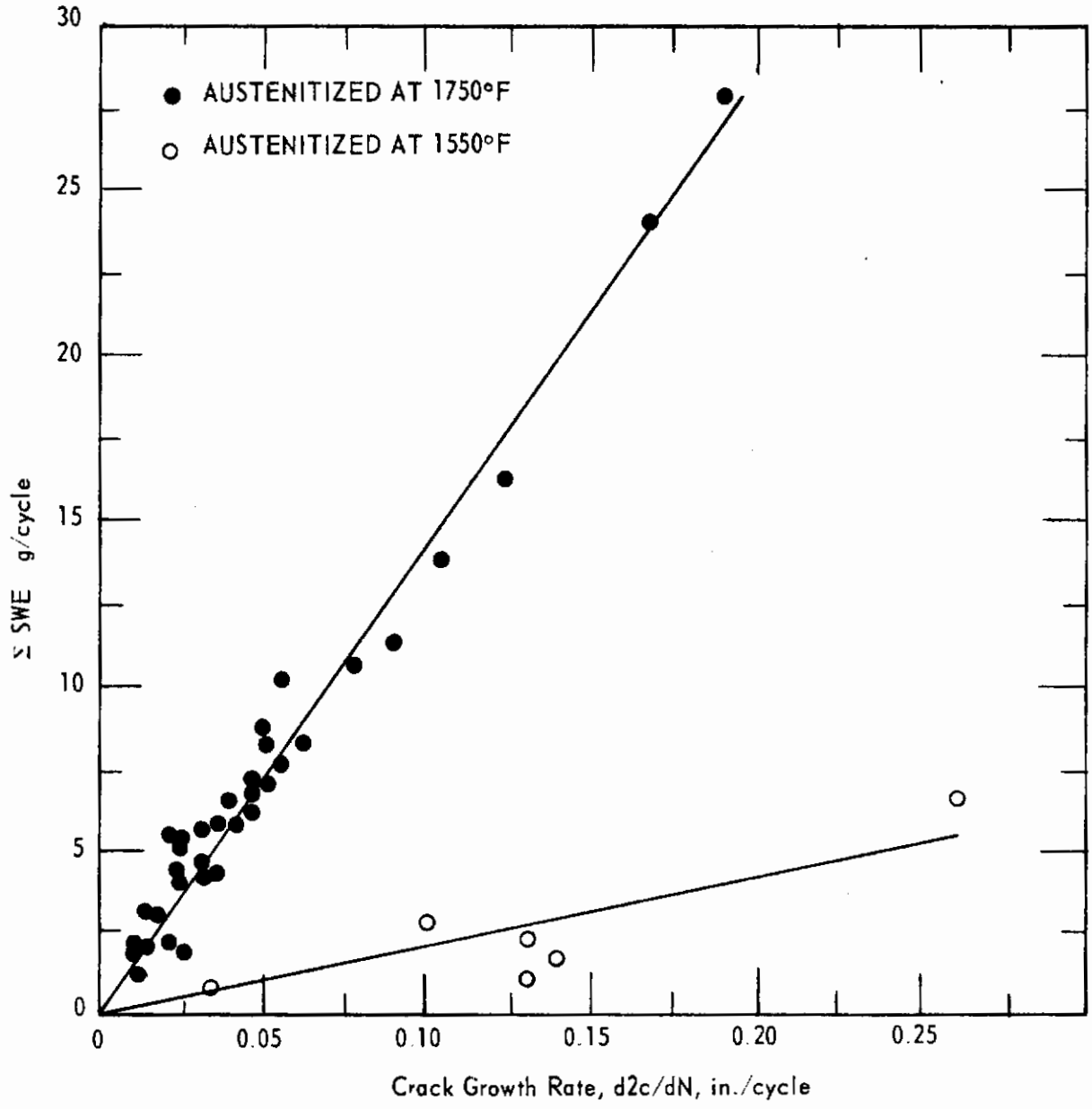

Figure 70. Relationship Between Fatigue Crack Growth Rate and Stress Wave Emission for Two Conditions of D6aC Steel

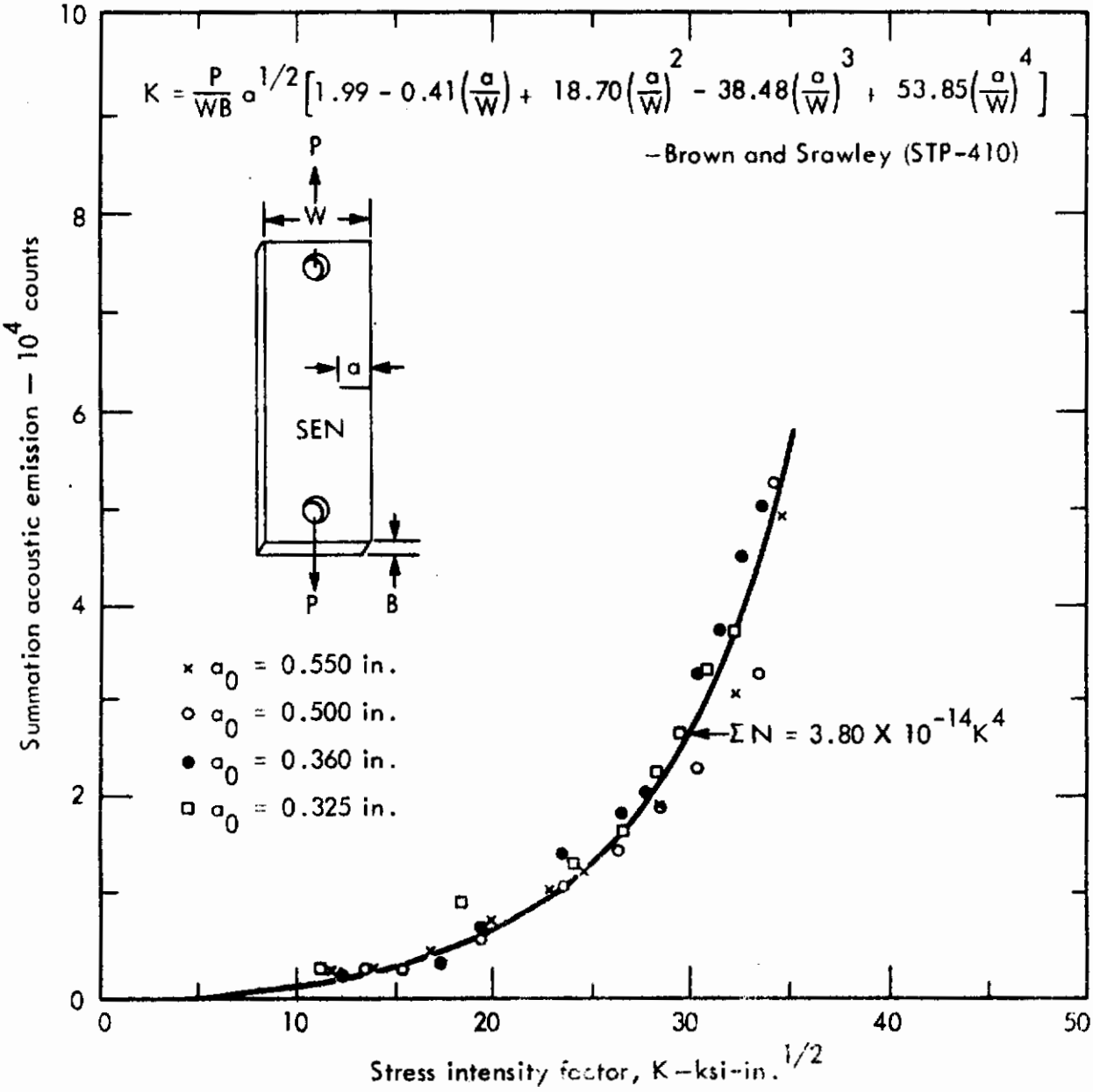

Figure 71. Summation of Acoustic Emission as a Function of Stress-Intensity Factor-7075T6

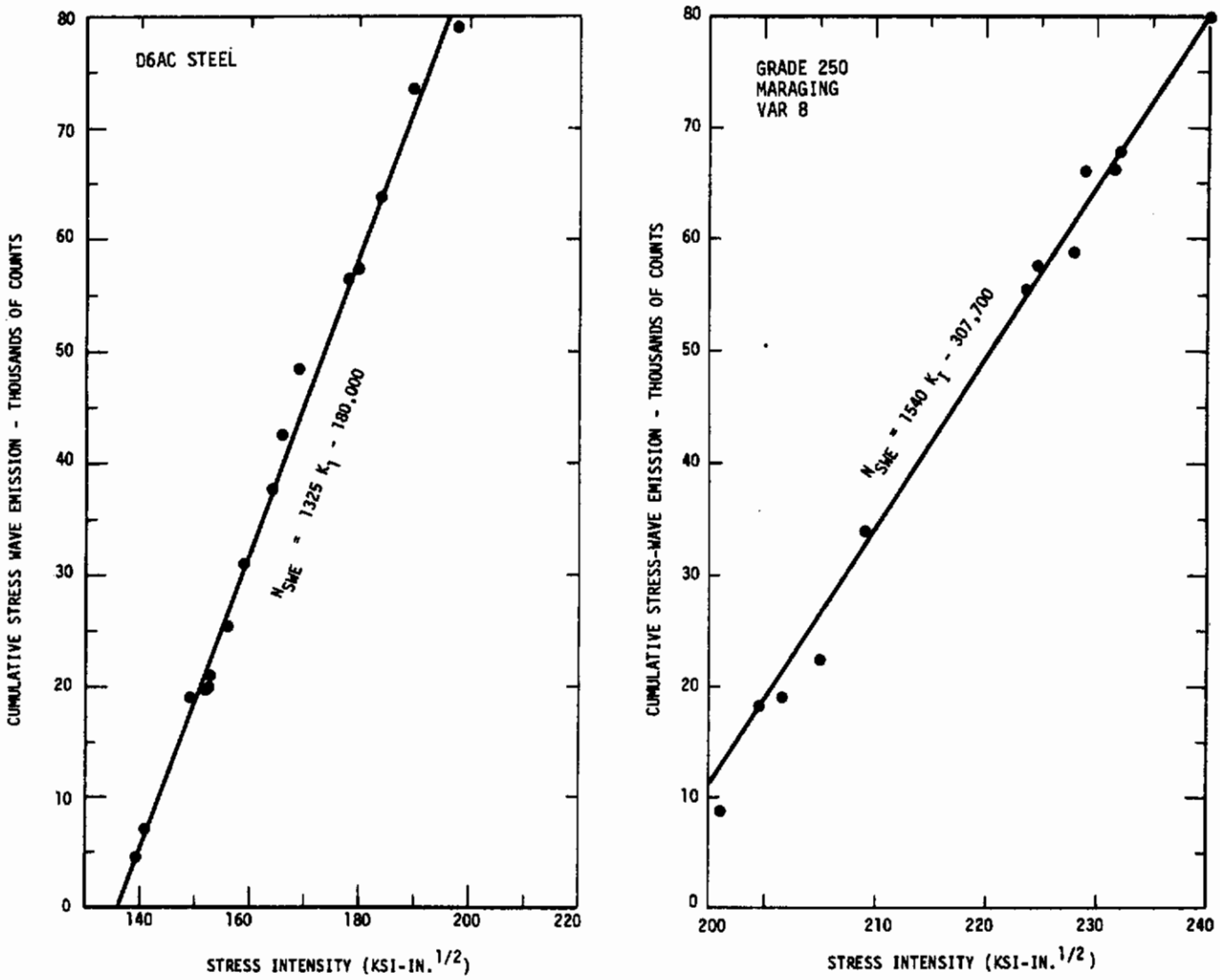

Figure 72. Relationship Between Stress Intensity and Cumulative Count for Materials Under Constant Load and Subjected to Stress-Corrosion Cracking in 70°F Water

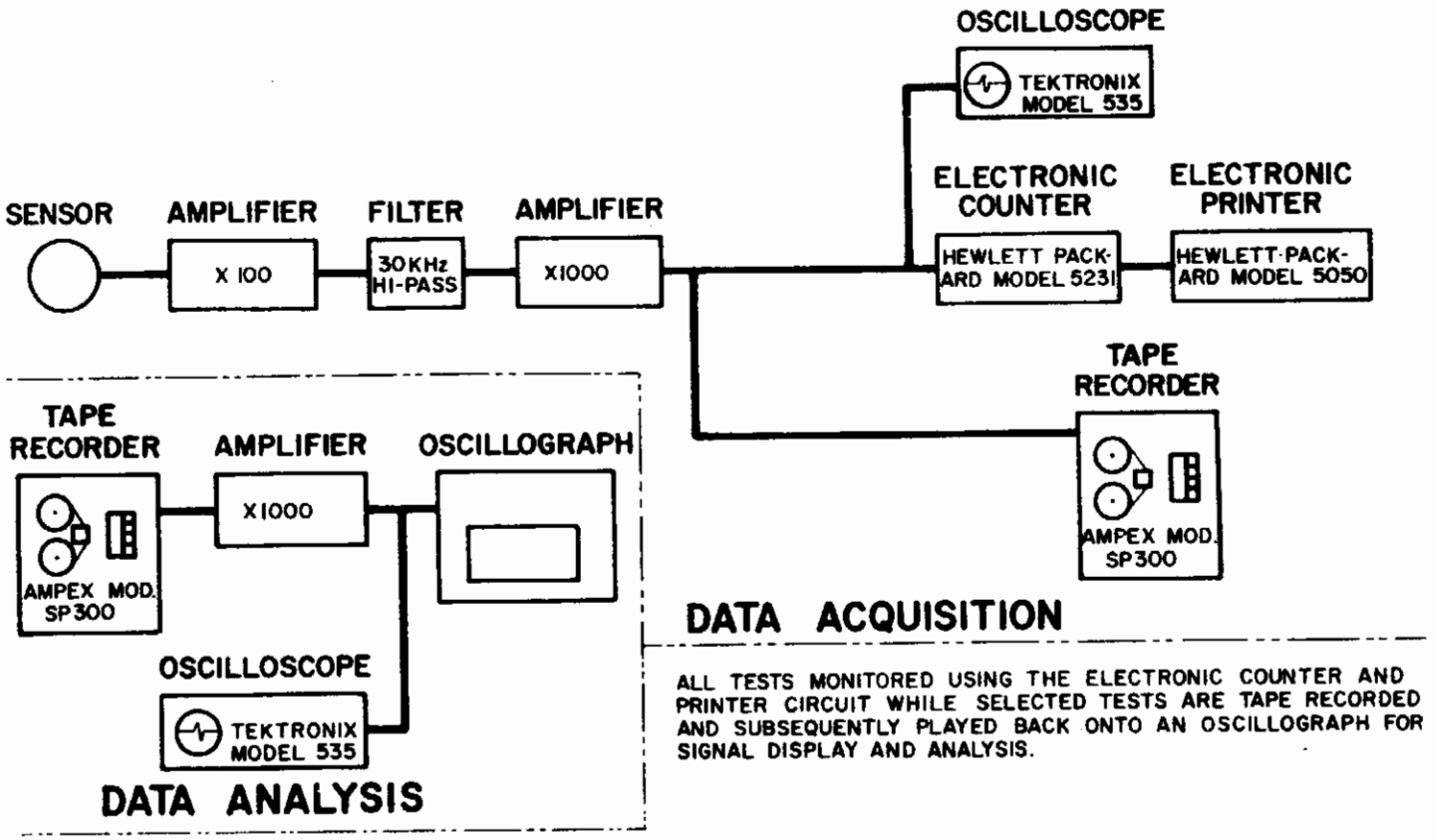

Figure 73. Schematic of Instrumentation System Used in Contract 2788 Fracture Testing

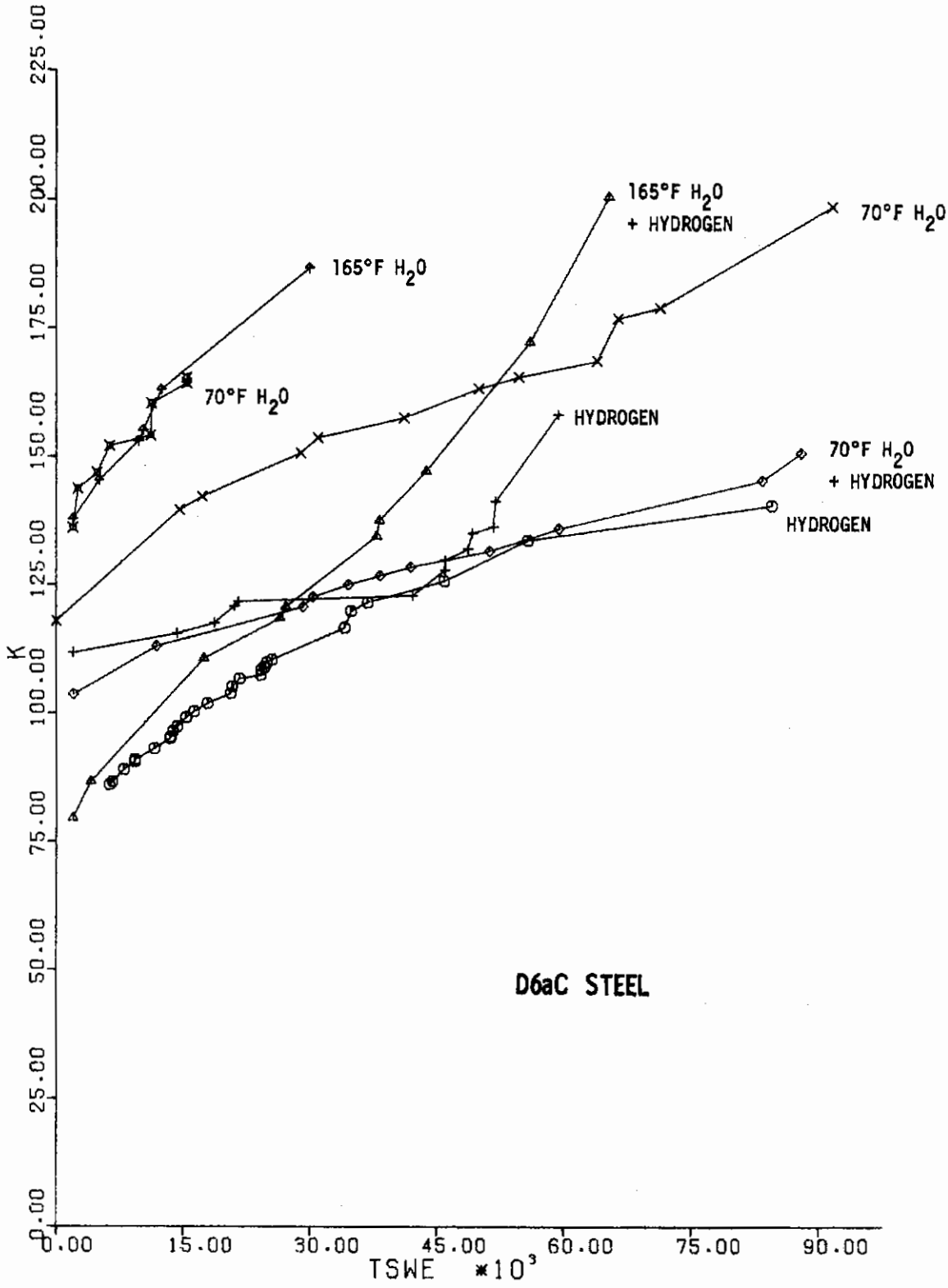

Figure 74. Relationship Between K and Count for 1100°F Tempered D6aC Steel Tested Under Constant Load-Crack Growth Produced by Hydrogen and Water

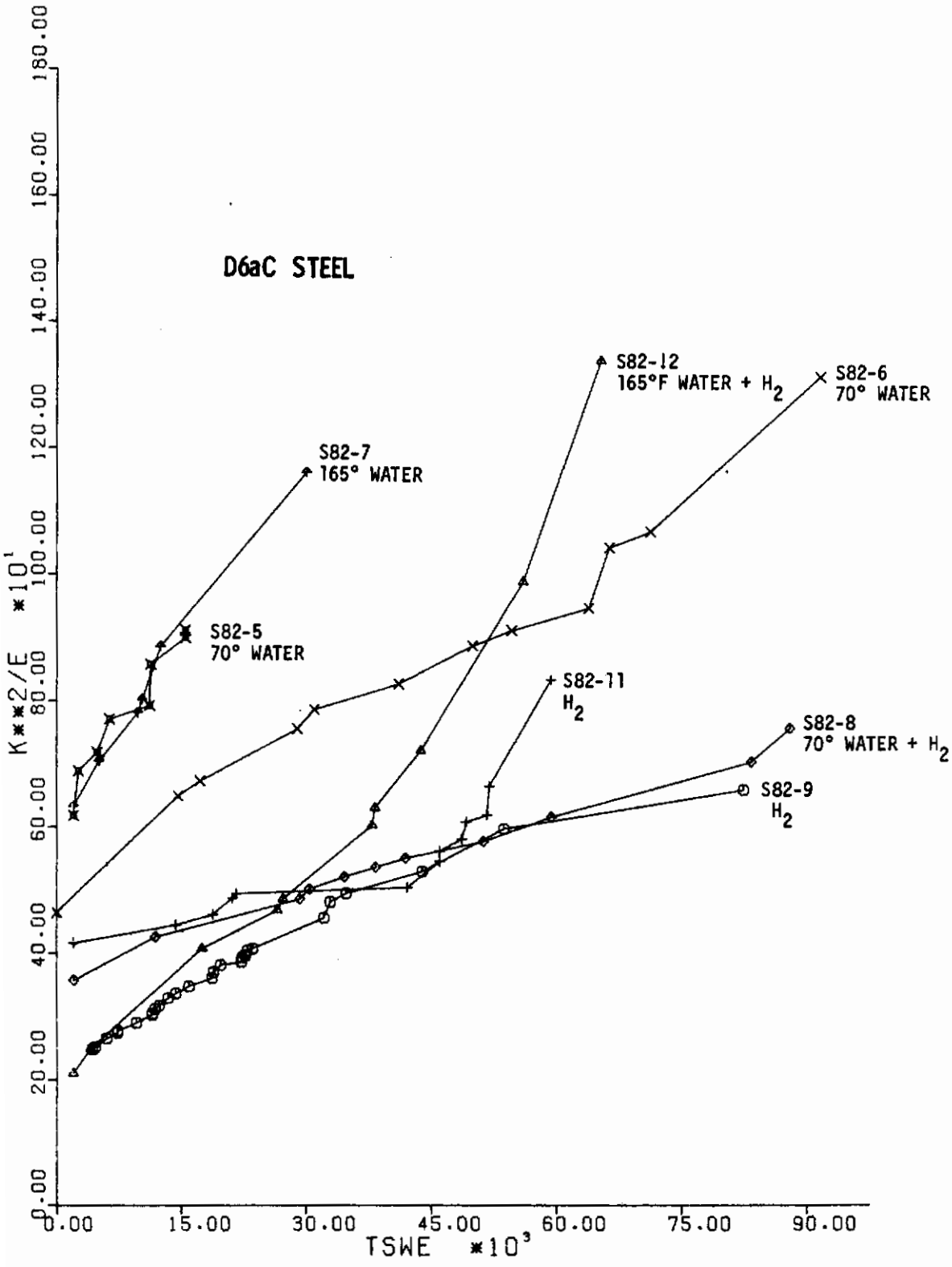

Figure 75. Relationship Between K^2/E and Count in D6aC

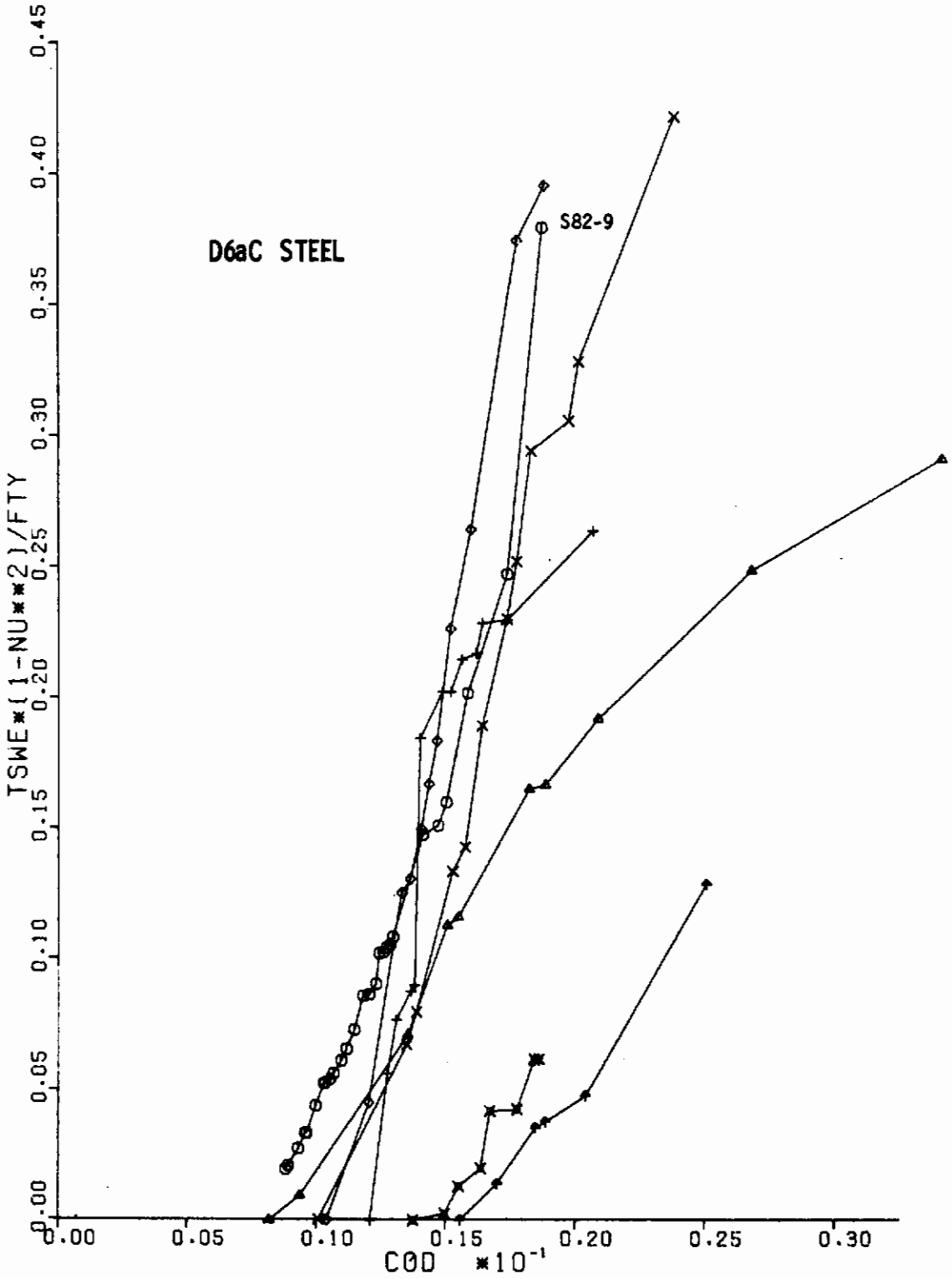

Figure 76. Relationship Between Count and Crack-Opening Displacement in D6aC

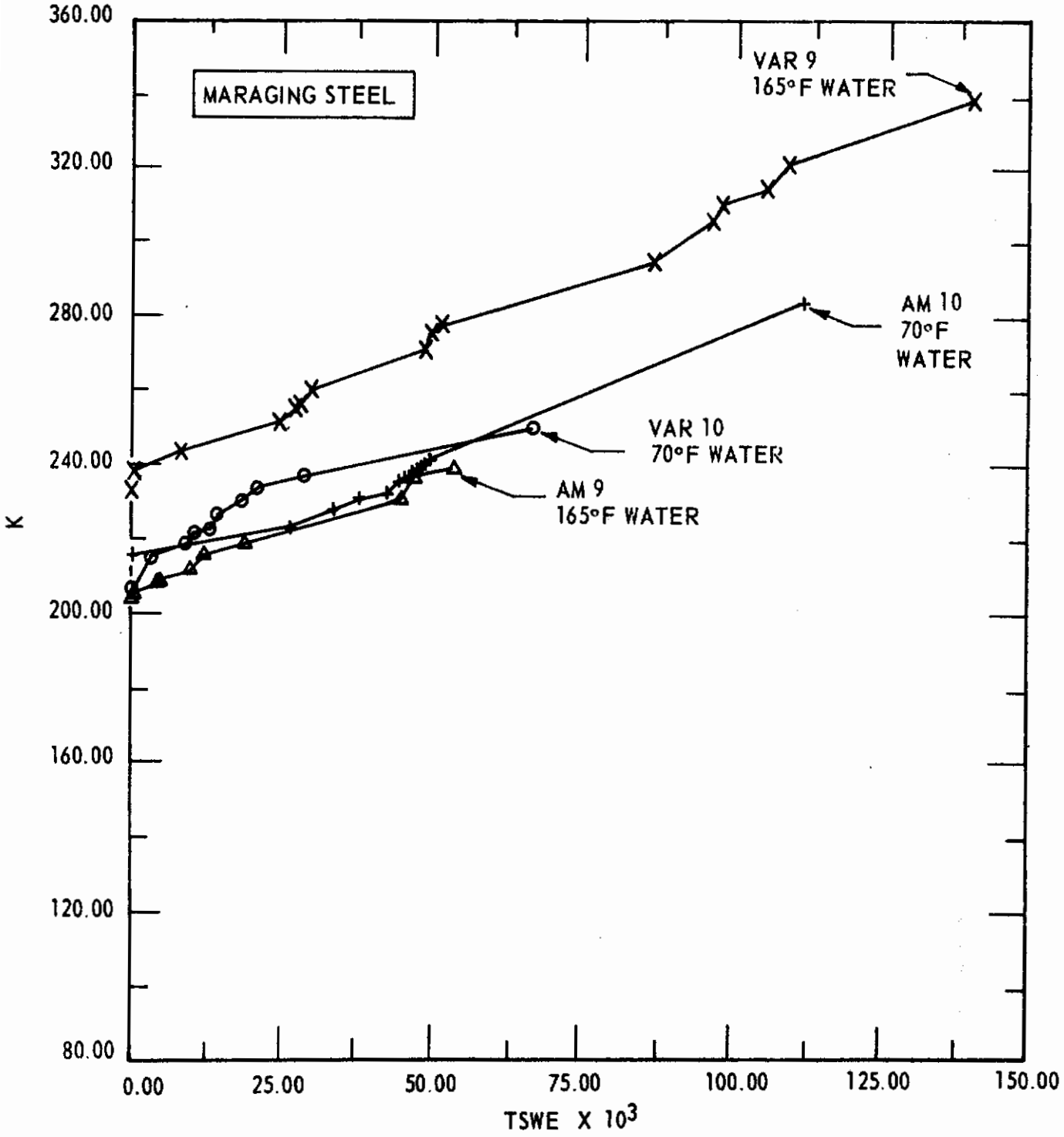

Figure 77. Relationship Between K and Count for 18% Nickel Maraging Steel Under Constant Load - Crack Growth Produced by Water at 70 and 165°F

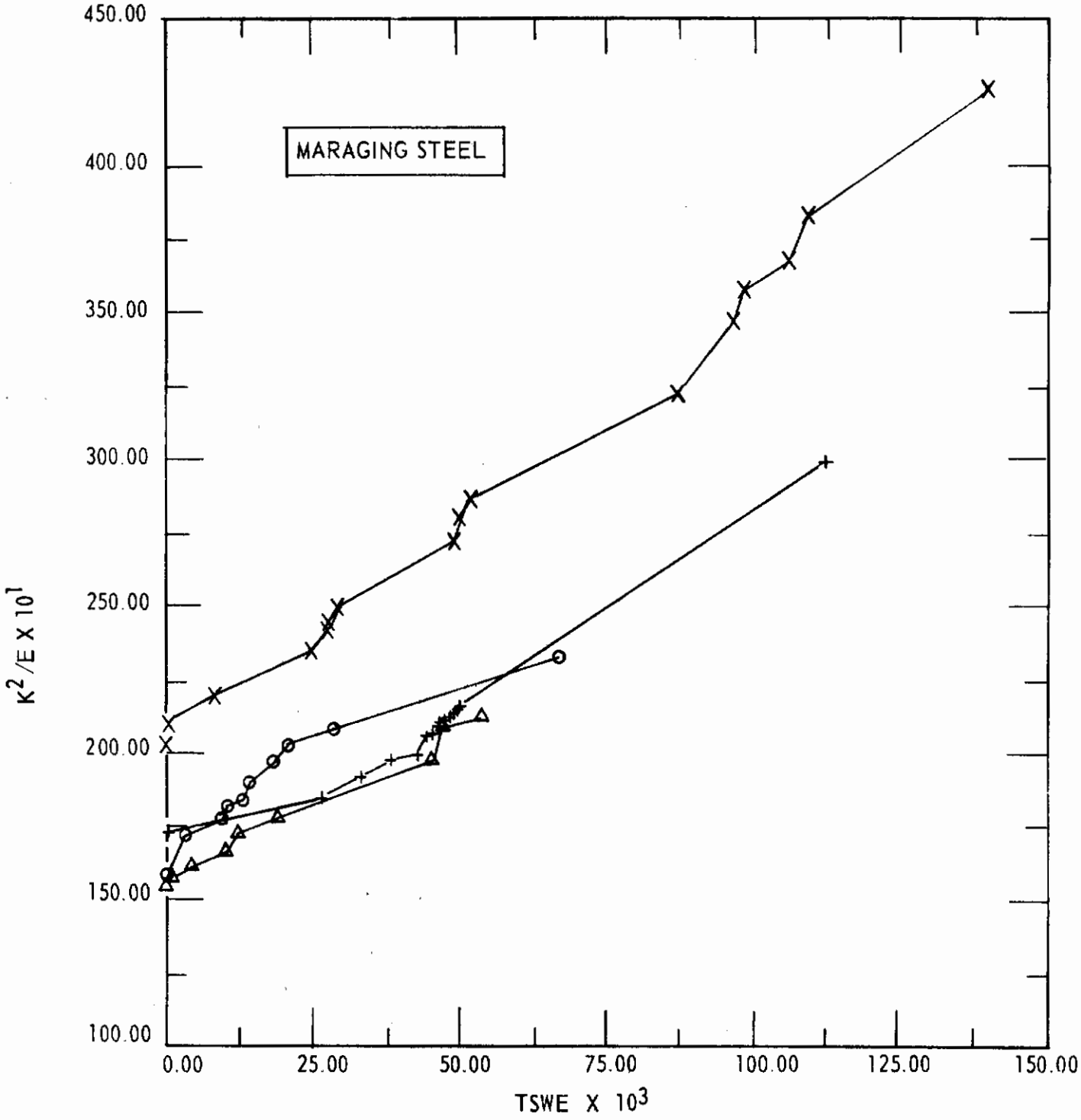

Figure 78. Relationship Between K^2/E and Count in Maraging Steel

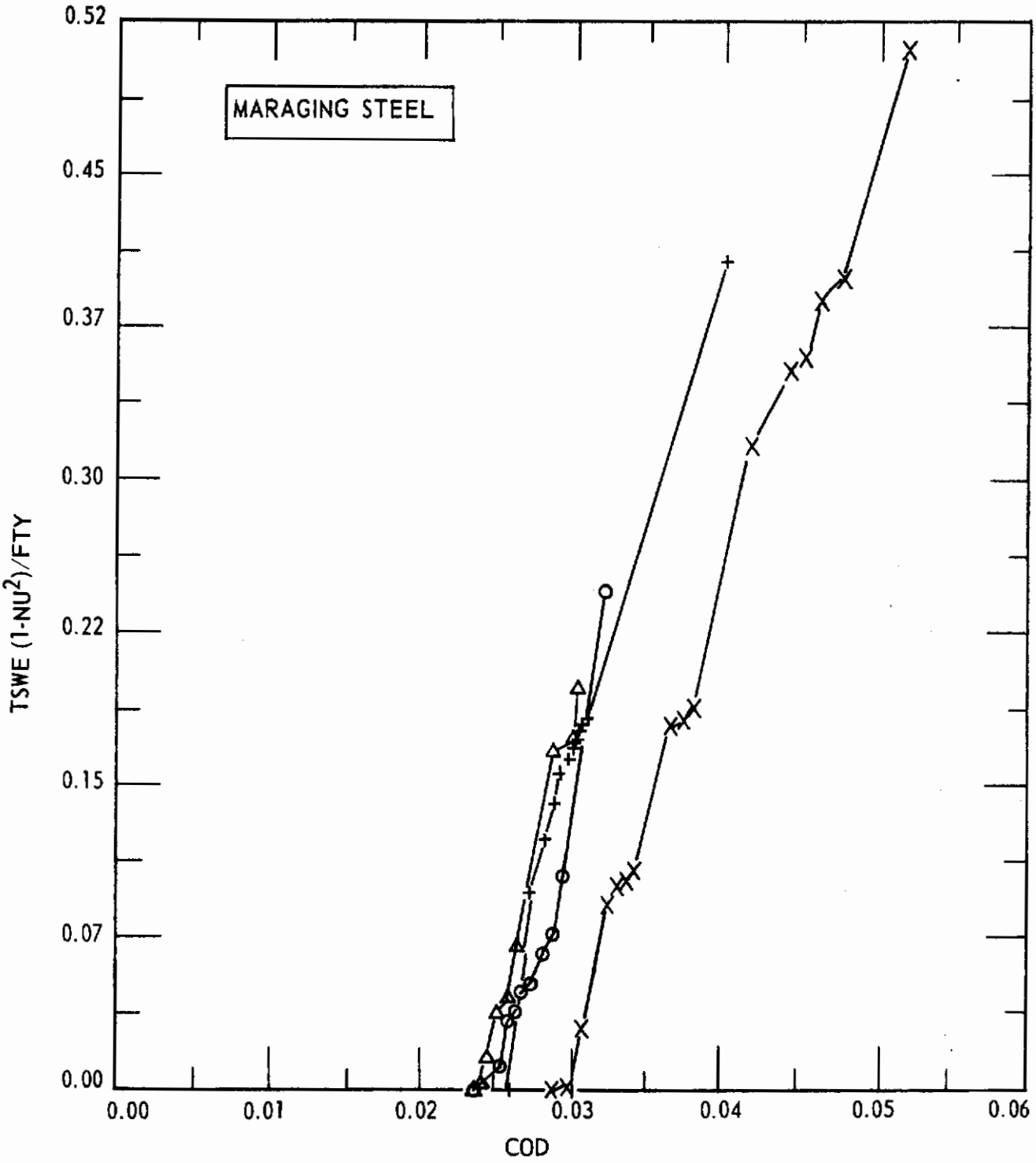

Figure 79. Relationship Between Count and Crack-Opening Displacement in Maraging Steel

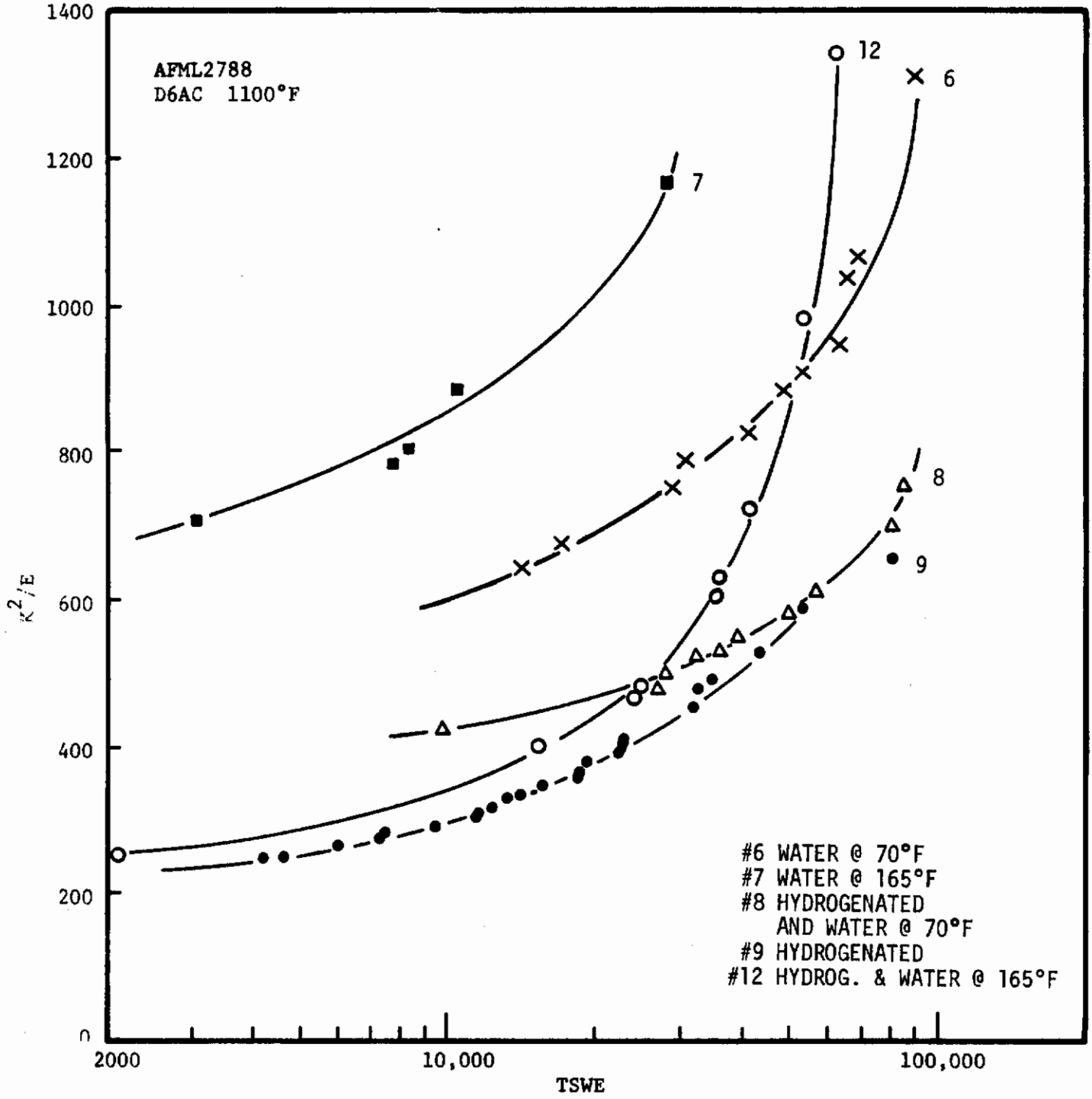

Figure 80. Relationship Between K^2/E and Count on Semi Log Paper - Same Tests as in Figure 75.

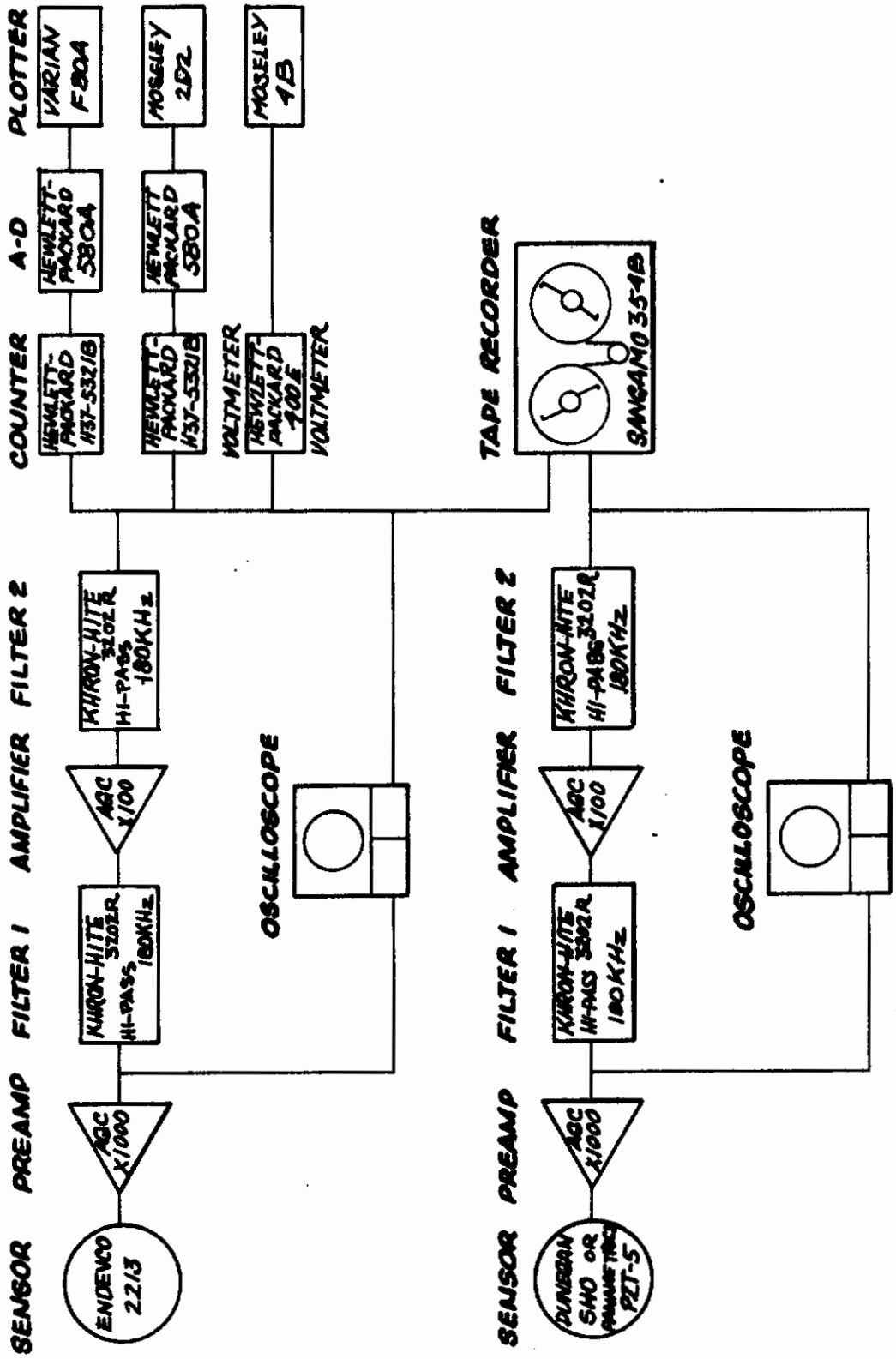

Figure 81. Schematic of Instrumentation System Used in ARPA Fracture Testing

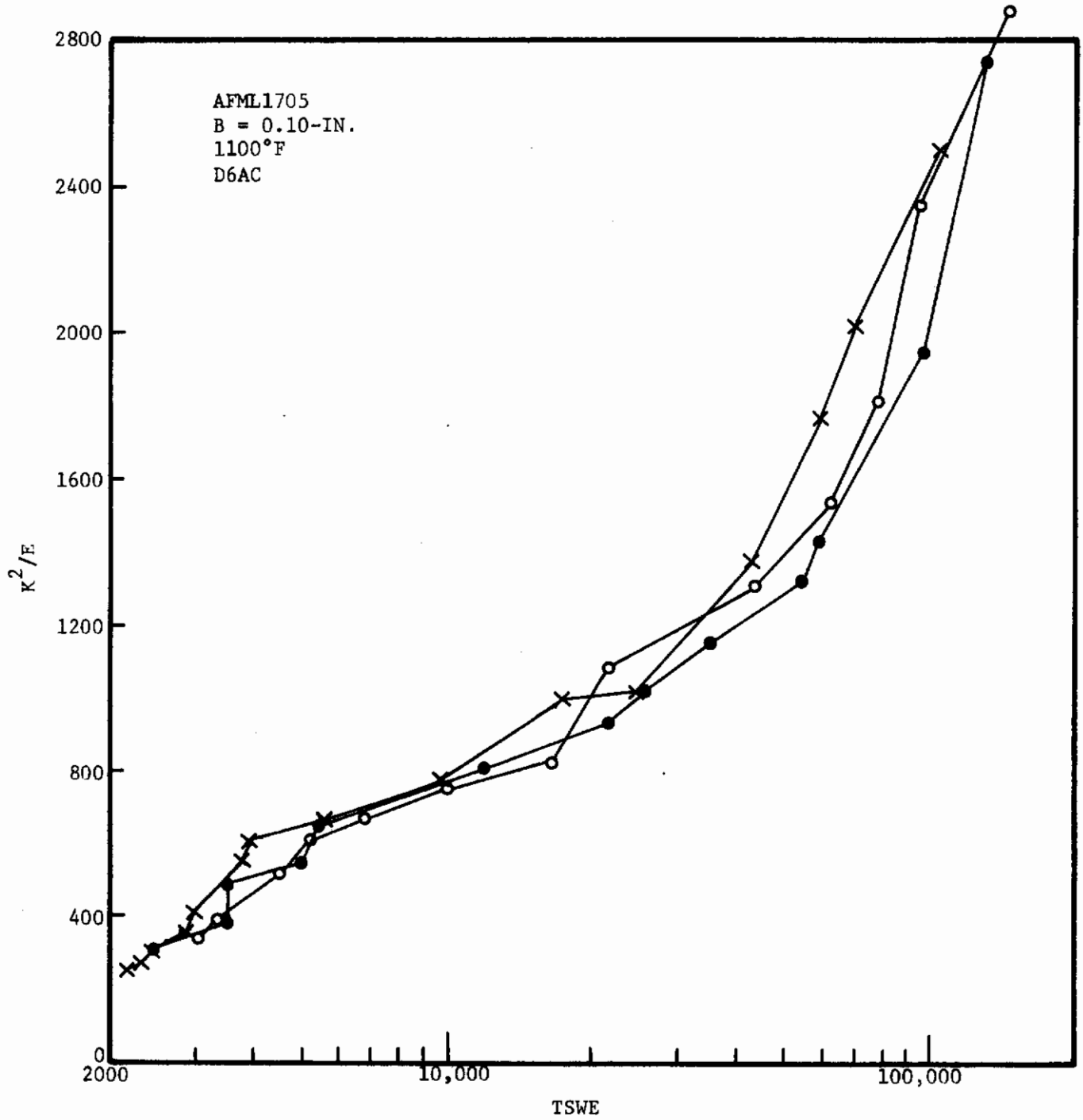

Figure 82. Relationship Between K^2/E and Count in Rising Load Tests of 1100°F D6aC Steel 0.10-in. Thick

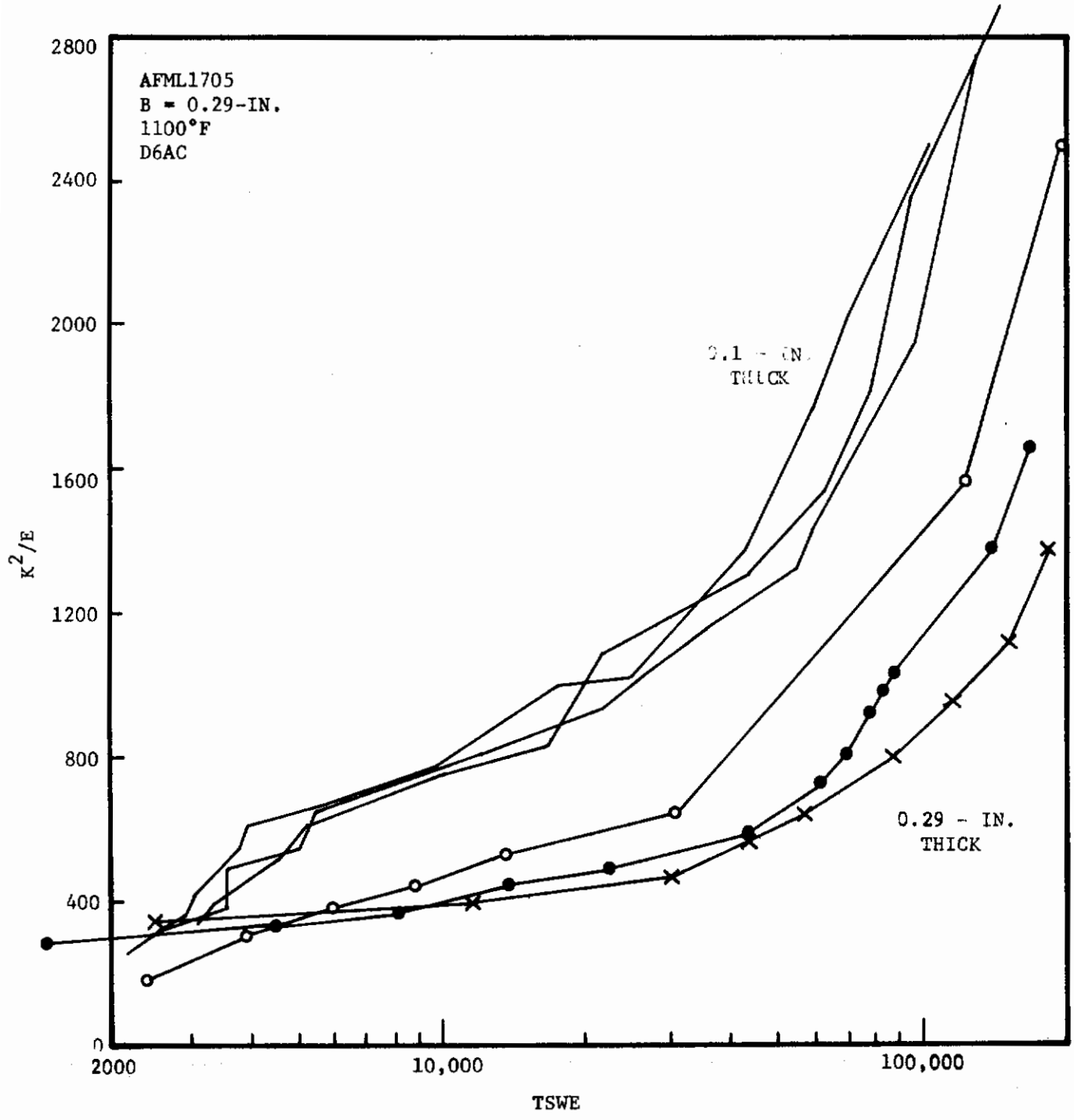

Figure 83. Relationship Between K^2/E and Count in Rising Load Tests of 1100°F D6aC Steel Showing Effect of Thickness

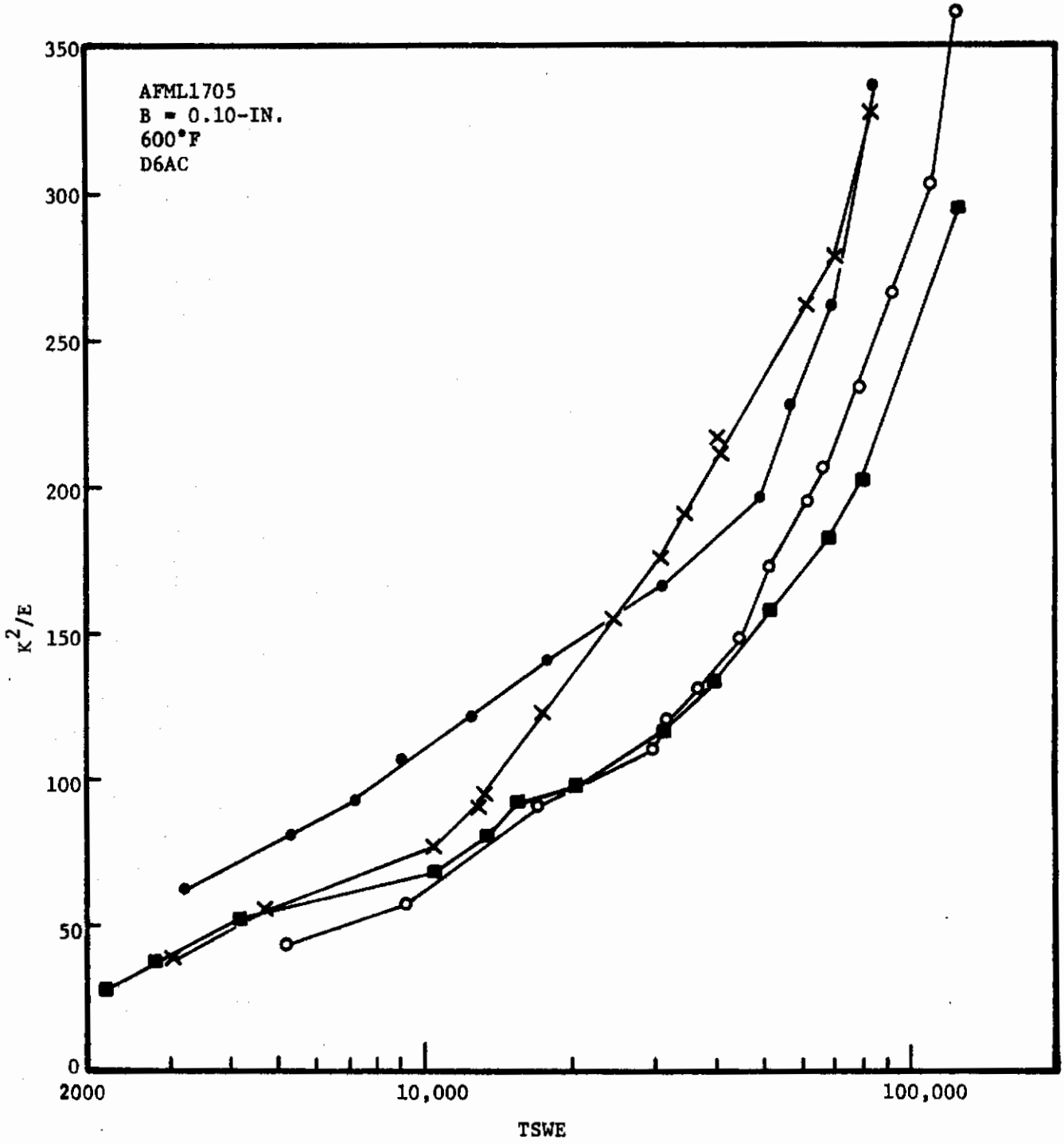

Figure 84. Relationship Between K^2/E and Count in Rising Load Tests of 600°F Temper D6aC Steel 0.10 in. Thick

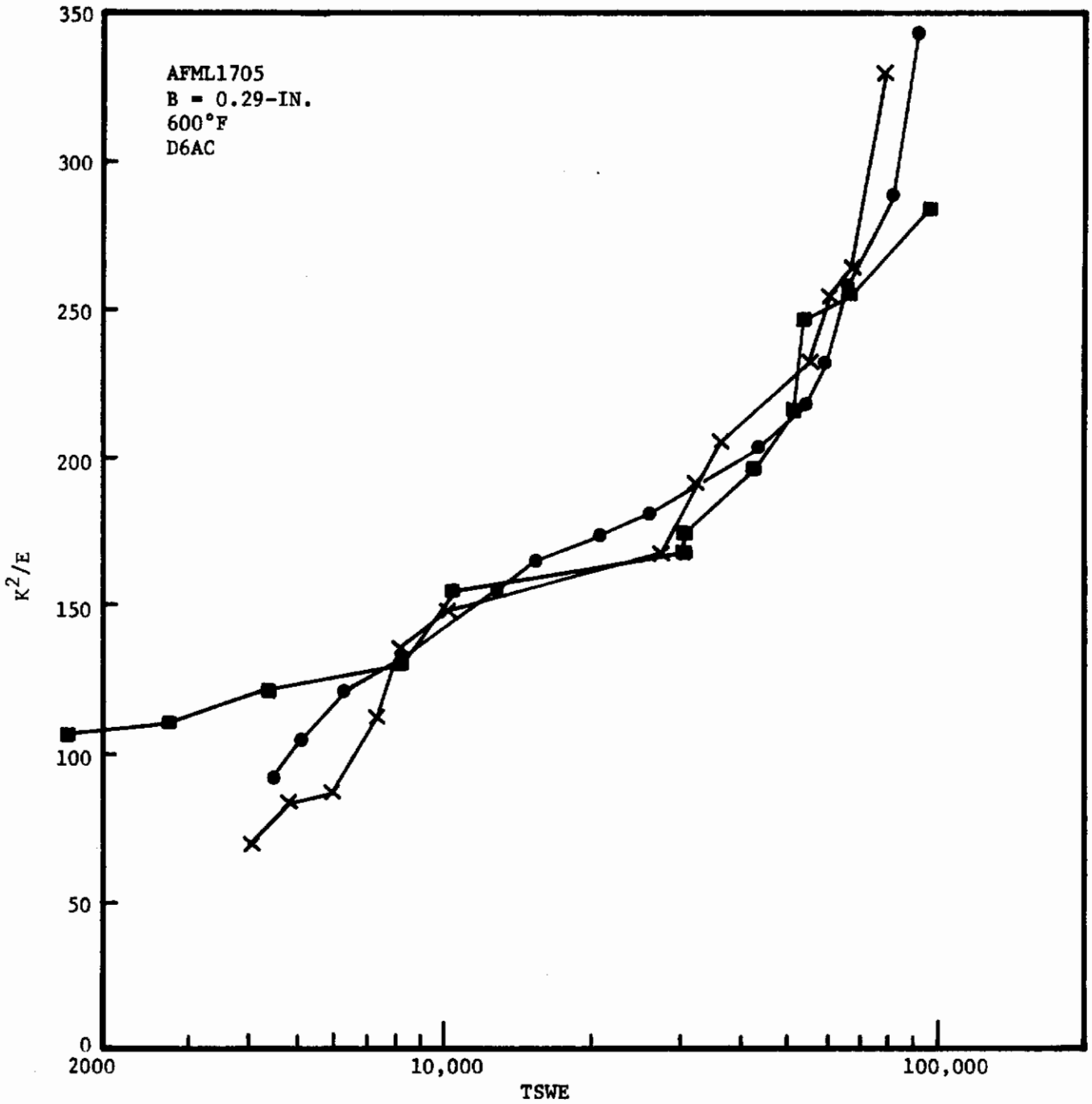

Figure 85. Relationship Between K^2/E and Count in Rising Load Tests of 600°F Temper D6aC Steel 0.29 in. Thick

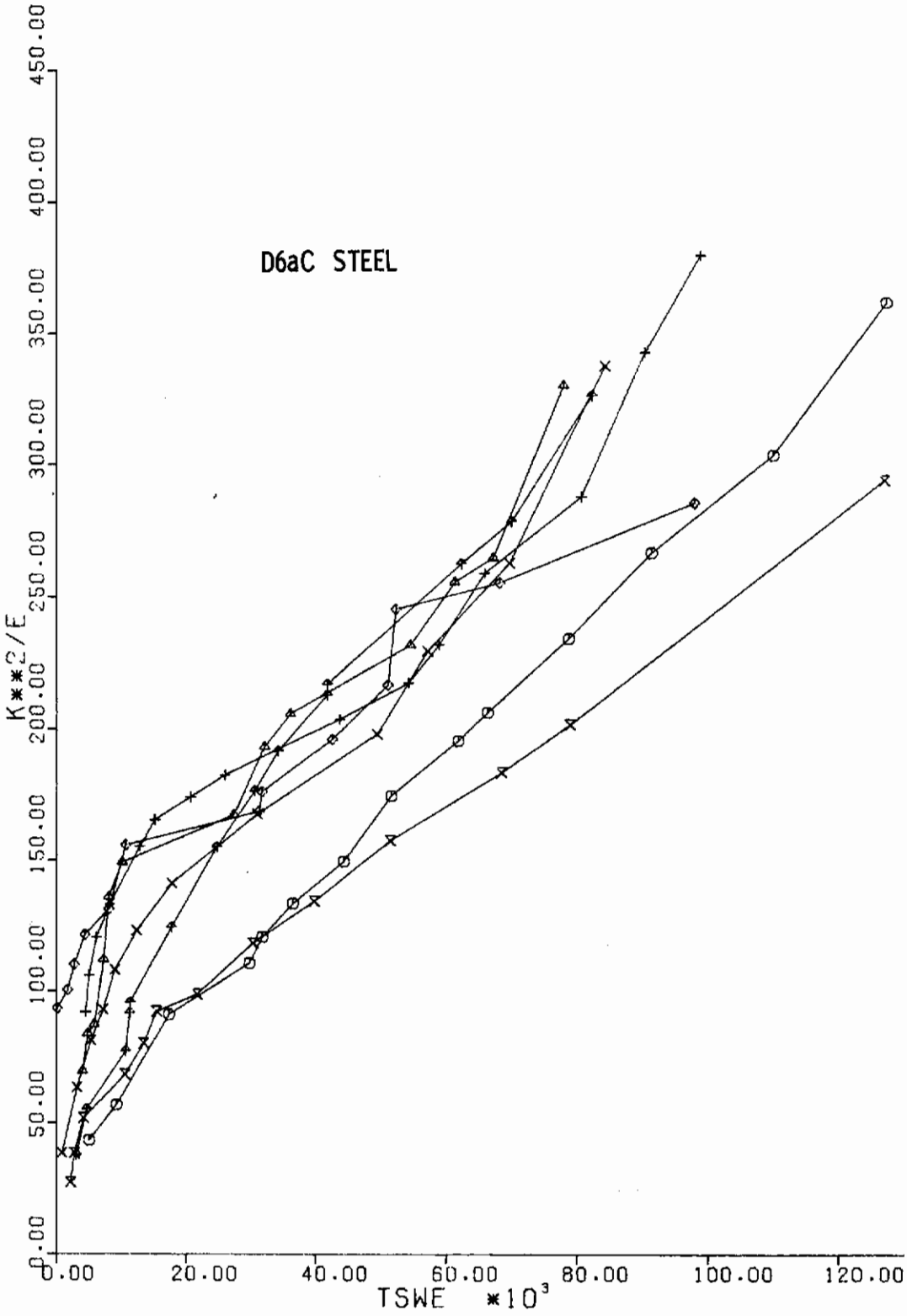

Figure 86. Relationships Shown in Figures 84-85 as Computer Printout

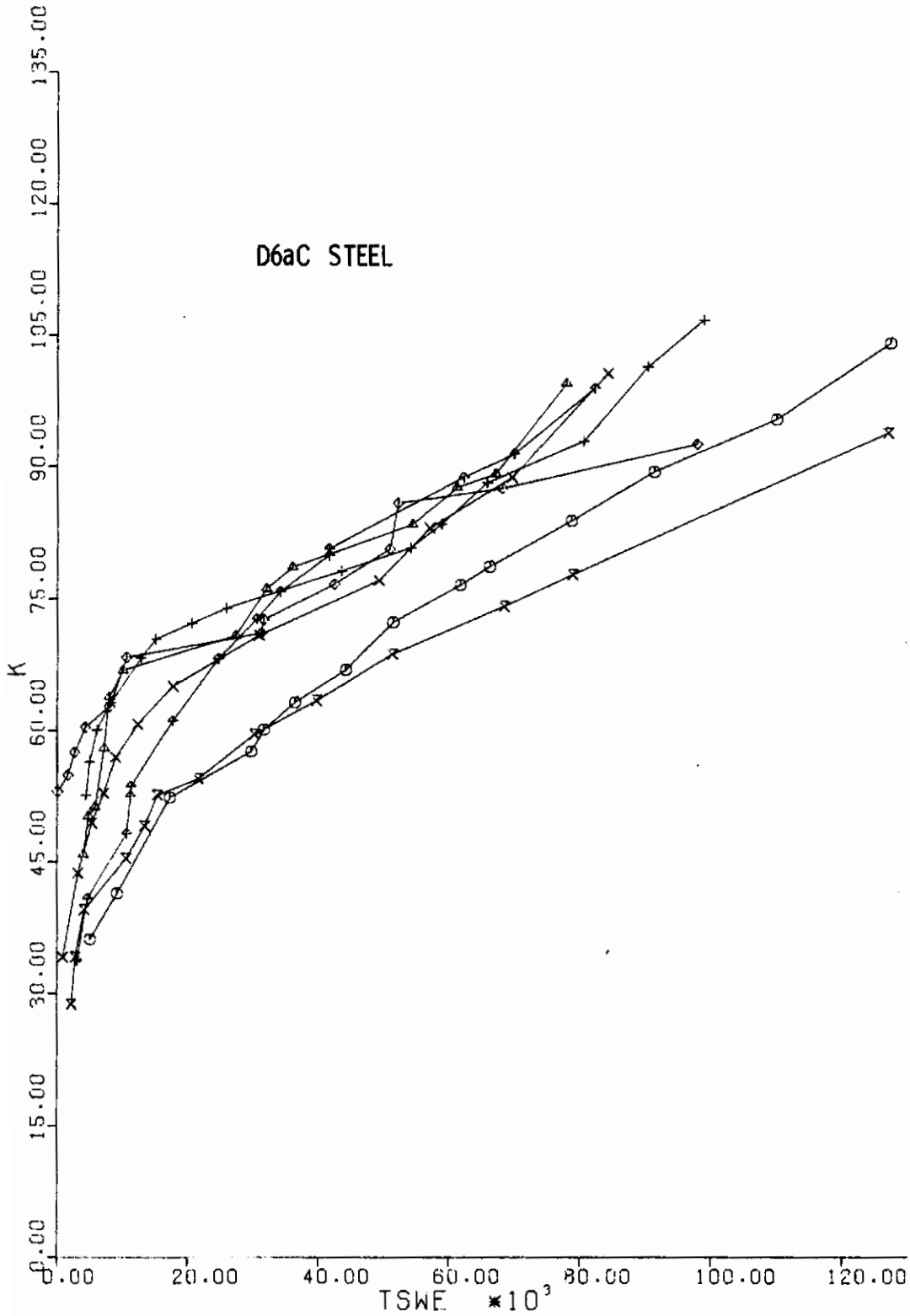

Figure 87. Relationship Between K and Count in Rising Load Tests of 600°F Temper D6aC Steel - 0.10 and 0.29-in. Thick

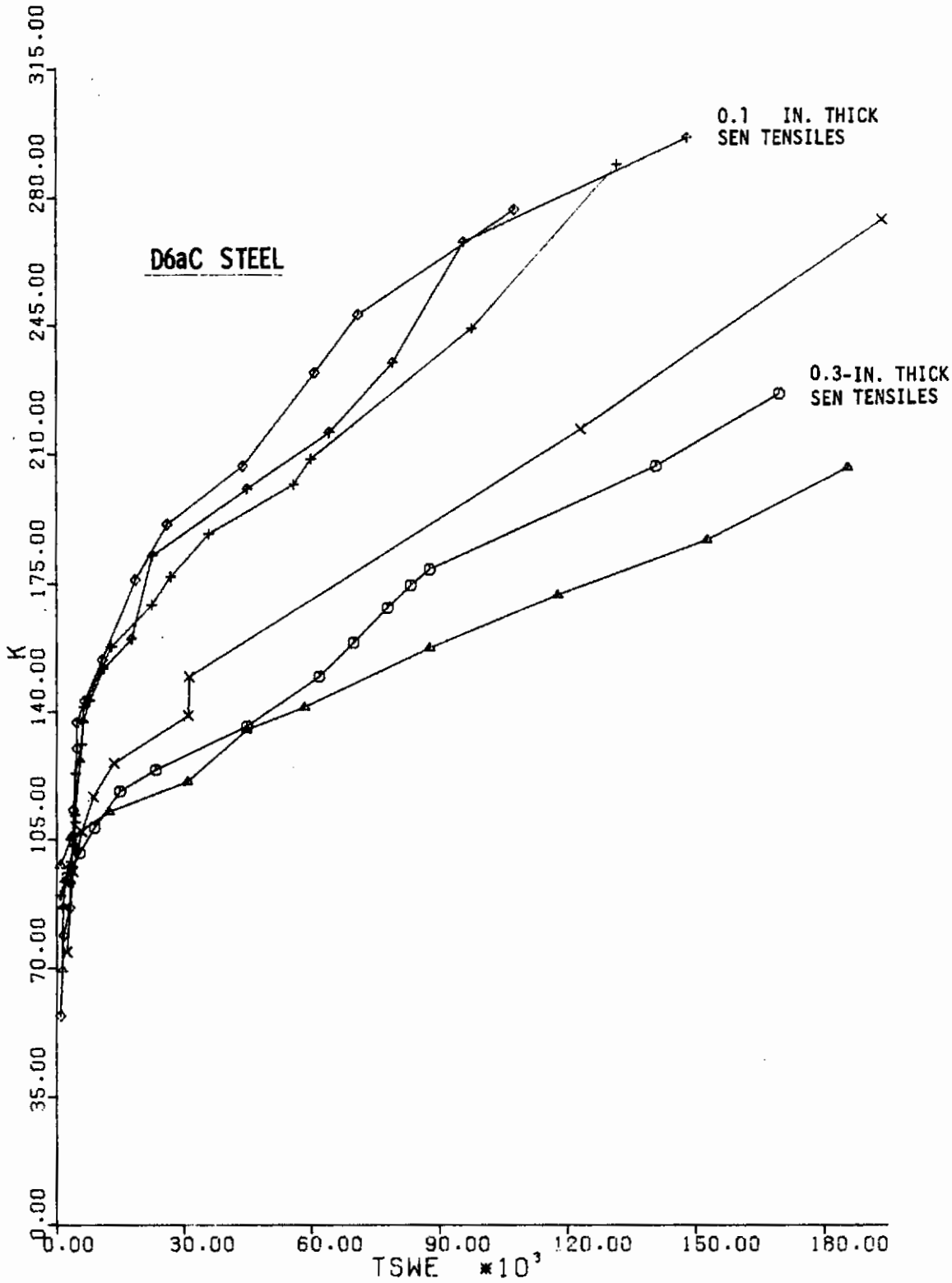

Figure 88. Relationship Between K and Count in Rising Load Tests of 600°F Temper D6aC Steel - 1100°F Tempered D6aC Steel

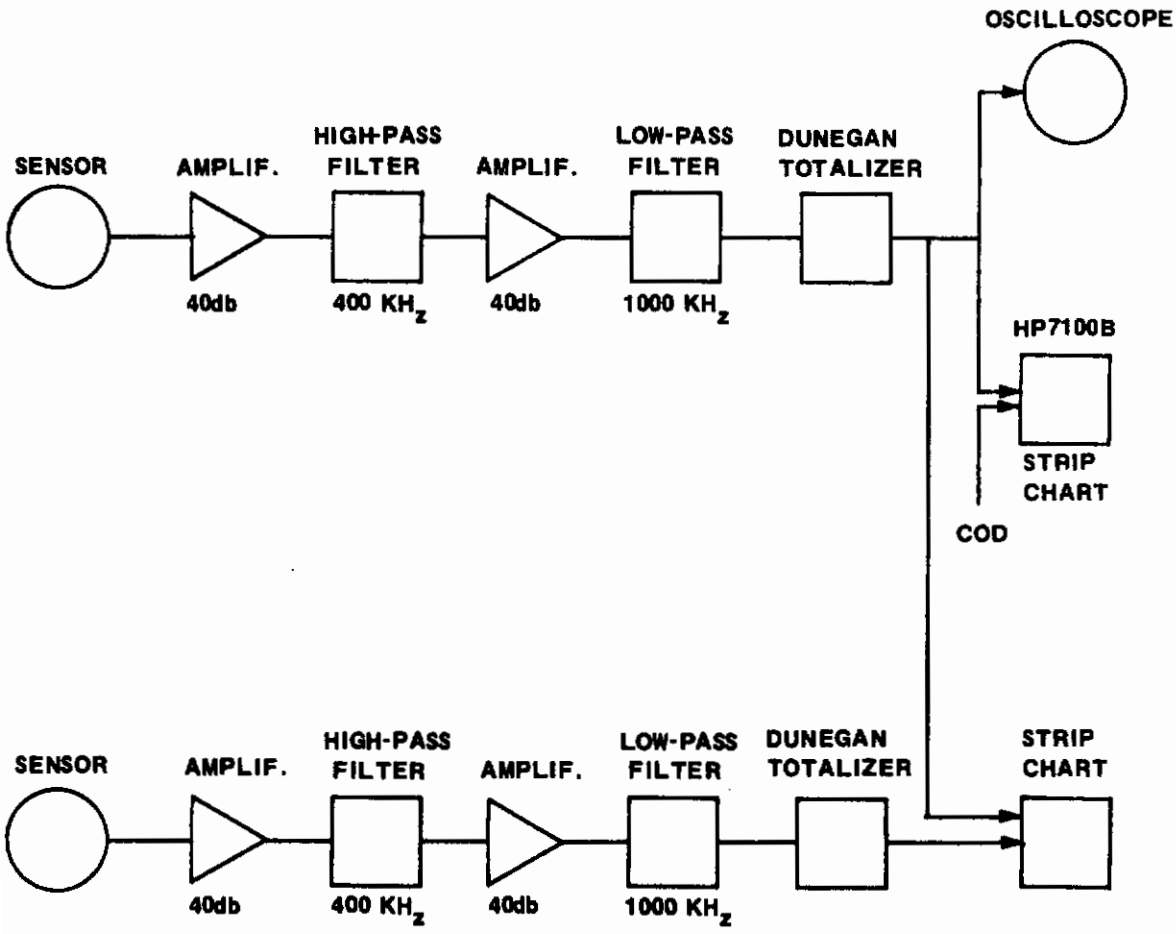

Figure 89. SWAT System for Low-Cycle High-Stress-Intensity Fatigue

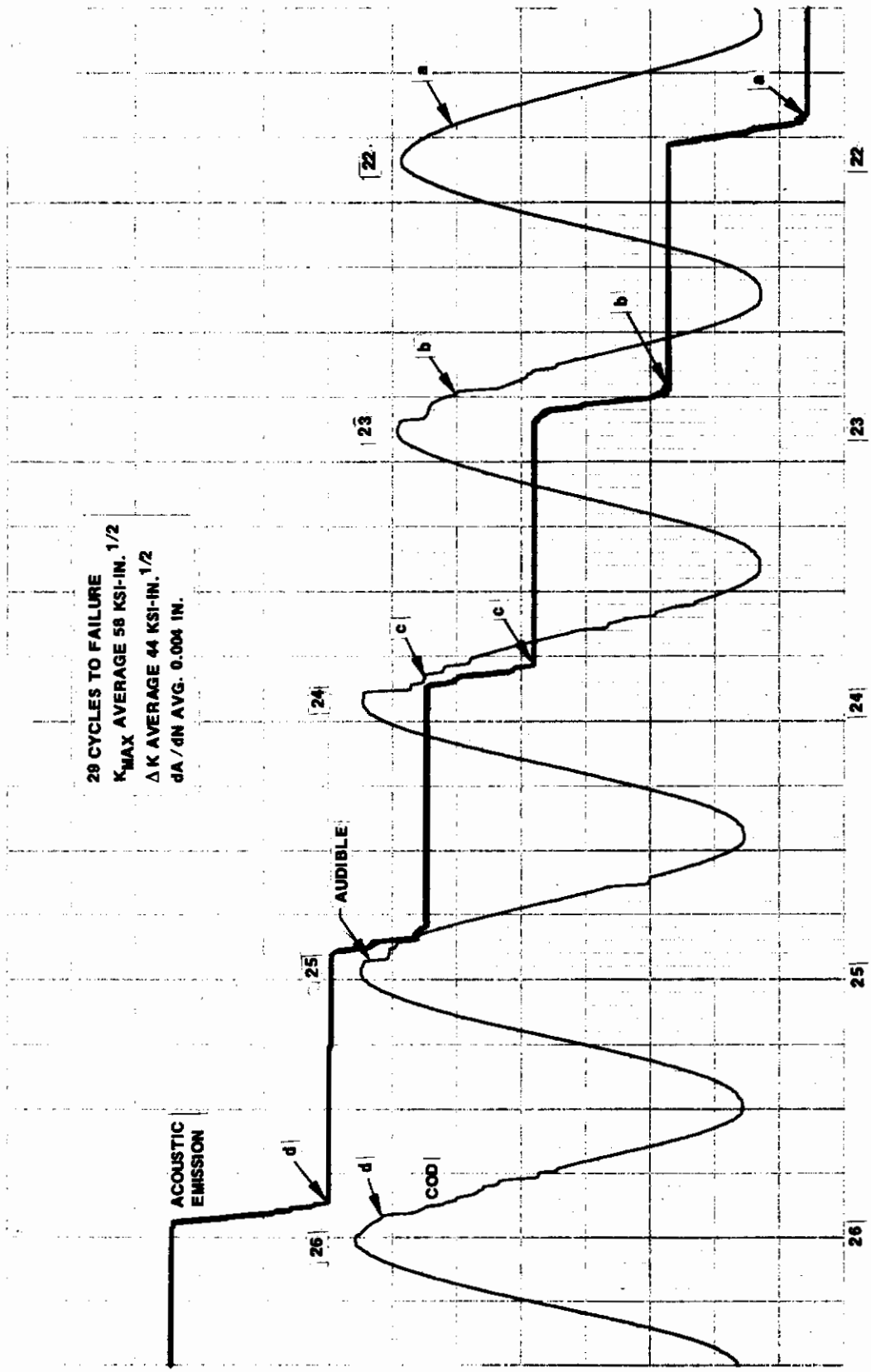

Figure 90. Fatigue Cracking in 600°F D6aC Specimen 6S42 - 0.29-in. Thick

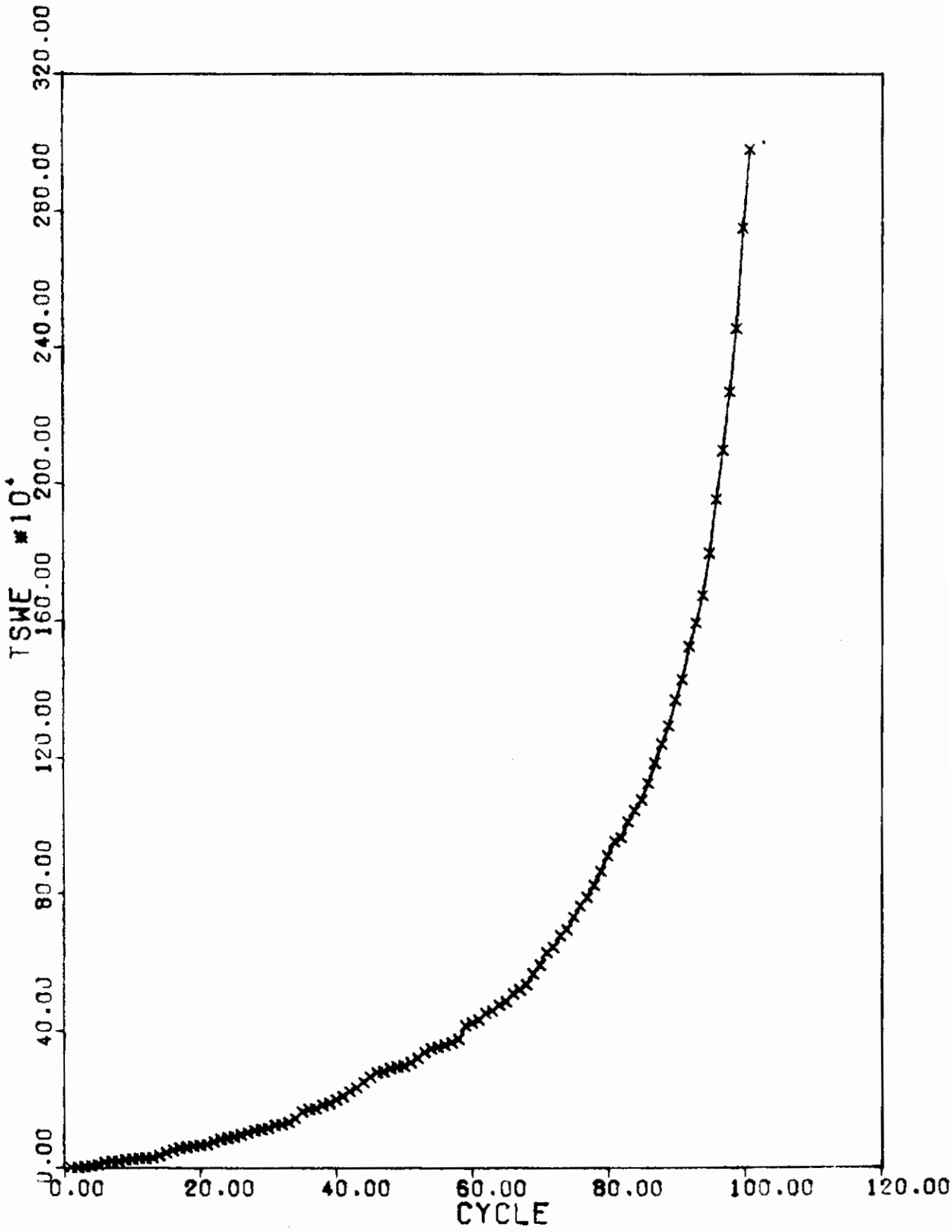

Figure 91. Relationship Between TSWE and Cycle Number for 1100°F D6aC Specimen 6S26 0.1 in. Thick

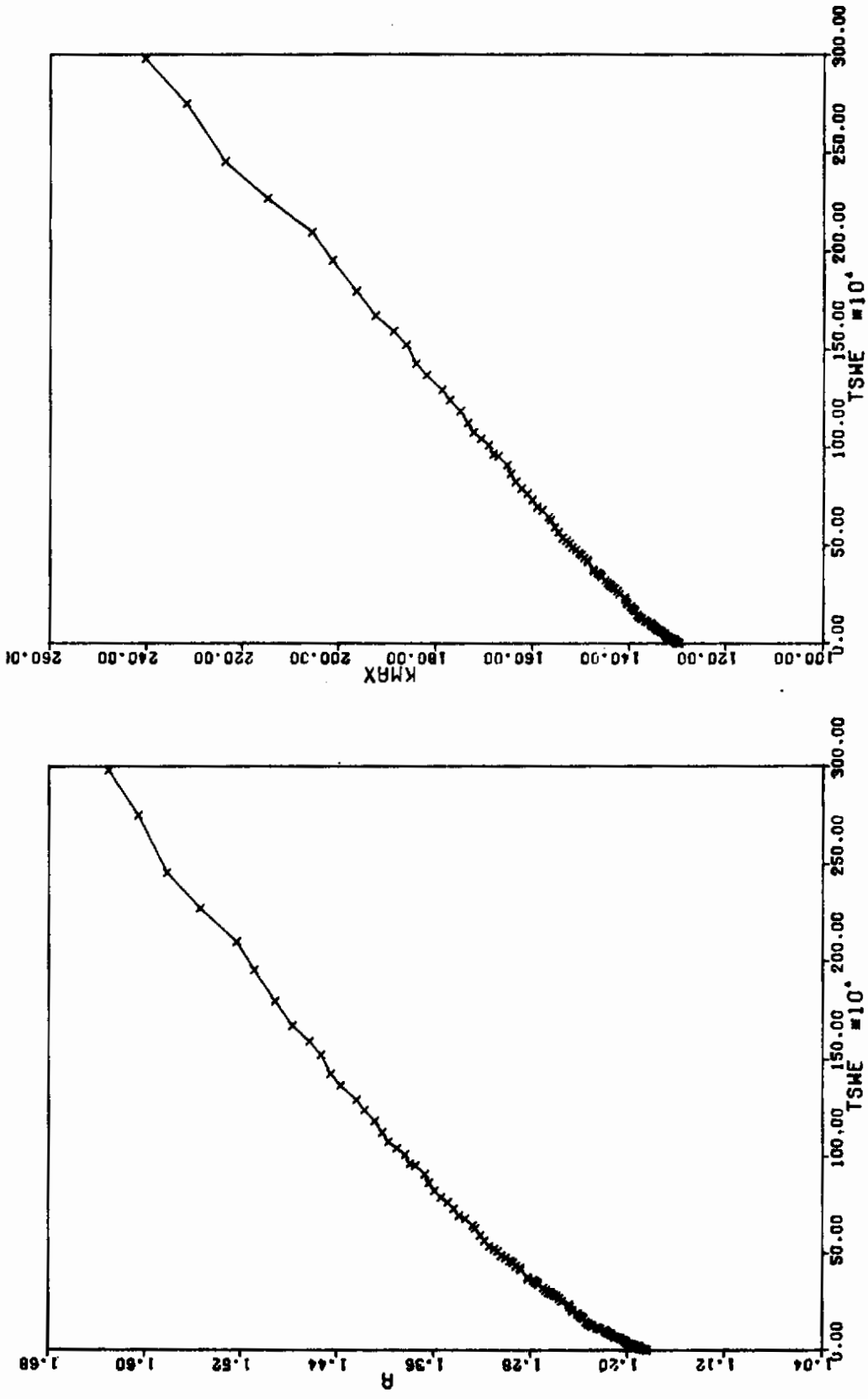

Figure 92. Relationship Between Crack Growth and TSWE in 1100°F D6aC Specimen 6S26 - 0.1-in. Thick

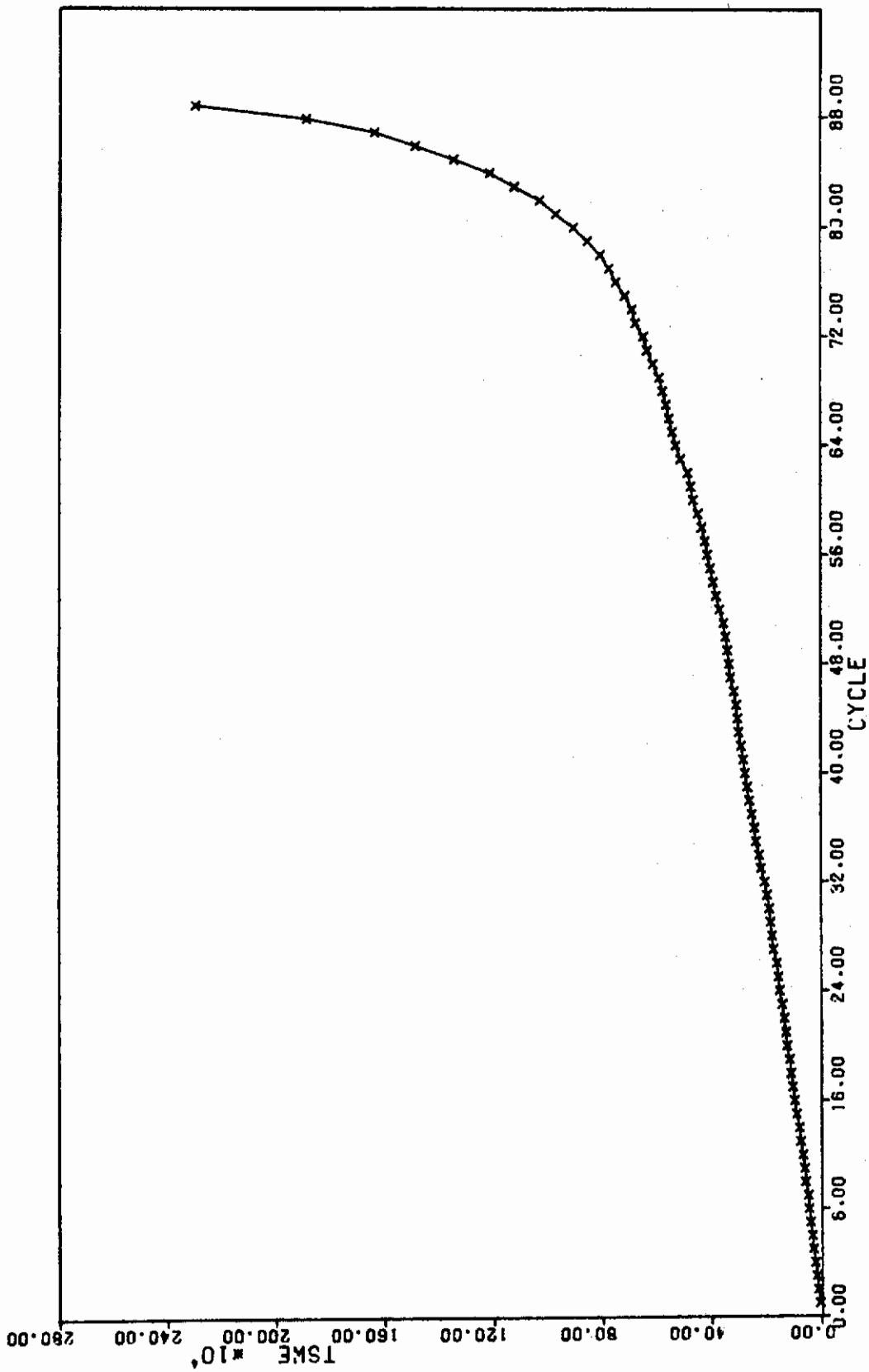

Figure 93. Relationship Between TSWE and Cycle Number for 1100°F D6aC Specimen 6S27 Subjected to Corrosion Fatigue - 0.1-in. Thick

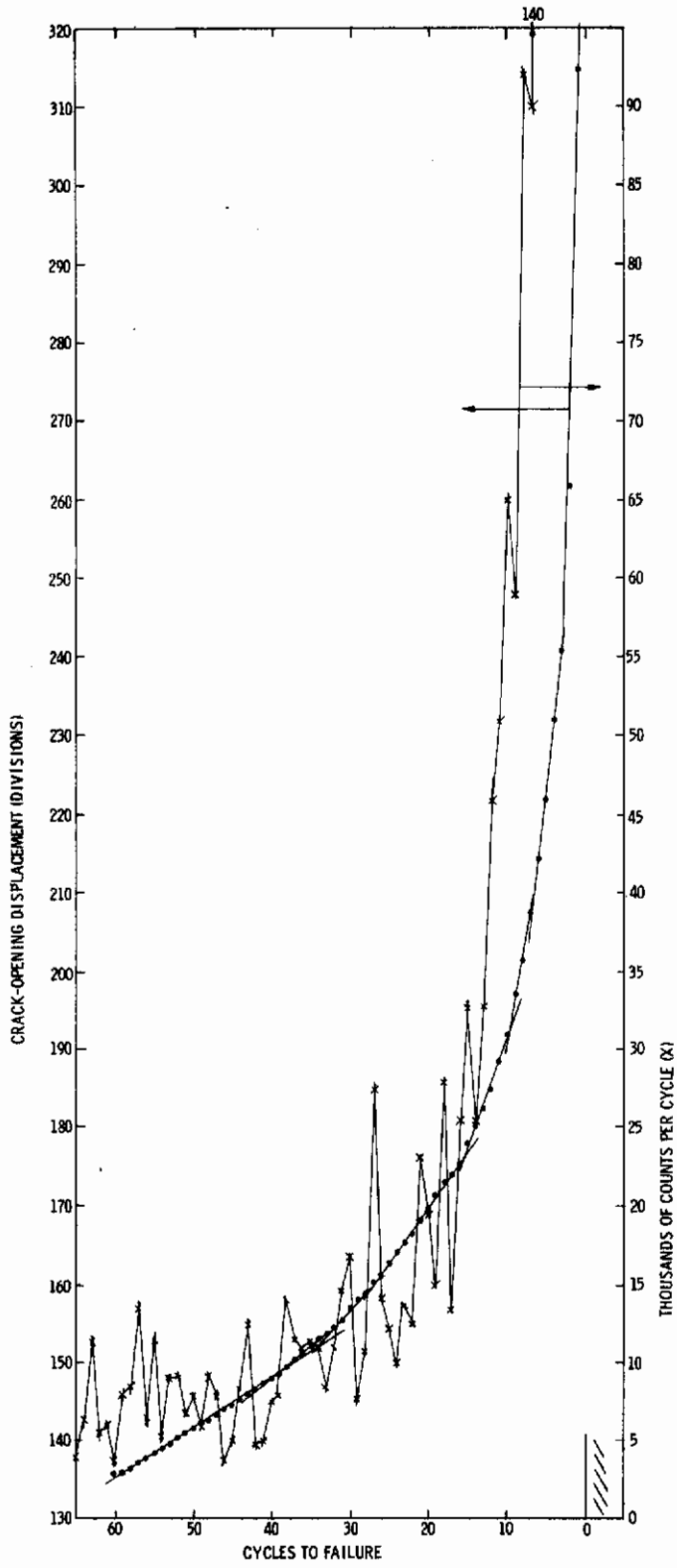

Figure 94. Correlation Between COD and TSWE as a Function of Cycle Number in 1100°F D6aC Specimen 6S27 Subjected to Corrosion Fatigue - 0.1-in. Thick

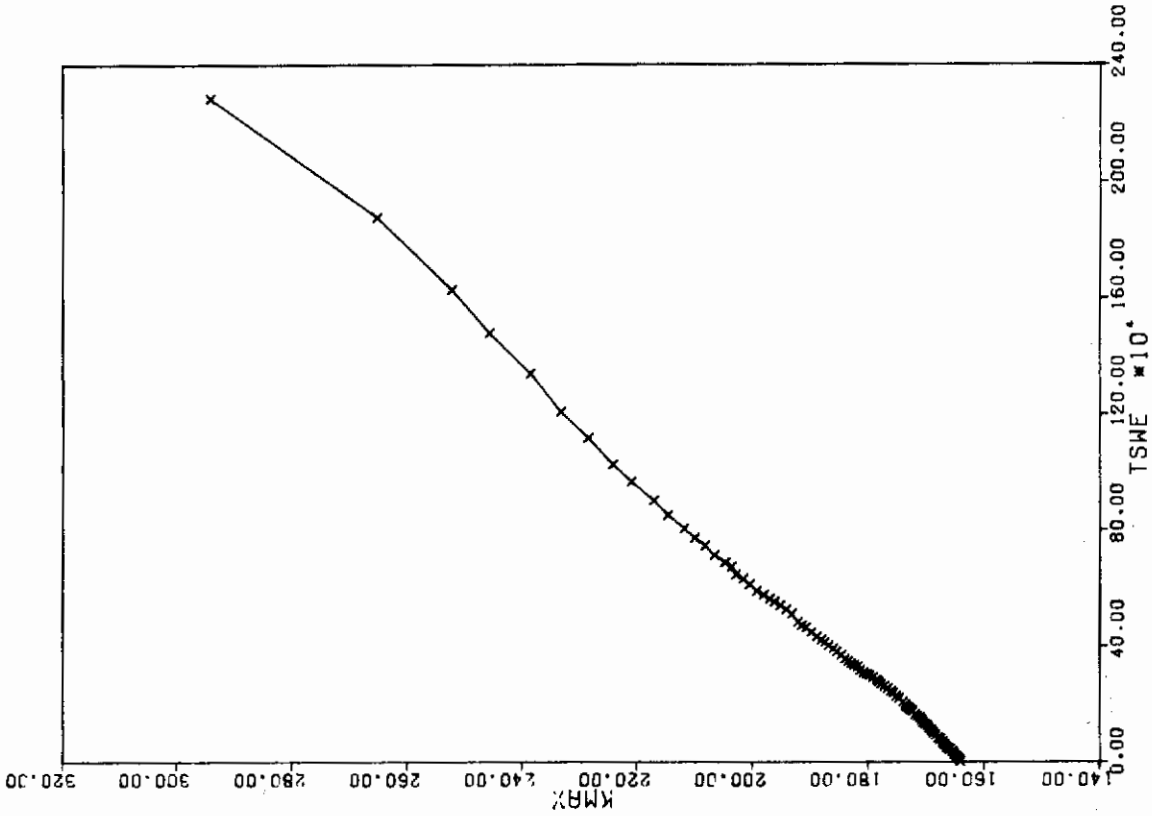

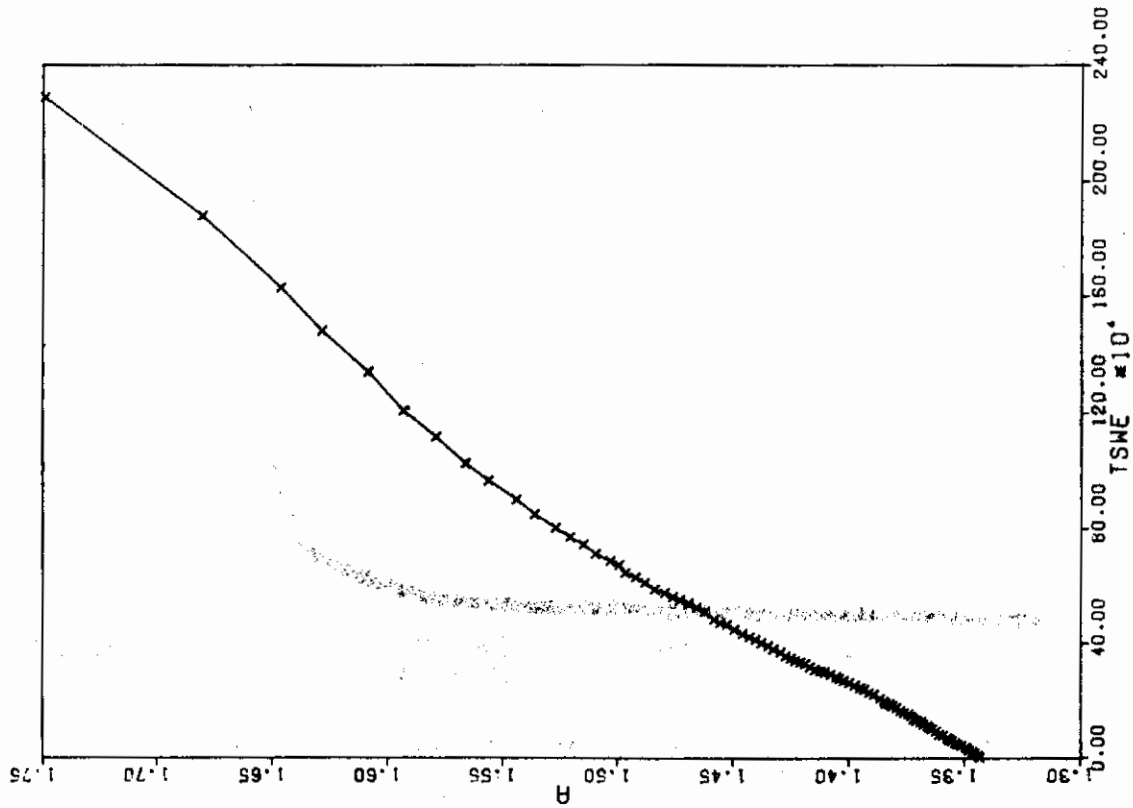

Figure 95. Relationship Between Crack Growth and Cumulative Stress-Wave Count (TSWE) in 1100°F D6aC Subjected to Corrosion Fatigue

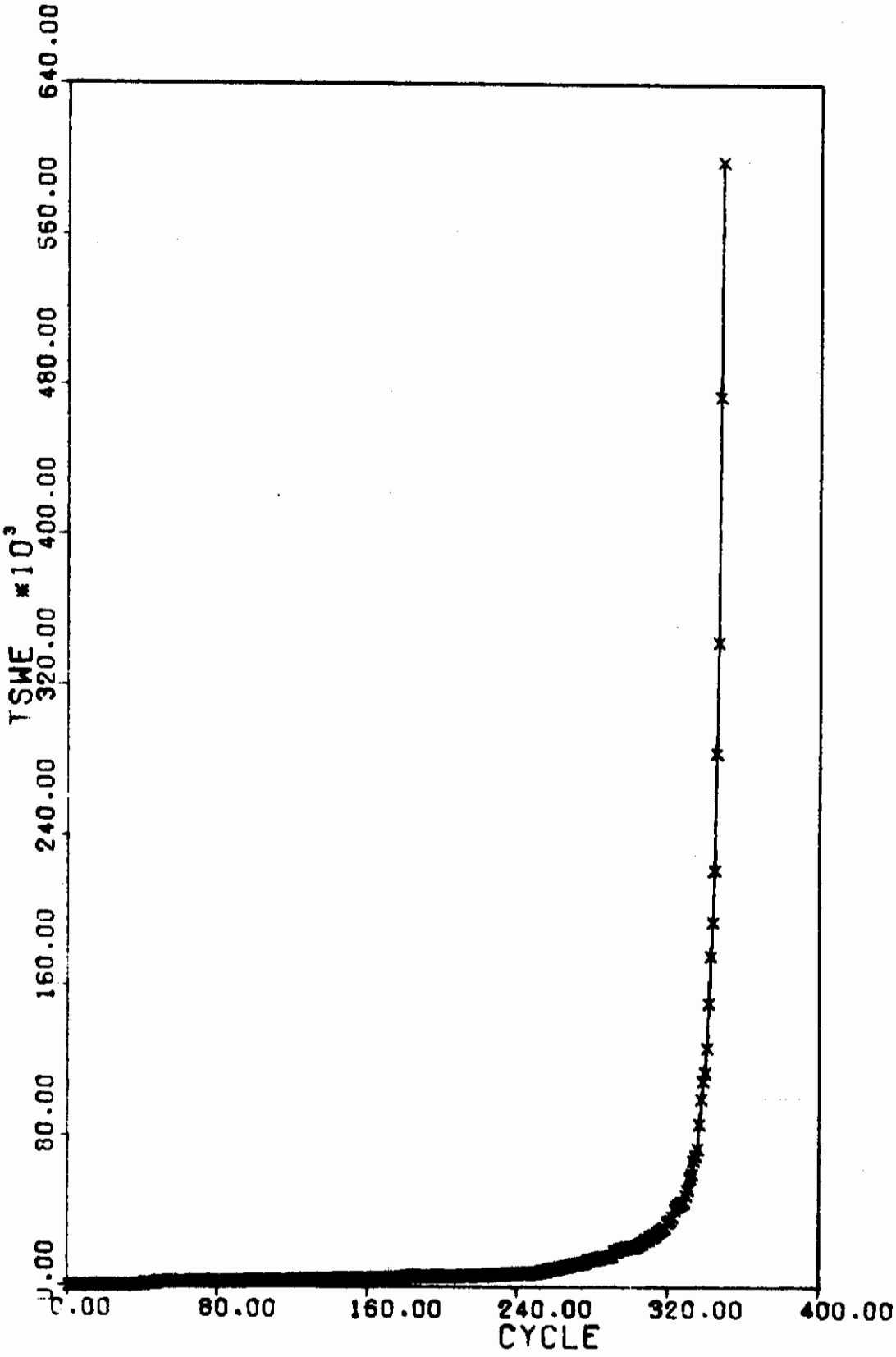

Figure 96. Relationship Between TSWE and Cycle Number for 1100°F D6aC Specimen 6S46 0.29 in. Thick

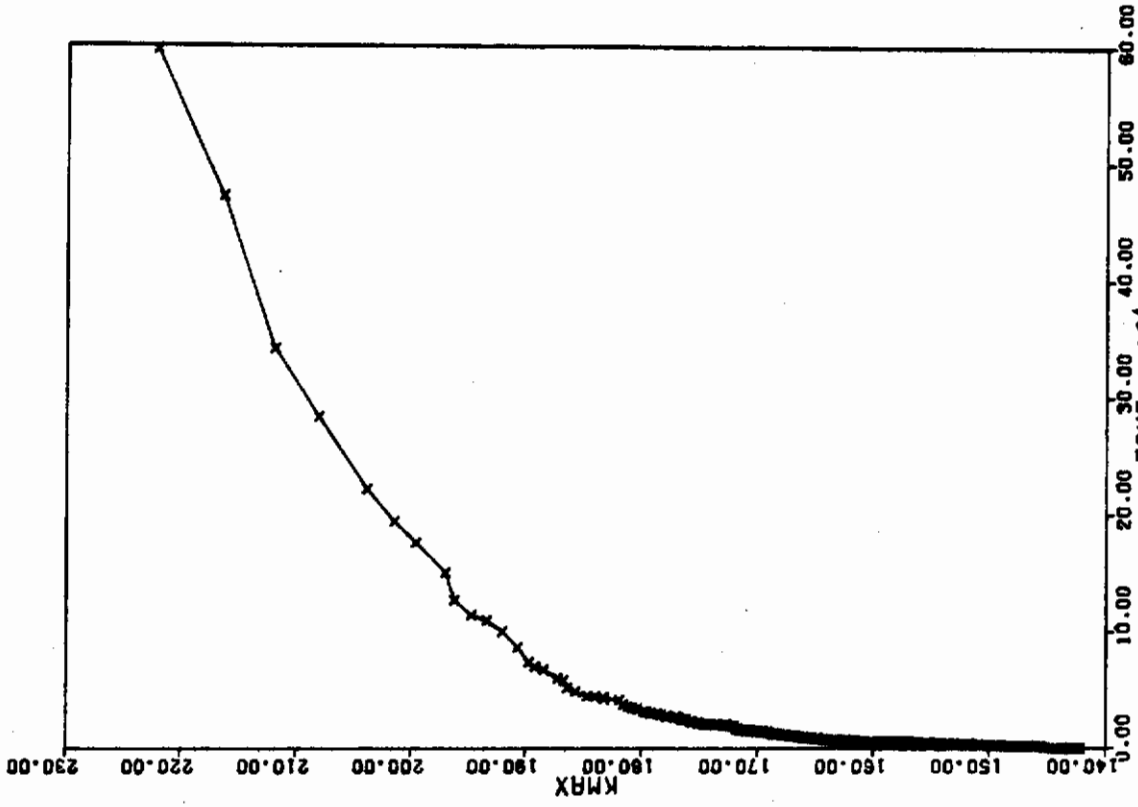

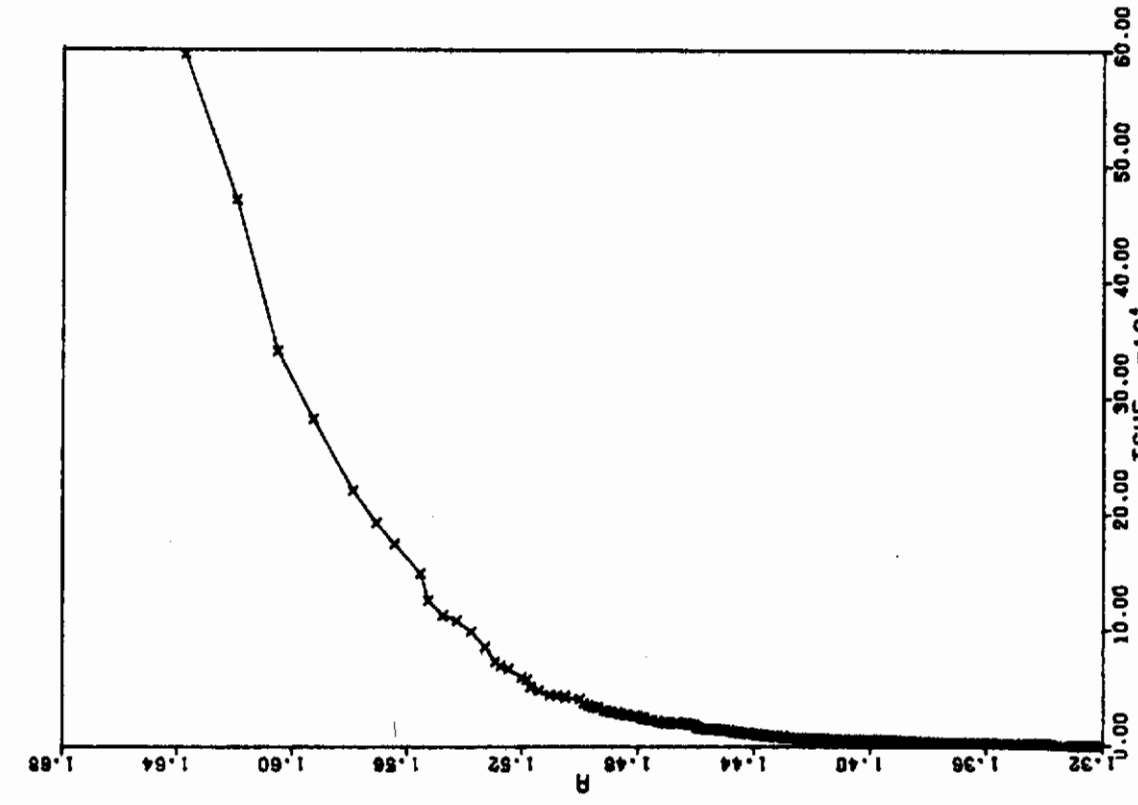

Figure 97. Relationship Between Crack Growth and TSWE in 1100°F D6aC Specimen 6S46 - 0.29-in. Thick

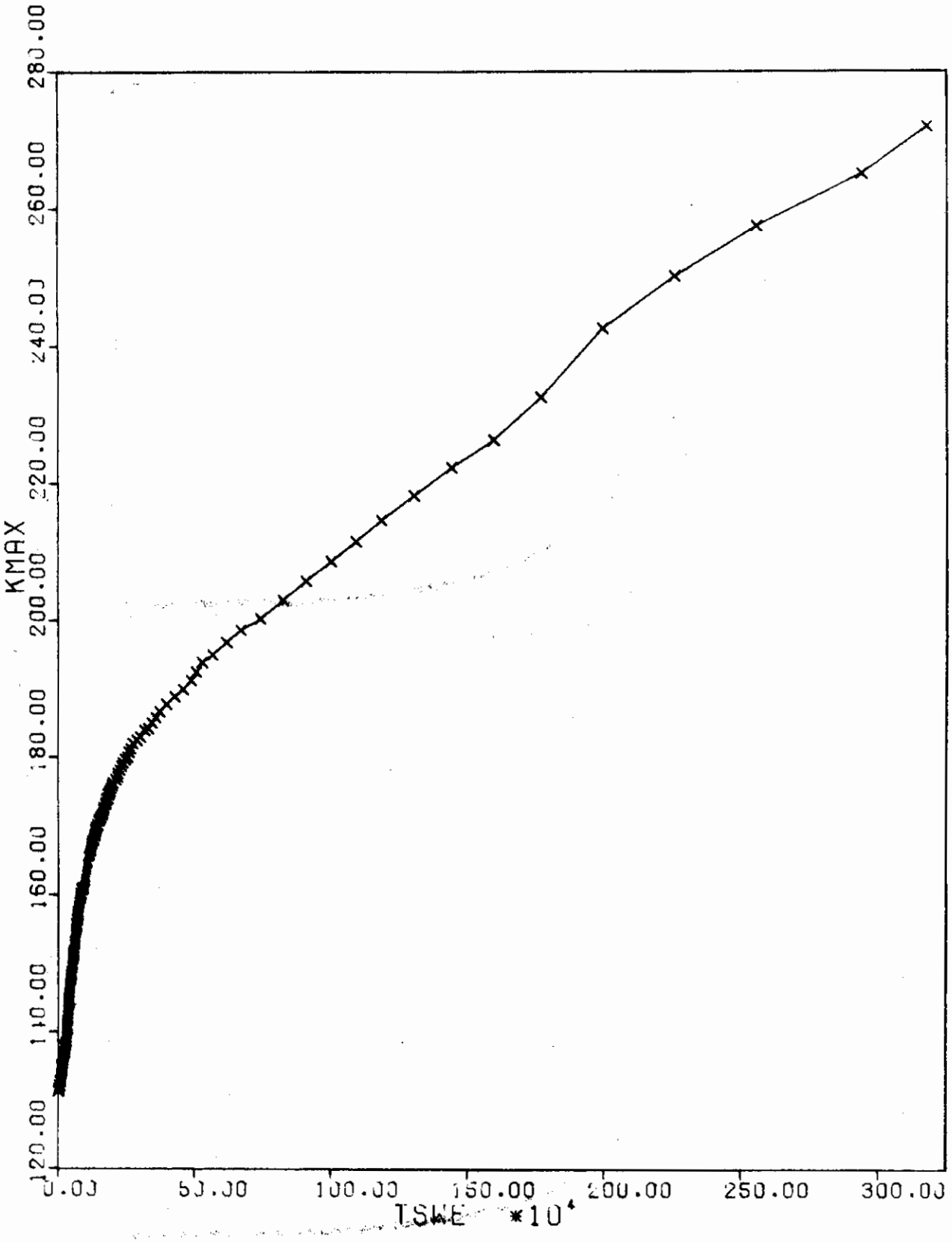

Figure 98. Relationship Between K_{max} and TSWE in 1100°F D6aC Specimen 6S47 Subjected to Corrosion Fatigue 0.29 in. Thick

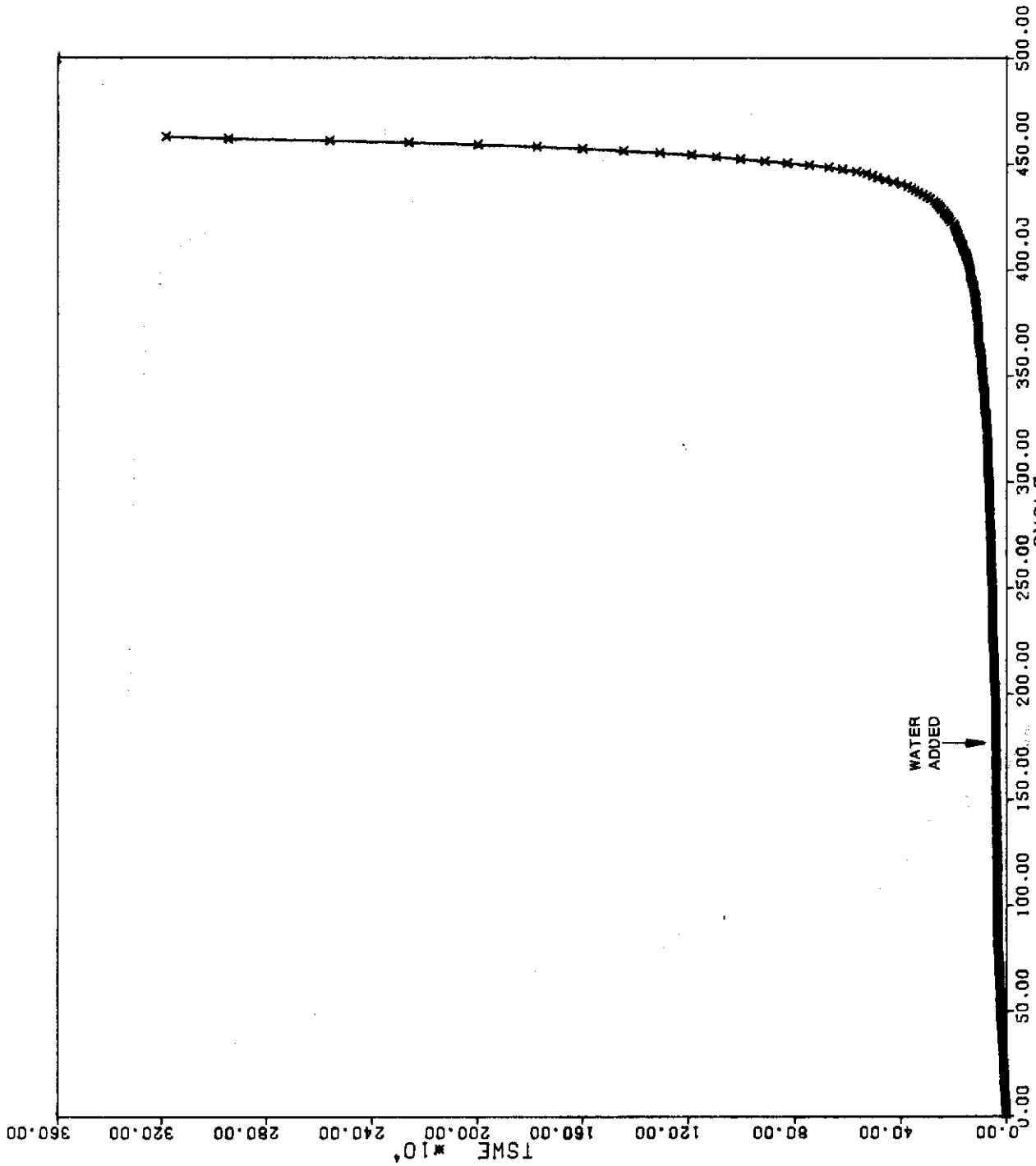

Figure 99. Relationship Between TSWE and Cycle Number in 1100°F D6aC Specimen 6S47 Subjected to Corrosion Fatigue - 0.29-in. Thick

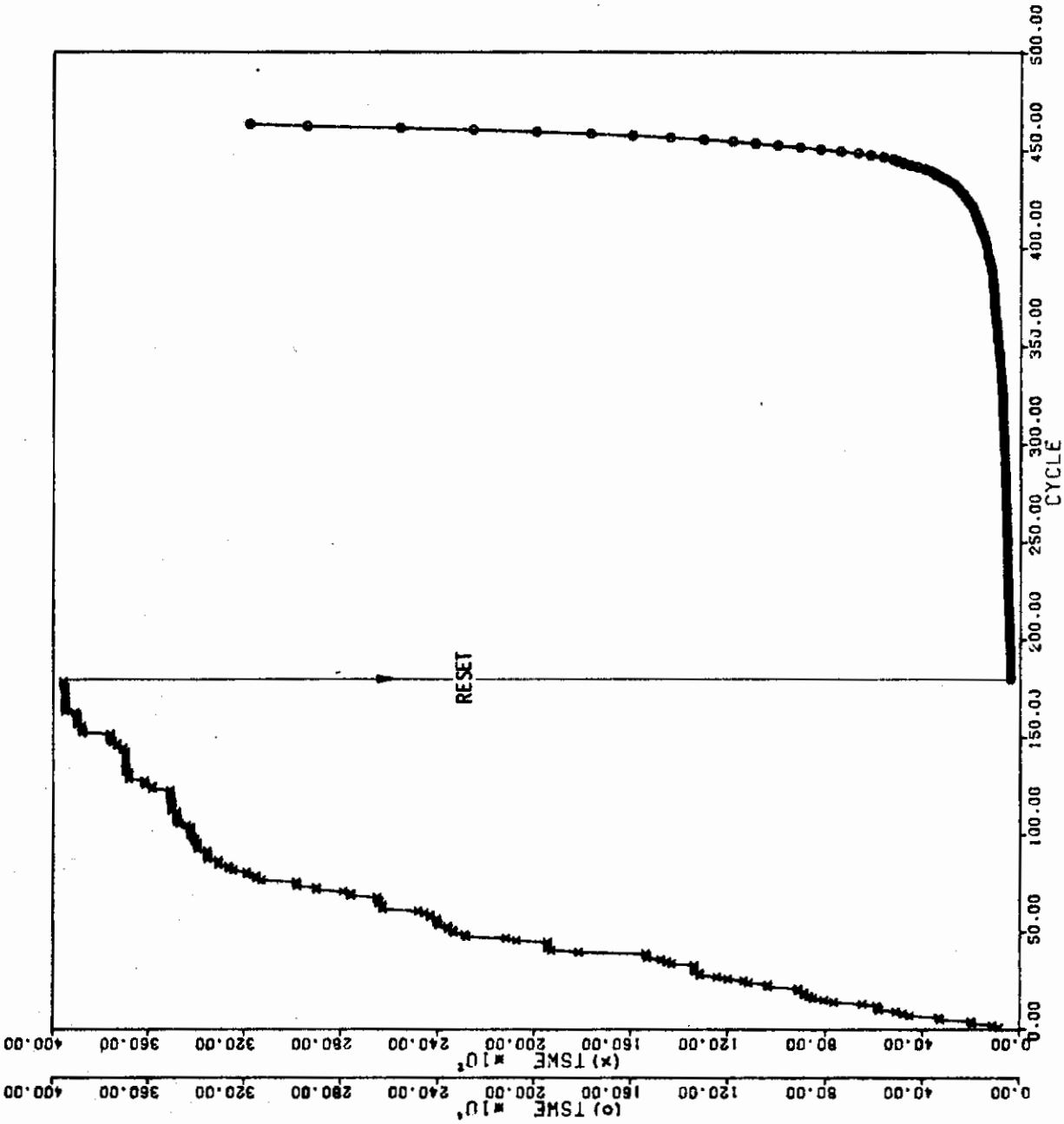

Figure 100. Relationship Between TSWE and Cycle Number in 1100°F D6aC Specimen 6S47 Subjected to Corrosion Fatigue - 0.29-in. Thick

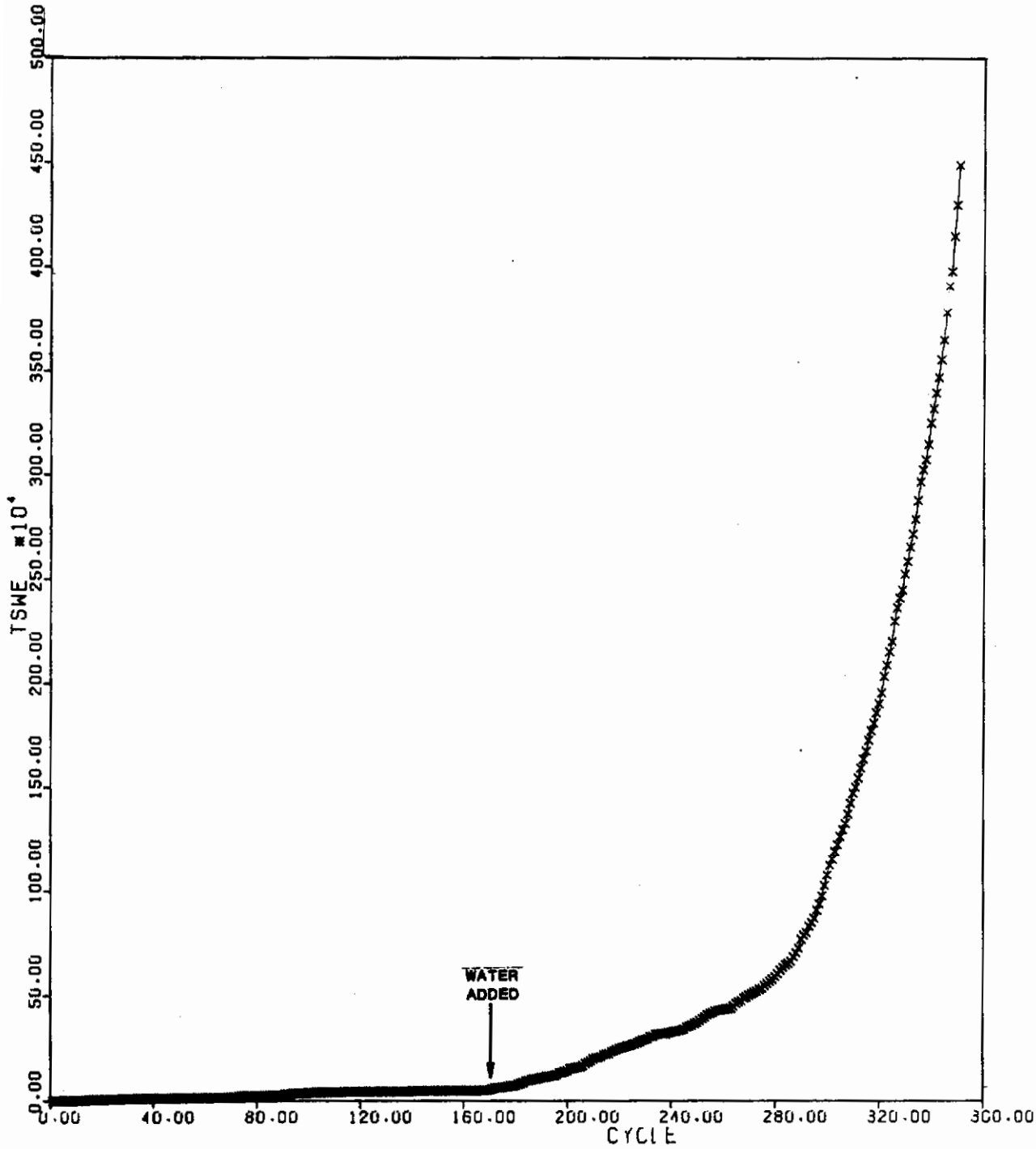

Figure 101. Effect of Corrosion Fatigue on Relationship Between TSWE and Cycle Number for 600°F D6aC Specimen 6S23 - 0.1-in. Thick

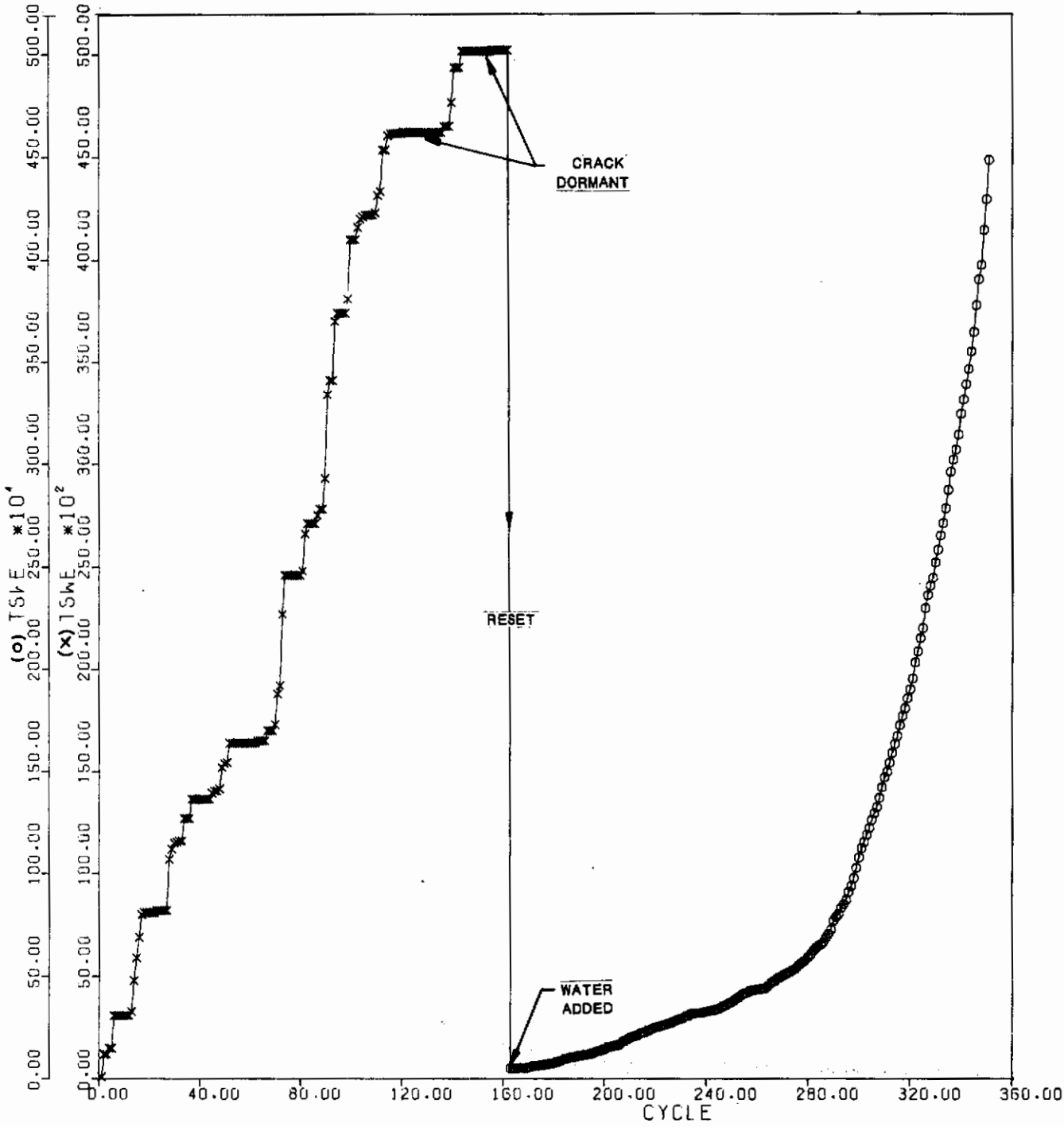

Figure 102. Effect of Corrosion Fatigue on Relationship Between TSWE and Cycle Number for 600°F D6aC Specimen 6S23 - 0.1-in. Thick

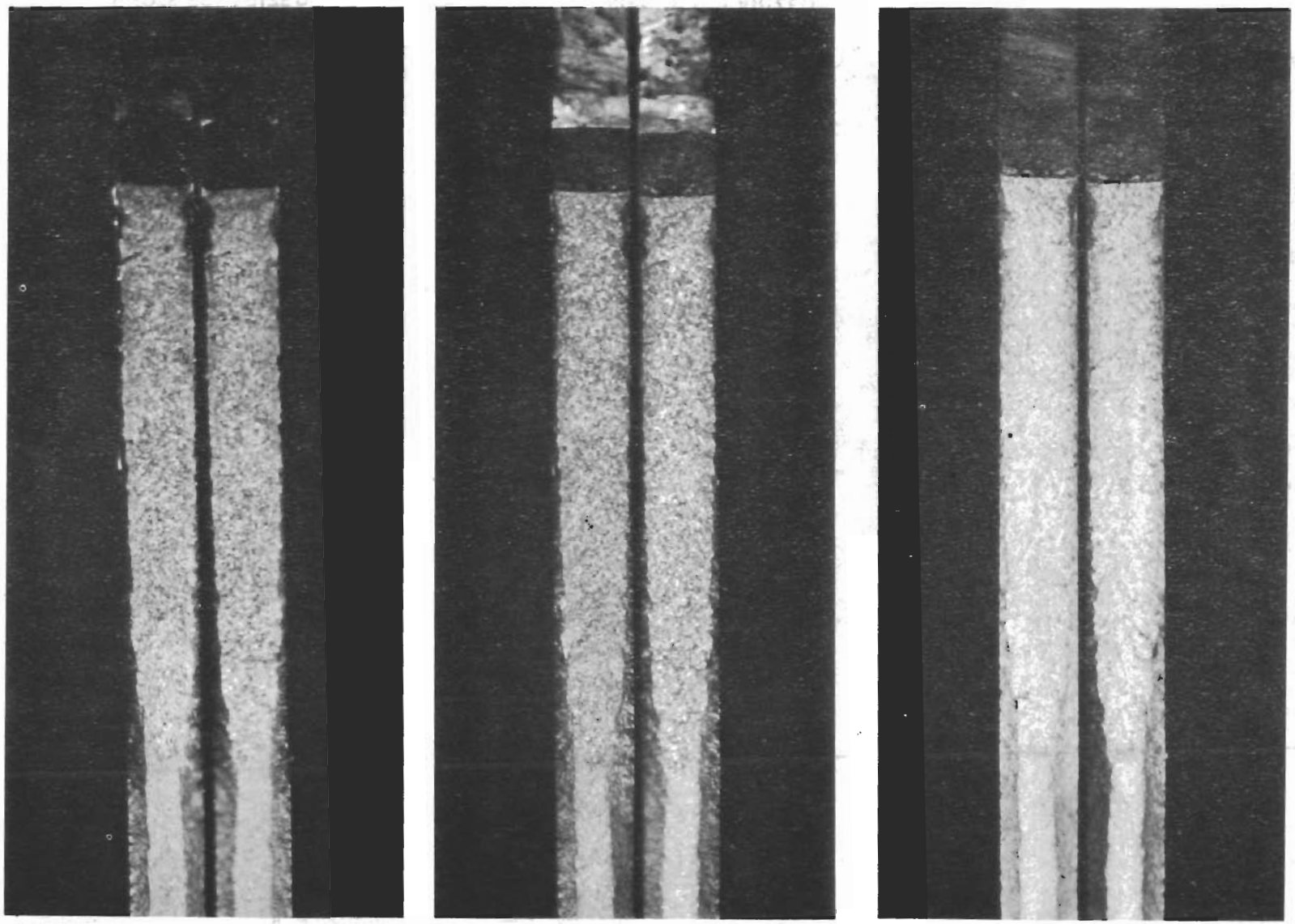

Figure 103a. 600°F Tempered D6aC Specimen 6S22 Tested for 296 Cycles with Water - 0.1-in. Thick (5X photograph at 90° to the flat fracture)

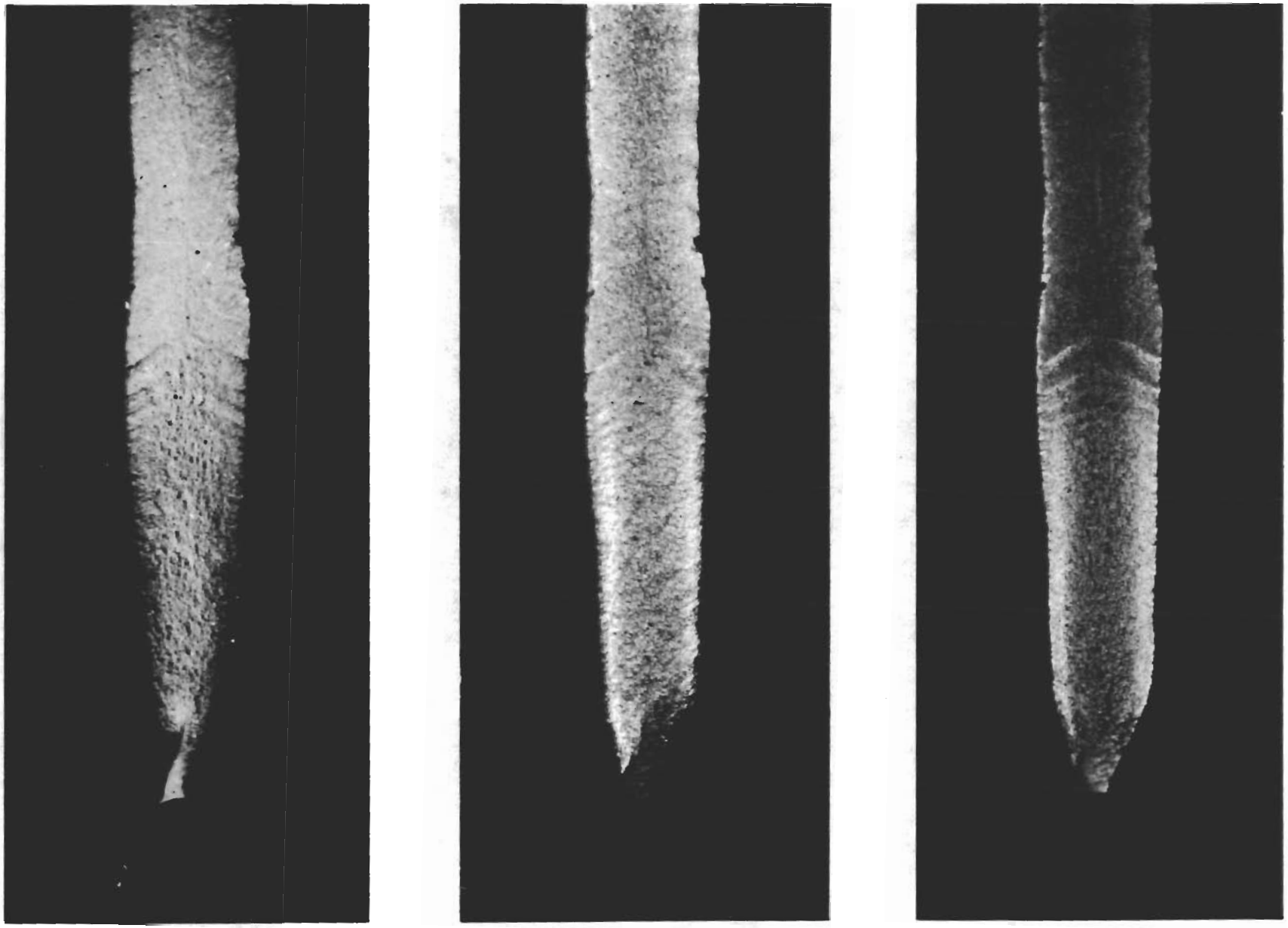

Figure 103b. 1100°F Tempered D6aC Specimen 6S27 Tested for 500 Cycles with Water - 0.1-in. Thick (5X photograph at 90° to the oblique fracture)

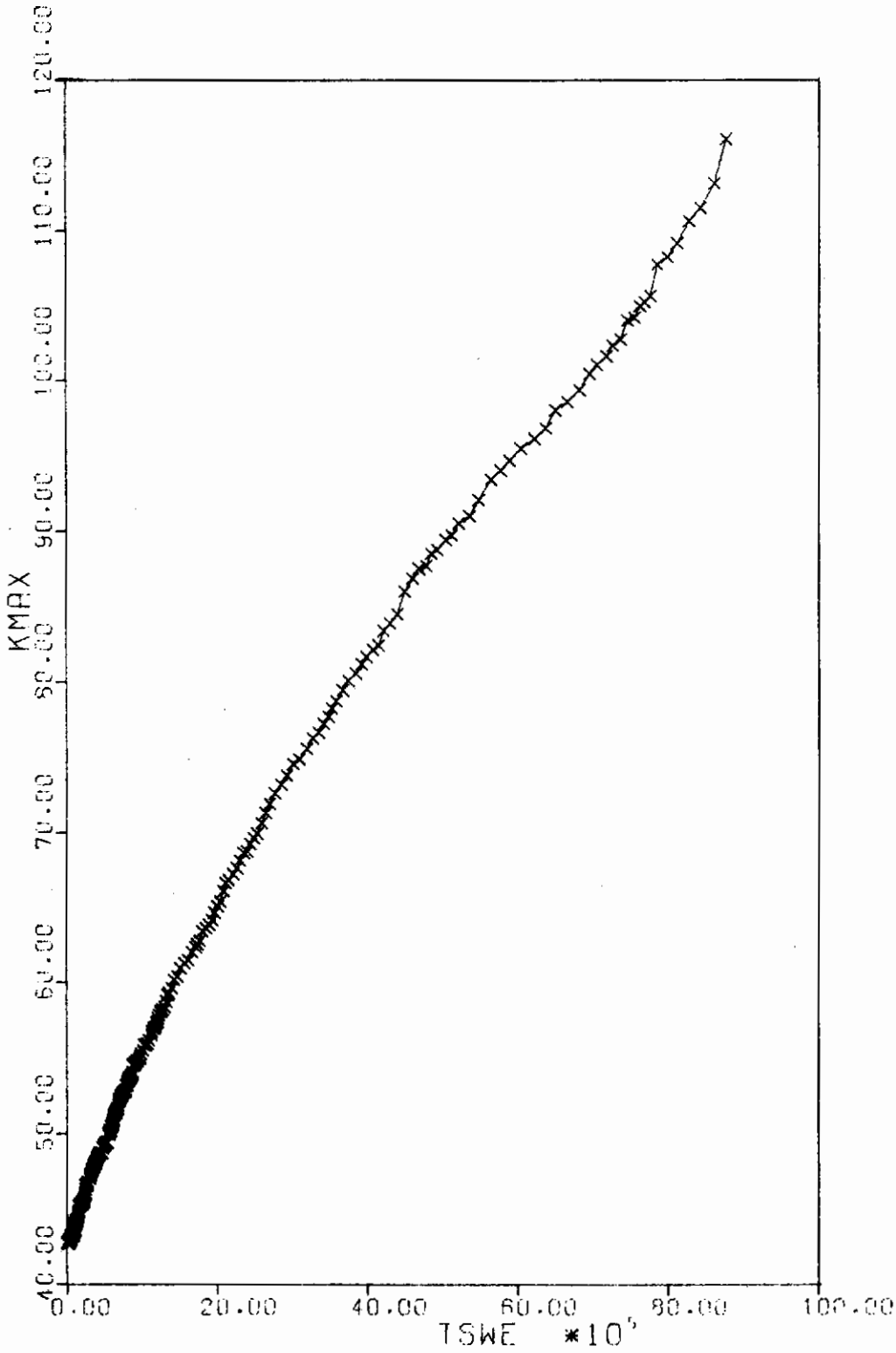

Figure 104. Relationship Between K_{max} and TSWE in 600°F D6aC Specimen 6S22 Subjected to Corrosion Fatigue 0.1 in. Thick

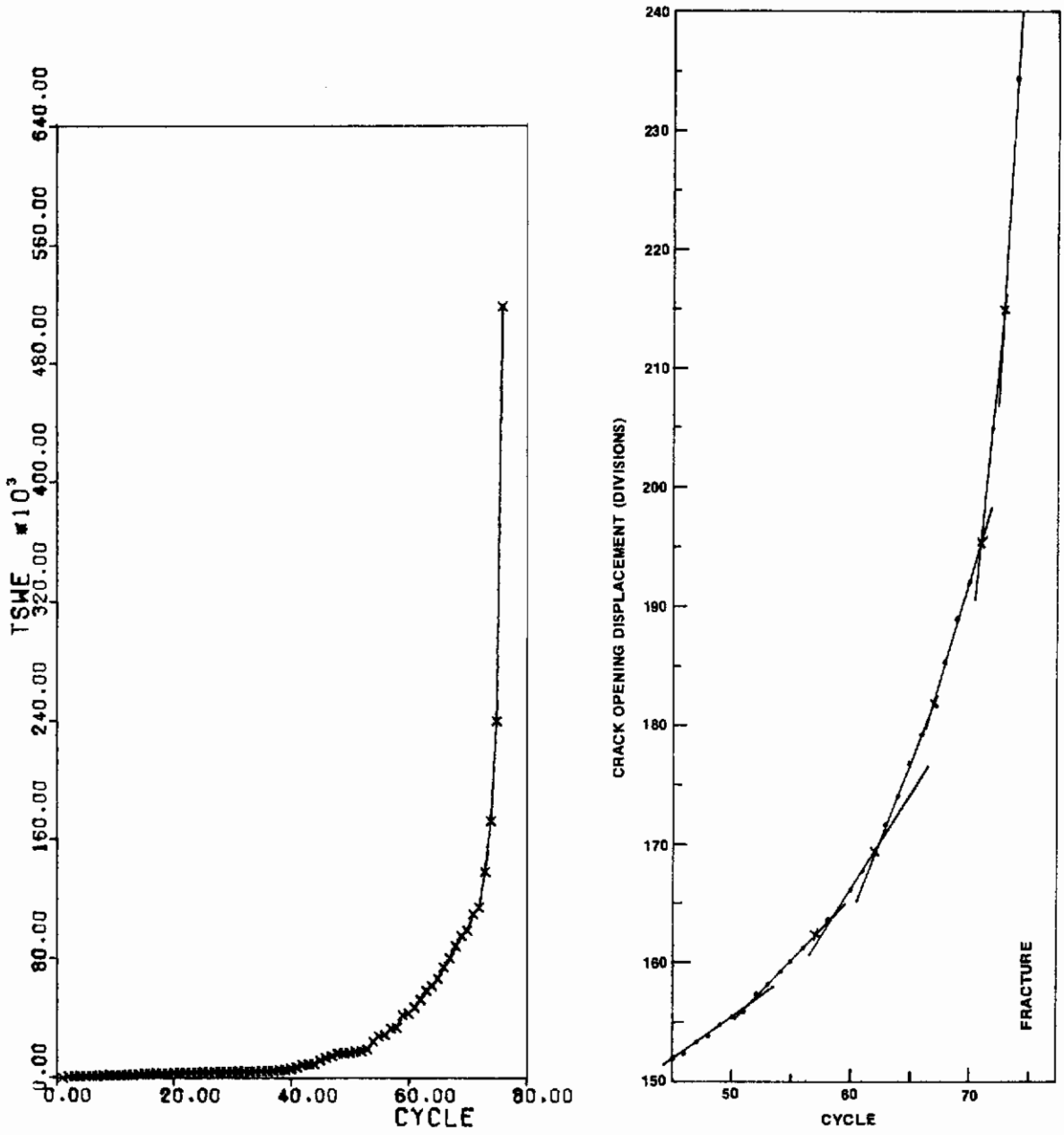

Figure 105. Correlation Between COD and TSWE as a Function of Cycle Number in Solution Treated and Aged 6Al-4V Titanium Specimen SS21 - 0.1-in. Thick

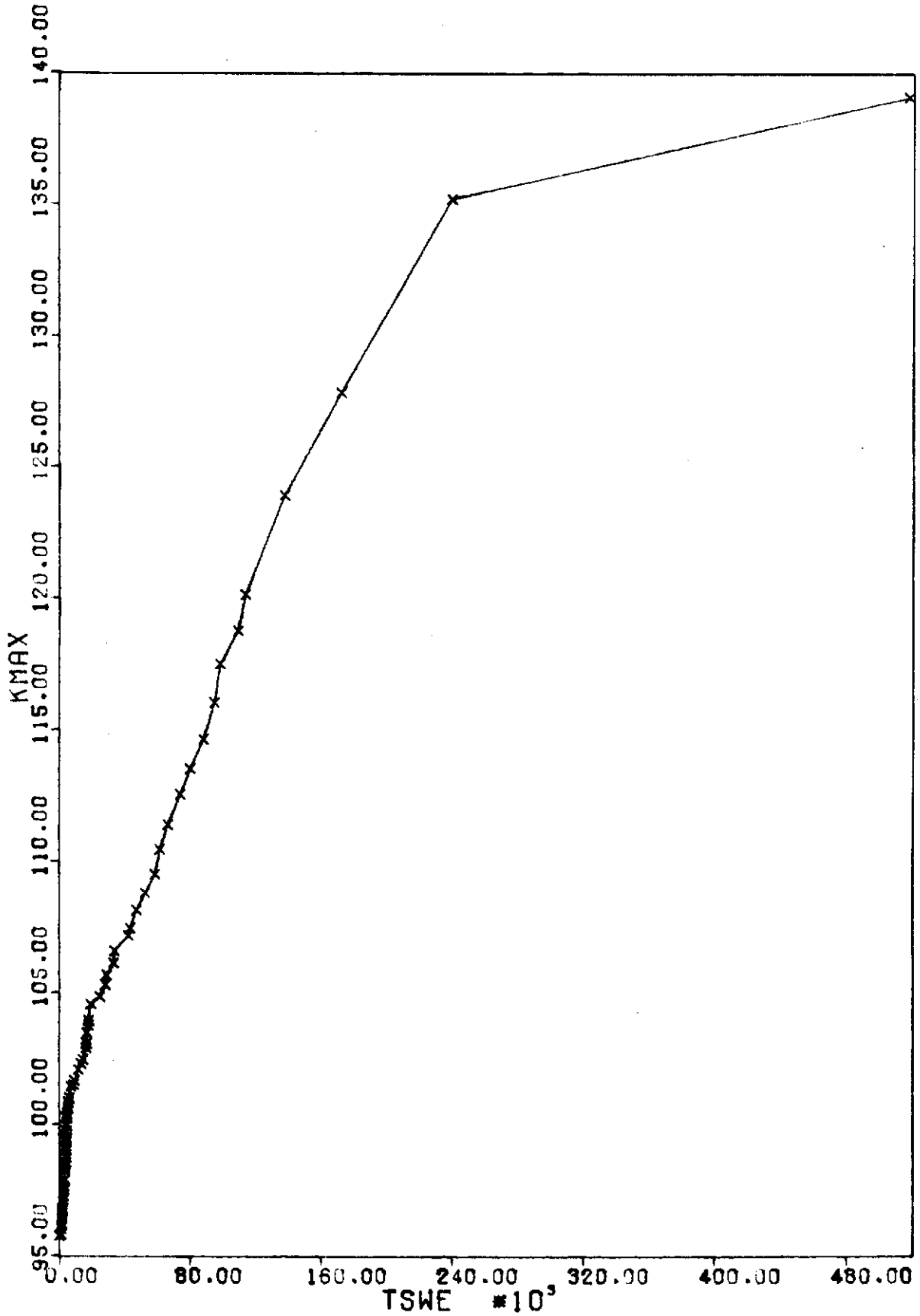

Figure 106. Relationship Between K_{max} and TSWE in Solution Treated and Aged 6Al-4V Titanium Specimen SS21 0.1 in. Thick

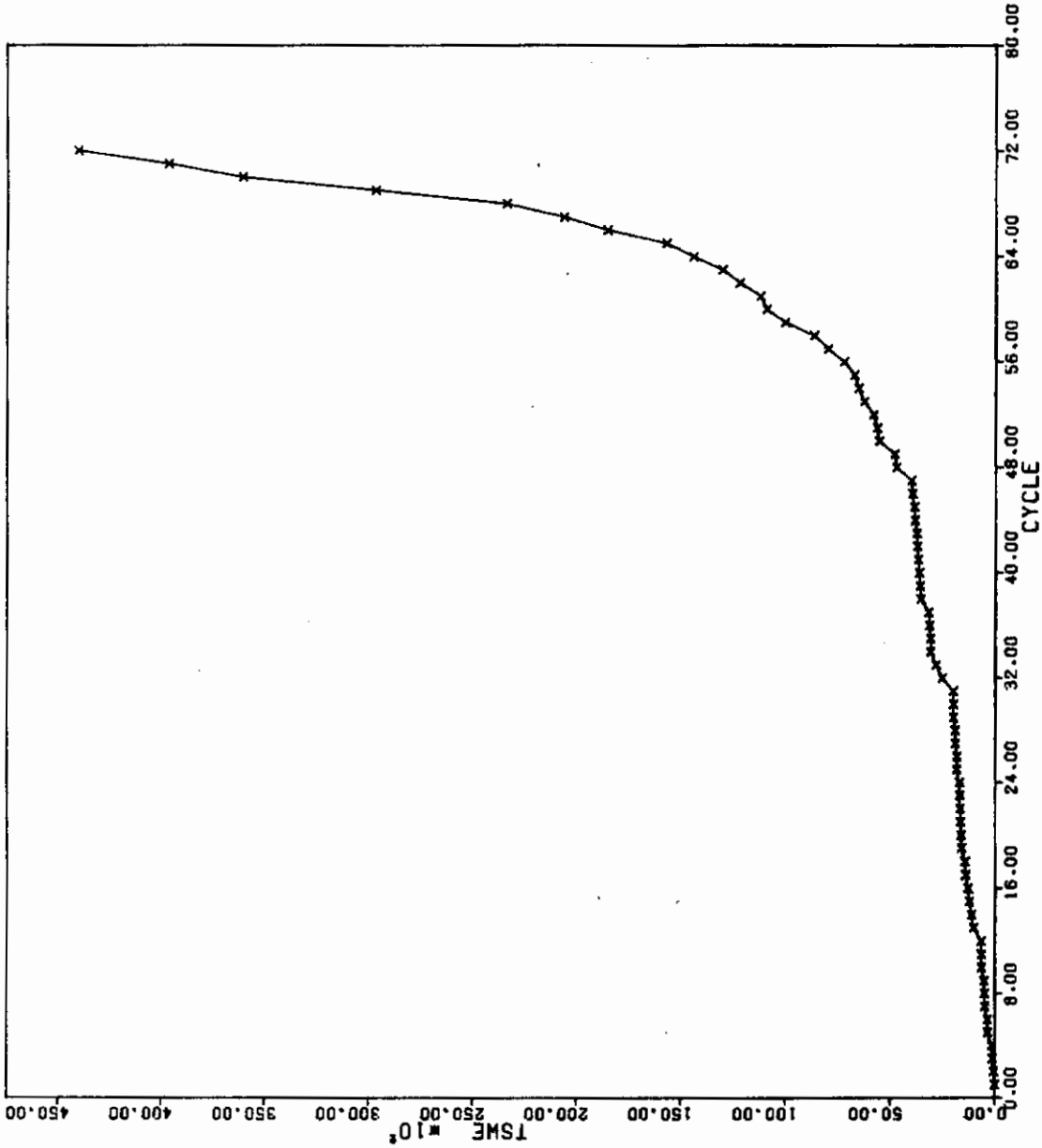

Figure 107. Relationship Between TSWE and Cycle Number for Annealed 6Al-4V Titanium Specimen ES23 - 0.1-in. Thick

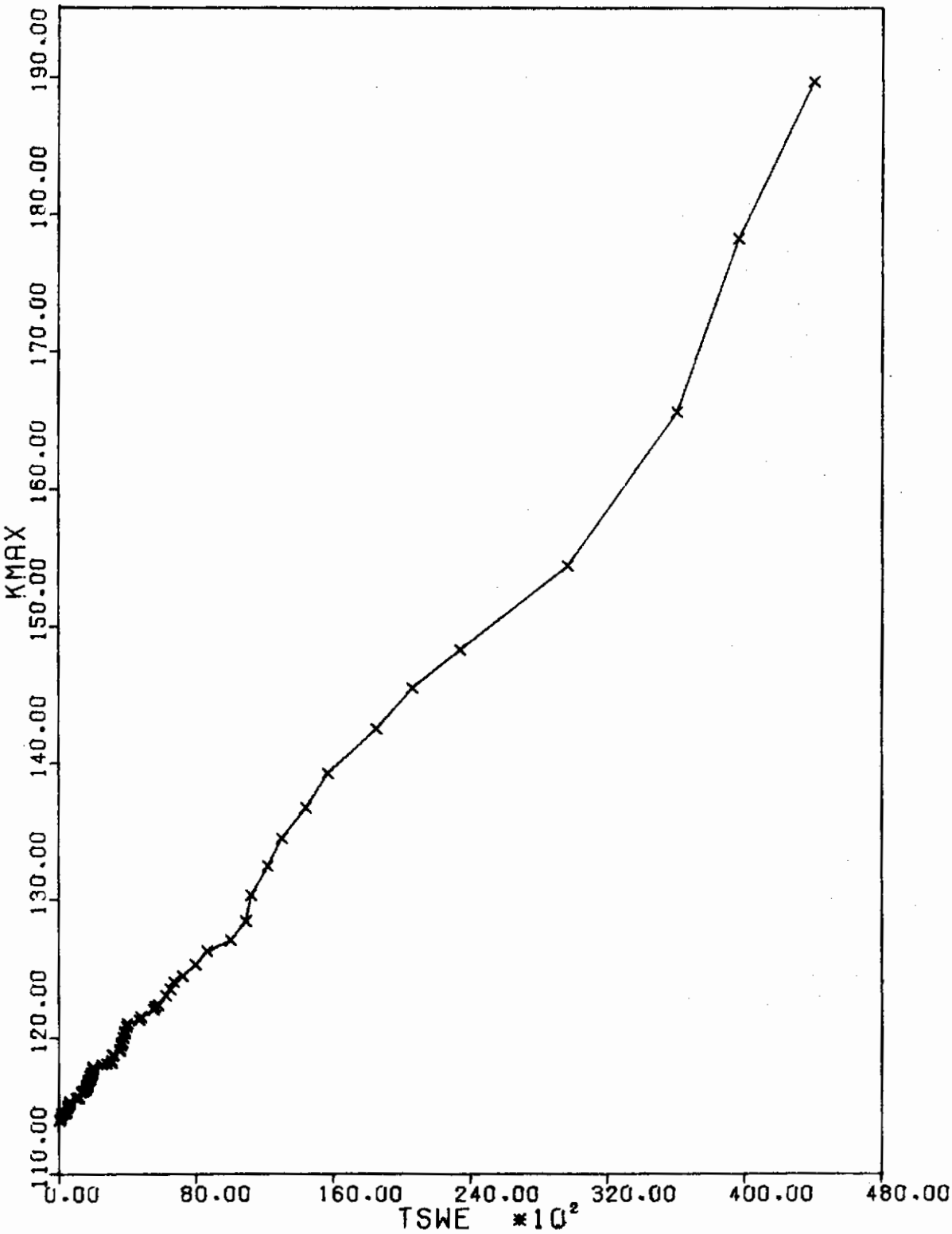

Figure 108. Relationship Between K_{max} and TSWE in Annealed 6Al-4V Titanium Specimen ES23 0.1 in. Thick

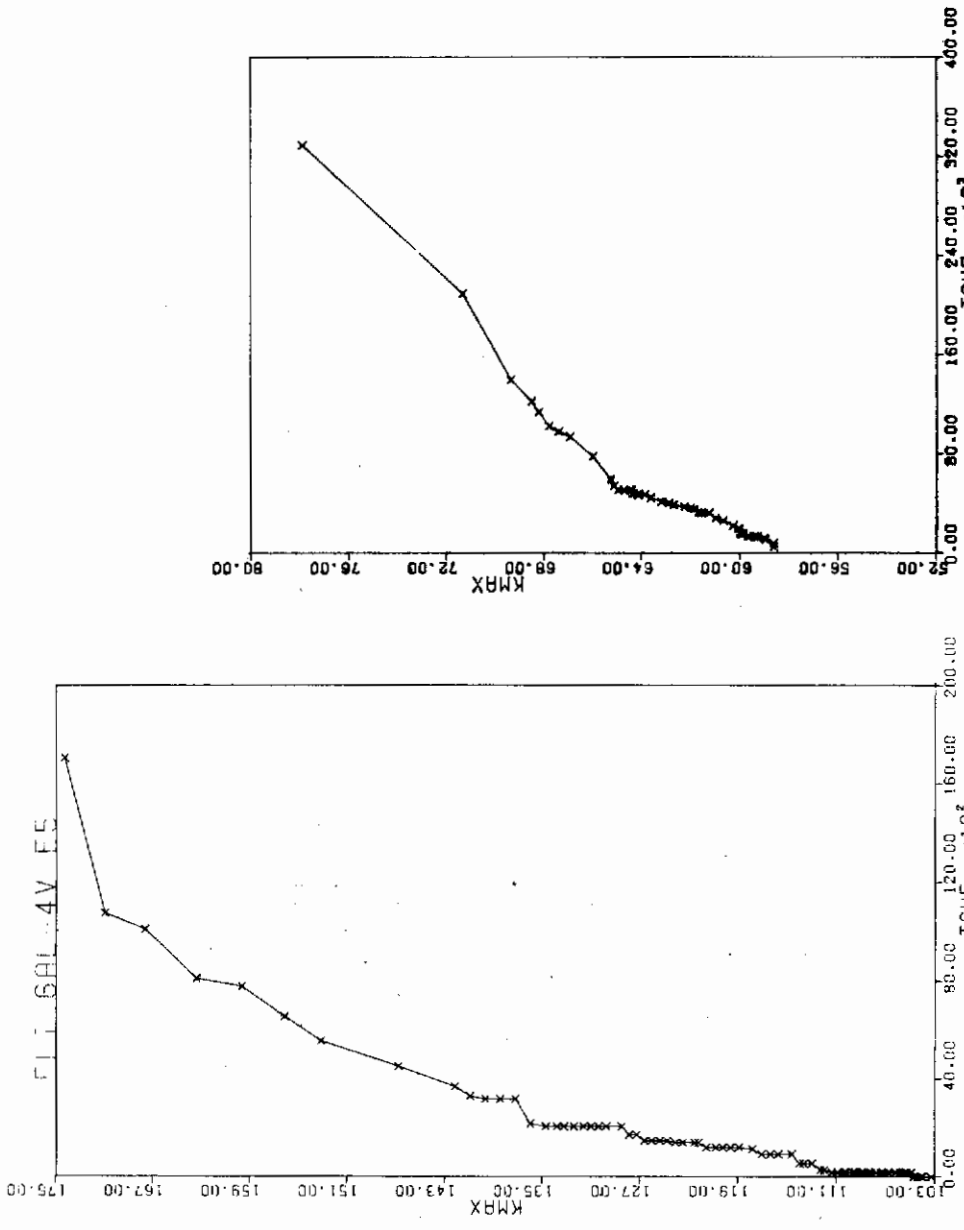

Figure 109. Relationship Between K_{max} and TSWE in Two Heat Treatments of 6Al-4V Titanium - 0.27-in. Thick

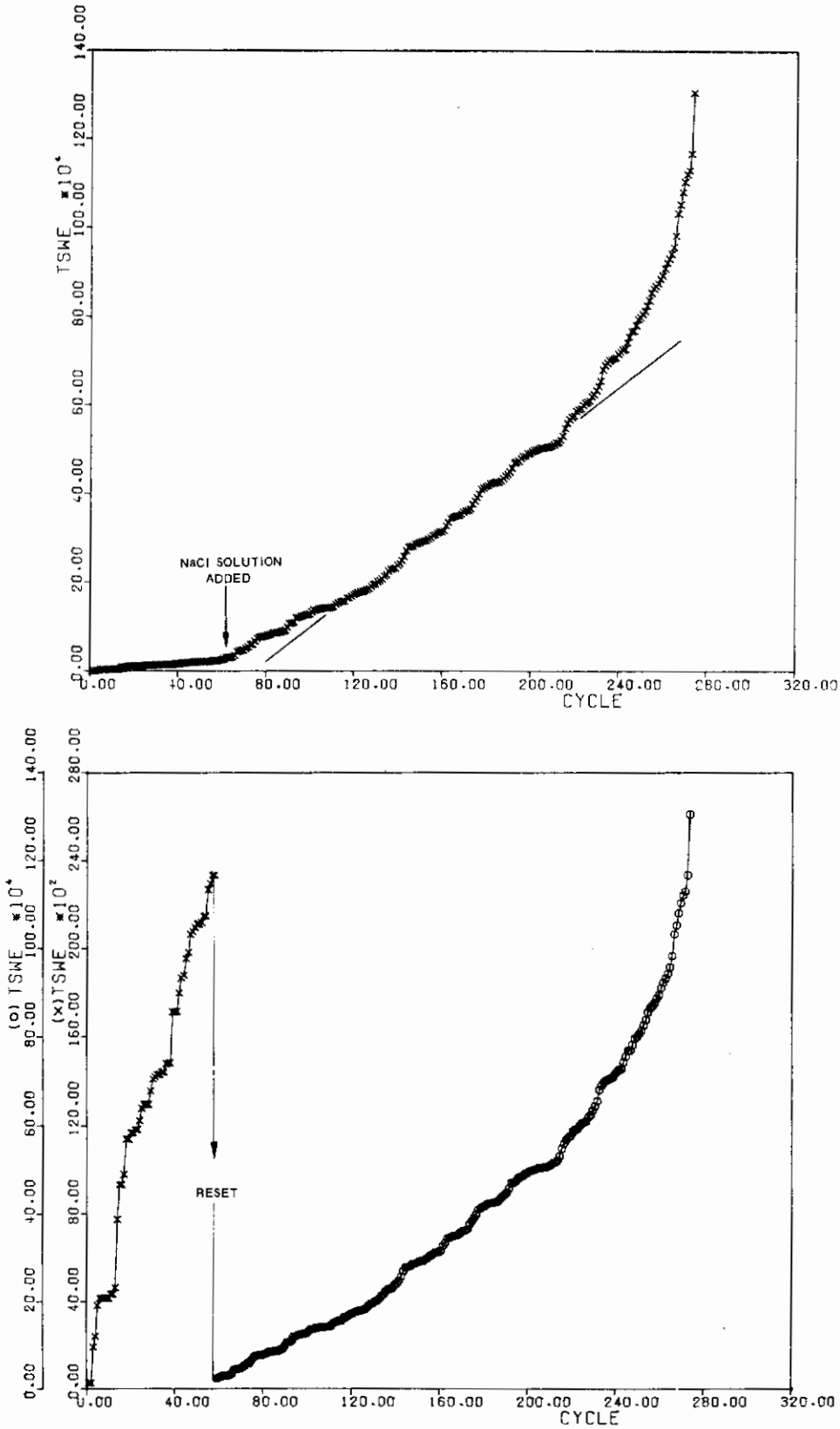

Figure 110. Relationship Between TSWE and Cycle Number in 7075-T6 Aluminum Subjected to Corrosion Fatigue - 0.26-in. Thick

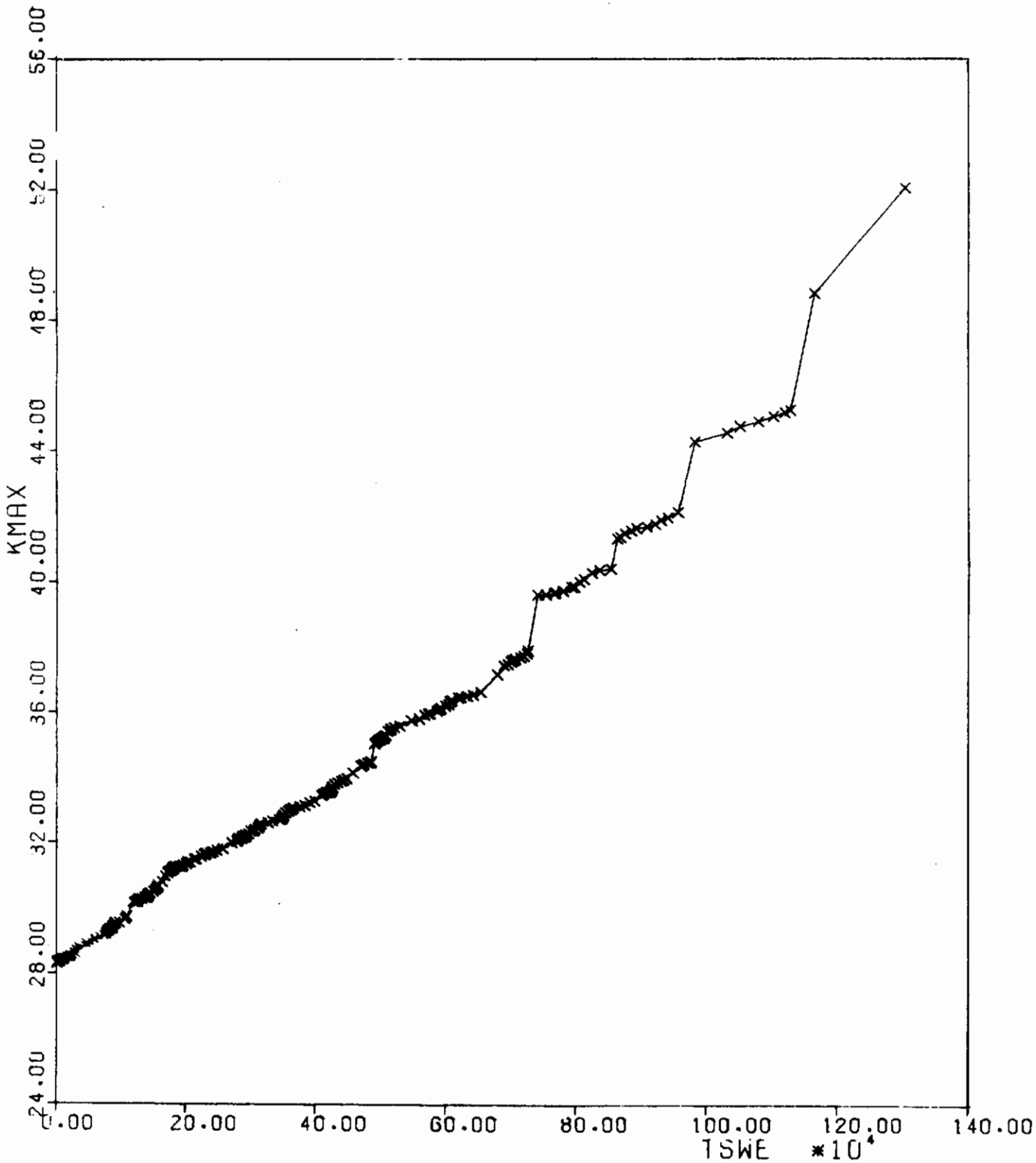

Figure 111. Relationship Between K_{max} and TSWE in 7075-T6 Aluminum Specimen BS-1 0.26 in. Thick

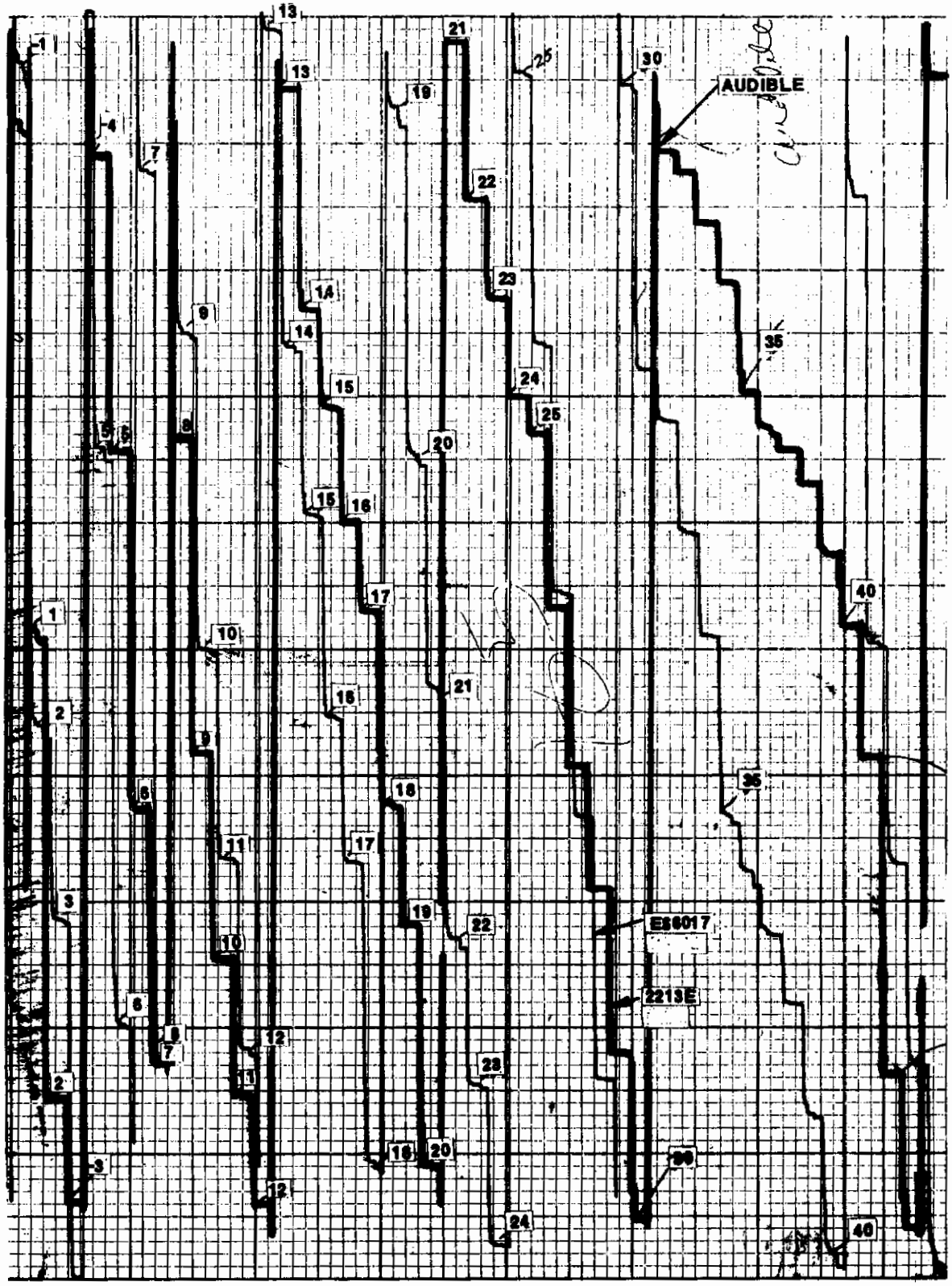

Figure 112. Stress-Wave-Emission Count from Two Sensors Shortly Before Failure of 7075-T6 Aluminum Specimen BS-1 - Cycle Numbers are Indicated

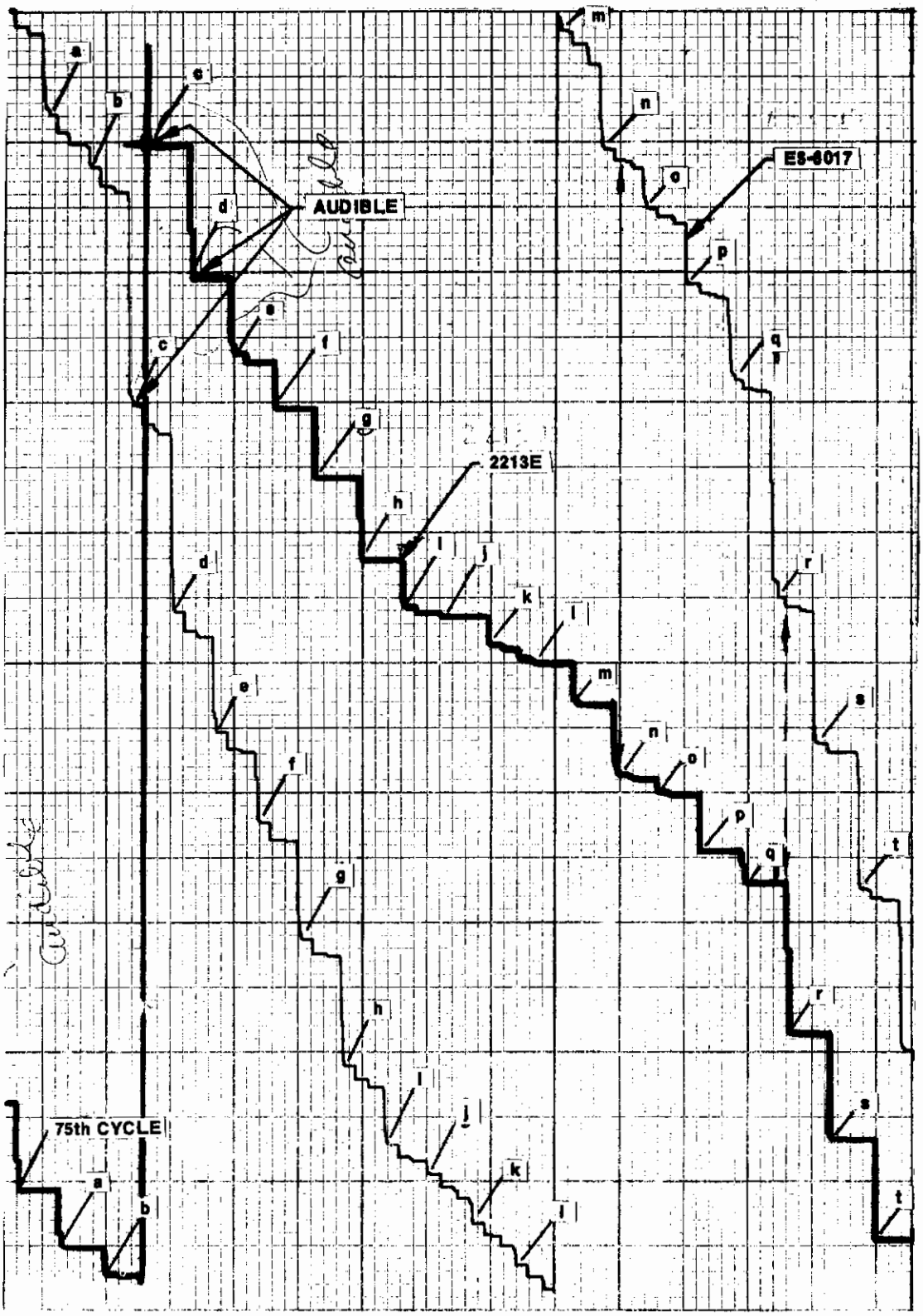

Figure 113. Stress-Wave-Emission Count from Two Sensors 90 Cycles Before Fracture of 7075-T6 Aluminum Specimen BS-1 - Corresponding Signals Indexed Alphabetically

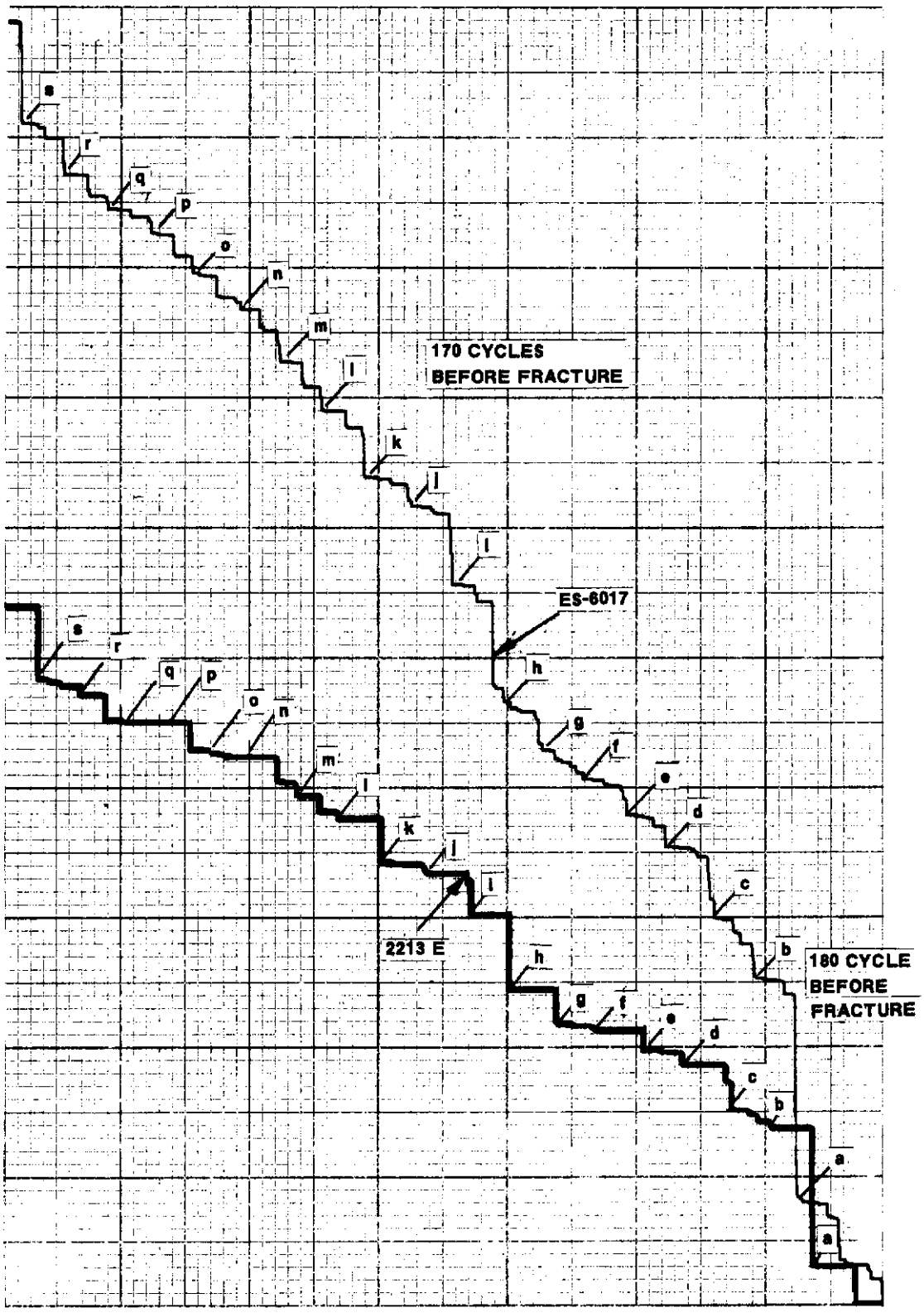

Figure 114. Stress-Wave-Emission Count from Two Sensors 180 Cycles Before Fracture of 7075-T6 Aluminum Specimen BS-1 - Corresponding Signals Indexed Alphabetically

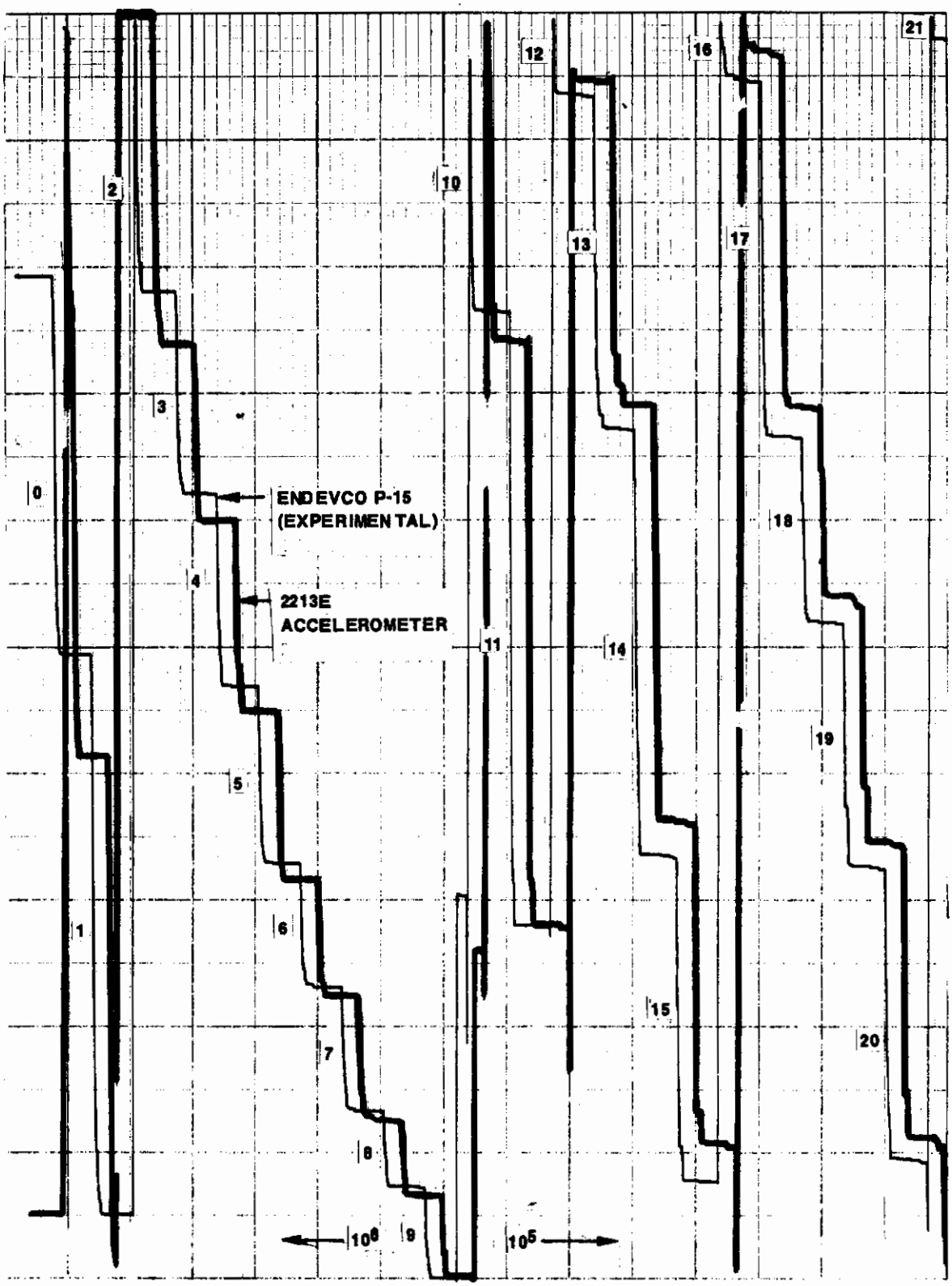

Figure 115. Stress-Wave-Emission Count from Two Sensors Shortly Before Fracture of 1100°F D6aC Specimen 6S27 - Cycle Numbers are Indicated

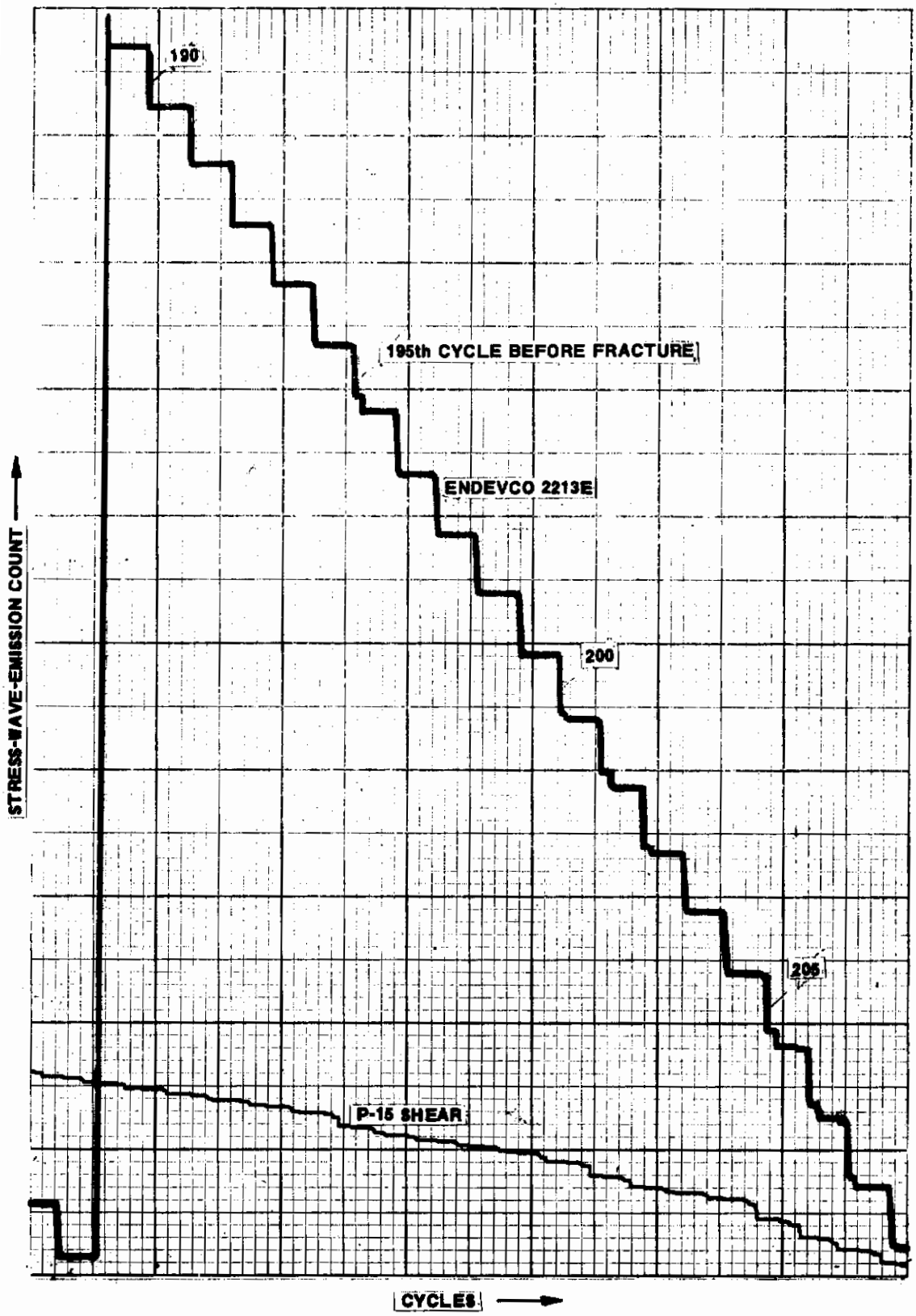

Figure 116. Stress-Wave-Emission Count from Two Sensors 200 Cycles Before Fracture of 1100°F D6aC Specimen 6S27 - Cycle Numbers are Indicated

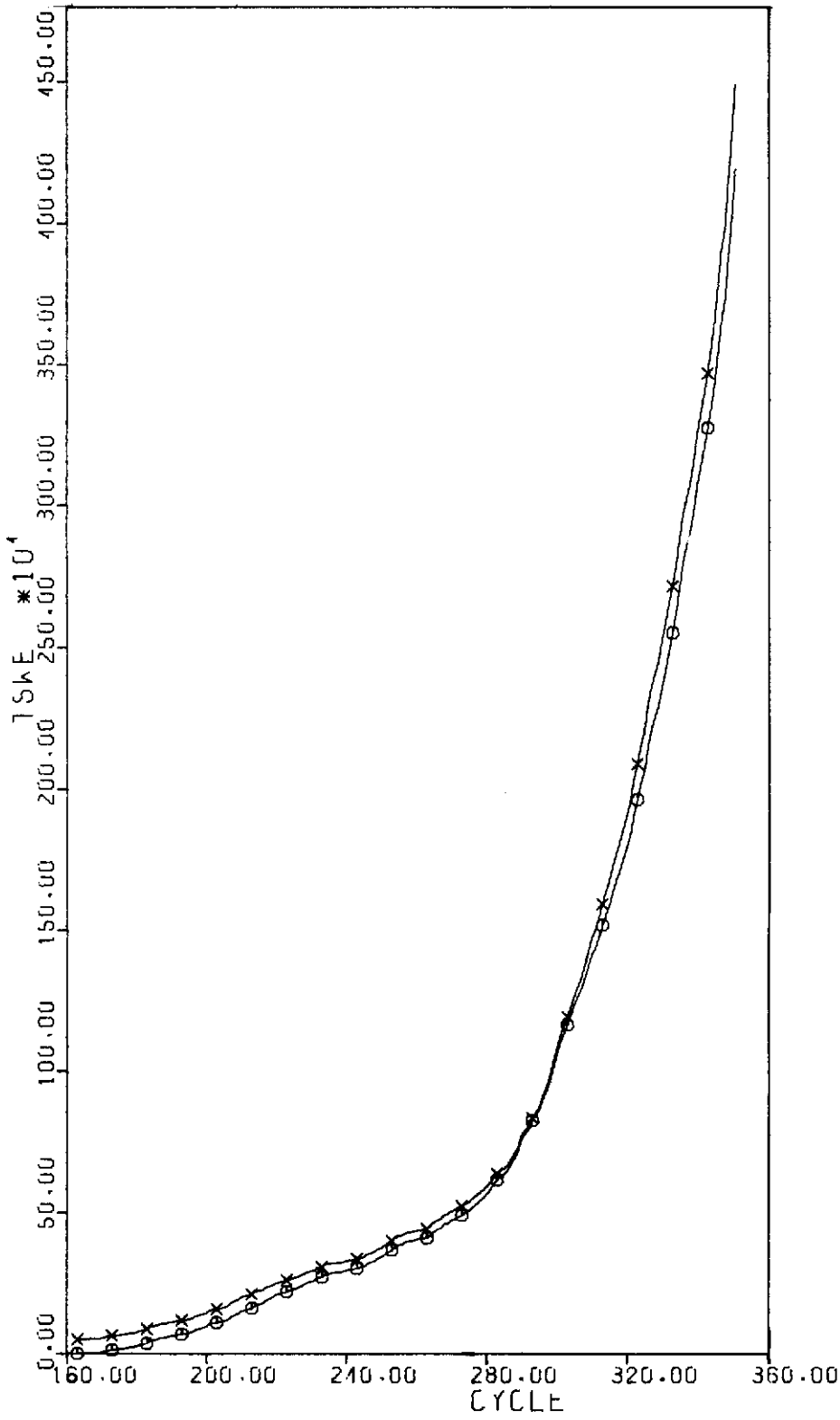

Figure 117. Count versus Cycle Number as Obtained from Two Sensors on 600°F D6aC Specimen 6S23

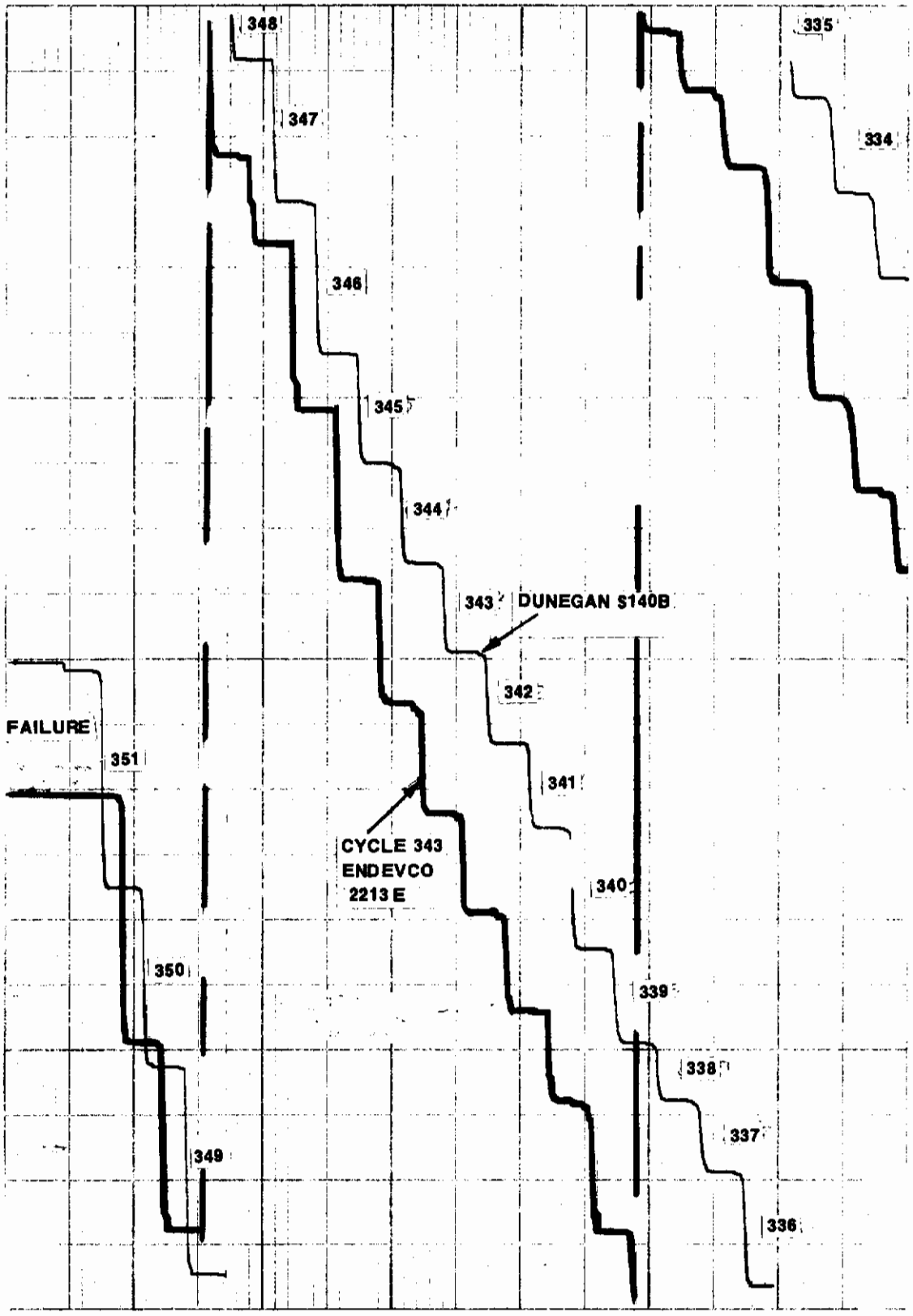

Figure 118. Stress-Wave Emission Count from Two Sensors Shortly Before Fracture of 600°F D6aC Specimen 6S23 - Last 15 Cycles

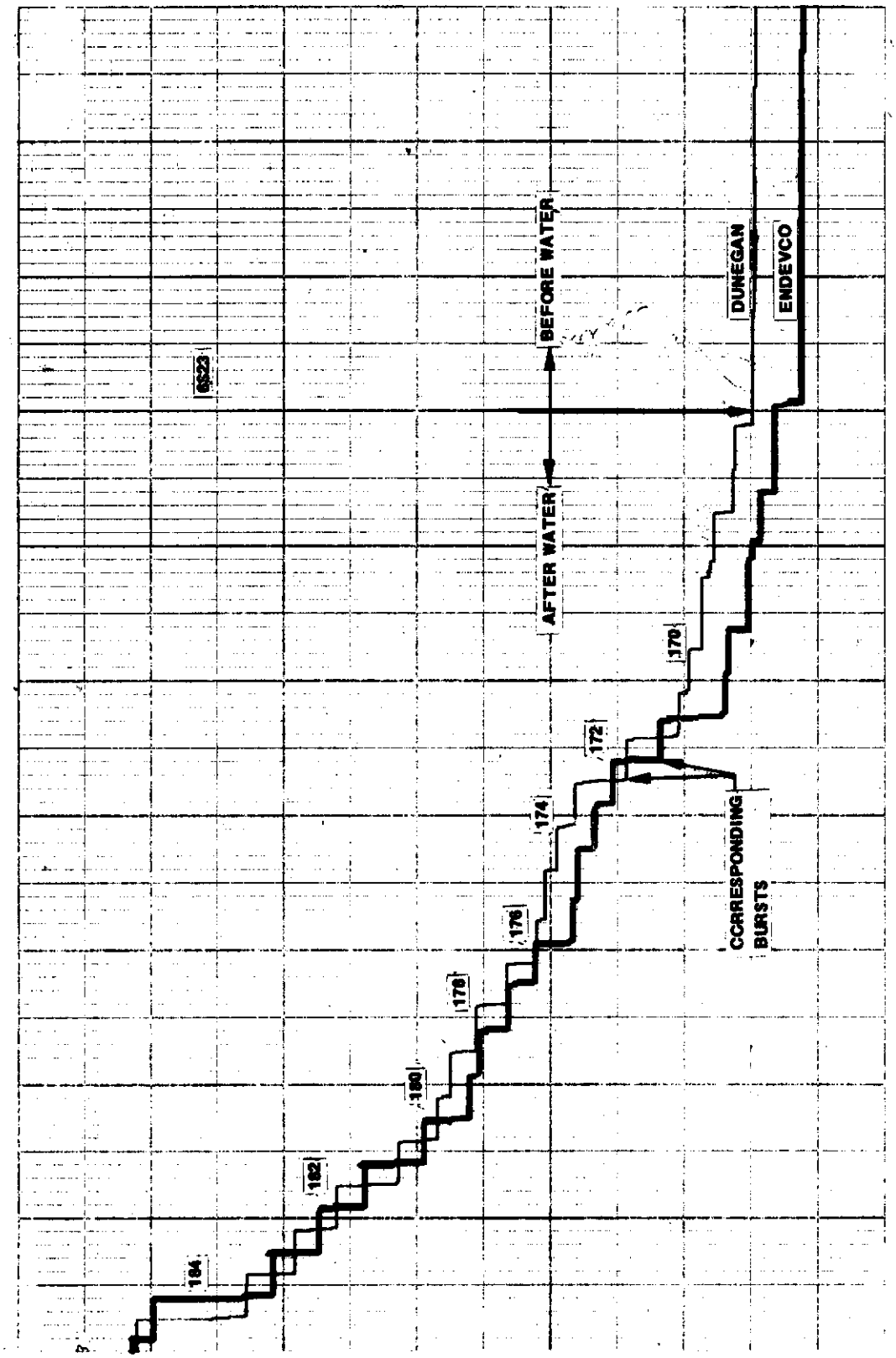

Figure 119. Stress-Wave-Emission Count from Two Sensors at the Time of Adding Water - 188 Cycles Before Fracture of 600°F D6aC Specimen 6S23

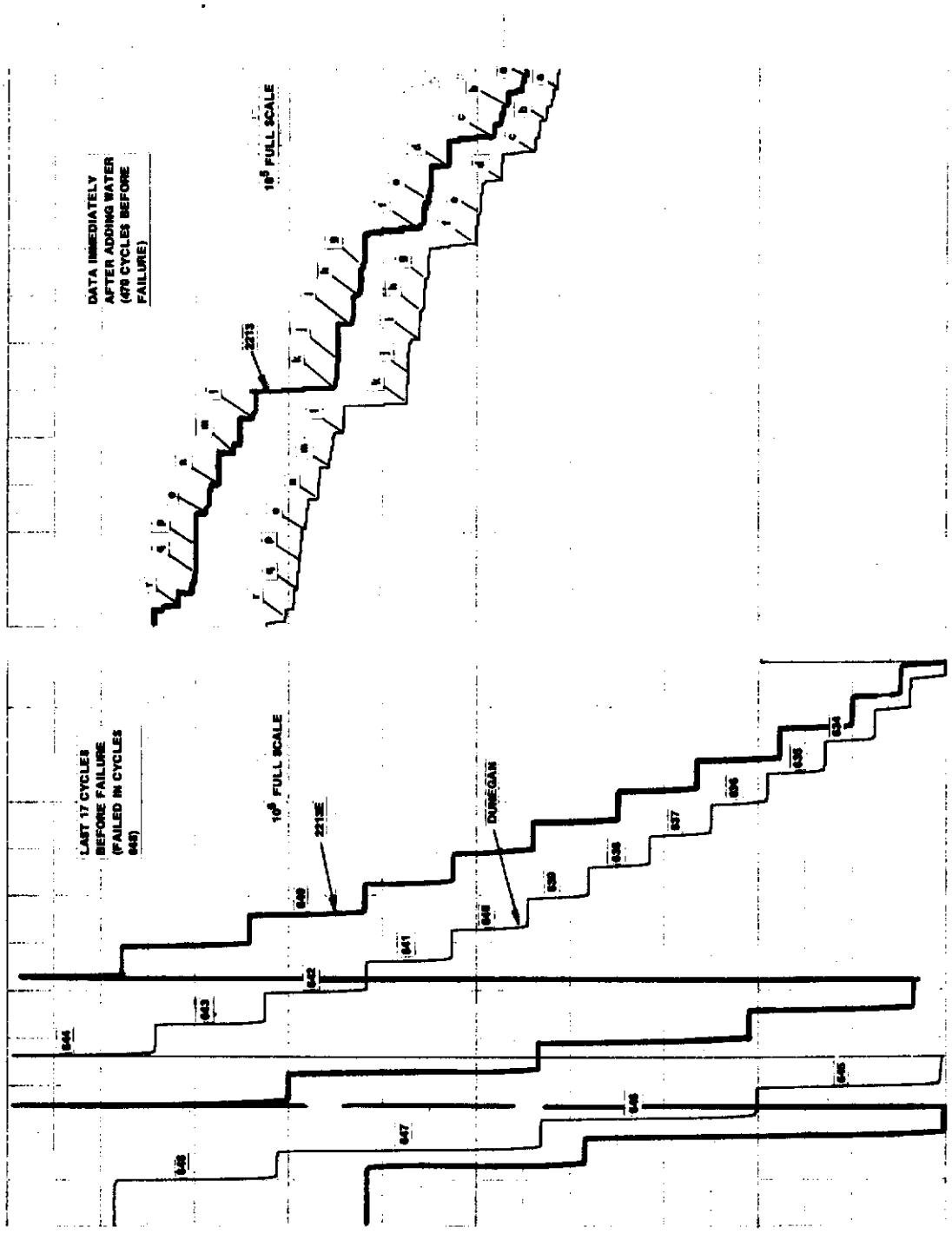

Figure 120. Stress-Wave-Emission Count from Two Sensors Shortly Before Fracture and 470 Cycles Before Fracture of 100°F D6aC Specimen 6947

UNCLASSIFIED

Security Classification

DOCUMENT CONTROL DATA - R&D

(Security classification of title, body of abstract and indexing annotation must be entered when the overall report is classified)

1. ORIGINATING ACTIVITY (Corporate author) Aerojet Solid Propulsion Company P.O. Box 13400 Sacramento, California 95813	2a. REPORT SECURITY CLASSIFICATION UNCLASSIFIED 2b. GROUP

3. REPORT TITLE

Development of a Nondestructive Testing Technique to Determine Flaw Criticality

4. DESCRIPTIVE NOTES (Type of report and inclusive dates)

Final Report, 1 March 1969 through 30 June 1971

5. AUTHOR(S) (Last name, first name, initial)

Hartbower C.E., Morais C. F., Rueter W.G., et al

6. REPORT DATE	7a. TOTAL NO. OF PAGES	7b. NO. OF REFS
January 1972	229	56

8a. CONTRACT OR GRANT NO. F33615-68-C-1705 b. PROJECT NO. c. d.	9a. ORIGINATOR'S REPORT NUMBER(S) 9b. OTHER REPORT NO(S) (Any other numbers that may be assigned this report)

10. AVAILABILITY/LIMITATION NOTICES

Approved for Public Release; Distribution Unlimited.

11. SUPPLEMENTARY NOTES	12. SPONSORING MILITARY ACTIVITY
	Air Force Materials Laboratory Air Force Systems Command Wright Patterson AFB, Ohio

13. ABSTRACT

This report presents the findings of a study to develop a nondestructive testing technique to determine flaw criticality based upon stress-wave emission. The research included an evaluation of various sensors and instrumentation systems, and several materials and material conditions tested to failure in rising load and low-cycle, high-stress-intensity fatigue. The fracture testing utilized a linear-elastic fracture-mechanics approach. Acoustic emission was the basis of the nondestructive inspection technique.

The stress-wave-analysis technique (SWAT) was shown to be a highly sensitive nondestructive inspection method, capable of detecting growing defects at least an order of magnitude smaller than any other known NDI method and, with a computerized system, capable of locating one or more defects in real time. Thus, the stress-wave-analysis technique (SWAT) can be used for in-service, continuous, NDI. When defects emit stress-waves and yet are too small to be confirmed by conventional nondestructive inspection, the suspect area is placed under surveillance using an array of transducers. When the defect approaches critical crack size, the acoustic-emission count rate increases markedly, providing a precursor of crack instability and failure.

DD FORM 1 JAN 64 1473

UNCLASSIFIED

Security Classification

UNCLASSIFIED

Security Classification

14. KEY WORDS	LINK A		LINK B		LINK C	
	ROLE	WT	ROLE	WT	ROLE	WT
Acoustic-Emission Instrumentation Sensor Response Instrumentation Systems Acoustic-Emission as a Precursor of Failure Fracture Testing Subcritical Crack Growth in Low Cycle High Stress Intensity Fatigue						

INSTRUCTIONS

1. ORIGINATING ACTIVITY: Enter the name and address of the contractor, subcontractor, grantee, Department of Defense activity or other organization *(corporate author)* issuing the report.

2a. REPORT SECURITY CLASSIFICATION: Enter the overall security classification of the report. Indicate whether "Restricted Data" is included. Marking is to be in accordance with appropriate security regulations.

2b. GROUP: Automatic downgrading is specified in DoD Directive 5200.10 and Armed Forces Industrial Manual. Enter the group number. Also, when applicable, show that optional markings have been used for Group 3 and Group 4 as authorized.

3. REPORT TITLE: Enter the complete report title in all capital letters. Titles in all cases should be unclassified. If a meaningful title cannot be selected without classification, show title classification in all capitals in parenthesis immediately following the title.

4. DESCRIPTIVE NOTES: If appropriate, enter the type of report, e.g., interim, progress, summary, annual, or final. Give the inclusive dates when a specific reporting period is covered.

5. AUTHOR(S): Enter the name(s) of author(s) as shown on or in the report. Enter last name, first name, middle initial. If military, show rank and branch of service. The name of the principal author is an absolute minimum requirement.

6. REPORT DATE: Enter the date of the report as day, month, year; or month, year. If more than one date appears on the report, use date of publication.

7a. TOTAL NUMBER OF PAGES: The total page count should follow normal pagination procedures, i.e., enter the number of pages containing information.

7b. NUMBER OF REFERENCES: Enter the total number of references cited in the report.

8a. CONTRACT OR GRANT NUMBER: If appropriate, enter the applicable number of the contract or grant under which the report was written.

8b, 8c, & 8d. PROJECT NUMBER: Enter the appropriate military department identification, such as project number, subproject number, system numbers, task number, etc.

9a. ORIGINATOR'S REPORT NUMBER(S): Enter the official report number by which the document will be identified and controlled by the originating activity. This number must be unique to this report.

9b. OTHER REPORT NUMBER(S): If the report has been assigned any other report numbers *(either by the originator or by the sponsor)*, also enter this number(s).

10. AVAILABILITY/LIMITATION NOTICES: Enter any limitations on further dissemination of the report, other than those imposed by security classification, using standard statements such as:

(1) "Qualified requesters may obtain copies of this report from DDC."

(2) "Foreign announcement and dissemination of this report by DDC is not authorized."

(3) "U. S. Government agencies may obtain copies of this report directly from DDC. Other qualified DDC users shall request through _____."

(4) "U. S. military agencies may obtain copies of this report directly from DDC. Other qualified users shall request through _____."

(5) "All distribution of this report is controlled. Qualified DDC users shall request through _____."

If the report has been furnished to the Office of Technical Services, Department of Commerce, for sale to the public, indicate this fact and enter the price, if known.

11. SUPPLEMENTARY NOTES: Use for additional explanatory notes.

12. SPONSORING MILITARY ACTIVITY: Enter the name of the departmental project office or laboratory sponsoring *(paying for)* the research and development. Include address.

13. ABSTRACT: Enter an abstract giving a brief and factual summary of the document indicative of the report, even though it may also appear elsewhere in the body of the technical report. If additional space is required, a continuation sheet shall be attached.

It is highly desirable that the abstract of classified reports be unclassified. Each paragraph of the abstract shall end with an indication of the military security classification of the information in the paragraph, represented as *(TS), (S), (C), or (U)*.

There is no limitation on the length of the abstract. However, the suggested length is from 150 to 225 words.

14. KEY WORDS: Key words are technically meaningful terms or short phrases that characterize a report and may be used as index entries for cataloging the report. Key words must be selected so that no security classification is required. Identifiers, such as equipment model designation, trade name, military project code name, geographic location, may be used as key words but will be followed by an indication of technical context. The assignment of links, rules, and weights is optional.

☆U.S.Government Printing Office: 1972 — 759-086/633

UNCLASSIFIED

Security Classification